Measurement, Characterization and Modeling of Millimeter-Wave Channels: From 60 GHz to 5G

vorgelegt von
Dipl.-Ing.
Michael Peter
geb. in Wertheim

von der Fakultät IV – Elektrotechnik und Informatik
der Technischen Universität Berlin
zur Erlangung des akademischen Grades

Doktor der Ingenieurwissenschaften
– Dr.-Ing. –

genehmigte Dissertation

Promotionsausschuss:

Vorsitzender:	Prof. Giuseppe Caire, Ph.D.
Gutachter:	Prof. Dr.-Ing. Slawomir Stanczak
Gutachter:	Prof. Dr.-Ing. Thomas Kürner
Gutachterin:	Prof. Sana Salous, Ph.D.

Tag der wissenschaftlichen Aussprache: 18. Juli 2017

Berlin 2017

Abstract

Wireless communication and networking have become an important part of our daily lives. New standards and devices promise higher data rates, lower latency and higher reliability. However, there is consensus that the currently used frequency bands below 6 GHz will be insufficient to meet rate requirements of future applications and the growing number of devices. Therefore, the use of frequency resources in the millimeter-wave range is targeted to increase the transmission bandwidths substantially.

Apart from the use for fixed directional radio links, millimeter-wave transmission was initially identified as a promising candidate for high-speed wireless networking of multimedia devices in homes. In most countries, 7 GHz of spectrum are available for unlicensed use in the 60 GHz frequency range. With the start of the research on mobile networks of the fifth generation (5G) it became apparent that the consideration of the millimeter-wave spectrum will also be indispensable for future small-cell deployment. Due to the short wavelength, however, the characteristics of the underlying radio channel differ significantly from those at lower frequencies. As a basis for further developments, the investigation of millimeter-wave channels is thus of particular importance.

This thesis addresses the measurement, characterization and modeling of millimeter-wave channels in application-specific scenarios inside rooms and vehicles as well as outdoors. Eleven selected publications constitute the core of this work. The introductory chapters put them into the context of the research area and introduce basic concepts and terms, which are helpful for the interpretation of the results. In addition, the channel measurement setups are described.

For the measurement campaigns in this work, mainly purpose-built modular setups were used that operate in the time domain and, despite a high measurement bandwidth, allow a very short measuring time. By rapid periodic repetition of the measurement process, this approach allows the acquisition of time-varying channels, or a fine spatial sampling when the receive antenna is moved during the measurement procedure. The resulting large number of acquired channel impulse responses offers decisive advantages for statistical evaluation.

A first comparative measurement campaign was conducted in a conference room at 60 GHz with different antenna configurations. The measurements were repeated at 5 GHz to analyze frequency-specific differences. Based on two further measurement campaigns, the propagation characteristics in the passenger cabin of a wide-bodied aircraft and a car are investigated. The environments differ from typical interior spaces not only in their dimensions, but also in the building materials. Shadowing by human bodies can severely affect millimeter-wave communication links. In addition to related evaluations for the above-mentioned measurement campaigns, the impact of human body shadowing on the direct propagation path is therefore systematically investigated and modeled based on dedicated measurements.

The investigations of outdoor channels are based on five independent measurement campaigns in urban environments and associated ray tracing simulations. First, the 60 GHz backhaul channel is considered in a residential area. By using directional antennas, multipaths were suppressed during the measurement and a range of several hundred meters could be achieved even with an impaired line of sight. The remaining four measurement campaigns were conducted with regard to microcellular millimeter-wave access scenarios and the investigation of the multipath characteristics of the underlying propagation channel with omnidirectional antennas in street canyons as well as on a city square. A very large number of channel impulse responses were acquired for each environment. Further frequency bands above 6 GHz were considered in addition to 60 GHz. For the latest measurement campaign, focusing on the analysis of the frequency-dependence of channel characteristics, a multi-frequency measurement setup was used that enabled simultaneous measurements of four frequency bands between 10 and 82 GHz.

To characterize the channels, the collected data is statistically evaluated and analyzed with respect to specific observations. The focus is on evaluations of the path loss, time dispersion by multipath propagation and the influence of human body shadowing. Models, associated parameters and fundamental conclusions on system design are derived from the results. The findings give information about their dependence on the propagation scenario and transmission frequency. They provide a solid basis for the validation and extension of future channel models.

Zusammenfassung

Drahtlose Kommunikation und Vernetzung sind zu einem wichtigen Teil unseres Alltagslebens geworden. Neue Standards und Endgeräte versprechen stets höhere Datenraten, geringere Latenz und größere Zuverlässigkeit. Allerdings besteht Einigkeit darüber, dass die derzeit genutzten Frequenzbänder unterhalb von 6 GHz nicht ausreichen werden, um den Ratenanforderungen zukünftiger Anwendungen und der wachsenden Anzahl von Endgeräten gerecht zu werden. Deshalb wird die Nutzung von Frequenzressourcen im Millimeterwellenbereich angestrebt, um die Übertragungsbandbreiten substantiell zu erhöhen.

Abgesehen vom Einsatz für Richtfunkverbindungen wurde die Millimeterwellenübertragung zunächst als aussichtsreicher Kandidat für eine sehr hochratige drahtlose Vernetzung von Multimedia-Geräten im Heimbereich entdeckt. In den meisten Ländern stehen dafür im 60 GHz-Bereich 7 GHz Bandbreite lizenzfrei zur Verfügung. Mit dem Beginn der Forschung zu Mobilfunknetzen der fünften Generation (5G) zeichnete sich schließlich ab, dass die Berücksichtigung des Millimeterwellen-Spektrums zukünftig auch für kleine Mobilfunkzellen unverzichtbar ist. Aufgrund der kurzen Wellenlänge unterscheiden sich die Eigenschaften der zugrundeliegenden Funkkanäle allerdings signifikant von denen bei niedrigen Frequenzen. Als Grundlage für weitere Entwicklungen kommt daher der Untersuchung von Millimeterwellenkanälen eine besondere Bedeutung zu.

Die vorliegende Arbeit beschäftigt sich mit der Vermessung, Charakterisierung und Modellierung von Millimeterwellenkanälen in anwendungsspezifischen Umgebungen – sowohl innerhalb von Räumen und Fahrzeugen als auch im Freien. Den Kern der Arbeit bilden elf ausgewählte Publikationen. Die einleitenden Kapitel dienen der Einordnung in das Themengebiet sowie der Einführung von Grundlagen und Begriffen, die zur Interpretation der Ergebnisse hilfreich sind. Darüber hinaus werden die verwendeten Kanalmesssetups beschrieben.

Für die Messkampagnen in dieser Arbeit wurden vorwiegend eigens entwickelte modulare Setups benutzt, die im Zeitbereich arbeiten und trotz einer hohen Messbandbreite eine sehr geringe Messdauer ermöglichen. Durch schnelle periodische Wiederholung des Messvorgangs erlaubt dieser Ansatz die Erfassung von zeitver-

änderlichen Kanälen, beziehungsweise eine feine räumliche Abtastung, wenn die Empfangsantenne während des Messablaufs bewegt wird. Die daraus resultierende hohe Anzahl von erfassten Kanalimpulsantworten bietet entscheidende Vorteile bei der statistischen Auswertung.

Eine erste vergleichende Messkampagne wurde in einem Konferenzraum bei 60 GHz mit verschiedenen Antennenkonfigurationen durchgeführt. Die Messungen wurden bei 5 GHz wiederholt, um frequenzspezifische Unterschiede zu analysieren. Basierend auf zwei weiteren Messkampagnen werden die Ausbreitungseigenschaften in der Passagierkabine eines Großraumraumflugzeugs sowie in einem Kraftfahrzeug untersucht. Die Umgebungen unterscheiden sich nicht nur in den Abmessungen von typischen Innenräumen, sondern auch in den verwendeten Materialien. Im Millimeterwellenbereich kann die Abschattung der Sichtverbindung durch Personen die Übertragung stark beeinträchtigen. Neben damit verbundenen Auswertungen für die oben genannten Messkampagnen wird die Abschattung deshalb auf Basis gesonderter Messungen für den direkten Ausbreitungspfad systematisch untersucht und modelliert.

Die Untersuchungen der Kanäle im Freien basieren auf fünf unabhängigen Messkampagnen im innerstädtischen Bereich und begleitenden Ray-Tracing-Simulationen. Hierbei wird zunächst der 60 GHz-Backhaul-Kanal mit Richtantennen in einem Wohngebiet betrachtet. Die restlichen vier Messkampagnen wurden im Hinblick auf Millimeterwellen-Access-Szenarien mit kleinen Mobilfunkzellen und die Untersuchung der Mehrwegeeigenschaften des zugrundeliegenden Ausbreitungskanals mit omnidirektionalen Antennen in Straßenschluchten sowie auf einem innerstädtischen Platz durchgeführt. Für jede Umgebung wurde eine sehr große Anzahl von Kanalimpulsantworten aufgezeichnet. Neben 60 GHz wurden weitere Frequenzbänder über 6 GHz berücksichtigt. Für die letzte Kampagne, mit der gezielt die Frequenzabhängigkeit der Kanaleigenschaften analysiert werden sollte, wurde ein Multifrequenz-Messaufbau verwendet. Er ermöglichte die simultane Messung von vier Frequenzbändern zwischen 10 und 82 GHz.

Zur Charakterisierung der Kanäle werden die gesammelten Daten statistisch ausgewertet und in Bezug auf besondere Beobachtungen analysiert. Der Fokus liegt dabei auf Auswertungen zum Pfadverlust, der Zeitdispersion durch Mehrwegeausbreitung und dem Einfluss von Abschattung durch Personen. Aus den Ergebnissen werden Modelle, zugehörige Parameter und grundlegende Rückschlüsse auf das Systemdesign abgeleitet. Die Resultate geben Aufschluss über deren Abhängigkeit vom Ausbreitungsszenario sowie der Übertragungsfrequenz. Sie bilden eine verlässliche Grundlage für die Validierung und Erweiterung zukünftiger Kanalmodelle.

Danksagung

Diese Seite sei all jenen Menschen gewidmet, die diese Arbeit ermöglicht haben.

Zunächst möchte ich mich bei Prof. Slawomir Stanczak für die Betreuung meiner Arbeit bedanken. Ebenso danke ich Prof. Thomas Kürner und Prof. Sana Salous für die gute Zusammenarbeit und die Bereitschaft, als Gutachter zur Verfügung zu stehen. Prof. Giuseppe Caire danke ich für die Übernahme des Vorsitzes.

Mein besonderer Dank gilt Wilhelm Keusgen für seine fachliche Anleitung, seinen praktischen Rat und die kollegiale Unterstützung während des gesamten Zeitraums, über die sich die Arbeit erstreckte. Insbesondere möchte ich mich außerdem bei Richard Weiler, Fabian Undi, Thomas Kühne, Andreas Kortke, Benjamin Schubert, Hung-Anh Nguyen, Mike Wisotzki, Panagiotis Paschalidis, Robert Felbecker und allen weiteren Kollegen bedanken, die mich in verschiedenen Phasen in vielfältiger Weise unterstützt haben – sei es durch fachliche Ratschläge und Diskussionen, Hilfe bei den Messungen, dem Verfassen gemeinsamer Publikationen oder wertvoller Gespräche und gemeinsamer Erfahrungen über den Kontext dieser Arbeit hinaus.

Ich bedanke mich innig bei meiner zauberhaften Freundin für ihre aufmunternde Quirligkeit, ihren Zuspruch und ihre Geduld. Weiterhin danke ich all meinen Freunden, Verwandten und Bekannten, die mich in den vergangenen Jahren begleitet und für das notwendige Gleichgewicht in meinem Leben gesorgt haben.

Diese Arbeit widme ich meinen Eltern und meinem Onkel Robert, denen ich damit meine tiefste Dankbarkeit und Wertschätzung entgegenbringen möchte.

List of Publications

This work is a thesis by publication. It is based on the selected publications listed above, which are reprinted in this document. Detailed references are given below and in the bibliography. In the preceding introductory chapters, supplementary background information is provided and the contributions are put into the context of the research area.

1 M. Peter, R. J. Weiler, W. Keusgen, T. Eichler, M. Kottkamp, and A. Nähring. Characterization of mm-wave channel sounders up to W-band and validation of measurement results. In *10th European Conference on Antennas and Propagation (EuCAP 2016)*, April 2016. DOI: 10.1109/EuCAP.2016.7481708

2 M. Peter and W. Keusgen. Analysis and comparison of indoor wideband radio channels at 5 and 60 GHz. In *3rd European Conference on Antennas and Propagation (EuCAP 2009)*, March 2009. INSPEC Accession Number: 10699120. Available online: http://ieeexplore.ieee.org/document/5068424 [07/2017].

3 M. Peter and W. Keusgen. Impact of antenna configuration and shadowing on the characteristics of the 60 GHz indoor wideband radio channel. In *XXIXth General Assembly of the International Union of Radio Science (URSI GA 2008)*, August 2008. Available online: http://www.ursi.org/proceedings/procGA08/papers/C10p1.pdf [07/2017].

4 M. Peter, W. Keusgen, and M. Schirrmacher. Measurement and analysis of the 60 GHz in-vehicular broadband radio channel. In *IEEE 66th Vehicular Technology Conference (VTC 2007-Fall)*, September–October 2007. DOI: 10.1109/VETECF.2007.183

5 M. Peter, R. Felbecker, W. Keusgen, and J. Hillebrand. Measurement-based investigation of 60 GHz broadband transmission for wireless in-car communication. In *IEEE 70th Vehicular Technology Conference (VTC 2009-Fall)*, September 2009. DOI: 10.1109/VETECF.2009.5378803

6 M. Peter, M. Wisotzki, M. Raceala-Motoc, W. Keusgen, R. Felbecker, M. Jacob, S. Priebe, and T. Kürner. Analyzing human body shadowing at 60 GHz: Systematic wideband MIMO measurements and modeling approaches. In *6th European Conference on Antennas and Propagation (EuCAP 2012)*, March 2012. DOI: 10.1109/EuCAP.2012.6206013

7 M. Peter, R. J. Weiler, T. Kühne, B. Göktepe, J. Serafimoska, and W. Keusgen. Millimeter-wave small-cell backhaul measurements and considerations on street-level deployment. In *2015 IEEE Globecom Workshops (GC Wkshps)*, December 2015. DOI: 10.1109/GLOCOMW.2015.7414178

8 M. Peter, R. J. Weiler, B. Göktepe, W. Keusgen, and K. Sakaguchi. Channel measurement and modeling for 5G urban microcellular scenarios. *Sensors*, 16(8):1330, 2016. DOI: 10.3390/s16081330

9 M. Peter, W. Keusgen, and R. J. Weiler. On path loss measurement and modeling for millimeter-wave 5G. In *9th European Conference on Antennas and Propagation (EuCAP 2015)*, April 2015. INSPEC Accession Number: 15416843. Available online: http://ieeexplore.ieee.org/document/7228939 [07/2017].

10 W. Keusgen, R. J. Weiler, M. Peter, and M. Wisotzki. Propagation measurements and simulations for millimeter-wave mobile access in a busy urban environment. In *9th International Conference on Infrared, Millimeter, and Terahertz Waves (IRMMW-THz 2014)*, September 2014. DOI: 10.1109/IRMMW-THz.2014.6955989

11 M. Peter, R. J. Weiler, F. Undi, F. El-Kanawati, S. Jaeckel, L. Raschkowski, L. Thiele, K. Sakaguchi, and W. Keusgen. Investigations on the frequency dependence of the delay spread in an UMi street canyon scenario. In *2016 International Symposium on Antennas and Propagation (ISAP)*, October 2016. INSPEC Accession Number: 16602061. Available online: http://ieeexplore.ieee.org/document/7821230 [07/2017].

Contents

Acronyms and Abbreviations

3D	Three-dimensional
3G	Third generation mobile network
3GPP	3rd Generation Partnership Project
4G	Fourth generation mobile network
5G	Fifth generation mobile network
ADC	Analog-to-digital converter
AGC	Automatic gain control
APDP	Average(d) power delay profile
AWG	Arbitrary waveform generator
BPF	Bandpass filter
CCDF	Complementary cumulative distribution function
CF	Crest factor
CFR	Channel frequency response
CIR	Channel impulse response
CL	Comparison level
COST	European Cooperation in Science and Technology
CRP	Carbon fiber reinforced plastic
CS	Channel sounder
CTF	Channel transfer function
D2D	Device-to-device
DAC	Digital-to-analog converter
deg	Angular degree
DKE	Double knife-edge
DMA	Deviation of maximum attenuation

DPP	Deviation of pseudo period
DSO	Digital sampling oscilloscope
DVD	Digital versatile disk
EASY-A	Enablers for Ambient Services & Systems Part A—60 GHz Broadband Links (project)
EMC	Electromagnetic compatibility
FCC	Federal Communications Commission
FCF	Frequency correlation function
FPGA	Field-programmable gate array
FRP	Floating reference point
FSRP	Free-space reference point
FWHM	Full width at half maximum
FZC	Frank-Zadoff-Chu
GO	Geometrical optics
GPU	Graphics processing unit
GRP	Glass fiber reinforced plastic
GSCM	Geometry-based stochastic channel model
GUI	Graphical user interface
HBS	Human body shadowing
HHI	Heinrich Hertz Institute
HIRATE	High Performance Digital Radio Testbed
HPBW	Half power beamwidth
IDR	Instantaneous dynamic range
IEEE	Institute of Electrical and Electronics Engineers
IF	Intermediate frequency
IFE	Inflight entertainment
IMMPL	Instantaneous maximum measureable path loss
IMT	International mobile telecommunications

IP	Intercept point
IPDP	Instantaneous power delay profile
IQ	Inphase/quadrature phase
ITU-R	International Telecommunication Union Radiocommunication Sector
LNA	Low noise amplifier
LO	Local oscillator
LOS	Line of sight
LS	Least squares
LTE-A	Long-Term Evolution Advanced (3GPP 4G technology)
LTI	Linear time-invariant
LTV	Linear time-variant
METIS	Mobile and wireless communications Enablers for Twenty-twenty (2020) Information Society (project)
MIMO	Multiple input multiple output
MiWEBA	Millimetre-Wave Evolution for Backhaul and Access (project)
MLS	Maximum length sequence
mm-wave	Millimeter wave
mmMAGIC	Millimetre-Wave Based Mobile Radio Access Network for Fifth Generation Integrated Communications (project)
MMPL	Maximum measureable path loss
MMSE	Minimum mean square error
MP3	MPEG (Motion Picture Experts Group) Layer-3
MPC	Multipath component
MTC	Machine-type communication
NF	Noise figure
NLOS	Non line of sight
NRP	Normalized received power
NYU	New York University
OFDM	Orthogonal frequency division multiplexing

OLOS	Obstructed line of sight
omni	Omnidirectional (antenna)
OO	Antenna configuration: omnidirectional at Tx and Rx
OS-CC	Open square, city center
OTA	Over the air
OV	Antenna configuration: omnidirectional at Tx and Vivaldi at Rx
PA	Power amplifier
PACF	Periodic autocorrelation function
PAPR	Peak-to-average power ratio
PAS	Power angular spectrum
PC	Personal computer
PDF	Probability density function
PDP	Power delay profile
PHY	Physical layer
PL	Path loss
pol.	Polarization
PPW	Perpendicular walk
QD	Quasi-deterministic
QuaDRiGa	Quasi Deterministic Radio Channel Generator
RF	Radio frequency
RMPC	Resolvable multipath component
RMS	Root mean square
RSE	Rear seat entertainment
RT	Ray tracing
RX, Rx	Receiver
SC-CC	Street canyon, city center
SC-RA	Street canyon, residential area
SCM	Spatial channel model

SE	Shadowing event
SIR	Signal-to-interference ratio
SISO	Single input single output
SNR	Signal-to-noise ratio
STC	Space-time coding
SUV	Sport utility vehicle
TDL	Tapped delay line
TOA	Time of arrival
TX, Tx	Transmitter
UMi	Urban microcellular
US	Uncorrelated scattering
UTD	Uniform geometrical theory of diffraction
UWB	Ultra wideband
VGA	Variable gain amplifier
VHT	Very high throughput
VNA	Vector network analyzer
VV	Antenna configuration: Vivaldi at Tx and Rx
WIGWAM	Wireless Gigabit With Advanced Multimedia Support (project)
WINNER	Wireless World Initiative for New Radio (project)
WLAN	Wireless local area network
WPAN	Wireless personal area network
WRC	World Radiocommunication Conference
WSS	Wide-sense stationary
WSSUS	Wide-sense stationary uncorrelated scattering

1 Introduction

1.1 Millimeter Waves for Wireless Communication

Wireless communication is an integral part of our lives today. Driven by the proliferation of smartphones and tablets, mobile data traffic has grown by 4000-fold over the past ten years and the uptrend continues. It is expected that there will be 11.6 billion mobile-connected devices by 2020—exceeding the world's projected population [Cis17]. Besides human-centric applications, machine-type communication (MTC) is expected to gain decisive influence on this development [NGM15].

In the course of the deployment and the growing popularity of fixed-line broadband internet, wireless local area networks (WLANs) based on the IEEE 802.11 standard family emerged as wireless short-range technology to connect computers in homes and offices. At the beginning of the millennium, when the packet-based data service has just been introduced in mobile networks of the second generation, first extensions of 802.11 already offered data rates up to 54 Mbit/s [BC13]. Most of today's multimedia devices support current releases of the standard for transmission in the 2.4 and 5 GHz bands.

The continuously growing number of devices in conjunction with the increasing data rates has made bandwidth to be a very rare resource. Utilizing spectrum at millimeter-wave (mm-wave) frequencies is therefore seen as one of the key elements to meet the requirements in the next decade. In the context of short-range indoor communication, the course for exploiting mm-waves was already set in 2001, when the Federal Communications Commission (FCC) released the 60 GHz band for unlicensed use in the United States. Incited by the availability of 7 GHz bandwidth, several 60 GHz standards have been developed—starting with WirelessHD and ECMA-387 in 2008 and IEEE 802.15.3c in 2009. Finally, in 2012, the 60 GHz technology found its way into the successful 802.11 family in form of an amendment for very high throughput (IEEE 802.11ad). The standard supports data rates up to 7 Gbit/s. Furthermore, it is backward compatible, which is seen as an important factor for the spread of 60 GHz technology in the future.

At the time when the FCC released the 60 GHz band—mainly due to the reasoning

that it is not useful for applications besides indoor short-range wireless systems because it lies in the oxygen absorption peak—the third generation (3G) of mobile networks was about to emerge. Millimeter waves were neither regarded as being suitable nor needed for mobile communications. However, the tremendous increase in mobile data traffic over the past years in the age of 4G caused a fundamental rethinking. Undoubtedly, the oxygen absorption imposes a physical restriction on the range of 60 GHz links. Moreover, the free-space path loss and the penetration losses are very high at mm-wave frequencies. However, utilizing much higher bands is the only way to increase the transmission bandwidth substantially. Furthermore, bands besides 60 GHz could be allocated and massive network densification has anyhow already led to continuously shrinking cell sizes and thus bridgeable distances. It is therefore taken for granted that mm-wave technology will find its way into 5G networks. They are expected to be ultra-dense and heterogeneous, seamlessly integrating cellular as well as WLAN radio access technologies to maximize the users' quality of experience [GPA+15, WPK+14a].

Extensive research is required to enable and advance the utilization of mm-waves. Since accurate channel models are needed as basis for system design, performance assessment and deployment, it is important to measure and characterize propagation at mm-wave frequencies [SEF+16]. A big challenge in this context are the many applications and associated propagation environments, mm-wave transmission is destined for [Gar12, ICT15b, NGM15]. Moreover, various bands besides 60 GHz are proposed for usage in 5G and are to be studied [Int15d, ICT16a].

In this dissertation, I present my work on the investigation and characterization of mm-wave channels. It is based on extensive channel measurement campaigns in several environments. Motivated by the availability of the unlicensed spectrum, they have a focus on 60 GHz. Although mainly indoor applications have initially been envisaged in this band, it is also well suited to conduct research on 5G mm-wave outdoor backhaul and access scenarios [WPK+14a, ICTa]. As it became apparent that a plurality of frequency bands might be considered for 5G implementations [Int15d], the investigations were extended to a larger frequency range. This is reflected by the later publications in this work, including results from 10 to 82 GHz. The findings have been submitted to the scientific community and standardization bodies. I believe that they substantially contribute to the understanding of mm-wave propagation and channel modeling for 5G, in particular with regard to the scenario- and frequency dependence of channel characteristics.

1.2 State of the Art and Research Gaps

The availability of appropriate channel models is seen as a key issue for the development of new wireless communication systems and the improvement of existing ones. Since there is a continuous need for rate and capacity enhancements, channel measurement and modeling are permanent research topics, at least since the development of the first digital cellular network was kicked off in the 1980s. Two formerly orthogonal research areas are involved in 5G channel model development: research on mm-wave propagation and research towards the evolution of cellular networks. Millimeter-wave transmission has typically been associated with indoor scenarios, whereas cellular networks are still operated at significantly lower frequencies.

In the following, a brief overview of representative publications on measurement campaigns is given and the main findings are summarized with special focus on the multipath characteristics of the channel. Furthermore, recent activities on 5G channel modeling and remaining research gaps are addressed.

1.2.1 Millimeter-Wave Channel Measurements in Indoor and In-Cabin Environments

Numerous mm-wave measurement campaigns were conducted since the 1990s, primarily related to short-range indoor communication in the 60 GHz frequency band. Smulders et al. performed narrowband and wideband measurements (2 GHz bandwidth) around 60 GHz in several indoor environments, using biconical horn antennas with omnidirectional radiation patterns [SW92a, SW92b, SC97]. Shadowing effects were found to be considerably more severe than at lower frequencies. The 60 GHz channel turned out to be clearly time-dispersive. Root-mean-square (RMS) delay spread values of 15–45 ns were observed in small rooms for line-of-sight (LOS) and obstructed line-of-sight (OLOS). Large indoor environments yielded values of 30–70 ns, with 100 ns as worst-case observation.

Droste and Kadel presented a measurement system, based on a vector network analyzer (VNA) and a positioner, with results at 17 and 60 GHz [DK95]. The delay spread was practically identical for both frequencies, ranging from 2 to 13 ns in a small room and from 8 and 25 ns in a corridor. The authors also demonstrated that measured paths can be reconstructed by calculating the angle-of-arrival pattern from the spatial Doppler spectra and combining it with the respective delay information and the geometry of the scenario.

The effect of antenna directivity was addressed by Manabe et al. by exemplary measurements at 60 GHz with a VNA and ray tracing in an empty room [MTS+94,

MMI96]. Four different types of receive antennas from omnidirectional to narrow-beam (5° half-power beam width) were employed along with an omnidirectional transmit antenna. With increasing directivity, the RMS delay spread decreased from 18 to 1 ns. Using circular instead of linear polarization was proposed to achieve a further reduction. However, the authors pointed out that the susceptibility of the links to blockage or shadowing by moving human bodies could be a drawback of using directive antennas. In contrast, based on VNA measurements at 62.5 GHz in six LOS indoor environments, Siamarou and Al-Nuaimi reported that the delay spread could not be reduced by using a directional antenna at the receiver (Rx) instead of an omnidirectional one [SAN01, ANS02]. The values, not exceeding 70 ns, were found to be practically identical for both antenna configurations. Furthermore, the authors concluded that the channel characteristics are determined by the principal structure of the environments and do not depend significantly on minor details like furniture and room fixtures.

Measurements at 60 GHz with a sliding correlator channel sounder, a directional horn at the Rx and an open-ended waveguide at the transmitter (Tx) were conducted by Xu et al. [XKR02]. The analysis yielded delay spread values from 5 to 47 ns in hallways and rooms when the Rx antenna pointed towards the Tx, and from 8 to 76 ns when it pointed into different directions. In addition, angular characteristics were derived by rotating the Rx antenna. The authors concluded that ray tracing of first order and second-order reflections is sufficient for channel prediction for LOS applications, but metallic objects and the wall structure need to be considered.

Zwick et al. performed measurements at 60 GHz in different rooms with a wideband time-domain channel sounder [ZBN05]. A measurement bandwidth of 5 GHz was realized by frequency concatenation. Delay spread values between 1 and 20 ns were observed (median: 3–9 ns), in tendency increasing with the room size. A relatively low path loss exponent of 1.33 was found for the office scenario. Based on the analysis, the authors propose a simple stochastic multipath channel model for office environments.

Recent measurement campaigns, mainly in the context of 5G research, have been increasingly focused on directional channel characteristics. They either are based on virtual array analysis, hence spatial sampling of the channel [GTW+11, MAB15], or directional scanning [DFM+14, KUW+15, MMS+09]. The evaluations in [GTW+11] indicate that diffraction around the objects blocking the LOS is a significant propagation mechanism at 60 GHz. The double-directional measurements in [MAB15] yielded directional spreads in the range 10–30 degrees for LOS and 25–60 degrees for NLOS. In [DFM+14] and [KUW+15], the channel was measured

in a small offices scenario at 60 GHz. Corresponding angle spreads are in the range 8–20 degrees and delay spreads in the range 4–11 ns. Only a few dominant specular multipath components could be identified in [KUW+15] and depolarization is not significant for most of the detected paths.

A comparative study based on measurements at 60 and 5 GHz in a conference room is part of this thesis [PK09] (see Section 4.1). The impact of the antennas is investigated in [PK08] (Section 4.2). Human body shadowing (HBS) is discussed in [PWRM+12] (see Section 4.5). The related measurements were conducted in a conference room, but the presented analysis is independent from the measurement environment.

There is only a limited number of publications on mm-wave propagation in vehicles. Investigations in an aircraft cabin with a real-time channel sounder at 60 GHz were made by Garcia et al. [GKT+09, GATM+11]. The delay spread was found to be strongly dependent on the antenna configuration and the Rx position (simulating the access point), but not exceeding 10 ns. The influence of time-variant human body shadowing in the same environment was statistically analyzed in [GKT+10]. In [PK07, PKS07], 60 GHz channel measurements in a wide-bodied aircraft passenger cabin were conducted by W. Keusgen and myself. The publication [PKS07] is part of this thesis and presented in Section 4.3.

The 60 GHz in-car channel was measured with VNA-based channel sounders in [STO+09, PFKH09, SJK10, NK12]. The derived delay spreads do not exceed 8 ns. In [SJK10], low values between 0.7 and 2.0 are reported, whereas the same environment yielded about four times higher values at ultra-wideband (UWB) frequencies around 7 GHz. The publication [PFKH09] is part of this thesis and discussed in Section 4.4.

1.2.2 Millimeter-Wave Channel Measurements in Outdoor Environments

Several publications also reveal early interest in mm-wave transmission and propagation aspects for outdoor applications, e.g. [VEDS88, TCS94, BS94, SA95, CR96]. Since channel characterization above 6 GHz was identified as a crucial research topic to pave the road for ultra-high capacity 5G networks, increasing efforts have recently been put into channel sounding and more relevant measurement data is becoming available from academic and industry sources with preliminary statistical and analytical characterizations. From 2011 onwards, various measurement campaigns in urban mircocellular environments have been carried out by the group around Professor Rappaport (University of Texas at Austin and NYU Wireless) at 28, 38, 60 and 73 GHz, using a wideband sliding correlator channel sounder with steerable directional horn anten-

nas at both the Tx and Rx [BDRQL11, RQT+12, RBDMQ12, RASM12, RGBD+13]. Hur et al. used a similar hardware setup for evaluations at 28 GHz in in-building, campus and urban environments [HCL+14, HCKP14, HCK+15]. The measurements were complemented by ray tracing simulations to enable statistical evaluations on additional urban scenarios [CBH+14, HBK+15].

The most important finding of these investigations is that multipath propagation is an issue for mm-wave outdoor propagation as it is for indoor scenarios. Buildings, the ground, cars and also small objects like trash cans or signs act as good reflectors. The path loss exponent was found to be close to two for LOS scenarios. Some variation towards smaller or larger values in the range between $n = 1.9$–2.5 were observed due to strong multipath or partially obstructed LOS conditions [RBDMQ12, RQT+12, RASM12, MHP98]. Trees primarily cause losses when they obstruct relevant propagation paths. Shadowing effects are more severe than at lower frequencies and losses caused by persons, trees and rooftops can be very high. Therefore, only LOS scenarios have formerly been considered for mm-wave communication. Although they are still the main focus, the presence of specular reflections with significant power also motivates the usage of mm-waves under OLOS or non-line-of-sight (NLOS) conditions for cell sizes up to a few hundred meters. It is assumed that electronically steerable antennas will enable to establish a link by pointing to one of the available reflection sources. In [BDRQL11, RQT+12], usable NLOS paths were found to be 10 to 40 dB weaker compared to LOS, where the losses can be limited by selecting always the strongest NLOS path. Diffuse scattering does not yield strong contributions and might be hard to exploit [SC97]. Assuming an intercept point that corresponds to free-space propagation, NLOS path loss exponents are in the range 3.2–4.2 in connection with a shadowing standard deviation of $\sigma = 8.4$–13.4 dB. These findings are similar to path loss results at lower frequencies, but related to smaller cell sizes and directional antennas.

Time dispersion in outdoor LOS scenarios was found to be relatively small (RMS delay spread typically below 20 ns), but the results are highly dependent on the environment as well as on the antennas [SC97, CR96]. Very low RMS delay spreads (up to only 1.4 ns) were observed for the peer-to-peer and cellular scenarios in [RBDMQ12, BDRQL11], where 25 dBi antennas were used at both sides. Values to be considered for point-to-point links with higher antenna gains can be even lower ($\tau_{\text{rms}} < 0.21$ ns with 45 dBi antenna gain according to E-band specifications observed in [KKV12]). When also (partially) obstructed LOS conditions are taken into account, the delay spread can take values up to 16 ns [RQT+12]. For NLOS, the delay spread further increases. Though average values are still moderate (7–24 ns),

maximum values exceeding 100 ns have been reported [RQT+12, RBDMQ12].

In summary, the RMS delay spread observed for mm-wave outdoor channels is of the same order of magnitude as for indoor channels, where values between 10 and 100 ns have been found [SC97, ZBN05]. It stays one order of magnitude below the delay spread emerging at traditional cellular frequencies—for example typical values up to 2 µs for microcellular sites at 900 and 1900 MHz can be found in [SRS90] and [FBR+94]. However, it should be emphasized that the mm-wave results are usually associated with directional antennas and transmission distances below 200 m.

1.2.3 Channel Modeling towards 5G

Early fundamental modeling work regarding radio propagation at high frequencies was done by Liebe, who published a mm-wave propagation model already in 1989 [Lie89]. It incorporates atmospheric effects such as oxygen and water vapor absorption and the impact of precipitation. Apart from them, however, propagation in free space is assumed.

Two 60 GHz channel models have been proposed in the framework of IEEE 802.11ad and IEEE 802.15.3c standards development [Foe02, MMS+10b]. Parameters are available for indoor environments such as offices, living rooms and lobbies. Many of the aforementioned measurement-based studies on indoor propagation also describe simple stochastic modeling approaches along with parameters for the specific environment. The models, however, are neither directly applicable to outdoor or large indoor environments (e.g., street canyons, city squares, stadiums) nor suitable for system-level evaluations in heterogeneous wireless networks.

Substantial work has been carried out during the last decades to elaborate reference channel models for cellular communications in the classical frequency bands. The most important outcomes are the 3rd Generation Partnership Project (3GPP) spatial channel models (SCMs) 3GPP-SCM and SCM-E [3rd03, BHS05], the European Cooperation in Science and Technology (COST) 273 model [Cor06], the Wireless World Initiative for New Radio (WINNER) I+II models [IST05, IST07] and the IMT-A channel model [Int09]. Since the models were insufficient to study multiple-input multiple-output (MIMO) configurations with large antenna arrays, they have been further extended towards three dimensions (3D), yielding the models of WINNER+ [WIN10], COST 2100 [LOP+12, VZ12] (partly 3D), 3GPP-3D [3rd15] and the related QuaDRiGa [JBTJ12, JRBT14].

Modeling activities for frequency bands above 6 GHz took place in the METIS [ICTb] and the MiWEBA [ICTa] project. In METIS, a map-based (deterministic) model, a stochastic model, and a hybrid model have been developed [ICT15a]. The

stochastic model provides several extensions of the WINNER+ and 3GPP-3D models and channel parameters for the range 50–70 GHz. The quasi-deterministic (QD) channel model proposed by MiWEBA [ICT14, WPK+16a] is an extension of the IEEE802.11ad 60 GHz channel model towards outdoor access, backhaul/fronthaul, and device-to-device (D2D) scenarios. Most relevant specular components are modeled deterministically, while other components are modeled stochastically.

Ray tracing (RT) has been shown to be a valuable approach to model mm-wave indoor as well as outdoor channels in a deterministic manner [PJK12, FRKP12, OHG15]. Moreover, such map-based prediction tools are increasingly seen as an alternative and complement to measurements to extract parameters for stochastic channel models [CBH+14, HBK+16]. Other simple geometric/map-based models have been proposed for specific scenarios such as street canyons with less computational complexity [KKV12, RFS10].

Based on the campaigns between 28 and 73 GHz, the group of Professor Rappaport proposed a statistical spatial channel model for system evaluations [SR15]. It is similar to 3GPP-3D, but e.g. introduces a LOS/NLOS blockage model. In the mmMAGIC project [ICTc], various measurement campaigns were carried out and a channel model has been proposed. It is based on the 3GPP-3D model, put provides several extensions and parameter tables for mm-wave frequencies [ICT16b]. Contemporary with the mmMAGIC initial channel model, a further 5G initial channel model has been proposed by a group of universities and companies [Aal15] and updated later [Aal16]. In 3GPP, related work was started in March 2016 and yielded a study with a recommended model above 6 GHz [3rd16a]. Its refinement and validation is ongoing.

1.2.4 Challenges and Research Gaps

The ultimate target of 5G channel modeling activities is to develop a flexible and comprehensive frequency-agile channel model, which enables accurate link and system level studies for 5G wireless networks. It should be valid over the entire frequency range from 0.5 to 100 GHz and for all relevant deployment and usage scenarios, including outdoor as well as indoor environments. Further requirements include the support of large bandwidth and very large antenna arrays [ICT16b, Aal16]. Despite considerable progress in recent years, much research is still needed to clarify fundamental questions and to validate, parametrize and enhance model features.

It is a major challenge to provide statistically reliable measurement data to put such a complex model on a solid foundation. In this context, coordinated channel measurements and evaluations will play a key role. Although numerous channel measurement campaigns have been reported in the literature, the amount of available

data is still limited. Since high-performance electronically steerable antennas or MIMO setups with many antenna elements are not yet available for measurement purposes, directional information is typically obtained by successively scanning all (relevant) angles with mechanically steerable directional antennas. The scanning takes a considerable time, and the number of observation points in space is therefore quite small. However, a large number of measurement points at various distances, multiple frequencies and for LOS as well as NLOS are needed for each deployment scenario to validate models, examine dependencies and extract precise parameters.

The comparison and fusion of results originating from independent measurement campaigns made by different researchers is a difficult task. The capabilities of channel sounders can differ greatly and the data processing may affect extracted parameters and conclusions. For example, it is obvious that the results may not only depend on the specific scenario, but also on the measurement antennas, the antenna deconvolution method, the evaluation thresholds and the measurement bandwidth. It is therefore of utmost importance to agree on common definitions and procedures. To investigate the dependence of channel characteristics on boundary conditions such as propagation environment or frequency, it is nevertheless favorable to utilize results that have been achieved with the same equipment and post-processing. In particular, the frequency dependence of channel characteristics has not yet been sufficiently investigated. Accurate quantitative comparisons in dynamic environments require channel sounding equipment that is able to capture multiple frequency bands simultaneously.

Beyond doubt, ray tracing is an attractive approach to predict the site-specific channel in a deterministic manner and to complement measurement results by simulations. The advantages are apparent: simulations are less costly and time consuming and provide all information about the channel in the space/angle and the delay domain without restrictions that are associated with measurement hardware. However, the requirements on model accuracy are very high, especially for outdoor scenarios when the number of dominant propagation paths is quite limited. It is crucial that the model well reproduces these paths, because they essentially determine the characteristics of the channel. In addition, measurements have shown that the received power and the RMS delay spread may vastly vary even in the same environment [RASM12, RBDMQ12]. Calibrating the ray tracer to a particular propagation scenario does not necessarily ensure a good prediction for a different scenario. It is therefore important to further evaluate the accuracy of ray tracing results and assess their applicability to stochastic modeling.

This thesis is based on comprehensive measurement campaigns in various indoor,

in-cabin and outdoor environments. In direct connection to the above-mentioned challenges, the investigations aim to extend the knowledge about site-specific mm-wave channels and highlight important issues with regard to measurement, data analysis and 5G channel modeling. The contributions are outlined in the following section.

1.3 Contributions and Structure of this Thesis

This work is a thesis by publication. It is based on ten peer-reviewed publications that I have authored as first author [PWK+16, PK09, PK08, PKS07, PFKH09, PWRM+12, PWK+15, PWG+16, PKW15, PWU+16] and one peer-reviewed publication with my co-authorship [KWPW14]. Thematically sorted, they are reprinted in Chapters 3–5, each assigned to a section (Sections 3.8–5.5).

In addition, I have authored [PKL08, PKB08, PKF07, PK07, PKK07] and co-authored [NMP+16, GPWK16, HOI+16, HPM+16, WPK+16b, WPK+16a, JPS+16, JMP+16, MPK+16, RSV+16, TvWA+16, WKM+16, WPK+15a, WPK+15c, GPWK15, HBK+15, NvWF+15, WKP+15, WPK+15b, WKNP14, WPK+14a, WPK+14b, WPKW14, HCK+15, JPK+13a, JPK+13b, KKPW13, FRKP12, GATM+11, KKK+11, KGF+11, SPF+11, FKP11, ULP+10, FKKP09, FKP08b, FKP08a, LKKP08b, LKKP08a, PGP06] further publications on mm-wave communication and channel modeling that are closely related to this work. They are referenced in this thesis where appropriate. Other co-authored papers are related to car-to-car channel measurement and modeling and outdoor propagation at lower frequencies [PNM+16, MPK+13, PMK+12, PMK+11a, PMK+11b, PMK+10, PKM+09, PWK+08a, PWK+08b, TPJ06].

The investigations leading to this work have been carried out to a large extent within the publicly funded research projects WIGWAM [WIG], EASY-A [EAS], MiWEBA [ICTa], METIS [ICTb] and mmMAGIC [ICTc].

An overview of the structure and contents of this thesis is given below.

Chapter 2: Wave Propagation and Channel Modeling

This chapter gives an overview of wave propagation mechanisms, channel description and fundamental modeling approaches. The representation of multipath channels and the characterization of random channels are addressed in more detail, since they are the basis for investigations in this work. The definitions and explanations aim to clarify the terms that are used in the course of the document and facilitate the interpretation of results.

Chapter 3: Channel Sounding Principles and Implementation

In this chapter, the concept of channel sounding is introduced along with implementation aspects such as sounding sequence selection, timing and calibration. Since several different measurement setups were used in the course of this work, which are only partly described in the respective publications, they are depicted in Section 3.5. Selected aspects on data processing and analysis are discussed in Section 3.6, and fundamental issues on the comparison of measurement results are taken up in Section 3.7. Section 3.8 opens the publication-based part of this thesis. It addresses the characterization of channel sounders and the validation of measurement results and involves exemplary measurement data from different channel sounder setups at 28 and 82 GHz. All subsequent sections in Chapter 4 and Chapter 5 are based on publications.

Chapter 4: Indoor and In-Vehicle Measurement Campaigns and Evaluations

This chapter is composed of six papers and is focused on the investigation of the 60 GHz channel in relation to ultra-high capacity WLANs and short-range links inside rooms and vehicles. Based on four independent channel measurement campaigns, evaluations for three enclosed spaces are presented, namely a conference room in the Heinrich Hertz Institute (HHI) building (Sections 4.1+4.2), a passenger cabin of a wide-bodied aircraft (Section 4.3) and a car (Section 4.4). In Section 4.2, the impact of the antenna configuration on the radio channel in the conference room is addressed. Since human body shadowing has a severe impact on the 60 GHz link, it is analyzed and modeled separately in Section 4.5. Although the related measurement campaign was conducted in the conference room, the results are not limited to this environment.

The presented investigations had initially been motivated by the increasing interest in utilizing the 60 GHz band for high data rate short-range communication after the release for unlicensed use by the FCC. In the context of current channel measurement and modeling activities for 5G mm-wave networks, where mm-waves are expected to be an integral part indoors as well as outdoors, the results have gained new topicality. Since a uniform methodology and the same tools were used for the indoor/in-vehicle and outdoor evaluations (presented in Chapter 5), the results feature good comparability and provide valuable insight into the scenario-dependence of mm-wave propagation.

Chapter 5: Outdoor Measurement Campaigns and Evaluations for Millimeter-Wave Backhaul and Access

In direct relation to 5G channel modeling activities, this chapter presents channel measurement campaigns and modeling aspects for microcellular outdoor scenarios at frequencies above 6 GHz. It is composed of five publications. They comprise results from five independent measurement campaigns in just as many environments. Section 5.1 addresses the small-cell backhaul channel in a residential area at 60 GHz. Based on the findings, fundamental conclusions on deployment and system design are derived. Section 5.2 presents comprehensive measurement and supportive ray tracing results for the urban access channel in two different street canyon scenarios and on an open square. The investigations focus on path loss modeling and statistical analysis of the delay spread. The associated measurement campaigns were conducted with the same setup, with identical bandwidth and they comprise a huge number of channel observations. Since the comparison and fusion of measurement results from different origins is increasingly important for 5G modeling, the impact of the measurement bandwidth and the number of samples on the path loss model parameters are addressed in Section 5.3. In Section 5.4, further aspects on path loss model refinement and a beamsteering-centric path loss modeling approach are presented. In addition to the comparisons between 10 and 60 GHz in Section 5.2, the frequency dependence of the channel's delay spread in a street canyon is analyzed explicitly in Section 5.5, based multi-frequency measurement data at 10, 28, 41 and 82 GHz, which has been acquired simultaneously.

1.4 Notation

Round brackets ( ) are used to signify the dependency variable for continuous and discrete quantities, namely signals and functions. Discrete quantities are signified by the subscript of the index at the dependency variable. Let $x(t)$ by a continuous quantity dependent on $t \in \mathbb{R}$, then the discrete quantity sampled at $t_n \in \mathbb{R}$, $n \in \mathbb{N}$, is written as $x(t_n)$.

The compact discrete form notation with square brackets [ ], $x[n] := x(t_n)$, is used in the case of equidistant sampling $t_n = nT$, $T \in \mathbb{R}$, $n \in \mathbb{N}$, and in relation to sequences. A sequence $\{s[n]\}$ of length N_{seq} is defined by its elements $s[n] \in \mathbb{C}$, $n = 0, 1, \ldots, N_{\text{seq}} - 1$. To simplify the notation, the braces in $\{s[n]\}$ are also omitted if the meaning is clear from the context. Hence $s[n]$ is used to denote the sequence as well as its elements. $\mathcal{F}\{\cdot\}$ denotes the Fourier transform.

The notation throughout the included papers slightly differs in some places.

However, the symbols are always clearly defined in the respective publications.

The term millimeter-wave (mm-wave) technically refers to electromagnetic waves with a wavelength between 1 and 10 mm, corresponding to radio frequencies between 30 and 300 GHz. In the context of 5G development, the term is usually used to denote frequency bands between 6 and 100 GHz. This approach is also adopted in this work, where the outdoor measurements at 10 and 28 GHz are part of the investigations for mm-wave access.

2 Wave Propagation and Channel Modeling

The wireless channel describes the alteration of the received signal against the transmitted signal. In the literature, different terms such as radio channel, wireless channel, propagation channel and mobile channel are used in a non-uniform manner. In this work, a distinction is made between the radio channel and the propagation channel, as illustrated in Figure 2.1 and e. g. proposed in [Ste92, SMB01, Gus14, Han15]. The term wireless channel or just channel is used as generic term to denote both types of channels.

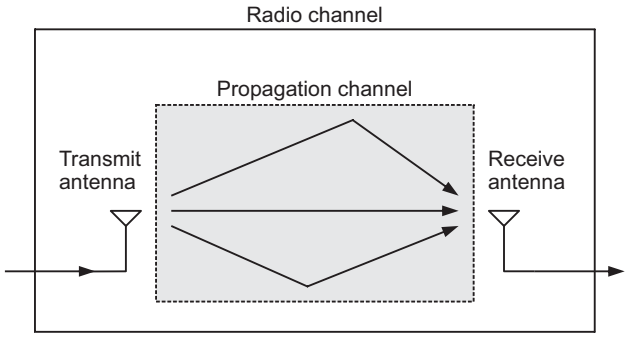

Figure 2.1: Distinction between radio channel and propagation channel.

The propagation channel is constituted by everything that affects wave propagation between the transmit and the receive antenna, namely the propagation medium (e. g. air) and any objects causing attenuation, reflection, diffraction and scattering. These effects, which are described in Section 2.1 in more detail, are the cause for multipath propagation and thus the time-dispersive nature of the channel. It is assumed that involved media are both linear and bilateral, which implies that the propagation channel is linear and reciprocal [Ste92]. The propagation channel is the channel that a radio system would experience when using isotropic Tx and Rx antenna elements [Gus14].

The radio channel is constituted by the transmit antenna, the propagation channel and the receive antenna and therefore includes antenna properties such as antenna gain as well as alignment errors and polarization effects. It depends on the antennas

whether the radio channel is reciprocal. According to [Ste92, Lia88] an antenna exhibits the same transmit and receive radiation pattern in free space, hence is reciprocal, if it is bilateral, linear and passive. If both antennas are reciprocal, so is the radio channel. Nonlinearities are usually small and can be neglected.

Section 2.1 first gives an overview of the wave propagation mechanisms that constitute the propagation channel with considerations on their frequency dependence. The concepts of deterministic and stochastic channel modeling are briefly introduced in Section 2.2. Section 2.3 addresses the representation of multipath channels and the characterization of random channels in more detail. Large-scale fading and path loss are finally introduced in Section 2.4.

2.1 Wave Propagation Mechanisms

Radio wave propagation is affected by various physical mechanisms, resulting in a more or less strongly distorted version of the original communication signal arriving at the receiver. Mechanisms to be considered are free-space propagation, object penetration, reflection, scattering, diffraction as well as absorption caused by atmospheric gases, fog and precipitation. To what extent each phenomenon contributes to the overall signal attenuation and distortion highly depends on the propagation scenario. The propagation mechanisms are briefly discussed in the following with focus on their relevance to indoor and outdoor links and their frequency dependence.[1]

2.1.1 Free-Space Propagation

Free-space propagation conditions can be assumed if the first Fresnel zone is substantially free of obstacles and atmospheric effects as well as reflections are negligible. As illustrated in Figure 2.2, the first Fresnel zone is an imaginary spheroid centered on the line of the direct transmission path with the antennas in the focal points. Its radius at any point P on the center line is given by [Par00]

$$r_{\mathrm{Fr},1} = \sqrt{\frac{\lambda d_1 d_2}{d}}, \tag{2.1}$$

where λ denotes the wavelength, d_1 is the distance of P from the Tx antenna, d_2 is the distance of P from the Rx antenna, and $d = d_1 + d_2$ is the distance between the Tx and Rx antenna.

[1] I provided parts of Section 2.1 as input to the white paper [The14].

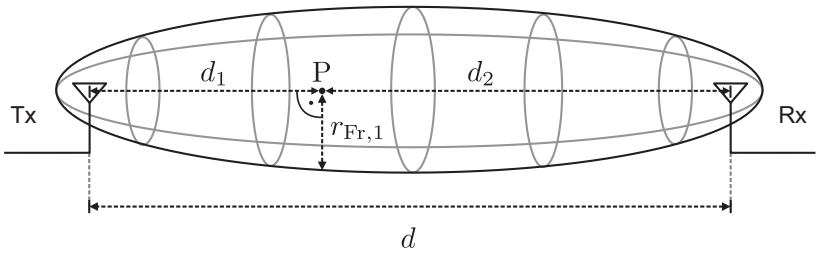

Figure 2.2: Illustration of first Fresnel zone and related quantities.

The radius takes its maximum in the middle of the link (for $d_1 = d_2 = \frac{d}{2}$):

$$r_{\mathrm{Fr},1,\max} = \frac{\sqrt{\lambda d}}{2}. \tag{2.2}$$

Hence, for a fixed link distance, the maximum radius scales with the square root of the wavelength. Values of 2.7, 1.2, 0.35 and 0.16 m e. g. arise for $d = 100\,\mathrm{m}$ and carrier frequencies of 1, 5, 60 and 300 GHz respectively. The radius of the first Fresnel zone is thus quite small at mm-wave frequencies. For typical 60 GHz indoor scenarios with $d \leq 20\,\mathrm{m}$, it remains below 16 cm.

Under free-space propagation conditions, the available power at the Rx antenna can be calculated from the well-known Friis equation [Fri46, Has93]

$$P_R = P_T G_T G_R \left(\frac{\lambda}{4\pi d}\right)^2, \tag{2.3}$$

where P_T, G_T and G_R are the transmit power, the gain of the Tx antenna (in the direction of the Rx antenna) and the gain of the Rx antenna (in the direction of the Tx antenna), respectively. Equation (2.3) is valid in the far-field of the transmit antenna, also denoted as Fraunhofer region [Rap02].

The free-space path loss L_{fs}, describing the loss between the Tx and the Rx antenna, is given by

$$L_{\mathrm{fs}} = \left(\frac{4\pi d}{\lambda}\right)^2 = \left(\frac{4\pi d f_c}{c}\right)^2, \tag{2.4}$$

where f_c denotes the carrier frequency, and c is the speed of light in vacuum. In dB scale this can be expressed as

$$\begin{aligned} L_{\mathrm{fs|dB}} &= 20\log_{10}\left(\frac{4\pi d f_c}{c}\right) \\ &= 20\log_{10} d + 20\log_{10} f_c + 20\log_{10}\left(\frac{4\pi}{c}\right). \end{aligned} \tag{2.5}$$

Accordingly, the free-space path loss scales quadratically with link distance and

carrier frequency. If either the distance or the range is doubled, it increases by 6 dB. A transmitted signal at 60 GHz therefore undergoes a 36 dB higher attenuation on the same way to the Rx compared to a signal at 1 GHz. In principle, it is possible compensate the higher path loss at mm-wave frequencies by increasing the antenna gain. High-gain directional antennas can easily be applied for fixed point-to-point links. For point-to-multipoint and mobile links, however, fixed directional antennas can only be used to a limited extent. Corresponding systems must be capable of achieving adaptive gains with steerable antennas to achieve a good link budget.

2.1.2 Atmospheric Effects

The most relevant atmospheric effects to be considered in the mm-wave frequency range include oxygen and water vapor absorption as well as fog and precipitation. Above all, they cause attenuation in excess to the free-space path loss, but may also result in depolarization or multipath propagation. Figure 2.3 shows the frequency dependence of the specific attenuation due to dry and moist air from 1 to 1000 GHz according to [Lie89]. Confining to distances below 1 km, attenuation caused by atmospheric gases can be neglected up to 50 GHz—it remains below 0.5 dB. Between 50 and 70 GHz, the oxygen absorption becomes effective. Its maximum is reached at 60 GHz and exhibits 15 dB/km under standard conditions. The second relevant absorption peak within the mm-wave band occurs at 183 GHz and is caused by water vapor resonance (≈29 dB for relative humidity of 44% under standard conditions). Besides the resonance contributions, it is visible in Figure 2.3 that the attenuation of moist air tends to increase with frequency due to the water vapor continuum spectrum, which mainly affects propagation for frequencies above 100 GHz and high humidity.

Losses due to fog or precipitation also scale exponentially with the link distance. Specific attenuation values caused by fog and rain (derived from [Lie89]) reveal that neither the one nor the other is relevant for frequencies below 5 GHz if distances below 1 km are considered. Stratus (dense fog with visibility ≤70 m) has a visible impact above 80 GHz (≥3 dB/km) and becomes severe above 200 GHz (≥10 dB/km). Drizzle or steady rain have little relevance below 30 GHz (≤ 1 dB/km), even above they are not a crucial issue for distances up to 1 km (3–4.4 dB/km above 70 GHz). In contrast, values up to 11 dB/km arise for heavy rain and up to 40 dB/km for downpour. However, it must be kept in mind that such conditions are always linked to a very small probability of occurrence.

In summary, bad weather conditions as well as oxygen absorption have a minor influence on mm-wave outdoor links up to around 100 m [SEF+16]. Above, they can

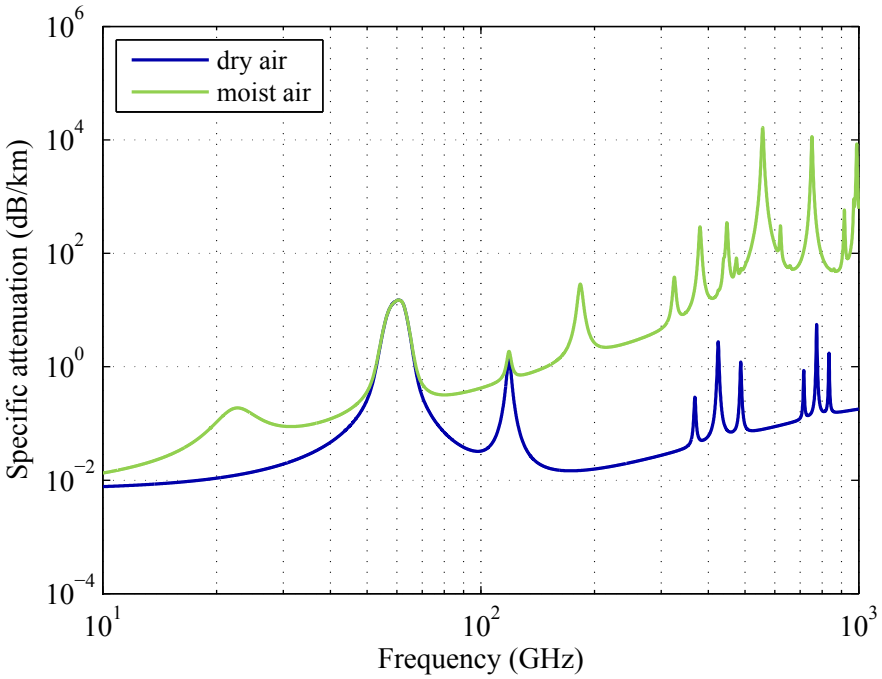

Figure 2.3: Specific attenuation due to dry air and moist air (water vapor concentration: $7.5\frac{\text{g}}{\text{m}^3}$, relative humidity: 44%) under standard conditions, derived from [Lie89].

become relevant. For longer distances, such as 1 km, they are a crucial issue. For mm-wave indoor communication, any atmospheric effects can be neglected.

2.1.3 Penetration Losses

Electromagnetic waves are more or less strongly attenuated when they propagate through objects. It is well known that the specific attenuation factor (defined in dB/m) scales with the conductivity σ of the material. σ is usually modeled as a function of frequency as $\sigma = c' f_c^{d'}$, with the tabulated values c' and d' [Int15a, SEF+16]. For many typical building materials, d' is close to 1, so that σ increases linearly with frequency [Int15a].

In the lower GHz frequency range, it is possible to achieve coverage inside buildings from a base station outside—typical penetration losses are between a few dB up to around 20 dB [DRX98]. Up to 8 GHz, frequency dependence is less an issue in practice [OKI09]. However, the attenuation caused by exterior wall materials becomes very high in the mm-wave band [SEF+16, Cor95, LLH94]. Assuming the dielectric properties given in [Cor95], a concrete wall of 15 cm thickness gives rise to penetration losses above 100 dB at 60 GHz, compared to 10 dB at 5 GHz.

The building entry loss also largely depends on the building type, especially on

the type of windows and the percentage of the windowed area. The reason is that traditional window glass can have a very low loss on the one hand [SS03, LLH94]. On the other hand, losses caused by glass with metallic tints and coating can be as high as 30 dB, even in the lower GHz frequency range [ARY95].

Depending on the building structure, inside separating walls can exhibit very different characteristics. Typical lightweight constructions involve plasterboard, which is almost transparent for low frequencies and also cause limited attenuation to mm-waves. In [LLH94], losses of 2.1 dB and 2.8 dB are reported at 60 GHz for single plasterboards of 10 and 14 mm thickness. Between 5.1 and 8.1 dB were observed for a hollow two-layered plasterboard wall [SMI+97]. Movable partitions made of cloth-covered plywood lead to losses of the same order of magnitude (3.4–10.1 dB measured in [SMI+97]).

With regard to indoor links, it can be concluded that the isolation between rooms is highly dependent on the types of interior walls. It is frequently assumed that there is no interference between systems in adjacent rooms. However, this is only true if solid brick or concrete interior walls are involved. Lightweight construction walls provide only limited isolation. In order to assess building entry and penetration losses, it is crucial to model windowed areas accurately [SS03]. Millimeter-wave outdoor links will probably not rely on propagation through buildings on the one hand. On the other hand, isolation might not be guaranteed if glass facades are involved, and interference can become an issue.

2.1.4 Reflection

Reflection is the main cause for multipath propagation and arises from a wave impinging on a surface that is large compared to the wavelength [YWK98, IY02]. A specular reflection takes place if the surface is flat and smooth. The reflected amount of energy depends on the material properties, the incident angle and the polarization of the wave. It can be calculated from the Fresnel reflection coefficients [Par00, LFR96, LLH94]. For a plane wave that propagates in air and impinges on a plane surface, the reflection coefficient for parallel polarization is given by

$$r_{\parallel} = \frac{\varepsilon_r \cos\alpha - \sqrt{\varepsilon_r - \sin^2\alpha}}{\varepsilon_r \cos\alpha + \sqrt{\varepsilon_r - \sin^2\alpha}}, \tag{2.6}$$

where ε_r is the complex relative permittivity of the medium and α is the angle of incidence with respect to the normal of the surface. For perpendicular polarization, the reflection coefficient is given by

$$r_{\perp} = \frac{\cos\alpha - \sqrt{\varepsilon_r - \sin^2\alpha}}{\cos\alpha + \sqrt{\varepsilon_r - \sin^2\alpha}}. \tag{2.7}$$

According to (2.6) and (2.7), the reflection coefficients are frequency-independent as long as ε_r is not a function of frequency.[2] However, since the thickness of walls and objects is limited, a series of reflections is caused inside the material between the two boundary layers, which are to be taken into account by extended models [Cor95, LLH94, Int15a]. They result in fluctuations of the reflected energy as a function of material thickness, incident angle and frequency. The fluctuations are pronounced if the materials exhibits only low losses and if the thickness of the slab is of the order of the wavelength. Moreover, if the dielectric slab is thin relative to the wavelength, a large amount of power may penetrate the medium and the reflected power is weaker.

Further frequency dependence of reflection behavior is caused by surface roughness. If the surface is rough, the reflection is diffuse, spreading the energy in many directions rather than reflecting it in a single direction. The effect is also denoted as scattering on non-uniform surfaces [McD96]. The Rayleigh criterion can be used to determine whether a specular or a diffuse reflection can be expected. For an irregular surface, it can be formulated as [Par00]

$$C = \frac{4\pi\sigma\cos\alpha}{\lambda}, \tag{2.8}$$

where σ is the standard deviation of the surface irregularities. The reflection is said to be specular if $C < 0.1$ and highly diffuse for $C > 10$ [Par00]. For normal incidence, this means that a surface is definitely rough if σ is in the order of the wavelength. Measurements indicate that roughness has distinct influence on the reflected power in the specular direction if it is of the order of $\frac{\lambda}{10}$ [LLH94]. The losses can be taken into account by introducing scattering reduction factors that decrease the reflection coefficients [LFR96, LLH94].

Typical materials in indoor environments appear smooth in the lower GHz range. At mm-wave frequencies, surface roughness may take effect, but the diffused power is usually small. In outdoor scenarios, however, the roughness of materials such as brick walls is much larger and the components reflected in non-specular directions may be even stronger than the component reflected in the specular direction [LLH94].

[2] As mentioned in Section 2.1.3, the conductivity σ is a strong function of frequency. It affects the imaginary part of ε_r. However, a linear frequency dependency is implicitly eliminated by the conversion equations [Int15a]. As a result, ε_r is only slightly dependent on frequency for typical construction materials.

2.1.5 Scattering

The term scattering is commonly used to denote either diffuse reflections on non-uniform surfaces [McD96] as introduced in Section 2.1.4 or the interaction of an electromagnetic wave with objects whose dimensions are comparable to the wavelength. Depending on the shape of the objects, the incoming wave is spread out into many directions, and it is hardly possible to predict the effects in a deterministic manner. This particularly applies to cases with a large number of irregularly shaped obstacles, e. g. the foliage of trees [SVE88]. In path loss models, only the overall losses caused by foliage are taken into account (see Section 2.1.7). In conjunction with geometry-based channel models, scattering is considered as additional random model component on top of the specular multipaths [CRB+07, SPH+10].

2.1.6 Diffraction

When a radio wave encounters sharp irregularities like edges and corners of a dense object with large dimensions relative to the wavelength, diffraction occurs—an apparent bending of the wave around the edge or corner [Par00]. Consequently, a radio signal may be received behind the obstacle even if it is completely impenetrable. As for reflection, the phenomenon depends on the properties of the object, the angle of incidence, polarization and frequency. At frequencies up to a few GHz, it is important to consider diffraction for outdoor propagation to predict the field strength accurately, since the diffracted field around objects and building edges can contribute substantially to the total received power. With increasing frequency, diffracted power decreases. However, as will be shown in Section 4.5, diffraction effects at mm-wave frequencies are nevertheless important to be considered in conjunction to human body shadowing [PWRM+12, WPK+16b]. This also applies to cases where propagation paths are obstructed by tree trunks or lamp posts [GPWK16].

2.1.7 Vegetation Losses

Vegetation is an important factor for outdoor links. Foliage gives rise to attenuation, scattering and depolarization [RSR+02, Shu02, SVE88]. Vegetation movement due to wind can also cause time-variant fading [CE09]. The effects are influenced by numerous factors such as path length through foliage, vegetation type, vegetation density, seasonal conditions, wetness and frequency [DL95, SVE88, Sev97].

Losses as well as their variance clearly tend to increase with frequency. Reported attenuations caused by single trees range from 11 dB at 3.5 GHz to more than 30 dB at 57.6 GHz [DSA99, SVE88]. A clear growth between 9.6 and 28.8 GHz was observed

in [SVE88], whereas the difference between 28.8 and 57.6 GHz was less pronounced. The larger variance at higher frequencies can be explained by the smaller Fresnel zone, since groups of leaves and gaps either block the signal or let it pass relatively unhindered [DSA99]. In wet conditions, the attenuation typically increases by 4–7 dB [DL95, DSA99].

2.2 Channel Modeling Approaches

A channel model aims to reproduce the typical behavior of the channel, which is constituted by the superposition of the propagation mechanisms described in Section 2.1. Since the overall behavior can be very complex, simplifications are made to obtain a models with manageable complexity. Two categories can be distinguished: deterministic and stochastic models.

2.2.1 Deterministic Modeling

In principle, all details of wave propagation and thus the channel may be obtained by solving the Maxwell's equations with boundary conditions that make allowance for the walls and objects within the environment. However, this approach is impracticable due to the enormous computational effort. Therefore, ray tracing (RT) has been proposed for modeling propagation in indoor as well as outdoor scenarios [PJK12, FRKP12, OHG15]. RT is based on geometrical optics (GO) and much less demanding in computation [Hus94]. The propagation is described by straight lines, called rays, each corresponding to a propagation path. Target of the ray tracing tool (ray tracer) is to find all valid rays between the Tx and the Rx and to compute their interaction with the environment. At a boundary between two adjacent media—when a ray hits a wall or an obstacle—the incident ray is split up into a reflected and a transmitted one. In this simplified model, scattering and the finiteness of the surfaces as well as their roughness are usually neglected. The results are therefore most accurate if all objects are large compared to the wavelength and surfaces are smooth. Diffraction can be taken into account by involving the uniform geometrical theory of diffraction (UTD) [KP74]. The ray tracer provides reproducible results for a given scenario and thus represents a site-specific deterministic channel model.

In this work, ray tracing simulations are presented in Section 5.2 for urban microcellular outdoor environments. Based on comparisons with measurement data, the prediction accuracy is analyzed with respect to the large-scale and small-scale characteristics of the channel.

2.2.2 Stochastic Modeling

Stochastic channel models are based on the assumption that the channel is influenced by so many objects and unknown factors that it can be regarded as random. It is therefore described statistically in form of probability distributions, stochastic processes and their characteristic parameters. The parameters are usually derived from measurement data.

The most fundamental component of a stochastic channel model is the path loss model. It determines the received power in a local area (see Section 2.4). Wideband models also aim to reproduce the multipath structure of the channel. The structure is most-widely illustrated and characterized by the power delay profile (PDP) as well as the power angular spectrum (PAS) [Han15]. The tapped delay line (TDL) model can be seen as simplest multipath channel model. It describes the channel as a (time-variant) linear filter, where the random filter taps tend to decrease with increasing delay. Their expectation values are defined by the PDP. Its shape can be directly derived from measurement data [HZK+97] or modeled by an exponentially decaying function. The variations of the tap amplitudes are described by a random processes, e. g. based on Rayleigh or Rice distributions [Pro01, Has93, Kat02].

The popular Saleh-Valenzuela model describes the PDP as a single or a superposition of multiple exponentially decaying functions, which are denoted as clusters [SV87, Smu95, PKH+98, KZPW99]. In the course of the development of standardized 60 GHz indoor channel models, the approach was modified to an exponential decay in both delay directions with respect to the cluster peaks [MMS+09, MMS+10a, MEP+10].

The delay spread can be derived from the PDP and quantifies the time dispersion of the channel (see Section 2.3.5). It is closely related to frequency coherence and thus e. g. determines the inter-symbol interference in a single-carrier transmission and the frequency flatness of the subcarriers in a multicarrier transmission [Han15, Rap02]. The angular spread is the corresponding parameter in the spatial domain. It can be calculated from the PAS and represents a measure to assess the effectiveness of spatial and angular diversity and spatial multiplexing for multi-antenna systems.

Geometry-based stochastic channel models (GSCMs), which are most relevant in conjunction with cellular networks and 5G standardization, are based on a different approach. Instead of describing the PDP and other characterizing channel functions directly, they model a random distribution of electromagnetic field scatterers, which are described by their coordinates or their delays and angles [IST05, IST07, WIN10, LOP+12, 3rd15, 3rd16a]. The approach is similar to site-specific modeling, but based on an imaginary propagation scenario with manageable complexity. The model is

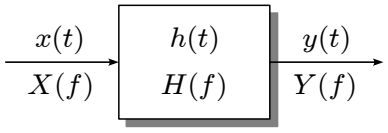

Figure 2.4: Channel as linear time-invariant system.

specified by a set of characteristic parameters, such as the delay spread or the angular spread. It must be ensured by a suitable parametrization that the model output matches the target values.

In this thesis, the focus is on the characterization and modeling of mm-wave multipath channels based on measurements, including evaluations of the PDP, the fading behavior and statistical analysis of the path loss and delay spread. The theoretical background and definitions are described in Section 2.3. Additional aspects on estimating the PDP and related parameters from measurement data are discussed in Section 3.6.

2.3 Representation and Characterization of Multipath Channels

In this Section, the mathematical representation of multipath channels is introduced—from the time-invariant channel to the full description of the time-variant directional channel. The random time-variant channel represents the basis for channel characterization and modeling. It is described in Section 2.3.3 along with common simplifying assumptions. The time-of-arrival parameters, which are widely used in this thesis to characterize multipath channels in the delay time domain, are treated in Section 2.3.5.

2.3.1 Time-Invariant Channel

In a multipath propagation scenario, the received signal is constituted by a superposition of delayed and attenuated versions of the transmitted signal. As long as the transmitter, receiver and objects in the propagation environment do not move, the channel represents a linear time-invariant (LTI) system.

System Functions

It is well-known from system theory that an LTI system is fully characterized by either its impulse response $h(t)$ or its transfer function $H(f)$ (see Figure 2.4). For wireless

channel description, the equivalent baseband representation is used for convenience [Dur00, Pro01]. The input-output relationship in the time domain is given by

$$\begin{aligned} y(t) &= h(t) * x(t) \\ &= \int_{-\infty}^{\infty} h(\tau) x(t-\tau)\, d\tau, \end{aligned} \tag{2.9}$$

where $x(t)$ and $y(t)$ denote the transmitted and the received signal, and $h(t)$ is the channel impulse response (CIR) [Dur00, Pro01]. Equivalently, the relation can be expressed in the frequency domain by

$$Y(f) = H(f)X(f) \tag{2.10}$$

with the Fourier pairs

$$x(t) \quad \circ\!\!-\!\!\bullet \quad X(f) \tag{2.11}$$

$$y(t) \quad \circ\!\!-\!\!\bullet \quad Y(f) \tag{2.12}$$

$$h(t) \quad \circ\!\!-\!\!\bullet \quad H(f). \tag{2.13}$$

$X(f)$ is the spectrum of the input signal and $Y(f)$ is the spectrum of the output signal. $H(f)$ is denoted as channel transfer function (CTF) or channel frequency response (CFR).

Infinite Resolution Model

The CIR is composed of a superposition of multipath components (MPCs) and can be expressed as a sum of time-shifted complex-weighted Diracs $\delta(t)$ [Has93]:

$$h_p(t) = \sum_{k=0}^{K-1} a_k e^{j\psi_k} \delta(t - \tau_k), \tag{2.14}$$

where K, a_k, ψ_k and τ_k denote the number of MPCs, the magnitude, phase and the delay time[3] of the k-th MPC, respectively. Assuming that each physical propagation path or "ray" (see Section 2.2.1) can be resolved on the delay time axis, each MPC in the CIR corresponds to one propagation path. In this infinite resolution case, K

[3]This designation is already chosen with regard to the description of time-variant multipath channels in Section 2.3.2, where the equivalent of the parameter t is the parameter τ, which describes the time difference $\tau = t' - t$, denoted as *delay time* or *delay*, with $t' = t + \Delta t$. Thus t is absolute time and τ is relative time, but both parameters have the unit of time. For the sake of clarity, the terms *delay (time)* and *delay (time) domain* are used in accordance with other literature.

can be very large.

A multipath channel is called time-dispersive since it expands and "smears" the signal on the delay time axis. In the frequency domain, (2.14) yields

$$\begin{aligned} H_p(f) &= \mathcal{F}\{h(t)\} \\ &= \sum_{k=0}^{K-1} a_k e^{j\psi_k} e^{-j2\pi f \tau_k}. \end{aligned} \tag{2.15}$$

Accordingly, at each frequency, $H_p(f)$ is constituted by the sum of all complex path weights multiplied by the respective Fourier coefficient. This results in fluctuations of $|H_p(f)|$ over frequency, denoted as frequency selectivity.

Limited Bandwidth and Sampling

Any practical radio system and channel sounder has a finite bandwidth and therefore $h_p(t)$ cannot be observed directly. Assuming a complex baseband sounding signal $s(t)$ that is bandlimited with bandwidth B, i.e. $S(f) = 0$ for $|f| > \frac{B}{2}$, only $h_b(t)$ is observable, which is a version of $h_p(t)$ limited to the same bandwidth. However, without loss of generality, $h_p(t)$ can be replaced by $h_b(t)$ for an arbitrary input signal $x(t)$ if $X(f) = 0$ for $|f| > \frac{B}{2}$ [AMH04].

A digital receiver system yields a delay time discrete version of the output signal, and the measured CIR is therefore also discrete. If the sampling frequency $f_s = \frac{1}{T}$ meets the condition $f_s \geq B$ (sampling theorem), $h_b(t)$ is fully described by its samples $h_b(nT)$, $n \in \mathbb{Z}$, where T is the sampling period. $h_b(t)$ can then be reconstructed from the samples $h_b(nT)$ by ideal lowpass interpolation:

$$h_b(t) = \sum_{n=-\infty}^{\infty} h_b(nT) \mathrm{sinc}\left(f_s\left(t - nT\right)\right), \tag{2.16}$$

with $\mathrm{sinc}(x) = \frac{\sin(\pi x)}{\pi x}$. Note that if $h_b(t)$ is causal and delay-limited with maximum delay $\tau_{\max}$[4], the summation may be limited to $n \in [0, N-1]$ with $N = \left\lfloor \frac{\tau_{\max}}{T} \right\rfloor + 1$.

Inserting (2.16) into (2.9) yields [AMH04]

$$\begin{aligned} y(t) &= \sum_{m=-\infty}^{\infty} h_b(mT) \int_{-\infty}^{\infty} \mathrm{sinc}\left(f_s\left(t - mT\right)\right) x(t-\tau)\, d\tau \\ &= T \sum_{m=-\infty}^{\infty} h_b(mT) x(t - mT). \end{aligned} \tag{2.17}$$

[4]This assumption is not *exactly* compatible with the bandwidth limitation of $h_{\mathrm{bl}}(t)$. However, the resulting errors can be kept small. Furthermore, a measured $h_{\mathrm{bl}}(t)$ drops below the noise level beyond a certain delay.

Since the output signal $y(t)$ is also bandlimited with bandwidth B, it can be sampled without loss of information and it can be written

$$y(nT) = T \sum_{m=-\infty}^{\infty} h_b(mT)x\left((n-m)T\right), \tag{2.18}$$

which yields the compact discrete form notation

$$y[n] = \sum_{m=-\infty}^{\infty} h[m]x[n-m], \tag{2.19}$$

with $y[n] = y(nT)$, $x[n] = x(nT)$, $h[n] = Th(nT)$.

Finite Resolution Model

The bandwidth limitation translates to a finite resolution τ_{res} in the delay time domain. It is inversely proportional to B and most frequently defined as $\tau_{\text{res}} = \frac{1}{B}$. The system is not able to separate propagation paths arriving within an interval smaller than τ_{res}. In the model (2.14), this may be considered by grouping propagation paths according to [Sch03]

$$h_p(t) = \sum_{l=0}^{L-1} \sum_{m=0}^{M_l-1} a_{l,m} e^{j\psi_{l,m}} \delta(t - \tau_{l,m}), \tag{2.20}$$

with $K = \sum_{l=0}^{L-1} M_l$. In (2.20), the one-dimensional index k is split into the double index (l, m), where l subscripts the main paths and m the sub-paths. Approximating the delays of the sub-paths that cannot be resolved, and thus give rise to the same main path, by the average delays

$$\tau_l = \frac{1}{M_l} \sum_{m=0}^{M_l-1} \tau_{l,m}, \tag{2.21}$$

and coherently combining the respective sub-paths yields the CIR

$$h_\delta(t) = \sum_{l=0}^{L-1} \delta(\tau - \tau_l) \sum_{m=0}^{M_l-1} a_{l,m} e^{j\psi_{l,m}}. \tag{2.22}$$

The second sum acts as weighting factor of the l-th (main) path. Using the definitions

$$c_l = \sum_{m=0}^{M_l-1} a_{l,m} e^{j\psi_{l,m}}, \;\; \beta_l = \left|c_l\right|, \;\; \phi_l = \arg\left\{c_l\right\}, \tag{2.23}$$

where c_l is the complex gain or weight of the l-th main path, (2.22) can be rewritten as

$$\begin{aligned} h_\delta(t) &= \sum_{l=0}^{L-1} c_l \delta(t-\tau_l) \\ &= \sum_{l=0}^{L-1} \beta_l e^{j\phi_l} \delta(t-\tau_l). \end{aligned} \tag{2.24}$$

As can be seen, (2.24) has the same form as (2.14) and the models only differ in their interpretation. Each (resolvable) MPC in (2.24) may result from a superposition of multiple propagation paths with different amplitudes and phases. This fact is especially important if the channel is not static, but variant with respect to time or space (see Sections 2.3.2 and 2.3.4).

The model can be further simplified by introducing a discrete delay time approximation. Starting from (2.14), the delay axis is divided into equally spaced intervals, called bins. The bin size is typically chosen as $\frac{1}{B}$, which results in the discrete delays $\tau_l = \frac{l}{B},\ \ l = 0, 1, \ldots, L-1$, where $[\tau_l, \tau_{l+1})$ bounds the l-th bin. The complex weights of all propagation paths (sub-paths) falling into $[\tau_l, \tau_{l+1})$ are summed up and assigned to the delay τ_l. The form of the CIR is the same as (2.24). However, not every bin may contain a path. The complex gain of empty bins is $c_l = 0$. The upper limit $L-1$ represents the last non-empty bin.

In mobile communication scenarios, the channel is not static, but time-variant. However, the description of the LTI channel is nevertheless of great importance. In conjunction with channel sounding, the channel is usually assumed to be static within the time interval it takes to acquire a CIR.

2.3.2 Time-Variant Channel

If scatterers in the propagation environment or at least one of the wireless stations are in motion, the channel becomes time-variant. A linear time-variant (LTV) system can be described by one of its four system functions [Bel63, Kat97, DR00][5]. The most frequently used system function, the time-variant CIR $h(t, \tau)$, was introduced by Zadeh [Zad50]. It gives the input-output relationship

$$y(t) = \int_{-\infty}^{\infty} h(t, \tau) x(t-\tau)\, d\tau. \tag{2.25}$$

[5] *Bello* [Bel63] describes eight system functions. However, four system functions are dual functions of the other four. Therefore, the considerations may be limited to the first set of Bello functions, which are commonly used in the literature.

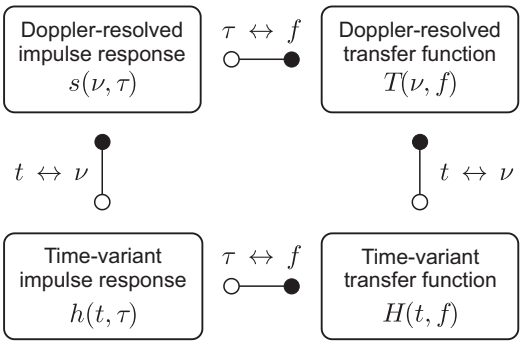

Figure 2.5: System functions of the linear time-variant channel and relations via the Fourier transform.

The frequency domain representation is obtained by Fourier transform with respect to the delay time variable τ. It yields the time-variant CTF $H(f, t)$. The input-output relationship is given by

$$y(t) = \int_{-\infty}^{\infty} H(t, f) X(f) e^{j2\pi f t} \, df. \tag{2.26}$$

The remaining two system functions, namely the Doppler-resolved transfer function $T(f, \nu)$ and the Doppler-resolved impulse response $s(\nu, \tau)$ can be derived by Fourier transform with respect to the time variable t, which translates to the Doppler shift (Doppler frequency) ν in the spectral domain. Figure 2.5 depicts all four system functions and their cyclic relation via the Fourier transform. It should be noted that frequency f and time t are no longer valid transform pairs as in the time-invariant case.

In analogy to the time-invariant formulation (2.24), the time-variant CIR can be modeled as [Has93]

$$\begin{aligned} h_\delta(t, \tau) &= \sum_{l=0}^{L(t)-1} c_l(t) \delta(\tau - \tau_l(t)) \\ &= \sum_{l=0}^{L(t)-1} \beta_l(t) e^{j\phi_l(t)} \delta(\tau - \tau_l(t)). \end{aligned} \tag{2.27}$$

The coefficients $c_l(t)$ are now a function of time. Assuming that each (resolvable) MPC is composed of multiple uncorrelated paths, $\beta_l(t)$, $\phi_l(t)$ and thus $c(t)$ is subject to fast fluctuations in a typical mobile scenario. Even a user movement of a fraction of the wavelength may result in significant changes. The effect is denoted as small-scale fading. Referring to (2.22)–(2.24), the reason is that $a_{l,m}$, $\psi_{l,m}$ and M_l become a function of time. Since the phases $\psi_{l,m}(t)$ vary quickly and each weight $c_l(t)$ results from the phasor summation $\sum_{m=0}^{M_l(t)-1} a_{l,m}(t) e^{j\psi_{l,m}(t)}$, $c_l(t)$ is also subject to

fast fluctuations. The amplitudes $a_{l,m}(t)$ and the delays $\tau_l(t)$ change more slowly over time.[6] The number of MPCs $L(t)$ is constant unless a main path is blocked or a new one emerges. Such events result in shadow fading, which is attributed to mid-scale or large-scale variations of the channel [Rap02, Has93].

The time-variant CTF can be modeled as

$$H_\delta(t,f) = \sum_{l=0}^{L(t)-1} c_l(t) e^{-j2\pi f \tau_l(t)}. \tag{2.28}$$

Accordingly, the value of $H(t,f)$ at each frequency results from a coherent summation of all weights $c_l(t)$ multiplied by the rotation operator. Therefore, $|H(t,f)|$ is subject to fast fluctuations at each frequency. Provided that there are multiple MPCs, this even holds for the case that each MPC consists of only one propagation path, thus the amplitudes $\beta_l(t)$ are virtually constant and only the phases $\phi_l(t)$ vary.

For the bandlimited case, similar considerations as for the LTI system can be made with respect to time discretization, yielding the input-output relation [AMH04]

$$y[n] = \sum_{m=-\infty}^{\infty} h[n,m]x[n-m], \tag{2.29}$$

with $y[n] = y(nT)$, $x[n] = x(nT)$ and $h[n,m] = Th[nT, mT]$. The sampling frequency $f_s = \frac{1}{T}$ must fulfill $f_s \geq B + 2\nu_{\max}$, where $\nu_{\max}$ is the maximum Doppler shift.

2.3.3 Random Time-Variant Channel

As introduced in Section 2.3.2, the channel in a mobile scenario is time-variant. If the movement of the user and scatters is regarded as random, the system functions become stochastic processes. In principle, a full characterization would require the identification of the multidimensional probability density functions (PDFs) of the system functions. However, this is not feasible in practical cases. Therefore, the system functions are usually described by their correlation functions using simplifying assumptions [Bel63, Sia09].

Correlation Functions

For each system function, the related correlation function can be calculated by ensemble averaging [Bel63, Ste92]:

[6] Note that the delays are fixed for the equidistant bin model. Changes of main paths transfer to changes of $c(t)$.

$$R_h(t,t';\tau,\tau') = E\left\{h(t,\tau)h^*(t,\tau)\right\}, \tag{2.30}$$
$$R_H(f,f';t,t') = E\left\{H(f,t)H^*(f',t')\right\}, \tag{2.31}$$
$$R_T(f,f';\nu,\nu') = E\left\{T(f,\nu)T^*(f',\nu')\right\}, \tag{2.32}$$
$$R_s(\tau,\tau';\nu,\nu') = E\left\{s(\tau,\nu)s^*(\tau',\nu')\right\}. \tag{2.33}$$

Mobile radio channels are commonly assumed to be wide-sense stationary (WSS) over a short time periods or small spatial distances. The correlation functions of a WSS channel do not depend on the particular time instants, but only on their time difference $\Delta t = t - t'$, which is denoted as autocorrelation stationarity. Wide-sense stationarity furthermore implies mean stationarity, which means that the expectations are not a function of time [Ste92]:

$$E\left\{h(t,\tau)\right\} = \mu_h(t,\tau) = \mu_h(t+\Delta t,\tau)\ \ \forall \Delta t \in \mathbb{R}, \tag{2.34}$$
$$E\left\{H(t,f)\right\} = \mu_H(t,\tau) = \mu_H(t+\Delta t,\tau)\ \ \forall \Delta t \in \mathbb{R}. \tag{2.35}$$

If received signals that have traveled different propagation paths exhibit uncorrelated attenuations, phase shifts and delay times, this is called uncorrelated scattering (US). For US, the frequency correlation functions are no longer dependent on the particular frequencies, but only on their frequency difference $\Delta f = f - f'$. US and WSS channels are time-frequency duals [Bel63]. The US channel may be regarded as a WSS channel in the frequency variable f. Combining both US and WSS characteristics, leads to wide-sense stationary uncorrelated scattering (WSSUS), which is equivalent to wide-sense stationarity with respect to both time t and frequency f. The four correlation functions of a WSSUS channel can be written as [Ste92]

$$R_h(t,t+\Delta t;\tau,\tau') = P_h(\Delta t,\tau)\delta(\tau-\tau'), \tag{2.36}$$
$$R_H(t,t+\Delta t;f,f+\Delta f) = R_H(\Delta t,\Delta f), \tag{2.37}$$
$$R_T(\nu,\nu';f,f') = P_T(\nu,\Delta f)\delta(\nu-\nu'), \tag{2.38}$$
$$R_s(\tau,\tau';\nu,\nu') = P_s(\nu,\tau)\delta(\nu-\nu')\delta(\tau-\tau'). \tag{2.39}$$

The interrelation of the correlation functions via the Fourier transform is shown in Figure 2.6 along with the naming used in [Kat02].[7]

[7] It should be noted that, in the strict sense, only $R_H(\Delta t,\Delta f)$ is a correlation function. The other functions shown in Figure 2.6 represent power spectral densities. They are linked to the corresponding correlation functions by δ-functions with respect to all resolved (US) variables according to (2.36), (2.38) and (2.39).

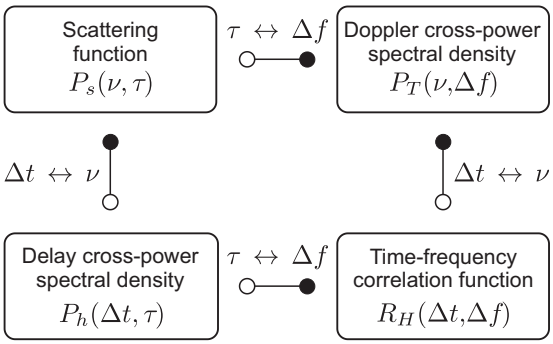

Figure 2.6: Correlation functions of the random time-variant channel and relations via the Fourier transform.

Several sub-functions can be derived, which are widely used to characterize channels and to derive characteristic parameters. They are introduced in the following.

Frequency and Time Coherence

The frequency correlation function (FCF) is obtained from $R_H(\Delta f, \Delta t)$ by setting the time difference to zero:

$$R_H(\Delta f) = R_H(\Delta f, \Delta t)\Big|_{\Delta t=0}. \tag{2.40}$$

The FCF characterizes the frequency coherence of the channel. A quantitative measure is given by the coherence bandwidth B_{coh}. It can be defined as the frequency separation at which the normalized frequency correlation function [Sal13]

$$\rho(\Delta f) = \frac{R_H(\Delta f)}{\sqrt{E\left\{\left|H(f,t)\right|^2\right\} E\left\{\left|H(f+\Delta f,t)\right|^2\right\}}} \tag{2.41}$$

decreases to a certain level, typically 0.9 or 0.5.

In this work, $B_{\mathrm{coh},0.9}$ denotes the frequency separation, where the correlation falls below 0.9 for the first time. It is interpreted as the range over which two frequency points have a strong potential for correlation. In this regard, $B_{\mathrm{coh},0.9}$ is used as indication, whether channel equalization is required for the transmission and to assess the minimum carrier spacing in a multi-carrier system. In addition, $B_{\mathrm{coh},0.5}$ is defined as the separation, where the correlation falls and remains below 0.5. Two frequency points that are separated by Δf are only weakly/moderately correlated if $\Delta f \geq B_{\mathrm{coh},0.5}$. In view of a multi-carrier system, the usage of uncorrelated subcarriers is desirable to exploit frequency diversity.

By analogy, the time correlation function is used to characterize the time coherence

and is obtained by setting the frequency difference to zero:

$$R_H(\Delta t) = R_H(\Delta f, \Delta t)\Big|_{\Delta f=0}. \tag{2.42}$$

The time separation, where the normalized function

$$\rho(\Delta t) = \frac{R_H(\Delta t)}{\sqrt{E\left\{\left|H(f,t)\right|^2\right\} E\left\{\left|H(f,t+\Delta t)\right|^2\right\}}} \tag{2.43}$$

decreases to a certain level, such as 0.9 or 0.5, is called coherence time T_{coh}.

Power Delay Profile

The power delay profile (PDP) $P_h(\tau)$ results from $P_h(\Delta t, \tau)$ by setting the time difference to zero or from integrating over ν in $P_s(\nu, \tau)$. It can be obtained by ensemble averaging over CIRs [Bul02, Ste92]:

$$P_h(\tau) = E\left\{|h(t,\tau)|^2\right\} = E\left\{|h(\tau)|^2\right\}. \tag{2.44}$$

The PDP indicates the decay of multipath power with respect to the delay, discounting small-scall fading effects. It is the most widely used descriptive function and basis for the definition of several characteristic parameters. In accordance with the prevalent notation in the literature, the subscript is also omitted in this work and the PDP is denoted as $P(\tau)$.

Based on channel measurements, the PDP is usually derived by assuming ergodicity, which allows to replace the ensemble average by a time average. The PDP estimate based on a time series of channel observations (CIR snapshots) is then calculated as

$$\hat{P}(\tau) = \frac{1}{K}\sum_{k=1}^{K} |h(t_k,\tau)|^2, \tag{2.45}$$

where K denotes the number of snapshots considered for averaging, and t_k is the time instant of the k-th snapshot.

It is worth mentioning that the related terminology is not used consistently in the literature. Frequently, $|h(\tau)|^2$ (without the expectation) is denoted as PDP, whereas "multipath intensity profile" is used for this expression in [GGS+05] and "instantaneous power delay profile" (also abbreviated by PDP) in [KWA+07]. According to [Rap02] the PDP may be obtained by taking the spatial average of "multipath intensity profiles". In [CWM02], the "PDP" (meaning $|h(\tau)|^2$) measured at one location is referred to as "local PDP" and the PDP averaged over various locations within one

room as the "small-scale averaged PDP".

In this work, the term average(d) power delay profile (APDP) is generally used to refer to a PDP estimate according to (2.45) or (2.49). It is also symbolized by $\bar{p}(\tau)$. Irrespective of whether a time-variant or a space-variant channel (see Section 2.3.4) is considered, $p(\tau) = |h(\tau)|^2$ is denoted as instantaneous power delay profile (IPDP), even though, in the strict sense, the IPDP is not a PDP, but one sample for estimating the PDP if ergodicity holds.

The PDP is the basis for characterizing the time dispersion of the channel. The corresponding parameters are defined in Section 2.3.5.

2.3.4 Directional Time-Variant Channel

In the last decade, smart antenna and MIMO systems have gained in importance due to large capacity gains in comparison to conventional systems. They make use of beamforming and space-time coding (STC) techniques to utilize the directional and spatial properties of the channel. To assess the performance of such systems, a channel description is required that accounts for the directions of the transmitted and received signals.

System Functions

Formally, the time-variant CIR can be extended by a directional component [Kat02]:

$$h(t,\tau) \rightarrow h(t,\tau,\varphi), \tag{2.46}$$

with $h(t,\tau,\varphi)$ being denoted as time-variant angle-resolved impulse response.[8] The angle φ e. g. denotes for example the azimuth angle at the receive station. In the same way, the CIR it can be extended by the elevation angle and the angles at the transmitter side. Adding the polarization as further parameter, results in the full double-directional polarimetric representation of the propagation channel [SMB01]. With regard to subsequent measurements and analyses in this work, however, these straightforward extensions can be omitted.

Fourier transform of $h(t,\tau,\varphi)$ with respect to the angle φ results in system functions depending on the aperture x, which lies in the space domain:

$$g(t,\tau,x) = \int_{-\infty}^{\infty} h(t,\tau,\varphi) e^{-j2\pi(x/\lambda)\sin\varphi}\, d(\sin\varphi), \tag{2.47}$$

[8] An analogous approach can be found in [DR00], where the time-variant impulse response is extended by a position vector $\mathbf{r}$. The corresponding spectral domain is the wavevector domain with dependence on $\mathbf{k}$.

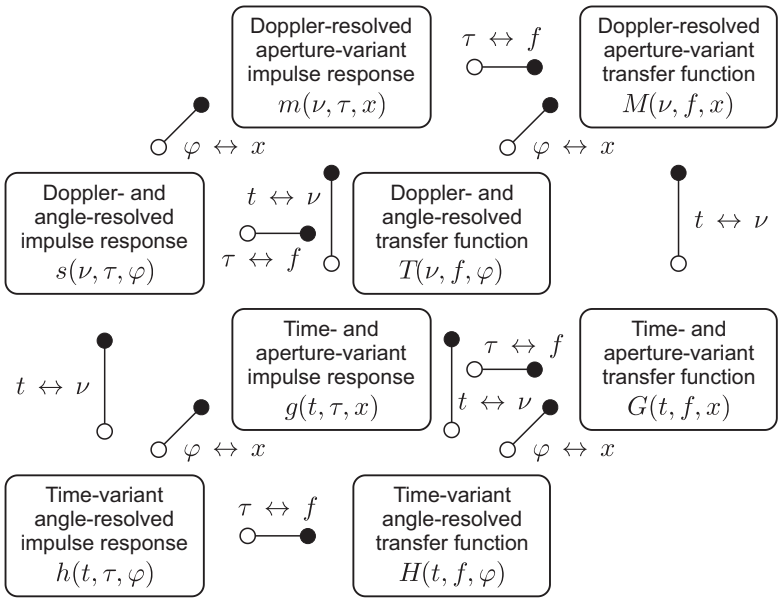

Figure 2.7: System functions of the directional time-variant channel and relations via the Fourier transform [Kat02].

where $g(t, \tau, x)$ is denoted as time- and aperture-variant impulse response.[9] Equation (2.47) reveals that MPCs arriving with different angles superimpose coherently in the space domain, resulting in fluctuations of $g(t, \tau, x)$ over x. The behavior is dual to the behavior with respect to t and f.

The directional time-variant channel depends on three variables and can thus be described by means of eight system functions that are interrelated via the Fourier transform. They are illustrated in Figure 2.7.

In many cases, the channel can be regarded as either time *or* space-variant. Observation of a static channel over space yields the aperture-variant impulse response $g(\tau, x)$ and the aperture-variant transfer function $G(f, x)$.

Correlation Functions

The random directional time-variant channel can be characterized by one of its eight correlation functions, which are illustrated in Figure 2.8. Uncorrelated scattering with respect to φ is assumed, which transfers to wide-sense stationarity with respect to x.

The correlation function of $g(\tau, x)$ is given by

$$\begin{aligned} R_g(\tau, \tau'; \Delta x) &= E\left\{h^*(\tau, x) h(\tau', x + \Delta x)\right\} \\ &= P_g(\tau, \Delta x)\delta(\tau' - \tau), \end{aligned} \tag{2.48}$$

[9] Equation (2.47) shows that strictly speaking the Fourier transform is performed with respect to $\sin\varphi$, which translates to x/λ.

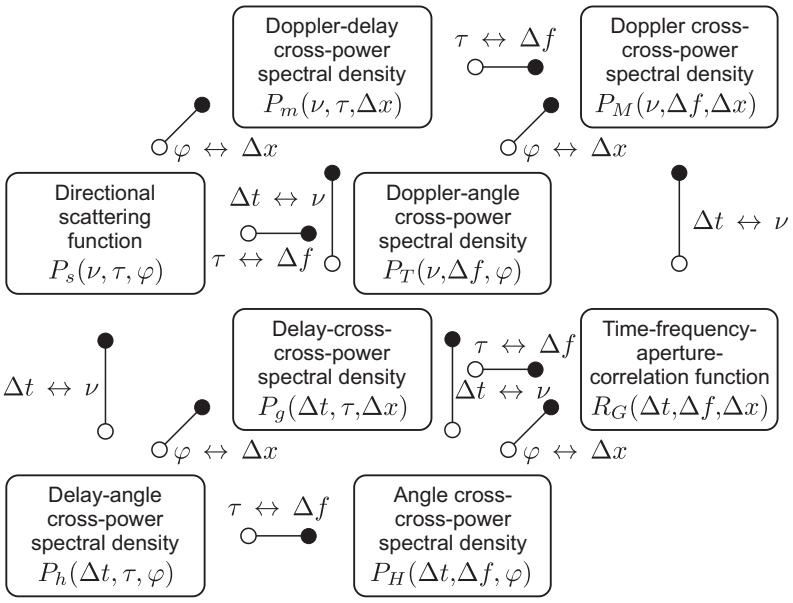

Figure 2.8: Correlation functions of the directional time-variant channel and relations via the Fourier transform [Kat02].

where $P_g(\tau, \Delta x)$ is denoted as delay cross-power spectral density of the space-variant channel. Assuming ergodicity with respect to x, $P_g(\tau)$ can be estimated from a set of observations according to

$$\hat{P}_g(\tau) = \frac{1}{K} \sum_{k=1}^{K} |g(\tau, x_k)|^2, \tag{2.49}$$

where x_k is the position of the observation point of the k-th snapshot.

2.3.5 Time-of-Arrival Parameters

To quantify the characteristics of multipath channels in the delay time domain, a family of measures is used, which are denoted as time-of-arrival (TOA) parameters. They are derived from the PDP. In the following definitions, τ denotes the excess delay, which is defined as the delay relative to the first time where $P(\tau)$ exceeds a given threshold X.

Based on the assumption that the duration of the PDP is limited, the maximum excess delay is defined as

$$\tau_{\max} = \max \{\tau \,|\, P(\tau) \geq X\}\,. \tag{2.50}$$

It is thus given as the delay interval from the first time where the PDP exceeds X and the last time it falls below it. The threshold is typically defined relative to the

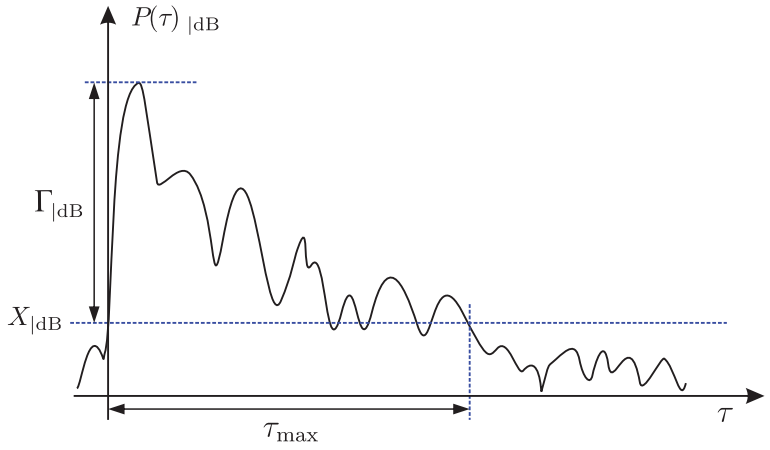

Figure 2.9: Illustration of PDP and applied threshold Γ.

maximum of the PDP:

$$X_{|\mathrm{dB}} = 10 \log_{10} \max \{P(\tau)\} - \Gamma_{|\mathrm{dB}}, \tag{2.51}$$

where Γ is denoted as relative evaluation threshold. The definitions are illustrated in Figure 2.9 Typical values for Γ range from 10 to 40 dB. 20 and 30 dB are used most widely.

The mean excess delay τ_m is the first order moment of the PDP. With the above assumptions it can be calculated by

$$\tau_\mathrm{m} = \frac{\int_0^{\tau_\mathrm{max}} \tau P(\tau)\, d\tau}{\int_0^{\tau_\mathrm{max}} P(\tau)\, d\tau}, \tag{2.52}$$

or, for the discrete case, by

$$\tau_\mathrm{m} = \frac{\sum_{l=0}^{L-1} \tau_l P(\tau_l)}{\sum_{l=0}^{L-1} P(\tau_l)}. \tag{2.53}$$

The RMS delay spread, here also denoted only as delay spread (DS), is the most common measure to describe the time dispersion of the channel. It is given by the second central moment of the PDP:

$$\begin{aligned} \tau_\mathrm{rms} &= \sqrt{\frac{\int_0^{\tau_\mathrm{max}} (\tau - \tau_\mathrm{m})^2 P(\tau)\, d\tau}{\int_0^{\tau_\mathrm{max}} P(\tau)\, d\tau}} \\ &= \sqrt{\frac{\int_0^{\tau_\mathrm{max}} \tau^2 P(\tau)\, d\tau}{\int_0^{\tau_\mathrm{max}} P(\tau)\, d\tau} - \tau_\mathrm{m}^2} \end{aligned} \tag{2.54}$$

or

$$\begin{aligned}\tau_{\mathrm{rms}} &= \sqrt{\frac{\sum_{l=0}^{L-1}(\tau_l - \tau_{\mathrm{m}})^2 P(\tau_l)}{\sum_{l=0}^{L-1} P(\tau_l)}} \\ &= \sqrt{\frac{\sum_{l=0}^{L-1}\tau_l^2 P(\tau_l)}{\sum_{l=0}^{L-1} P(\tau_l)} - \tau_{\mathrm{m}}^2}.\end{aligned} \tag{2.55}$$

The TOA parameters, in particular the RMS delay spread, play an important role in the literature as well as in this work when characterizing and comparing multipath channels. Several aspects related to their estimation from measurement data are addressed in Section 3.6.

It shall be mentioned that parameters for the angular dispersion can be defined in the same way based on the power angular profile or power angular spectrum $P(\varphi)$, which can e. g. be derived from the directional scattering function by integrating over ν and τ (see Section 2.3.4). Details can e. g. be found in [Xu00, LR01].

2.4 Large-Scale Fading and Path Loss

2.4.1 Large-Scale Fading

In a mobile multipath propagation scenario, the envelope of a received signal is subject to fluctuations. They are caused by the superposition of multipaths as described in Section 2.3. These fluctuations, which typically occur in a short time interval when the receiver travels over a distance of the order of the wavelength, are denoted as multipath fading or small-scale fading [Par00, Rap02].

The converse of small-scale fading is large-scale fading. It refers to fluctuations of the local average received power when the mobile moves over a distance that is orders of magnitude larger than the wavelength. They are caused by propagation paths that change their strength, disappear or emerge. Usually, the local average received power is not modeled directly, predicted via the path loss. Path loss represents the channel-induced attenuation between the transmitter and the receiver. It is modeled as a function of distance and describes the channel at a macroscopic level. Apart from the fact that path loss models are an essential part of comprehensive models, they are useful to determine the coverage area of a communication system as well as interference from neighboring cells using the same frequency.

2.4.2 Path Loss

Path loss (PL) can be defined as the ratio of the effective transmitted power to the received power [Rap02]. It may include the antenna gains or not, thus refer to the

radio channel or the propagation channel. In this work, the latter definition is used. Based on the transmitted power P_T and the local average received power $\bar{P}_R$, the PL is defined as

$$\begin{aligned} L_{\mathrm{PL|dB}} &= 10\log_{10}\left(\frac{P_T}{\bar{P}_R}G_T G_R\right) \\ &= P_{T|\mathrm{dBm}} - \bar{P}_{R|\mathrm{dBm}} + G_{T|\mathrm{dBi}} + G_{R|\mathrm{dBi}}\,, \end{aligned} \tag{2.56}$$

where G_T is the gain of the transmit antenna and G_R is the gain of the receive antenna.[10] The calculation aims to decouple antenna effects and provide the PL that would be experienced with isotropic antennas, even though directional ones might by employed. In good approximation, this applies to strongly LOS-dominant propagation conditions with aligned antennas and to setups with low-gain antennas which are omnidirectional in azimuth or which have a pattern that is at least sufficiently wide to cover the relevant propagation section of the environment.

In cases where the LOS PL shall be characterized based on measurements with low-gain antennas, it is meaningful to compensate alignment errors by reducing G_T and G_R in (2.56) in accordance with the deviation of the LOS direction from the main beams. Thus, G_T is interpreted as the gain of the transmit antenna in the direction of the receive antenna and G_R as the gain of the receive antenna in the direction of the transmit antenna. As a prerequisite, the antenna patterns and the angular deviations must be known. Furthermore, the alignment errors must be small enough to ensure that the LOS path is well within the main beam, for example within the half power beamwidth (HPBW).

If mechanically or electronically steerable directional antennas are used for the measurements, the omnidirectional (quasi-isotropic) channel may be synthesized by appropriate scanning of all directions and synthesizing the results [SSKW05]. Otherwise, the PL obtained with directional antennas does not only depend on the antenna patterns, but also on the "alignment strategy". For LOS-dominant conditions, it is apparent that the received power is maximized when the transmit and receive antennas point to each other. However, this is not the case for NLOS. An alignment strategy that delivers meaningful results using directional setups with antenna steering, is to determine the pointing directions that maximize the received power. However, it should be noted that the result deviates from the omnidirectional (quasi-isotropic) PL. The deviations increase with increasing antenna gains and multipath richness. To enable a proper interpretation of PL evaluations, it is therefore important to clearly specify how the PL has been determined.

Under free-space propagation conditions, L_{PL} is equal to the free space loss L_{fs}

[10] Note that in the absence of small-scale fading, the local average received power $\bar{P}_R$ is practically equal to the received power P_R.

(see Section 2.1.1), which is given by

$$L_{\mathrm{fs|dB}} = 20\log_{10}\left(\frac{4\pi d}{\lambda}\right), \tag{2.57}$$

where d is the Tx-Rx distance and λ denotes the wavelength. For convenience, a reference distance d_0 is introduced in the expression and the total PL for a given wavelength is expressed by the sum of the PL at d_0 and the excess loss as a function of d relative to d_0:

$$L_{\mathrm{fs}}(d)_{\mathrm{|dB}} = L_{\mathrm{fs}}(d_0)_{\mathrm{|dB}} + 20\log_{10}\left(\frac{d}{d_0}\right). \tag{2.58}$$

The reference distance should be chosen such that it is in the far field, but smaller than any distance occurring in the communication scenario ($d_0 < d$). A typical value for mm-wave frequencies is $d_0 = 1\,\mathrm{m}$.

For multipath scenarios, the free-space equation is no longer applicable. Following the well-known PL exponent model, also referred to as log-distance law, the PL is modeled as [FBR+94]

$$L_{\mathrm{PL}}(d)_{\mathrm{|dB}} = \overline{L}_{\mathrm{PL}}(d_0)_{\mathrm{|dB}} + 10n\log_{10}\left(\frac{d}{d_0}\right) + X_\sigma, \tag{2.59}$$

where the intercept point $\overline{L}_{\mathrm{PL}}(d_0)$ is the mean PL at the reference distance and n is the PL exponent, which characterizes how fast the PL increases with respect to Tx-Rx distance. X_σ is a zero-mean Gaussian random variable (in dB) with standard deviation σ. It takes into account that the PL does not only depend on the distance, but also on the specific propagation environment and the locations of the Tx and the Rx. The effect is denoted as shadow fading. The PL exponent model with shadow fading according to (2.59) is used as standard model in this work.

In the literature, also more sophisticated PL models can be found, especially for NLOS scenarios. The distance-dependent power exponent defines several validity ranges and applies different PL exponents for each range. In [Ake88] a model with four ranges is derived from measurement data at 1900 MHz within a building. It implicitly includes penetration losses due to walls and floors. Partition-based PL models explicitly incorporate penetration losses by considering the number and type of obstructions like walls, furniture or trees [Xu00, Rap02]. These models provide site-specific results, but are universally applicable for scenarios with different geometries.

Atmospheric effects have been introduced in Section 2.1.2. They are not relevant

for indoor propagation. In outdoor scenarios at mm-wave frequencies, they roughly start to affect the PL at link distances above 100 m. Since the targeted cell radius is of the same order of magnitude, they are typically not taken into account for mm-wave small cell scenarios. However, for larger distances, it is necessary to include additional terms in (2.59), since the effects scale exponentially with distance, and the log-distance law is no longer valid. Confining to good weather conditions and frequencies up to 100 GHz, mainly the oxygen absorption peak in the 60 GHz band is relevant.

3 Channel Sounding Principles and Implementation

In this chapter, the principles of channel sounding and selected aspects on implementation, data processing and parameter extraction are introduced. In addition, the channel sounder setups used in this work are described in more detail. In Section 3.7, fundamental issues on the comparison of measurement results are touched. They are closely related to the characterization of channel sounders and the validation of measurement results. These topics are addressed in Section 3.8, which contains the first publication in this thesis. All subsequent parts are based on publications.

3.1 Measurement Techniques

The basic idea of channel sounding is to capture one of the system functions described in Section 2.3. Omitting the angle dependence, which is linked to the antenna setup, the task is to determine $h(t, \tau)$ or $H(t, f)$.

The bandlimited time-invariant channel can be identified from (delay time discrete) measurements as long as it is sampled at least at Nyquist rate. However, independent from discretization, the time-variant channel is only measurable if the support area of its scattering function is smaller than one [Bel69, KP05, PW06]. A closely related but more restrictive criterion for defining an underspread channel was initially used by Kozek [Koz97]. It is based on the rectangular area defined by the minimum and maximum values of the support in each dimension, namely $A = \{\tau \in [0, \tau_{\max}], \nu \in [-\nu_{\max}, \nu_{\max}] \ll 1$ or equivalently

$$2\tau_{\max}\nu_{\max} \ll 1, \tag{3.1}$$

where $\tau_{\max}$ is the maximum delay (filter memory) and $\nu_{\max}$ is the the maximum occurring Doppler frequency (filter bandwidth). Criterion (3.1) is helpful to assess measurability in practice.

In this work, the most critical case with regard to measurability is given by the urban microcellular access scenarios. The maximum relevant delay in the considered

street canyons is assumed to be 2 µs, corresponding to 600 m propagation distance. For a static environment, values observed in the measurement results were typically below 1 µs. The maximum Doppler frequency is assumed to be caused by a single-bounce reflection on the front of a vehicle with a speed of 50 $^{\mathrm{km}}/_{\mathrm{h}}$ at the highest measured frequency, namely 82.5 GHz. This yields $2\tau_{\max}\nu_{\max} \approx 2 \times 2\,\mu\mathrm{s} \times 2 \times 3.8\,\mathrm{kHz} = 0.031 \ll 1$, confirming measurability under the given assumptions.

Regardless of the measurement technique, one of the most important figures of a channel sounder is its delay resolution τ_{res}, also known as temporal resolution or multipath resolution. It determines the separability of successive multipath components in the CIR on the delay axis. It is inversely proportional to the measurement bandwidth B and typically defined as

$$\tau_{\mathrm{res}} = \frac{1}{B}. \tag{3.2}$$

Basically, the corresponding τ_{res} is to be interpreted as an upper limit in performance, that is as minimal achievable value.

Wideband channel measurements can be roughly divided into direct pulse measurements, correlation-based measurements and swept-frequency measurements [Rap02]. The first two are usually referred to as time-domain sounding, whereas the last one is referred to as a frequency-domain sounding. The principles are introduced in the following along with fundamental requirements. They focus on waveforms and implementations used in this work. In general, there is a large variety of waveforms and possible channel sounder setups. A comprehensive overview can e. g. be found in [Sal13].

3.1.1 Frequency-Domain Channel Sounding

Measurements in the frequency domain are mostly performed with a vector network analyzer (VNA). It is used to determine the forward transmission gain S_{21} by exciting the channel with a single-tone signal at a certain frequency and observing the output at the receiver side. During a frequency sweep, the procedure is repeated for K_f frequency points $f_k = k\Delta f$, $k = -\left\lfloor \frac{K_f}{2} \right\rfloor \ldots \left\lceil \frac{K_f}{2} \right\rceil - 1$, where Δf is the frequency spacing. The principle is illustrated in Figure 3.1, where $X(f)$ is the spectrum of the sounding signal (transmitted signal) and $Y(f)$ is the spectrum of the received signal.

The forward transmission gain at the frequency points f_k is a sampled version of the channel transfer function: $H(f_k) = S_{21}(f_k) = \frac{Y(f_k)}{X(f_k)}$. To allow the reconstruction of $H(f)$ from $H(f_k)$ and the transform to the delay domain without aliasing errors, the following condition must be fulfilled:

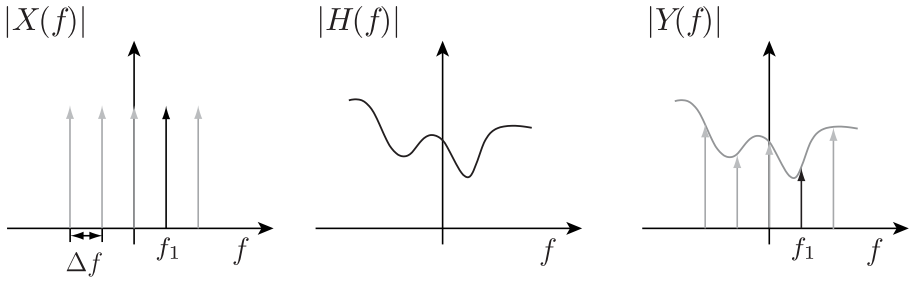

Figure 3.1: Illustration of frequency-domain measurement.

$$\Delta f \leq \frac{1}{\tau_{\max}}, \tag{3.3}$$

where $\tau_{\max}$ is the maximum excess delay of the channel. The condition can be interpreted as fulfilling the sampling theorem for frequency-domain sampling.

VNA-based setups can usually cover a large bandwidth $B = (K-1)\Delta f$ and achieve a high signal-to-noise ratio (SNR). To avoid measurement errors, the channel must be quasi-static over the sweep time T_{sweep}:

$$T_{\text{sweep}} \ll T_{\text{coh}}. \tag{3.4}$$

Continuous measurements can be performed by periodically repeating the frequency sweep. Naturally, the minimum time between two consecutive CTF observations cannot be lower than T_{sweep}. Since for wideband measurements T_{sweep} is typically at least a few hundred milliseconds, the applicability of VNA-based wideband sounding is limited to static or very slowly time-varying channels [ZBN05, SAN10]. A further restriction is that a phase-stable cable connection is needed between Tx and Rx [FHZ13, SAN10, ZBN05]. This is usually not a major issue for indoor scenarios, but imposes limits on the usability for outdoor measurements. Swept-frequency measurements without these restrictions require dedicated setups as e. g. presented in [SFRC16].

3.1.2 Time-Domain Channel Sounding

The impulse response of an LTI system corresponds to the output signal of a system fed by a Dirac impulse $\delta(t)$. The most straightforward method to perform continuous time-domain wideband channel sounding is therefore to excite the channel with a Dirac impulse train

$$\text{III}_{T_p}(t) = \sum_{m=-\infty}^{\infty} \delta\left(t - mT_p\right), \tag{3.5}$$

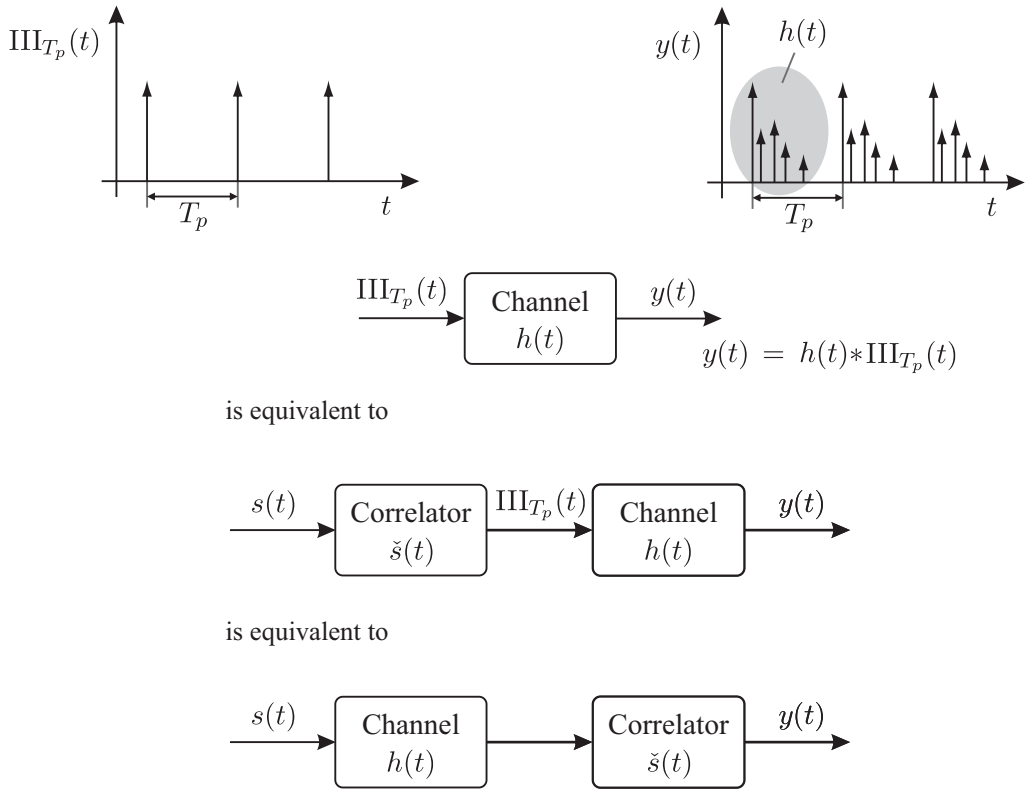

Figure 3.2: Principle of time-domain correlation channel sounding.

where T_p is the spacing of consecutive pulses (signal period). Since it is not possible to generate Dirac pulses in practice—they would have infinite bandwidth—very short pulses are used instead. The main problem of this approach is that the signal exhibits an extremely high peak-to-average power ratio (PAPR) or crest factor (CF) which heavily limits the achievable dynamic range of a pulse-based sounding system. Especially at mm-wave frequencies, where the transmit power is very limited and the path loss is high, the technique is ill-suited to achieve an adequate SNR. Therefore, the majority of time-domain wideband measurements make use of correlation techniques. The approach is based on the transmission of periodic sounding signals with exceedingly good autocorrelation properties and a low CF. At the receiver, the signal is correlated with the original sounding signal and yields an estimation of the CIR. This measurement principle exploits the commutativity of elements in an LTI system.[1] It is illustrated in Figure 3.2, where $s(t)$ denotes the transmitted sounding signal which results from a periodic repetition of $\check{s}(t)$, and $y(t)$ is the received signal.

The correlation can be performed in the analog domain, e. g. by a sliding correlator

[1]It should be noted that commutativity does not hold in an LTV system. However, for correlation-based channel sounding of time-variant channels, it is assumed that the channel is static over one period of the sounding signal and thus only to change between successive observations.

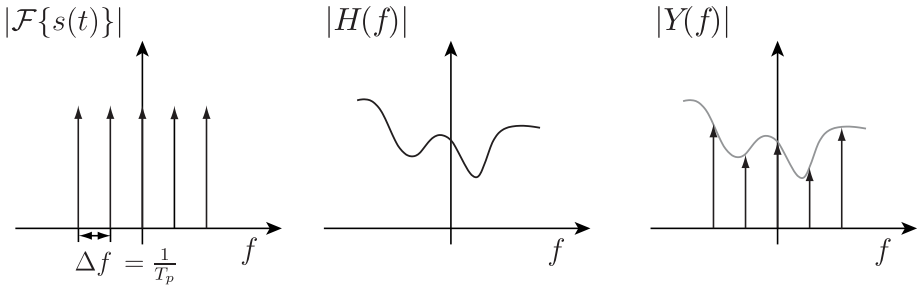

Figure 3.3: Frequency-domain illustration of time-domain measurement.

[Cox72, AR04, XKR02], in real-time in the digital domain by a microprocessor [CFM93] or an FPGA [KKPW13], or offline in the digital domain during post-processing on a personal computer (PC). Sliding correlation channel sounders make use of time dilatation to reduce the sampling rate at the receiver. Details can be found in [Cox72, AR04, XKR02]. The following considerations refer to systems with full-rate digital sampling as used in this work.

The correlation gain G_{corr} can be defined as the improvement of the effective SNR compared to a single pulse. Based on a sequence with perfect autocorrelation it is given by

$$G_{\mathrm{corr|dB}} = 10 \cdot \log_{10} N_{\mathrm{seq}}, \tag{3.6}$$

where N_{seq} is the length of the sequence. The periodic sounding signal exhibits a line spectrum with the frequency spacing

$$\Delta f = \frac{1}{T_p}, \tag{3.7}$$

where T_p is the signal period. Figure 3.3 illustrates a continuous TD measurement in the frequency domain.

In contrast to the frequency-domain measurement, where the channel is successively sampled at different frequency points, the channel is excited at all frequency points "simultaneously" (within T_p). Therefore, TD channel sounders are faster than VNA-based systems—the minimum measurement time is equal to T_p. The channel must be static during this time to avoid errors:

$$T_p \ll T_{\mathrm{coh}}. \tag{3.8}$$

In other words, the coherence time of the channel determines the upper limit of the sequence duration. The lower limit results from the maximum excess delay $\tau_{\max}$ according to

$$T_p \geq \tau_{\max}. \tag{3.9}$$

The condition must be fulfilled to avoid an overlap of consecutive measured CIRs.

Averaging over several consecutive sequence periods at the receiver (waveform averaging) is an appropriate method to further improve the effective SNR without increasing the sequence duration and the number of samples to be stored unnecessarily [CFM93]. If N_{avrg} denotes the averaging factor, the averaging gain is given by

$$G_{\mathrm{avrg|dB}} = 10 \cdot \log_{10} N_{\mathrm{avrg}} \tag{3.10}$$

and together with the correlation gain adds up to the processing gain

$$G_{\mathrm{proc|dB}} = G_{\mathrm{avrg|dB}} + G_{\mathrm{corr|dB}}\,. \tag{3.11}$$

If averaging is applied, however, the measurement time T_m needed to determine one CIR is no longer equal to T_p, but given by $N_{\mathrm{avrg}}T_p$. As a consequence, the condition (3.8) must be substituted by the more restrictive condition

$$T_m = N_{\mathrm{avrg}}T_p \ll T_{\mathrm{coh}}. \tag{3.12}$$

A time-variant CIR sampled with the measurement repetition rate $r_{\mathrm{rep}} = \frac{1}{T_{\mathrm{rep}}}$ can be transformed to the Doppler domain if the sampling theorem is fulfilled with respect to the maximum Doppler frequency ν_{max}:

$$r_{\mathrm{rep}} \geq 2 \cdot \nu_{\mathrm{max}}. \tag{3.13}$$

As a matter of principle, $T_{\mathrm{rep}} = \frac{1}{r_{\mathrm{rep}}}$ cannot be smaller than T_m.

Due to the short measurement time, TD systems are suitable for measuring time-variant channels. Moreover, they enable to capture a spatial small-scale set of channel observations in a short time span by continuously varying the position of the receive (or the transmit) antenna and measuring during movement. Transformation from the aperture to the angle domain is feasible if the spacing of the samples Δx satisfies

$$\Delta x \leq \frac{\lambda}{2}. \tag{3.14}$$

It ensures the possibility of estimating angles of arrival (or departure) from a spatially sampled channel if it is static over the acquisition time. Spatial sampling is also feasible using a VNA. However, it is not possible to measure during the movement and the overall acquisition time for a spatial data set is substantially higher.

In practice, the sounding signal $s(t)$ is generated by a digital-to-analog converter (DAC) that is periodically repeating the sequence $s[n]$, $n = 0 \ldots N_{\mathrm{seq}} - 1$, according

to

$$s(t) = \sum_{n=-\infty}^{\infty} s[n \mod N_{\text{seq}}]p(t - nT), \tag{3.15}$$

where T is the sampling period. $p(t)$ is a pulse shape function that is determined by the digital low-pass filter in the DAC and the analog reconstruction filter.

Condition (3.8) ensures that the received signal is quasi-periodic. This is an advantageous property, because it means that the circular convolution theorem can be applied and the discrete Fourier transform (DFT) becomes an exact dual of the bandlimited time-domain signal [CLW69, CFM93]. The transmission equation for one period can therefore by expressed as

$$Y[k] = S[k]H[k], \quad k = 0, 1, \ldots, N_{\text{seq}} - 1, \tag{3.16}$$

where $Y[k]$, $S[k]$ and $H[k]$ denote the DFT representations of the received signal, the transmitted signal and the CTF, respectively.

In a real sounding system, the received signal is not only determined by the multipath channel, but also influenced by the Tx and Rx hardware and distorted by noise. The complete transmission equation is given by

$$Y[k] = S[k]H_{\text{Rx}}[k]H[k]H_{\text{Tx}}[k] + N[k], \tag{3.17}$$

where $H_{Rx}[k]$ and $H_{Tx}[k]$ are the DFT representations of the transfer functions of the analog receiver and transmitter chain, respectively. $N[k]$ represents additive noise at the receiver.

3.2 Sounding Sequences

As introduced in Section 3.1.2, quasi time-continuous TD channel sounding makes use of a periodic sounding signal $s(t)$. It is transmitted over the channel and observed at certain time instants at the receiver side. The quality of the measurement results depends on the characteristics of the sounding signal. If the channel sounder does not use more than one transmit branch at one frequency simultaneously, two properties of sounding signals are of importance: good periodic autocorrelation properties, which are directly related to spectrum flatness, and a low CF. Assuming digital signal generation, sounding signals are derived from sequences with exceedingly good correlation properties . Additional constraints on applicable sequences, such as the number of discrete amplitudes or phases, may be imposed by the hardware.

3.2.1 Definitions

One period of the periodic autocorrelation function (PACF) of the complex sequence $s[n]$, $n = 0, 1, \ldots, N_{\text{seq}} - 1$, is given by [Lü92]

$$R[m] = \sum_{n=0}^{N_{\text{seq}}-1} s^*[n]s[n+m \mod N_{\text{seq}}], \quad m = 0, 1, \ldots, N_{\text{seq}} - 1. \tag{3.18}$$

We have $R[0] = E$, where $E = \sum_{n=0}^{N_{\text{seq}}-1} |s[n]|^2$ is the energy of the sequence. The PACF is called perfect if $(E > 0)$

$$R[m] = \begin{cases} E & m = 0 \\ 0 & m \neq 0. \end{cases} \tag{3.19}$$

Here, a sequence whose PACF is given by (3.19) is referred to as a perfect sequence. The absence of sidelobe values in the PACF ensures that the achievable instantaneous dynamic range, defined as the ratio of the strongest to the weakest observable MPC in the CIR, is not limited by the sequence itself. The amplitude spectrum $|S[k]|$, where $S[k]$ is the DFT of $s[k]$, of a perfect sequence is ideally flat with [Lü92]

$$|S[k]|^2 = E, \quad k = 0, 1, \ldots, N_{\text{seq}} - 1. \tag{3.20}$$

Assuming ideal lowpass reconstruction, all tones of a sounding signal based on a perfect sequence therefore have the same magnitude. Consequently, the achievable SNR on each tone is not biased by the transmit signal.

A sequence is called uniform if all elements have the magnitude one. If the sequence can be written in the form

$$s[n] = e^{\frac{j2\pi}{P}\gamma[n]}, \quad n = 0, 1, \ldots, N_{\text{seq}} - 1, \quad 0 \leq \gamma(n) < P, \tag{3.21}$$

where $\gamma[n]$ is a sequence with integer elements, it is denoted as P-phase sequence [Lü92]. A P-phase sequence only exhibits phases from P equidistant angles.

According to the DFT relationships, a real-valued sequence has a conjugate complex symmetric spectrum of the form

$$S[k] = S^*[N_{\text{seq}} - k]. \tag{3.22}$$

If N_{seq} is even, this in particular implies that $S\left[\frac{N_{\text{seq}}}{2}\right] \in \mathbb{R}$. Furthermore, $S[0] \in \mathbb{R}$ for real-valued sequences of arbitrary length, because $S[0] = \sum_{n=0}^{N_{\text{seq}}-1} s[n]$ cannot contain an imaginary part if all elements of $s[n]$ are real-valued.

The CF of the sequence $s[n]$ can be defined as

$$\mathrm{CF}_{\mathrm{seq}} = \frac{\max_{0\leq n\leq N_{\mathrm{seq}}-1} |s[n]|}{\sqrt{\frac{1}{N_{\mathrm{seq}}} \sum_{n=0}^{N_{\mathrm{seq}}-1} |s[n]|^2}}. \tag{3.23}$$

The PAPR is the square of the CF. Corresponding values are often specified in dB. Since $\mathrm{CF}_{|\mathrm{dB}} = 20 \log_{10} \mathrm{CF}$ and $\mathrm{PAPR}_{|\mathrm{dB}} = 10 \log_{10} \mathrm{PAPR}$, $\mathrm{CF}_{|\mathrm{dB}} = \mathrm{PAPR}_{|\mathrm{dB}}$. It is noteworthy that the PAPR of a sequence is directly related to its energy efficiency η as e. g. defined in [Lü92], namely $\mathrm{PAPR} = \frac{1}{\eta}$. All uniform sequences achieve maximum energy efficiency and exhibit the minimum $\mathrm{CF}_{\mathrm{seq}}$ of 0 dB.

It is frequently assumed that using a sequence with $\mathrm{CF}_{\mathrm{seq}} = 0\,\mathrm{dB}$ is sufficient to operate the power amplifier in its optimum point and thus enable the maximum Tx power without nonlinear distortions of the signal. However, this is not true, because the analog baseband sounding signal $s(t)$ must be considered.[2] Assuming ideal lowpass reconstruction, $s(t)$ is given by

$$s(t) = \sum_{n=-\infty}^{\infty} s[n \mod N_{\mathrm{seq}}] \frac{\sin\left(\frac{\pi}{T}(t-nT)\right)}{\frac{\pi}{T}(t-nT)}, \tag{3.24}$$

where T is the sampling period. $s(t)$ is periodic with $T_p = N_{\mathrm{seq}} T$. The CF of $s(t)$ is given by [Fri97]

$$\mathrm{CF}_c = \frac{\max_{t\in[0,T_p]} |s(t)|}{\sqrt{\frac{1}{T_p} \int_0^{T_p} |s(t)|^2 \, dt}}. \tag{3.25}$$

The minimal CF is 0 dB. It is achieved by a single-tone signal. Generally, the minimal CF that is achievable with a multitone signal is not known and only lower bounds can be specified. The upper limit is $10 \log_{10}(N_t)\,\mathrm{dB}$, where N_t denotes the number of tones. Although it has been shown that complex multitone signals with a low CF close to 0 dB do exist if N_t is sufficiently large, it is unknown how they can be constructed [Fri97]. In the case of real signals, the lower limit is approximately 3 dB higher. Suitable complex sounding sequences therefore outperform real-valued ones and are preferable if they can be generated by the Tx hardware.

Since the signal $s(t)$ according to (3.24) contains the sequence values $s[n]$, it is clear that CF_c cannot be smaller than $\mathrm{CF}_{\mathrm{seq}}$. On the other hand, it cannot become larger than $10 \log N_{\mathrm{seq}}\,\mathrm{dB}$. In the following, the sounding sequences that were used for the measurements in this thesis are described. They have a perfect or almost

[2] Following [Fri97], it would be even more accurate to use the real-valued radio frequency (RF) signal in the context of CF considerations with respect to optimizing the operation point of the RF power amplifier. However, relevant deviations would only arise if the signal bandwidth was close to the carrier frequency.

perfect PACF and yield signals with a low CF.

3.2.2 Sequences used in this Work

Binary pseudo noise (PN) sequences with maximum period length, also denoted as maximum length sequences (MLSs) or m-sequences, are sometimes referred to as the "optimal pseudo-random code for channel sounding" [OHI04]. This statement is to be understood in the context of binary sequences. Binary MLS can be generated by a linear-feedback shift register and defined by a primitive generator polynomial using Galois field theory [Lü92]. They exist for lengths $N_{\text{seq}} = 2^m - 1$, $m \in \mathbb{N}$, where m determines the degree of the polynomial. The bipolar (antipodal) sequence $s_{\text{MLS}}[n]$ with elements of $\{-1, 1\}$ can be derived from the binary sequence $s^{\text{bin}}_{\text{MLS}}[n]$ with elements of $\{0, 1\}$ by mapping $0 \to 1$ and $1 \to -1$. MLSs are real-valued P-phase sequences with $P = 2$. Its PACF is given by

$$R_{\text{MLS}}[m] = \begin{cases} N_{\text{seq}} & m = 0 \\ -1 & m \neq 0. \end{cases} \tag{3.26}$$

It is thus not perfect, but contains constant negative side values, which can be regarded as an offset. The instantaneous dynamic range is limited to $20 \log_{10} N_{\text{seq}}$ dB. However, there are several approaches to remove this offset, for example by modifying the original sequence [FM91, MSS92, Gol92], or by applying a mismatched filter [MF93]. The latter approach is implicitly followed when using the calibration signal for estimating the CTF as formulated in (3.31). Alternatively, a large sequence length can be chosen to ensure that the limiting factor is not the (non-perfect) PACF, but thermal noise.

MLSs are widely used for channel sounding, mainly due to their inexpensive implementation in hardware or software. They were also used in this work for the in-cabin measurements along with the time-domain setup CS 1 (see Section 3.5.1), since only a single-channel DAC was available for generating a real-valued sequence.

To create perfect sequences with $N_{\text{seq}} > 4$, the transition to complex sequences is required [Lü92]. A method to construct uniform perfect sequences with quadratic lengths $N_{\text{seq}} = M^2$, $M \in \mathbb{N}$, was proposed by Frank et al. in [FZH62]. Frank sequences can be defined by

$$s_{\text{Frank}}[n] = e^{\frac{j2\pi p}{\sqrt{N_{\text{seq}}}}\left(n \mod \sqrt{N_{\text{seq}}}\right)\left\lceil \frac{n}{\sqrt{N_{\text{seq}}}} \right\rceil}, \quad n = 0, 1, \ldots, N_{\text{seq}} - 1, \tag{3.27}$$

where $p \in \mathbb{N}$ is relatively prime to M. For $p = 1$, this corresponds to the definition

used in [Lü92]. Frank sequences belong to the class of P-phase sequences, where $P = \sqrt{N_{\text{seq}}}$.

They were generalized by Chu [Chu72] to sequences of arbitrary length, which are known as Zadoff-Chu or Frank-Zadoff-Chu (FZC) sequences. They can be constructed by

$$s_{\text{FZC}}[n] = (-1)^{\lambda n} e^{\frac{j\pi n^2}{N_{\text{seq}}}}, \quad n = 0, 1, \ldots, N_{\text{seq}} - 1. \tag{3.28}$$

Each $\lambda \in \mathbb{N}$ which is relatively prime to N_{seq} yields a different sequence of the same length. FZC sequences are also P-phase sequences but their phase number is larger than for Frank sequences, namely $P = N_{\text{seq}}$ if N_{seq} is odd and $P = 2N_{\text{seq}}$ if N_{seq} is even. Frank and FZC sequences were used as basis for the measurements with the time domain setup CS 3.

For the indoor measurements with CS 1, real-valued (RV) multitone sequences based on FZC sequences were used. They are denoted as RV multitone sequences in the following. Based on the complex sequence $s[n]$ of length N_{seq} with its DFT $S[k]$, a real-valued sequence $s'[n]$ of length $N'_{\text{seq}} = 2N_{\text{seq}}$ was constructed by satisfying the symmetry condition (3.22) and $S[0] \in \mathbb{R}$ as follows:

$$s'[n] = \text{IDFT}\left\{S'[k]\right\} \text{ with } S'[k] = \begin{cases} C \cdot S[k] & 0 \leq k \leq \frac{N'_{\text{seq}}}{2} - 1 \\ C \cdot S[0] & k = \frac{N'_{\text{seq}}}{2} \\ C \cdot S^*\left[N'_{\text{seq}} - k\right] & \frac{N'_{\text{seq}}}{2} + 1 \leq k \leq N'_{\text{seq}} - 1, \end{cases} \tag{3.29}$$

where $C = 2e^{-j \arg\{S[0]\}}$. The real-valued sequence is perfect if the original sequence is perfect. Uniformity, however, is not preserved.

Figure 3.4 shows the computed CF of the sounding signals based on the aforementioned sequences as a function of N_{seq}. The results confirm that Frank and FZC sequences are preferable in view of achieving a low CF_c. For relevant lengths ($N_{\text{seq}} \geq 100$), the RV multitone sequences yield a CF_c that is approximately 2 dB larger than for the underlying FZC sequences.

For the most recent measurement with CS 4, the time-frequency swapping approach described in [Fri97] was applied to FZC sequences to create "optimized multitone sequences". They do no longer hold the P-phase property and uniformity, but yield a CF_c close to 0 dB. The same approach was used to create sequences for CS 2. Due to hardware constraints, they were converted into real-valued sequences with double the length by (3.29) and are denoted as optimized RV multitone sequences in this work. Their CF_c is close to 3 dB.

Finally, however, it should be noted that in practice the CF is only an indication of the achievable modulation of the power amplifier (PA) and the expectable

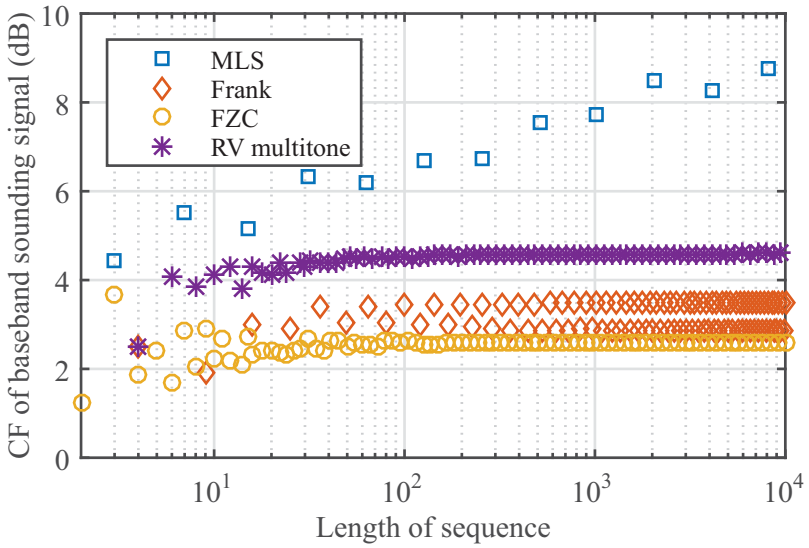

Figure 3.4: Crest factor CF_c of baseband sounding signal for maximum length sequences (MLS), Frank sequences (Frank), Frank-Zadoff-Chu sequences (FZC) and real-valued multitone sequences derived from Frank sequences (RV multitone) as a function of the sequence length N_{seq}.

performance. As long as out-of-band emissions do not violate the provisions of the test license, distortions of the signal that are caused by signal peaks falling into the nonlinear region of the PA, can be accepted to a certain extent and are partially compensated (in-band) by the calibration as described in Section 3.4. Error effects depend on the particular sequence in combination with hardware impairments. Ultimately, the performance of suitable sequences should therefore be determined by tests in the course of system calibration as outlined in Section 3.4.

3.3 Timing and Triggering

To implement correlation-based channel sounding, a trigger signal is needed at the Rx side, which is synchronous to the sounding signal. The structure of both signals is shown in Figure 3.5. The sounding signal with period T_p is transmitted continuously. A trigger pulse is generated periodically with period T_{rep}. T_{rep} must be an integer multiple of T_p. The measurement repetition rate or snapshot repetition rate is given by its reciprocal: $r_{\mathrm{rep}} = \frac{1}{T_{\mathrm{rep}}}$. Synchronization of the trigger signal with the sounding signal can either be ensured by generating both signals with the same device at the Tx side if more than one channel is available, or by generating them with different devices that are supplied with a synchronous reference clock. The reference signal may be distributed via cable or being generated independently at the Tx and the Rx

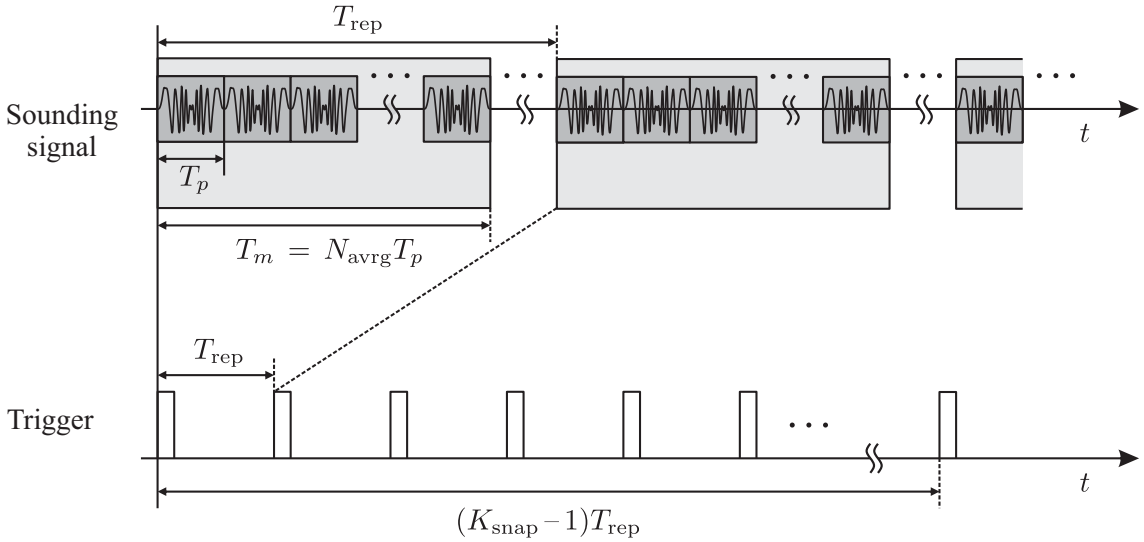

Figure 3.5: Structure and timing of sounding signal and trigger signal.

with highly stable frequency standards.

It is worth mentioning that an offset between the beginning of a sequence period and the trigger pulse, which can e. g. be caused by the travel time of the reference signal in the cable, is not relevant because it is compensated by calibration. However, if the absolute delay of the channel is to be evaluated, the offset must be constant over the entire time of the measurement campaign. The stability of the reference clock over T_m must be guaranteed in every case in order to avoid a degradation of the measurement dynamic.

The first trigger defines the start of the measurement run. Each time a trigger pulse is received by the Rx sampling unit, it acquires the signal within a window of duration $T_m = N_{\text{avrg}} T_p$. This corresponds to $N_m = N_{\text{avrg}} T_p r_{\text{ADC}}$ number of samples, where r_{ADC} is the sampling rate of the analog-to-digital converter (ADC). To maintain periodicity, it must be ensured that the calculation yields an integer N_m. Each acquired signal segment contains N_{avrg} periods of the sounding sequence, which are used for waveform averaging to improve the SNR. If $T_p r_{\text{ADC}}$ is an integer, the operation can be performed in the baseband without changing the sampling rate. If the averaging is to be performed on a sampled IF signal with r_{ADC} directly, it must be further ensured that the IF frequency f_{IF} is an integer multiple of $\frac{1}{T_p}$. The measurement run is completed when the predefined number of snapshots K_{snap} has been acquired, yielding one set of snapshots. The overall time needed to collect one set is $T_{\text{set}} = (K_{\text{snap}}–1) T_p + T_m$. Table 3.1 summarizes the fundamental timing conditions.

It should be noted that in practice additional constraints are imposed by the hardware. For example, a rearm time t_{rearm} after the acquisition of each snapshot

Table 3.1: Fundamental conditions for timing

Necessity	Condition	Comment
Always	C1: $T_{\text{rep}} = K_{\text{rep}} T_p, \;\; K_{\text{rep}} \in \mathbb{N}$	to maintain delay information
	C2: $T_m = N_m \frac{1}{r_{\text{ADC}}}, \;\; N_m \in \mathbb{N}$	to maintain periodicity, $T_m = N_{\text{avrg}} T_p$
	C3: $T_m \leq T_{\text{rep}}$	non-overlapping snapshots
For baseband averaging at sampling rate r_{ADC}	C4: $T_p = N_{\text{s}} \frac{1}{r_{\text{ADC}}}, \;\; N_s \in \mathbb{N}$	
For IF averaging at sampling rate r_{ADC}	C5: $f_{\text{IF}} = K_{\text{IF}} \frac{1}{T_p}$	in addition to C4

must be considered, which tightens C3 to $T_m + t_{\text{rearm}} \leq T_{\text{rep}}$. The rearm time is typically a function of other parameters like T_m itself and r_{ADC}. Overall, the relationships can be very complex and may not be sufficiently described in the data sheets of the devices so that tests are advisable to determine whether a parameter set is supported by the hardware.

3.4 Calibration

Regardless of the channel sounder setup, calibration is a prerequisite to obtain accurate and reproducible estimates of the channel. According to (3.17), the received sounding signal is not only determined by the channel itself, but also distorted by the frequency responses of the analog Tx and the Rx chains. They must be compensated by calibration. The principle of calibration, which is carried out before the channel measurements, is to insert a known channel H_{cal} into the transmission chain. Using the DFT representation, the received calibration signal is given by

$$Y_{\text{cal}}[k] = S[k] H_{\text{Rx}}[k] H_{\text{cal}}[k] H_{\text{Tx}}[k] + N_{\text{cal}}[k]. \tag{3.30}$$

Since $S[k]$ is known, (3.30) can be used to determine $H_{Rx}[k] H_{Tx}[k]$. However, using (3.30) in (3.17) and solving the equation for $H[k]$ yields

$$\begin{aligned} H[k] &= \frac{Y[k]}{S[k] H_{\text{Rx}}[k] H_{\text{Tx}}[k]} + N'[k] \\ &= \frac{Y[k]}{Y_{\text{cal}}[k]} H_{\text{cal}}[k] + N_c[k], \end{aligned} \tag{3.31}$$

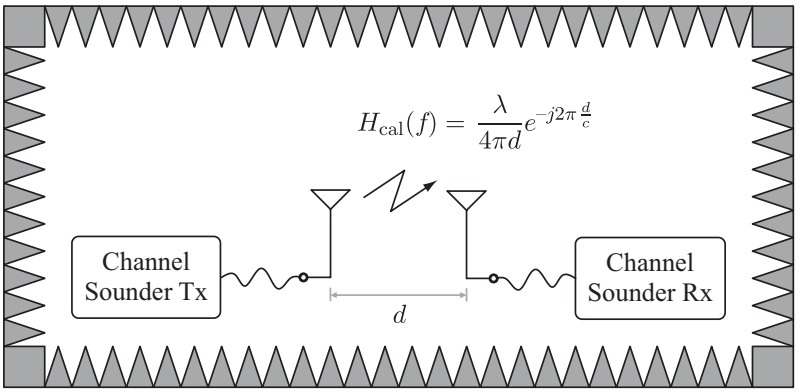

(a) Over-the-air calibration in an anechoic chamber, c denotes the speed of light.

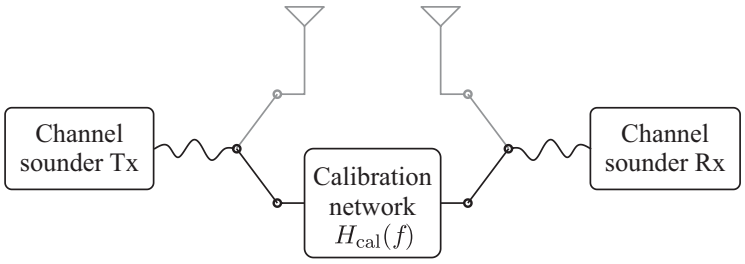

(b) Back-to-back calibration with a known calibration network.

Figure 3.6: Illustration of calibration methods.

where $N_c[k]$ represents the cumulative noise process from the measurement and the calibration. It is obvious from (3.31) that neither the (pulse-shaped) sounding sequence nor the CTFs of the Tx and Rx chain need to be explicitly known for the processing at the Rx side. The CTF can be simply estimated using the stored calibration signal. If the Rx involves an automatic gain control (AGC), the calibration measurement must be repeated for each AGC level. Besides setting the AGC, the system setup and the settings must not be changed after calibration.

The calibration can be performed either by over-the-air (OTA) transmission in an anechoic chamber or by substituting the measurement antennas with a calibration network which has been characterized in a separate step. The latter approach is also known as back-to-back calibration. The different methods are illustrated in Figure 3.6.

Since back-to-back calibration is usually much easier to carry out, it is used more frequently. This also applies to this work, where adjustable attenuators have been utilized as two-port calibration networks. However, it should be noted that the calibration methods are not identical and the results must be interpreted correctly. For OTA calibration, a known *propagation* channel is used as underlying "calibration channel". The properties of the measurement antennas are attributed to

the front-ends and calibrated out. In contrast, a known *radio* channel is inserted for back-to-back calibration—the measurement antennas are substituted. As a result, the measurement antennas are part of the (radio) channel in subsequent measurements. If the antenna characteristics are known, e. g. from independent measurements, they can be considered during post-processing. In this way, the results can again be linked to the propagation channel.

The stored calibration data allows to compensate for the unknown frequency-selective characteristics of the system components. In the course of calibration, the system may also be characterized and optimized. Following the definitions in Section 3.8, the goal is to maximize the instantaneous maximum measurable path loss (IMMPL) and the instantaneous dynamic range (IDR). Based on the same setup, which is used for calibration, this can be achieved by the following procedure:

- Step 1: Select a sequence of suitable length N_{seq} for creating the Tx sounding signal as described in Sections 3.2 and 3.3
- Step 2: Set the Tx power to a value that causes negligible nonlinear distortions (well below the 1 dB compression point of the PA; the shoulders in the spectrum of the Tx signal should be negligible, which may be checked with a spectrum analyzer)
- Step 3: Calibrate the system (for all AGC levels)
- Step 4: Set the attenuation of the calibration channel to a high value such that the measured CIR is dominated by thermal noise and determine the IMMPL
- Step 5: Set the attenuation of the calibration channel to the lowest value that is expected for the measurement campaign (several dB lower than the free-space PL with antenna gains at the minimum distance) and determine the IDR
- Step 6: Increase the signal level at the input of the Tx PA by a small value (e. g. 1 dB) and go back to Step 3 unless the input or output power of the PA reaches its maximum level stated in the data sheet, or the Tx power or the out-of-band emissions reach the maximum level permitted by the test license
- Step 7: Select the setting that maximizes the IMMPL under the condition that the IDR is larger than the targeted relative evaluation threshold, e. g. 40 dB (see also Section 3.6.2)

It is assumed that nonlinear effects in the Rx chain are avoided by suitable Rx design and AGC level adjustment. The procedure can also be used to compare the practical performance of different sounding sequences as mentioned in Section 3.2.2.

If the analog Tx hardware is strongly frequency-selective, it is advisable to compensate its frequency response by digital predistortion as far as possible. Although the frequency response of the overall transceiver chain is compensated during post-processing by taking into account the calibration measurement, predistortion can help to achieve equal performance over the entire bandwidth and improve the predictability of system behavior when nonlinear effects are not explicitly considered. In this work, linear digital predistortion was used in the setups CS 1 and CS 2, to reduce the frequency selectivity caused by the low-pass reconstruction filters.

3.5 Channel Sounder Setups used in this Work

In the course of this work, five channel sounder setups—four TD setups and one FD setup—were employed for the channel measurement campaigns. All of them involve commercial test and measurement equipment and in part dedicated hardware, which has been developed at the Fraunhofer Heinrich Hertz Institute (HHI). Since the setups are only partly described in the publication part of this thesis, they are introduced in this section. Several people were involved in the development and preparation of the setups. I therefore briefly describe my contribution at the end of each sub-section.

Table 3.2 gives an overview of all setups, their key features and parameters as well as references to the related sections. Slightly different setups were used for the exemplary characterization and validation measurements in Section 3.8. They are outlined in the respective publication.

3.5.1 Time-Domain Setups (CS 1–CS 4)

As visible in Table 3.2, the TD setups differ in their key features and characteristics. However, they all follow the same basic structure. It is shown in Figure 3.7. At the Tx, the baseband sounding signal is generated by a suitable device with a fast DAC. It is up-converted to the RF, typically via an intermediate frequency (IF), and sent via the transmit antenna. At the Rx, the received signal is down-converted to IF or baseband and sampled with a device that provides a fast ADC and a memory to store the data. It may additionally offer functionality for real-time data processing. Multiple channels can be realized by operating several Tx/Rx chains in parallel.

Two different variants were used in this work to ensure synchronization between Tx and Rx. Variant 1, where the reference clock is distributed via cable, was used for the indoor-, in-cabin and early outdoor measurements. In Variant 2, the reference clock is generated independently at the Tx and the Rx with highly stable frequency

Table 3.2: Overview of time-domain (TD) and frequency-domain (FD) channel sounder setups (CS 1–CS 5) used in this work; T&M stands for modular setups that comprise various interconnected commercial test and measurement instruments

Setup	CS 1	CS 2	CS 3	CS 4	CS 5
TD/FD	TD	TD	TD	TD	FD
Core components	T&M	T&M	HIRATE	T&M	VNA
Number of channels	1 Tx, 1 Rx	2 Tx, 2 Rx	2 Tx, 2 Rx	4 Tx, 4 Rx	1 Tx, 1 Rx
RF center freq. (GHz)	5, 61	60	10, 60.4	10.25, 28.5, 41.5, 82.5	61
Bandwidth (GHz)	1.0	3.0	0.25	1.5	22
Synchronization	cable	cable	cable or rubidium clock	rubidium clock	cable
Waveform averaging	offline	offline	real-time	real-time	-
Related sections	4.1–4.3	4.5	3.8, 5.1–5.4	5.5	4.4

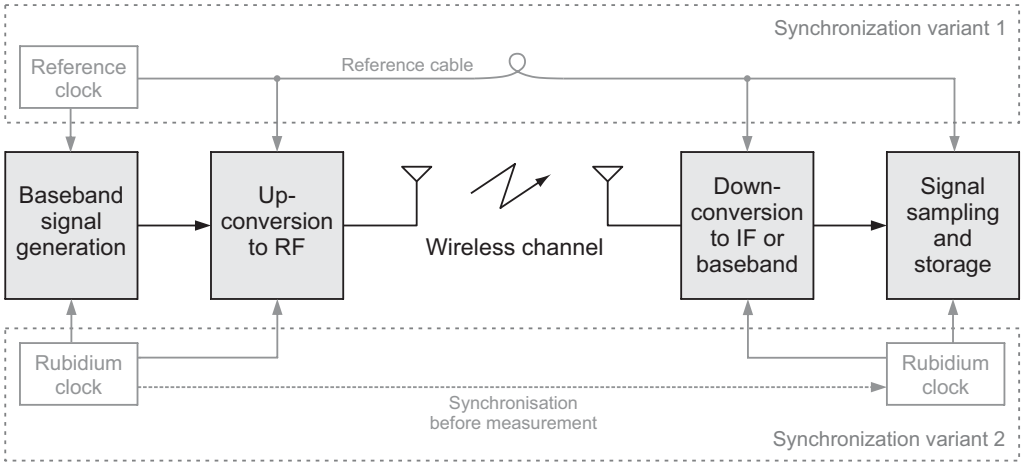

Figure 3.7: Principle structure of time-domain channel sounder setups CS 1–CS4.

standards based on rubidium clocks. A pair of suitable devices, also denoted as Synchronomat in the following, was used for the later outdoor measurements. The two clocks are synchronized to each other via cable before the calibration of the channel sounder and then separated. The devices also comprise an FPGA-based programmable trigger unit, which was used in the setups CS 2 and CS 4. More details can be found in [Wis07, PWK+08a].

SISO Setup (CS 1)

Starting the research for this work, a channel sounder for time-domain measurements was not available. Therefore, the first task was to build up a suitable setup based on existing laboratory equipment with regard to the following criteria: large bandwidth, high repetition rate and automatable measuring process, monitoring and data storage.

The resulting modular setup is illustrated in Figure 3.8. A dual-channel Agilent

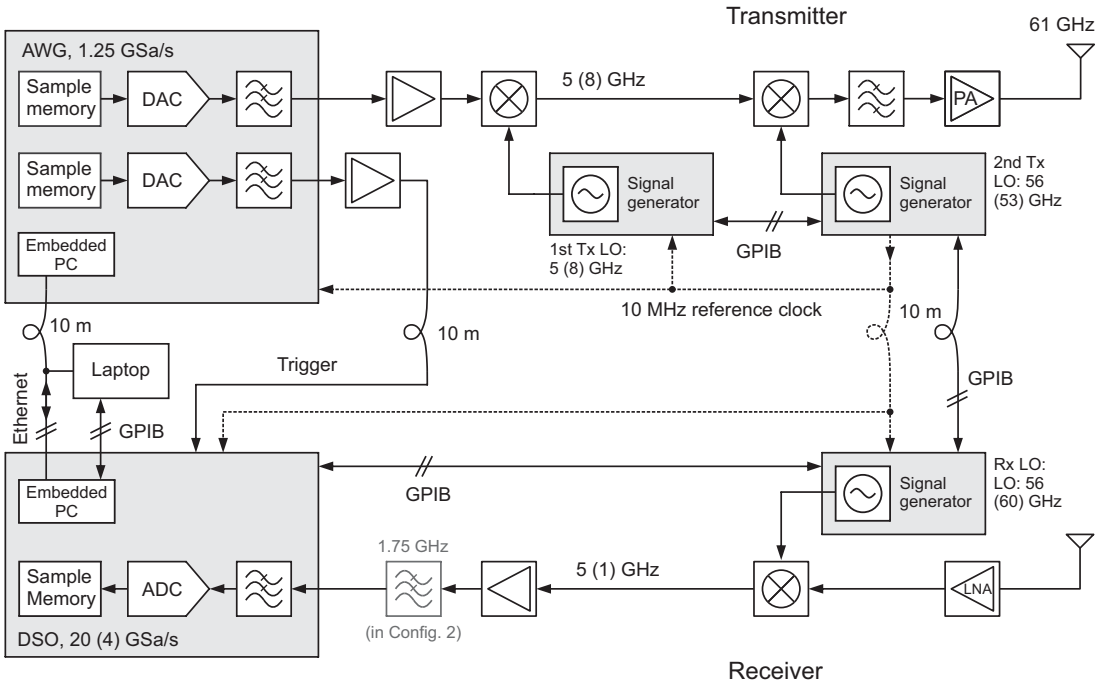

Figure 3.8: Schematic of SISO channel sounder setup CS 1.

N6030A arbitrary waveform generator (AWG) with a resolution of 15 bit, a sampling rate of 1.25 GSa/s and a modulation bandwidth of 500 MHz per channel serves as source for the baseband sounding signal. After the DAC, a reconstruction filter (cutoff frequency: 500 MHz) is applied, which is part of the AWG in the form of a 7-pole elliptical realization. For the measurements in this work, linear digital predistortion was used to reduce their frequency selectivity in a pre-calibration step.

The baseband sounding signal is first modulated onto an IF carrier of 5 GHz (or

8 GHz) by means of a double-balanced mixer. The local oscillator (LO) signal is provided by a signal generator. The resulting double-sideband IF signal is fed into a single-balanced RF mixer. The lower sideband and the LO signal are suppressed by a 58 to 62 GHz bandpass filter (BPF). A PA finally connects the mixer output to the transmit antenna. Numerous attenuators have been integrated into the setup to reduce reflections due to imperfect impedance matching of the components and to carefully optimize the signal levels at all input ports. For the sake of clarity, they are not shown in Figure 3.8. Figure 3.9 illustrates the up-conversion process by means of the signal spectra at the Tx side.

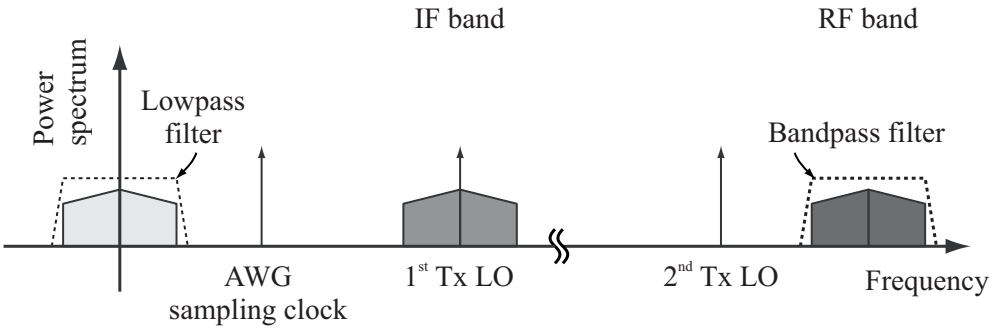

Figure 3.9: Up-conversion at Tx side for setup CS 1.

At the receiver side, the antenna signal is fed into a low noise amplifier (LNA) and down-converted to IF stage. Then the signal is amplified and directly sampled in the IF domain by an Agilent Infiinum 40 GSa/s digital sampling oscilloscope (DSO) with an analog bandwidth of 10 GHz and a resolution of 8 bit.

Figure 3.10 illustrates the down conversion to IF. Down conversion to complex baseband is performed afterwards in the digital domain. Synchronization of the equipment is ensured by distributing the 10 MHz reference clock via flexible coaxial cables.

It is worth mentioning that, as illustrated in Figure 3.8, the AWG provides two synchronized outputs, which can in principle be used as inphase/quadrature phase

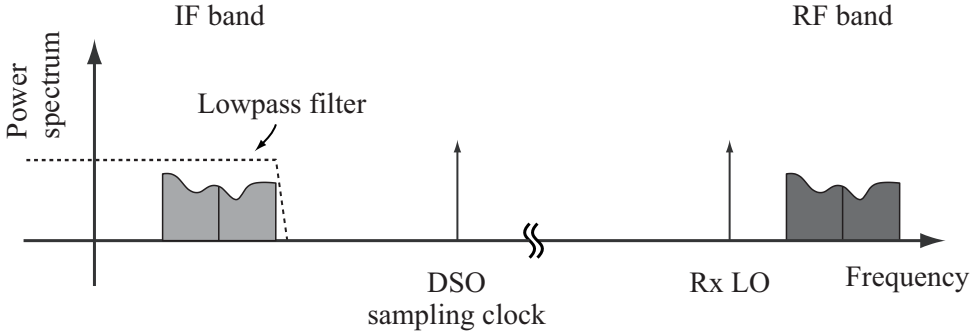

Figure 3.10: Down-conversion at Rx side for setup CS 1.

(IQ) branches to create a signal with 1 GHz IQ bandwidth in combination with an IQ modulator. However, as Channel 2 was needed for generating the trigger pulses as described in Section 3.3, it was no longer available for IQ signal generation.[3] Nevertheless, the above-described approach using a double-sideband mixer at the Tx and a (digital) complex down conversion at the Rx, allows to use 1 GHz bandwidth for channel sounding. A minor drawback is that only real-valued sequences can be applied, which reduces the degrees of freedom for CF optimization of the sounding signal (see Section 3.2).

Each time a trigger pulse is detected by the DSO, it captures $N_m = N_{\text{avrg}} T_p r_{\text{ADC}}$ samples as described in Section 3.3. The measurement is stopped when K_{snap} snapshots have been acquired. The number of snapshots is limited by the memory depth M_{Rx} of the DSO to $K_{\text{snap}} \leq \left\lfloor \frac{M_{\text{Rx}}}{N_m} \right\rfloor$, where M_{Rx} itself depends on N_m and r_{ADC}. Its maximum value is $M_{\text{Rx,max}} = 65.6\,\text{MSa}$ for the DSO settings in this work.

A General Purpose Interface Bus (GPIB) and an Ethernet connection are used to adjust the measurement parameters of the Tx and the Rx via laptop and to transfer the DSO data to an external hard disk. The whole measurement procedure is controllable via a graphical user interface (GUI), developed for this purpose. After a measurement run, the sample data of the IF signal is available on the hard disk. All necessary postprocessing is realized off-line in the digital domain. The calibration measurement was performed with an adjustable attenuator, which is frequency-flat over the measurement bandwidth. Table 3.3 summarizes the specifications of the measurement setup in relation with the settings for the measurement campaigns in the conference room and the aircraft passenger cabin.

The overall setup, photos with Vivaldi antennas are shown in Figure 3.11, also included a positioning device to move the receive antenna accurately over a certain distance d_m on a linear track during the measurement run. This allowed to analyze small-scale fading effects and to derive APDPs by spatial averaging. Prior investigations have shown that $d_m = 10\,\text{cm} \approx 20\lambda$ is a good choice for the given configuration. It ensures sufficient variation of the wave's phase, but prevents the delays of the

[3] The AWG provides additional trigger outputs, called markers, which enable system synchronization on waveform level in principle. However, although considerable efforts were made, attempts to achieve a sufficiently accurate synchronization based on the markers have not been successful. As the marker signals have lower bandwidth than the baseband signal outputs and hence the transition steepness of a trigger pulse is significantly lower, even small error effects due to noise or interference cause a considerable trigger jitter. Stimulating the DSO by the AWG marker output, up to ±200 ps overall jitter in the baseband signal were observed, which would have resulted in significant degradation of the measurement results. To circumvent this problem, the second channel of the AWG was used to generate trigger pulses in coherence with the sequence output on the first channel. By this means the overall jitter could be reduced to approximately ±50 ps.

Table 3.3: Specifications and settings of the SISO channel sounder setup CS 1 as used for measurements in the conference room and the aircraft cabin

	Configuration 1	Configuration 2
Environment	Conference room	Aircraft cabin
Related sections	4.1–4.2	4.3
Number of channels	Tx: 1, Rx: 1	Tx: 1, Rx: 1
Antennas	Tx: omni/Vivaldi	Tx: open waveguide
	Rx: omni/Vivaldi	Rx: omni
RF center frequency f_c	5 / 60 GHz	60 GHz
Transmit power P_T	12 dBm	
Measurement bandwidth B	1.0 GHz	
IF frequency f_{IF}	Tx: 5 GHz, Rx: 5 GHz	Tx: 8 GHz, Rx: 1 GHz
DAC clock rate (AWG) r_{DAC}	1.25 GSa/s	4 GSa/s
DAC resolution (AWG) Q_{DAC}	15 bit	
ADC sampling rate (DSO) r_{ADC}	20 GSa/s	4 GSa/s
ADC resolution (DSO) Q_{ADC}	8 bit	
Rx memory depth (DSO) M_{Rx}	65.6 MSa	
Type of sequence	RV multitone	MLS
Sequence duration T_p	1 µs	2.047 µs
Waveform averaging	offline, baseband	
Number of averages N_{avrg}	25	60
Measurement time T_m	25 µs	123 µs
Measurement repetition period T_{rep}	50 ms	
Number of snapshots per run K_{snap}	100	

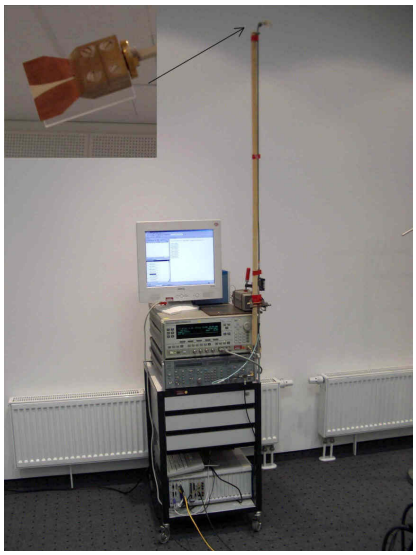

(a) Transmitter

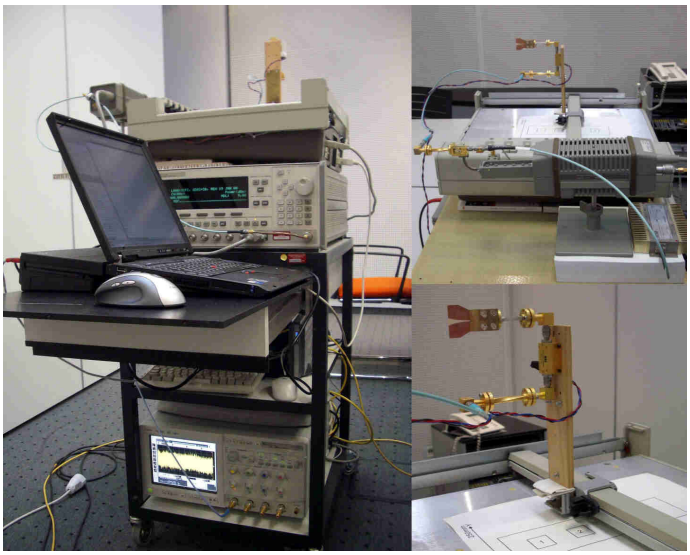

(b) Receiver

Figure 3.11: Channel sounder setup CS 1 with positioning device at the receiver.

propagation from changing substantially. A DSO trigger pulse had to be generated every 50 ms to achieve the desired spatial distance of 1 mm between two consecutive snapshots for the adjusted positioner velocity of 20 mm/s. The continuous motion did not affect the accuracy of the measurement because the system needed at most 123 µs to acquire one snapshot, corresponding to approx. $2.5 \cdot 10^{-3}\lambda$ at 60 GHz.

Contribution After initial consultation with W. Keusgen, all work related to CS 1 was done by myself. More specifically, I worked out the overall concept, built up the channel sounder setup from available test and measurement devices, created a Matlab-based software environment with a GUI to automate the entire measuring process, comprising Tx sounding signal generation and matched trigger signal generation based on a selectable sequence, control of the positioning device, segmented triggering of the oscilloscope, transfer of the data to the control PC and data preview. I optimized the setup to achieve a high output power and a high dynamic range with very low system-intrinsic distortions. This included a digital predistortion of the Tx signal to compensate the frequency response of the Tx chain up to IF level.

The developed methods and the software formed an essential basis for all further developments in the field of channel measurement at mm-wave frequencies and at 5.7 GHz for car-to-car communication, which were subsequently carried out by the work group headed by W. Keusgen at Fraunhofer HHI.

MIMO Setup (CS 2)

For the specific investigations on human body shadowing in Section 4.5, the SISO channel sounder setup CS 1 was extended to 2×2 MIMO by incorporating hardware modules that had been developed for a car-to-car channel sounder in the meantime. The modified channel sounder schematic is illustrated in Figure 3.12.

The original two-channel AWG has been replaced by two synchronized Euvis AWG452 modules. As the AWG modules allow clocking with up to 4 GSa/s, the measurement bandwidth could be increased from 1 GHz to 3 GHz. Several components from the car-to-car MIMO channel sounder [PWK+08a] are utilized in the setup, namely the reference clock containing a programmable trigger unit (Synchronomat) and several analog components (2 baseband amplifiers, 2 mixers and a synthesizer for the 1st LO). Their characteristics determine the IF frequency of 5.7 GHz. Besides providing the 10 MHz reference clock, the Synchronomat triggers the DSO in accordance with the predefined acquisition parameters. Thus, both AWG branches are available for baseband sounding signal generation. Dedicated reconstruction lowpass filters behind the DACs are not shown in Figure 3.12 because

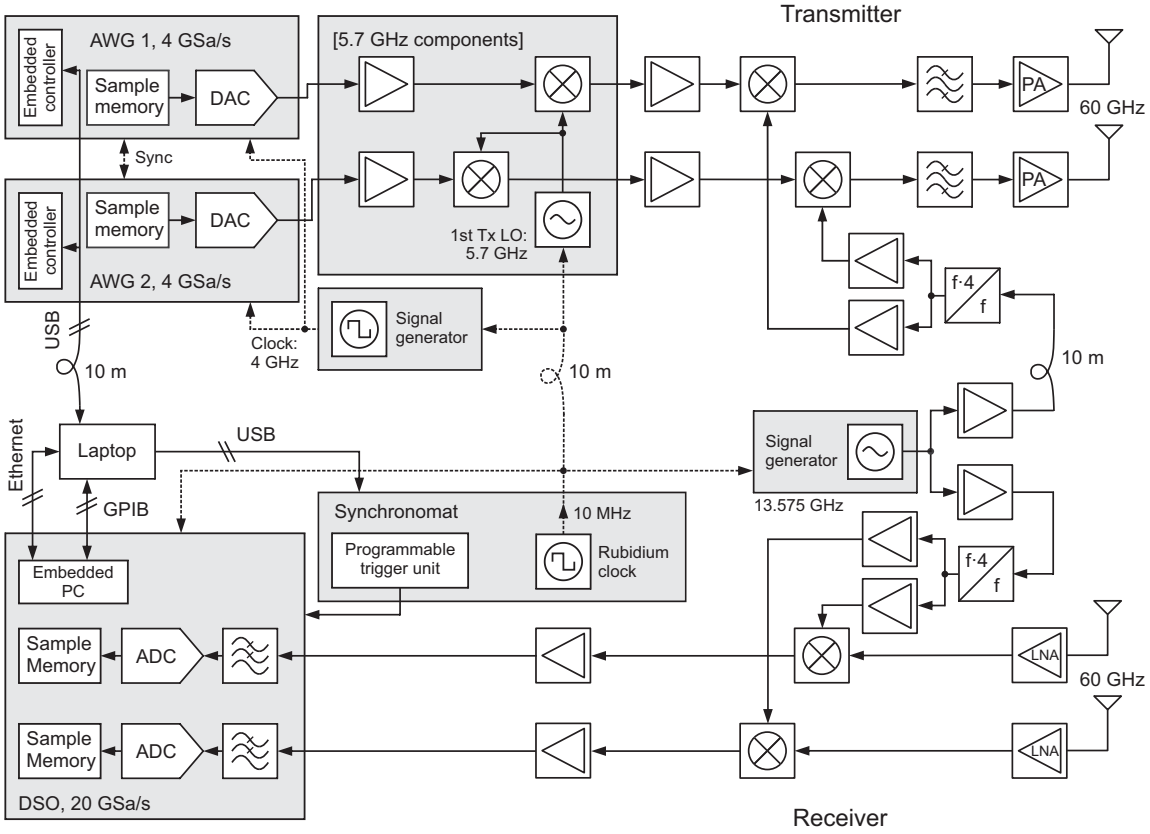

Figure 3.12: Schematic of MIMO channel sounder setup CS 2.

the subsequent baseband amplifiers exhibit a limited bandwidth and inherently perform the filtering. For the measurements, linear digital predistortion was used at the Tx to partially compensate the frequency selectivity of the DACs and the components up to IF in a pre-calibration step. Back-to-back calibration was performed with an adjustable RF attenuator for each Tx-Rx combination sequentially. Table 3.4 summarizes the specifications of the setup.

Contribution As described above, the CS 2 setup was largely based on CS 1. The Synchronomat device was developed by some colleagues, incorporating my advice on required trigger signal generation features and accuracy. All work related to the integration of the devices and components was done by myself. In collaboration with W. Wisotzki, I further developed the CS 1 software to support two channels and triggering via the Synchronomat.

HIRATE Setup (CS 3)

Chapter 5 describes early 5G mm-wave measurement campaigns in outdoor environments. Apart from the multi-frequency campaign in Section 5.5, all outdoor

Table 3.4: Specifications and settings of the MIMO TD channel sounder setup CS 2 as used for the human body shadowing measurements in Section 4.5

Number of channels	Tx: 2, Rx: 2
Antennas	Tx: omni, Rx: open waveguide
RF center frequency f_c	60.0 GHz
Transmit power P_T	10 dBm (each channel)
Measurement bandwidth B	3.1 GHz
IF frequency	5.7 GHz
DAC clock rate (AWG) r_{DAC}	4 GSa/s
DAC resolution (AWG) Q_{DAC}	12 bit
ADC sampling rate (DSO) r_{ADC}	20 GSa/s
ADC resolution (DSO) Q_{ADC}	8 bit
Rx memory depth (DSO) M_{Rx}	65.6 MSa
Type of sequence	Optimized RV multitone
Sequence duration T_p	0.67 µs
Waveform averaging	offline, baseband
Number of averages N_{avrg}	9
Measurement time T_m	6.0 µs
Measurement repetition period T_{rep}	9.0 ms
Number of snapshots per run K_{snap}	512

measurements were conducted with a time-domain setup that makes use of the HIRATE (High Performance Digital Radio Testbed) platform. It has been developed at Fraunhofer HHI to enable rapid implementation and testing of new wireless transmission concepts and signal processing algorithms. The device comprises a commercial FPGA platform and an in-house-developed converter board [KKPW13]. It is shown in Figure 3.13. The converter board carries two dual-channel DACs and ADCs and can be equipped with various modules such as clocks, frequency synthesizers and modulators to build up two parallel Tx/Rx chains with 250 MHz bandwidth and carrier frequencies up to several GHz. To cover mm-wave frequencies, the HIRATE is used in conjunction with external front-ends. For channel sounding, a dedicated FPGA implementation is available.

Although the system provides less bandwidth than the devices used in CS 1 and CS 2, it has been selected for the outdoor measurements, since it is easy to handle and allows real-time averaging, which is essential for achieving a sufficient SNR at mm-wave frequencies in connection with outdoor distances and omnidirectional antennas. The schematic of the setup in the full version as used for the dual-frequency measurements in the street canyon at 10 and 60 GHz is illustrated in Figure 3.14. For the single-frequency measurements at 60 GHz, the components of the 10 GHz

Figure 3.13: HIRATE platform: core component of the channel sounder setup CS 3.

branch were not needed.

In contrast to CS 1 and CS 2, a dual channel DAC in combination with an IQ modulator is available, so that a complex sounding sequence can be applied (Frank sequence of length 256 in the present case). Since the two channels are separated in frequency, the same sounding signal can be used. It is split at IF level. At 60 GHz, two PAs are combined to increase the Tx power. A common reference clock is used to derive the sampling clock of the DACs and the LO frequencies. All components up to IF stage are part of the actual HIRATE platform. For the purpose of the measurements, however, further components have been accommodated in the HIRATE housing as illustrated in Figure 3.14 to make the system compact.

At the Rx side, both channels are down-converted to the same IF and fed into variable gain amplifiers (VNAs). They are set by an AGC implemented in the FPGA, which uses the modulation of the ADC as an input. The FPGA also accomplishes the sequence-synchronous acquisition of the baseband signal and real-time waveform averaging. The resulting data is written to the on-board memory and can be downloaded to the hard disk of a connected Laptop, which is also used for system control. Synchronization of Tx and Rx is ensured by rubidium clocks as shown in Figure 3.14 or a reference cable. Table 3.5 summarizes the specifications and the settings of CS 3 in relation with the backhaul and access outdoor measurement campaigns presented in Sections 5.1–5.4.

Contribution The HIRATE platform and related software was developed by some of my colleagues at Fraunhofer HHI. I helped to build up the overall setup CS 3, incorporating two HIRATE devices. I tested and optimized the setup to achieve a high output power and dynamic range.

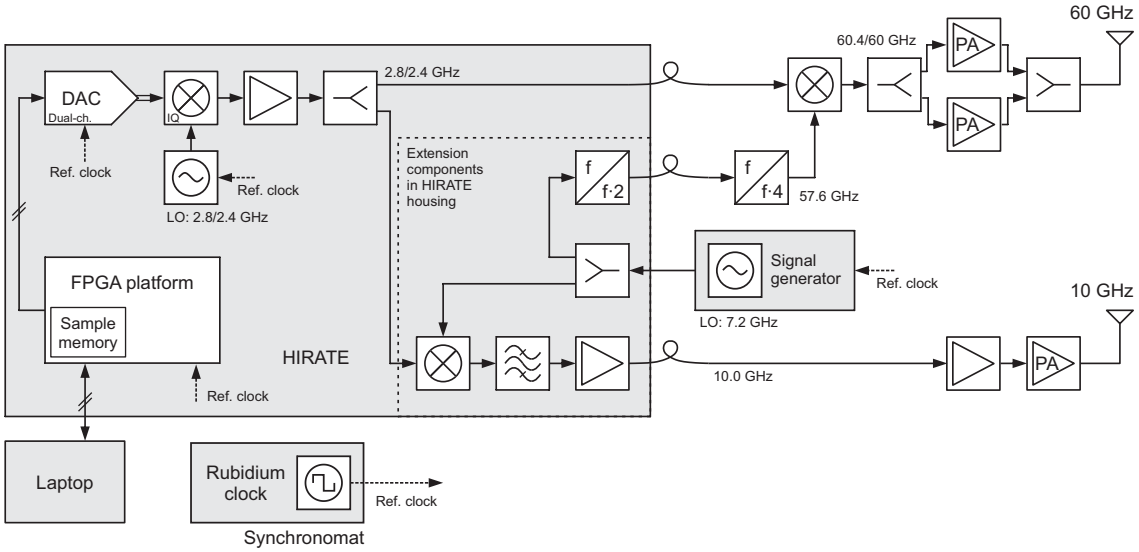

(a) Transmitter

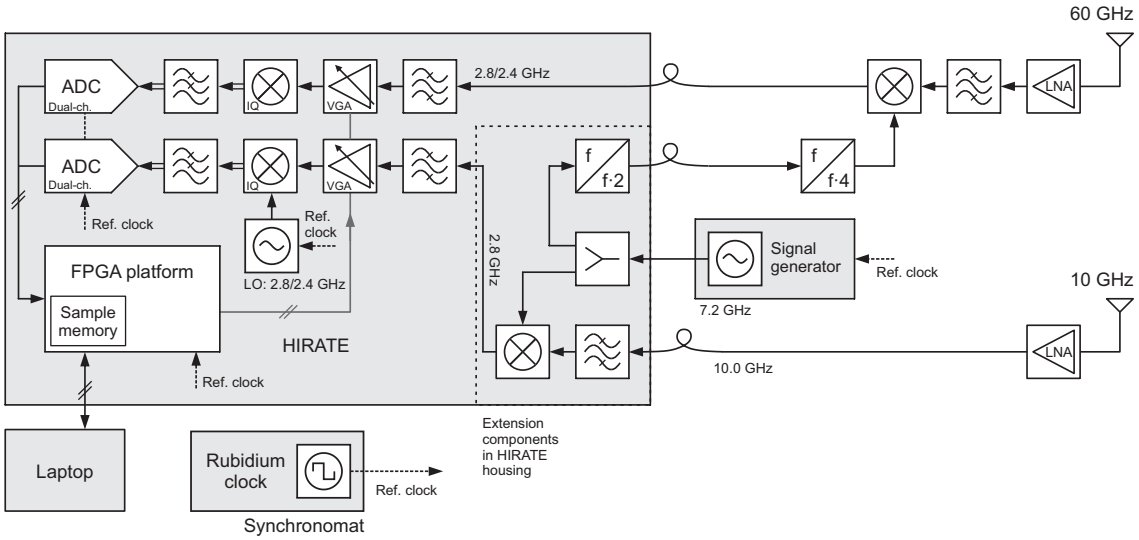

(b) Receiver

Figure 3.14: Schematic of the HIRATE channel sounder setup CS 3 in the full version for dual-frequency measurements. The frequency settings after the slash were used for the single-frequency measurements at 60 GHz.

Table 3.5: Specifications and settings of the HIRATE channel sounder setup CS 3 as used for the outdoor measurements in Sections 5.1–5.4. Values in brackets refer to the dual-frequency measurements, which are part of the evaluations in Section 5.2.

	Configuration 1	Configuration 2
Scenario	Outdoor access	Small-cell backhaul
Related sections	5.2–5.4	5.1
Number of channels	Tx: 1 per freq., Rx: 1 per freq.	Tx: 1, Rx: 1
Antennas	omnidirectional	20 dBi horns
RF center frequency f_c	60.0 GHz (60.4 & 10.0 GHz)	60.0 GHz
Transmit power P_T	15 dBm (15 & 20 dBm)	15 dBm
Measurement bandwidth B	250 MHz	250 MHz
IF frequency f_{IF}	2.4 GHz (2.8 GHz)	2.4 GHz
DAC clock rate r_{DAC}	250 MSa/s	
DAC resolution Q_{DAC}	16 bit	
ADC sampling rate r_{ADC}	250 MSa/s	
ADC resolution Q_{ADC}	8 bit	
Rx memory depth M_{Rx}	16 MSa per channel	
Type of sequence	Frank	
Sequence duration T_p	1.024 µs	
Waveform averaging	real-time, baseband	
Number of averages N_{avrg}	64	
Measurement time T_m	65.5 µs	
Measurement rep. period T_{rep}	0.80 ms	0.53 ms
Number of snapshots per run K_{snap}	62,500	60,000

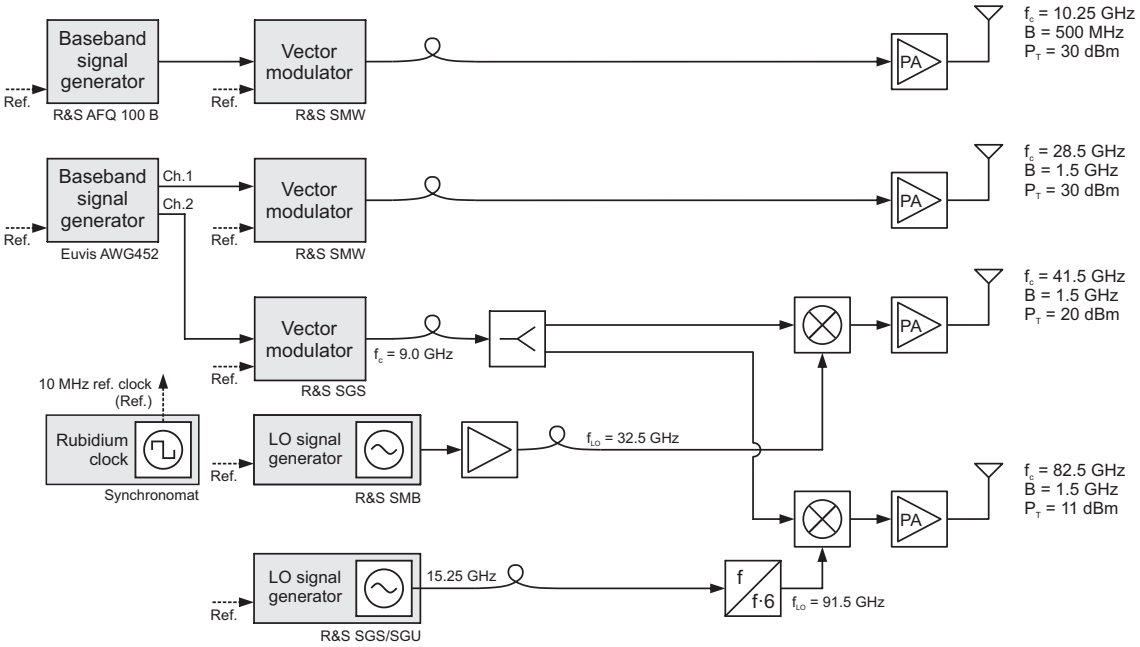

Figure 3.15: Schematic of the multi-frequency channel sounder setup CS 4: Tx side.

Multi-Frequency Setup (CS 4)

The most recent measurements in the street canyon were conducted with a modular multi-frequency wideband channel sounder setup based on dedicated hardware and test and measurement equipment. It features four parallel Tx/Rx branches and a measurement bandwidth up to 1.5 GHz. The schematics of the Tx and the Rx are illustrated in Figure 3.15 Figure 3.16. Photos are shown in Figure 3.17. Each branch is used for a different frequency band. However, the same baseband sounding signal with 1.5 GHz bandwidth is employed for 28, 41 and 82 GHz. Due to regulatory reasons, the bandwidth at 10 GHz is limited to 500 MHz, so that a separate baseband signal generator is needed. The generators periodically replay an optimized multitone sounding sequence. For the street canyon measurements presented in Section 5.5, the sequence duration was chosen as 2.56 µs. A transmit power of 30 dBm could be achieved at 10 and 28 GHz. It was lower for 41 GHz (20 dBm) and 82 GHz (11 dBm). At all frequencies, self-built omnidirectional antennas with vertical polarization and $\lambda/2$-dipole-like patterns at both the Tx and the Rx were used.

At the receiver side, the signals are amplified, down-converted, filtered and sampled at IF stage. The Rx supports real-time averaging over multiple sequence periods (waveform averaging). An averaging factor of $N_{\text{avrg}} = 100$ was used for the street canyon measurements. This results in a measurement time of $T_m = 256\,\mu\text{s}$. After averaging, the sample data can be directly streamed onto multiple parallel hard disks. Thus, the number of snapshots is only limited by the disk space. Synchronization

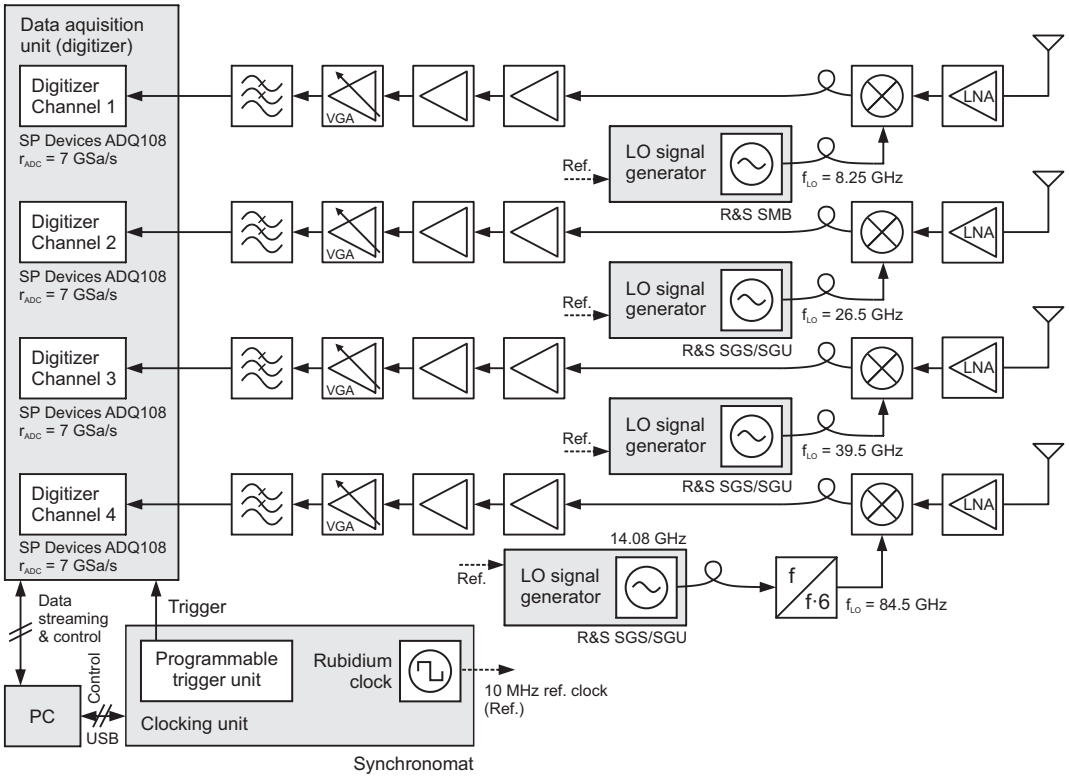

Figure 3.16: Schematic of the multi-frequency channel sounder setup CS 4: Rx side.

(a) Transmitter (b) Receiver

Figure 3.17: Photos of multi-frequency channel sounder setup CS 4.

Table 3.6: Specifications and settings of the multi-frequency channel sounder setup CS 4 as used for the street canyon measurement campaign in Section 5.5

Number of channels	4 at Tx, 4 at Rx (1 per freq.)			
Antennas	omnidirectional			
Channel	1	2	3	4
RF center frequency f_c (GHz)	10.25	28.5	41.5	82.5
Transmit power P_T (dBm)	30	30	20	11
Measurement bandwidth B (GHz)	0.5	1.5	1.5	1.5
DAC clock rate r_{DAC} (GSa/s)	0.6	4	4	4
DAC resolution Q_{DAC} (bit)	14	12	12	12
ADC sampling rate r_{ADC}	7 GSa/s			
ADC resolution Q_{ADC}	8 bit			
(Rx memory depth M_{Rx})	streaming to PC			
Type of sequence	Optimized multitone			
Sequence duration T_p	2.56 µs			
Waveform averaging	offline, baseband			
Number of averages N_{avrg}	100			
Measurement time T_m	256 µs			
Measurement repetition period T_{rep}	2.0 ms			
Number of snapshots per run K_{snap}	50,000			

between Tx and Rx is ensured via temperature-controlled rubidium clocks (Synchronomat devices). The specifications of CS 4 and the timing parameters for the street canyon measurement campaign are summarized in Table 3.6. The setup was calibrated on site for each channel via back-to-back measurement using adjustable attenuators.

Contribution The CS 4 setup was built up by some of my colleagues at Fraunhofer HHI. They also developed the software for control of the measuring process. I have defined the requirements and supported the development continuously through consultation and discussion.

3.5.2 Frequency-Domain Setup (CS 5)

In contrast to all other measurement campaigns, it was hardly possible to carry out measurements with a moving antenna for the desired transmit and receive positions in the car. Therefore, both antennas were fixed. In order to reduce small-scale fading effects as far as possible, the best delay resolution and thus the highest feasible measuring bandwidth was aimed for. This resulted in the use of a VNA-based

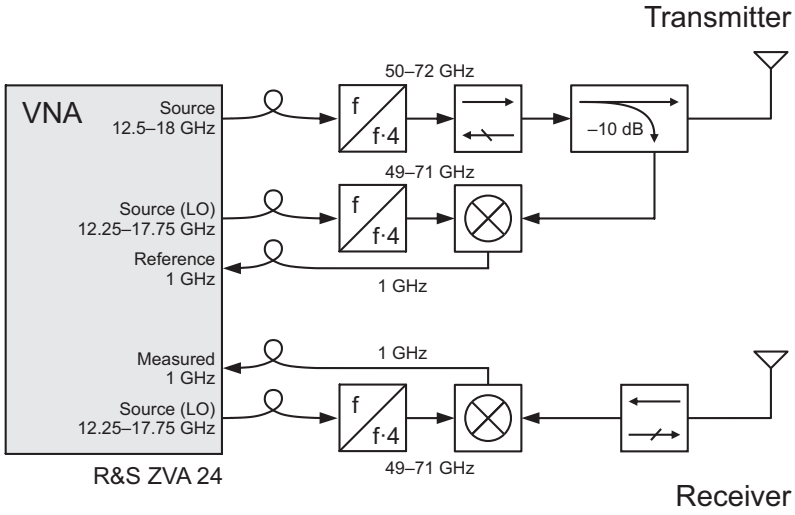

Figure 3.18: Schematic of the frequency-domain channel sounder setup CS 5.

frequency-domain setup. Its schematic is shown in Figure 3.18.

A Rohde & Schwarz ZVA24 vector network analyzer is the core component of the system. Since the measuring range of the device is limited to a maximum frequency of 24 GHz, modules for extending the frequency range have been built up from laboratory components. By using additional outputs of the ZVA24 which supply the LO signal for the up- and down-conversion of the RF signal and feedback of the reference signal on the measuring frequency of 1 GHz, the setup allows measurements from 50 to 72 GHz. The full bandwidth was used for the in-car measurements with a frequency spacing of $\Delta f = 4\,\mathrm{MHz}$. This resulted in a maximum observable delay of 250 ns, which was more than sufficient for the measurement scenario.

Contribution The setup CS5 was built up jointly by R. Felbecker and myself on the basis of available laboratory equipment.

3.6 Data Processing and Analysis

In general, the post-processing of the acquired data strongly depends on the desired analysis methods. For the measurements in this thesis, down-conversion to complex baseband was performed first when IF sampling had been used. It was followed by low pass filtering of each snapshot to eliminate outer band noise. If multiple periods of the sounding signal were acquired per snapshot, they were averaged coherently to improve the SNR. The data of the calibration measurement was used to equalize the frequency response of the measurement chain and to perform the correlation intrinsically in one step as described in Section 3.4. Both correlation and equalization

could be computed efficiently in a single step in the frequency domain according to (3.31). After these operations, a sequence of time- or space-variant CIRs was available.

In the following, several aspects of further processing are discussed which are most relevant for this work. They are related to the estimation of the PDP, the TOA parameters and the path loss or channel gain. A comprehensive overview of various processing and analysis methods for channel sounding data with detailed explanations and illustrative examples can be found in [Sal13].

3.6.1 Derivation of the APDP

In this work, it is assumed that the CIR at any instant in time or space is related to a stochastic process, which is wide-sense stationary (WSS) over a short time interval. PDPs are calculated by averaging over successively measured CIRs $h_k(\tau)$ at K receive points according to

$$\hat{P}(\tau) = \frac{1}{K} \sum_{k=0}^{K-1} |h_k(\tau)|^2 \,. \tag{3.32}$$

The aim of spatial sampling and averaging is to cause a phase shift of the MPCs of at least 2π in the observation/averaging window without significantly changing their delays and violating the WSS assumption [Sal13]. Depending on the setup and the measurement parameters, this may not always be fully achieved in practice and the APDP is only an estimate of the PDP.

For the indoor and in-cabin measurements in this work, the environment was kept static during the measurement procedure. Based on the definitions and considerations in Sections 2.3.1–2.3.3, there are three interpretations of APDPs derived by (3.32) in conjunction with a moving (Tx or Rx) antenna:

1. Moving the antenna introduces time variance and the time-variant channel is regarded as a two-dimensional stochastic process. The time-variant CIR is given by $h(t, \tau; \xi)$, where ξ is the random parameter. To estimate the $P_h(\tau) = E\{h(t, \tau; \xi)\}$, ensemble averaging (over ξ) is replaced by time averaging (over t) by assuming ergodicity. A limited number of discrete observation points in time x_k, $k = 0 \ldots K-1$, are available for the estimation.

2. Moving the antenna introduces space variance and the space-variant channel is regarded as a two-dimensional stochastic process. The space-variant CIR is given by $g(\tau, x; \xi)$ where ξ is the random parameter and x is the substitute of t in 1. To estimate $P_g(\tau) = E\{g(\tau, x; \xi)\}$, ensemble averaging (over ξ) is replaced

by space/aperture averaging (over x) by assuming ergodicity. A limited number of discrete observation points in space x_k, $k = 0 \dots K-1$, are available for the estimation.

3. The channel is regarded as a one-dimensional random process. The CIR is given by the $h(\tau;\xi)$, where ξ is the random parameter. $P_h(\tau)$ is estimated by ensemble averaging, where only a limited number of observations ξ_k, $k = 0 \dots K-1$ are available for the estimation.

Regardless of the interpretation, the results are, of course, always the same. An averaging over 10 cm was performed for the indoor and in-cabin environments, corresponding to $20\,\lambda$ at 60 GHz. During the outdoor measurements, additional time-variance was caused by pedestrians and vehicles. It superimposed with the time-/space variance caused by the moving receiver. The effects could no longer be completely separated from each other.

3.6.2 Estimation of TOA Parameters

The TOA parameters as quantitative measures of the PDP have been introduced in Section 2.3.5. Additional aspects on their estimation from measurement data are addressed in this section. The considerations aim at deriving the parameters directly from the measured APDP without employing path estimation algorithms.

Evaluation Threshold

The application of an evaluation threshold X as introduced in Section 2.3.5 is a practical method to limit the length of the PDP and to prevent noise and system-related distortions from affecting the estimated TOA parameters. The effect of noise can be further reduced by discarding values with $10\log_{10} P(\tau) < X_{|\mathrm{dB}}$.

In any case, X must be chosen well above the noise floor. Especially when a relative threshold Γ is used, it is important to check, whether this prerequisite is met for all measured scenarios. If, for a given Γ, X would include noise components, Γ must be reduced. However, it is important to note that the TOA parameters strongly depend on Γ. It it therefore essential to specify Γ or X in conjunction with TOA evaluations. Only results based on the same threshold can be directly compared. Since there is no commonly agreed value for X and it is problematic to fix a meaningful value that is applicable to measurement data from various channel sounders at different frequencies, is is advisable to use a relative threshold such as $\Gamma = 30\,\mathrm{dB}$ or $\Gamma = 20\,\mathrm{dB}$ to enable the comparison with TOA values in the literature.

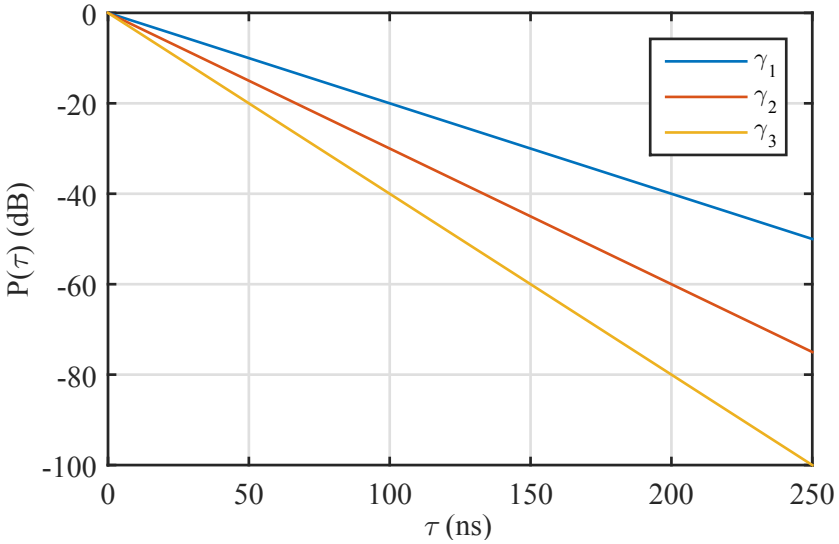

Figure 3.19: Exponentially decaying PDPs with the decay factors $\gamma_1 = 4.605 \cdot 10^7\,\mathrm{s}^{-1}$, $\gamma_2 = 6.908 \cdot 10^7\,\mathrm{s}^{-1}$ and $\gamma_3 = 9.210 \cdot 10^7\,\mathrm{s}^{-1}$.

For illustration, the influence of the evaluation threshold is investigated based on an exponentially decaying PDP

$$P(\tau) = \begin{cases} P_0 e^{-\gamma\tau}, & \tau \geq 0 \\ 0, & \tau < 0, \end{cases} \tag{3.33}$$

where $P_0 \in \mathbb{R}^{>0}$ is a power scaling factor and $\gamma \in \mathbb{R}^{>0}$ is the decay factor. Figure 3.19 illustrates three PDPs for $P_0 = 1$ and the decay factors $\gamma_1 = 4.605 \cdot 10^7\,\mathrm{s}^{-1}$, $\gamma_2 = 6.908 \cdot 10^7\,\mathrm{s}^{-1}$ and $\gamma_3 = 9.210 \cdot 10^7\,\mathrm{s}^{-1}$. These factors correspond to relative decays of 20 dB, 30 dB and 40 dB at 100 ns excess delay, respectively.

As the PDP according to (3.33) is a strictly monotonically decreasing function, evaluating TOA parameters with the relative threshold Γ is equivalent with evaluating $P(\tau)$ only up to the maximum excess delay $\tau_{\max}$ with

$$\tau_{\max} = \frac{\ln \Gamma}{\gamma}. \tag{3.34}$$

The moments of $P(\tau)$ can then be defined as

$$M_n = \int_0^{\tau_{\max}} \tau^n P(\tau)\, d\tau. \tag{3.35}$$

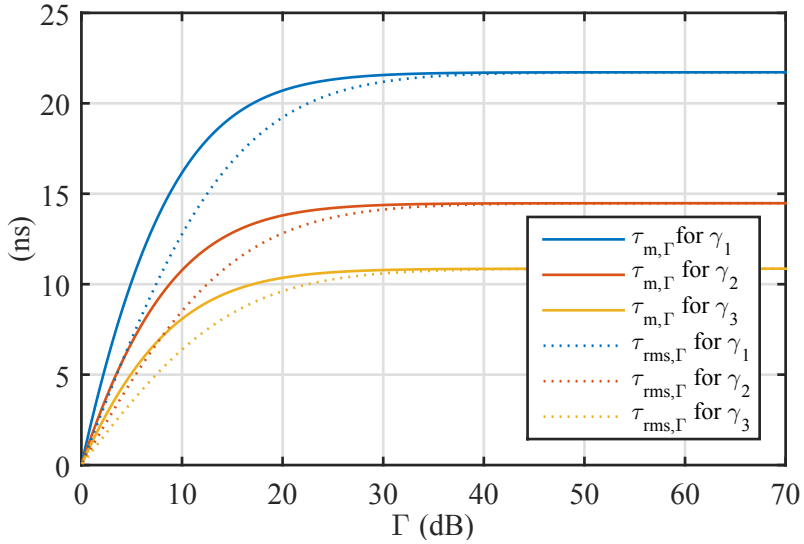

Figure 3.20: Calculated mean excess delay τ_m and RMS delay spread τ_rms as a function of the relative evaluation threshold Γ.

Using (3.33) yields

$$M_0 = P_0 \frac{1 - \frac{1}{\Gamma}}{\gamma}, \quad M_1 = P_0 \frac{1 - \frac{1+\ln\Gamma}{\Gamma}}{\gamma^2}, \quad M_2 = P_0 \frac{2 + \frac{-2-\ln\Gamma(2+\ln\Gamma)}{\Gamma}}{\gamma^3}. \tag{3.36}$$

The mean excess delay with respect to Γ is given by

$$\tau_{\mathrm{m},\Gamma} = \frac{M_1}{M_0} = \frac{1 - \Gamma + \ln\Gamma}{\gamma\,(1-\Gamma)} \tag{3.37}$$

and the RMS delay spread by

$$\tau_{\mathrm{rms},\Gamma} = \sqrt{\frac{M_2}{M_0} - \tau_\mathrm{m}^2} = \sqrt{\frac{1 - \frac{\Gamma \ln^2\Gamma}{(\Gamma-1)^2}}{\gamma^2}}. \tag{3.38}$$

The respective limits for $\Gamma \to \infty$ represent the true values of the mean excess delay and the RMS delay spread:

$$\tau_\mathrm{m} = \lim_{\Gamma\to\infty} \tau_{\mathrm{m},\Gamma} = \frac{1}{\gamma}, \quad \tau_\mathrm{rms} = \lim_{\Gamma\to\infty} \tau_{\mathrm{rms},\Gamma} = \frac{1}{\gamma}. \tag{3.39}$$

They are equal for an exponentially decaying PDP. Figure 3.20 shows τ_m and τ_rms as a function of Γ according to (3.37) and (3.38). The curves start from zero with a large slope and finally slowly tend to the asymptotic values $\frac{1}{\gamma_1} \approx 21.7\,\mathrm{ns}$, $\frac{1}{\gamma_2} \approx 14.5\,\mathrm{ns}$ and $\frac{1}{\gamma_3} \approx 10.9\,\mathrm{ns}$, respectively. It is obvious that both parameters will be heavily underestimated if the relative threshold is chosen too low, e. g. $\Gamma = 10\,\mathrm{dB}$. Since,

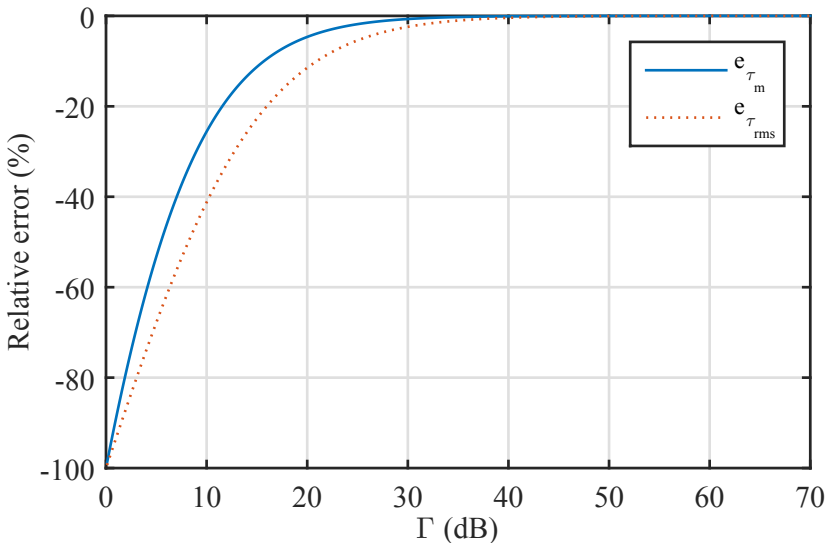

Figure 3.21: Relative estimation errors e_{τ_m} and e_{τ_rms} as a function of the relative evaluation threshold Γ.

for a given Γ, $\tau_{\mathrm{rms},\Gamma}$ is always smaller than $\tau_{\mathrm{m},\Gamma}$, the absolute estimation error for τ_rms is larger. Furthermore the absolute estimation errors increase with increasing dispersion of the channel (decreasing γ).

The relative error e_{τ_m} of τ_m is given by

$$e_{\tau_\mathrm{m}} = \frac{\tau_{\mathrm{m},\Gamma}}{\tau_{\mathrm{m},\infty}} - 1 = \gamma\tau_{\mathrm{m},\Gamma} - 1 = \frac{\ln\Gamma}{1-\Gamma}. \tag{3.40}$$

Equivalently, the relative error of the delay spread e_{τ_rms} can be calculated as

$$e_{\tau_\mathrm{rms}} = \frac{\tau_{\mathrm{rms},\Gamma}}{\tau_\mathrm{rms}} - 1 = \gamma\tau_{\mathrm{rms},\Gamma} - 1 \overset{\gamma>0}{=} \sqrt{1 - \frac{\Gamma\ln^2\Gamma}{(\Gamma-1)^2}} - 1. \tag{3.41}$$

The relative errors are independent from the decay factor γ. They are illustrated in Figure 3.21 as a function of Γ. The shape of both curves is equivalent with the ones shown in Figure 3.20, since the functions of the relative errors are only normalized versions of $\tau_{\mathrm{m},\Gamma}$ and $\tau_{\mathrm{rms},\Gamma}$ themselves. In Table 3.7, e_{τ_m} and e_{τ_rms} are summarized for $\Gamma \in \{10, 15, 20, 25, 30, 35, 40\}$ dB.

For the given exponential shape of the PDP, relative errors below 5% thus require a threshold above 25 dB. It should be noted that for PDPs exhibiting distinct strong MPCs, for example a strong LOS component in addition to a much weaker NLOS part, the errors can be significantly larger. It is therefore advisable to set the threshold as large as possible. For comparison reasons, it is useful to determine TOA values for several different thresholds.

Table 3.7: Relative estimation errors e_{τ_m} and e_{τ_rms} for selected values of the relative evaluation threshold Γ

Relative threshold Γ (dB)	Relative error e_{τ_m} (%)	Relative error e_{τ_rms} (%)
10	−26	−41
15	−11	−23
20	−4.7	−11
25	−1.8	−5.4
30	−0.69	−2.4
35	−0.25	−1.0
40	−0.092	−0.43

Frequency-Domain Windowing

An aspect, which has not been taken into account in the TOA estimation so far, is the effect of limited measurement bandwidth. Assuming a channel sounder which is calibrated to have a flat frequency response over the measurement bandwidth B, the effective sounding pulse is a sinc pulse and $h_b(t)$ is given by a superposition of sinc pulses according to (2.16). A PDP $P_b(\tau)$ determined by

$$P_b(\tau) = E\left\{|h_b(\tau)|^2\right\} \tag{3.42}$$

exhibits sidelobes (first sidelobe relative to the maximum: $-13\,\mathrm{dB}$) that cause errors in the estimation of the TOA parameters if applying (2.50)–(2.55) directly, because they are misinterpreted as multipath components if $\Gamma > 13\,\mathrm{dB}$. To circumvent this problem, a window function $W(f)$ is applied to the measurement data in the frequency domain. If $W(f)\big|_{|f|>\frac{B}{2}} = 0$, the bandlimited CIR with windowing is given by

$$\begin{aligned} h_w(t) &= \int_{-\infty}^{\infty} H(f)\cdot W(f) e^{2\pi f t}\, df \\ &= h(t) * w(t), \end{aligned} \tag{3.43}$$

where $w(t)$ is the window function in the (delay) time domain. The purpose of this windowing is to reduce the side lobes to such an extent that they are below the relative threshold. The effective sounding pulse becomes $w(t)$.

In this work, a Kaiser window was applied for all TOA evaluations and illustrations

of the CIR. It can be defined by [Kai74]

$$W_{\text{kaiser}}(f) = \begin{cases} \frac{I_0\left(\beta\sqrt{1-\left(\frac{2f}{B}\right)^2}\right)}{I_0(\beta)}, & -\frac{B}{2} \leq f \leq \frac{B}{2} \\ 0, & \text{otherwise,} \end{cases}$$

where I_0 is the zeroth-order modified Bessel function of the first kind and β is a non-negative real number that determines the trade-off between the mainlobe width and the sidelobe level in the time domain. Increasing β widens the mainlobe and decreases the amplitude of the sidelobes. The values $\beta = 5$ and $\beta = 6$, which yield side lobes of approximately $-37\,\text{dB}$ and $-44\,\text{dB}$, were used in conjunction with $\Gamma = 30\,\text{dB}$ and $\Gamma = 40\,\text{dB}$, respectively.

The original discrete form of the Kaiser window is given by [Kai74]

$$W_{\text{kaiser}}[k] = \begin{cases} \frac{I_0\left(\beta\sqrt{1-\left(\frac{2k}{N-1}-1\right)^2}\right)}{I_0(\beta)}, & 0 \leq k \leq N-1 \\ 0, & \text{otherwise,} \end{cases}$$

where N denotes the length of the window in samples.

Effective Sounding Pulse Width

The limited measurement bandwidth and the frequency-domain windowing yield an effective pulse with a certain width. If we assume that the number of MPCs in (2.27) is constant over a short time interval and also their delays are (virtually) constant, the PDP can be expressed as

$$P_\delta(\tau) = \sum_{l=0}^{L-1} \bar{\beta}_l^2 \delta(\tau - \tau_l), \tag{3.44}$$

where $\bar{\beta}_l^2 = E\left\{\beta_l^2\right\}$ is denoted as gain or (normalized) power of the l-th MPC.

Assuming that either the width of the effective sounding pulse is small enough to prevent a pulse overlap in the CIR, or the angles ϕ_l are statistically independent uniform variables over $[0, 2\pi)$ [SV87], the bandlimited PDP with windowing is

$$P_w(\tau) = \sum_{l=0}^{L-1} \bar{\beta}_l^2 \left|w(\tau - \tau_l)\right|^2. \tag{3.45}$$

It can be shown that the mean excess delay $\tau_{\text{m},w}$ and the RMS delay spread $\tau_{\text{rms},w}$ calculated on $P_w(\tau)$ using (2.52) and (2.54) overestimate the values $\tau_{\text{m},\delta}$ and $\tau_{\text{rms},\delta}$

calculated on $P_\delta(\tau)$ due to the width of the effective sounding pulse [SV87]:

$$\tau_{\mathrm{m},w} = \tau_{\mathrm{m},\delta} + \tau_{\mathrm{m,win}} \tag{3.46}$$

and

$$\tau^2_{\mathrm{rms},w} = \tau^2_{\mathrm{rms},\delta} + \tau^2_{\mathrm{rms,win}}, \tag{3.47}$$

with $\tau_{\mathrm{m,win}}$ and $\tau_{\mathrm{rms,win}}$ being the mean excess delay and the RMS delay spread of the effective sounding pulse calculated on $P_{\mathrm{win}}(\tau) = |w(\tau)|^2$ using (2.52) and (2.54). This can be taken into account when estimating the mean excess delay and the RMS delay spread from bandlimited measurement data by

$$\hat{\tau}_{\mathrm{m}} = \tau_{\mathrm{m}} - \tau_{\mathrm{m,win}} \tag{3.48}$$

and

$$\hat{\tau}_{\mathrm{rms}} = \sqrt{\tau^2_{\mathrm{rms}} - \tau^2_{\mathrm{rms,win}}}. \tag{3.49}$$

where τ_{m} and τ_{rms} denote the values calculated directly by (2.52) and (2.54) and $\hat{\tau}_{\mathrm{m}}$ and $\hat{\tau}_{\mathrm{rms}}$ are the improved estimations. The maximum excess delay estimation can be improved by

$$\hat{\tau}_{\mathrm{max}} = \tau_{\mathrm{max}} - \tau_{\mathrm{max,win}}. \tag{3.50}$$

If (3.50)–(3.48) are used with a relative threshold Γ, the same Γ should be applied for all calculations. However, in conjunction with a threshold, the modified values are approximations. For a large measurement bandwidth and highly dispersive channels, the corrections are usually negligible. Nevertheless, they are beneficial in order to reduce the relative estimation error if the time dispersion of the channel and the measurement bandwidth are small, and yield consistency for the edge case of a one-path channel. If the above assumptions related to (3.45) are met, which is at least approximately achievable by means of suitable averaging in estimating the PDP, the improved values also allow a direct comparison of TOA results—even if they are determined from measurement data of different bandwidth. The improved estimations were used for all outdoor channel evaluations in Chapter 5.

Discretized Time Delay Axis

A channel sounder provides a sampled version of the CIR and hence a sampled version $P_w(nT + t_0)$ of $P_w(\tau)$, where T is the sampling interval and $t_0 \in [0, T)$ is a random offset. If the TOA parameters are calculated on $P_w(nT + t_0)$, the results depend on t_0. To minimize deviations between different observations of the same $P_b(\tau)$ and allow the application of (3.48) and (3.49) for general cases, it is therefore

beneficial to use a small sampling interval. It can be reduced by upsampling the CIR in accordance with (2.16):

$$h_w(mT) = \sum_{n=-\infty}^{\infty} h_w(nT')\text{sinc}\left(\frac{1}{T'}\left(mT - nT'\right)\right), \tag{3.51}$$

where T' and T denote the sampling interval before and after upsampling, with $T < T'$. The oversampling ratio OSR can be defined as

$$\text{OSR} = (BT)^{-1}, \tag{3.52}$$

where B denotes the two-sided (double-sided) bandwidth. In this work, oversampling with OSR ≥ 4 was used for all TOA evaluations, even if not explicitly mentioned. The resulting variations of the TOA estimations with respect to t_0 are therefore negligible.

IPDP-Based TOA Evaluations

Formally, TOA parameters can also be calculated on IPDPs $p(\tau) = |h(\tau)|^2$, which is often done in the literature. As stated in [Bul02] in the context of correlation bandwidth evaluations, IPDP-based parameter estimations are not in conformity with the original definitions. The performance of a fixed wireless system in a static environment depends on the individual channel, which is fully described by its CIR. A direct link between system performance and correlation bandwidths derived from instantaneous measurements is not known [Bul02].

Nevertheless, irrespective of the deviation from the original definition, the IPDP-based TOA values can be regarded as quantitative measures for the characterization of CIRs. If numerous CIRs for one scenario are available, the analysis of the empirical distribution gives an indication of the variability of the channel. Furthermore, it is valuable to consider the case where the temporal resolution of the measurement system is very large. With increasing bandwidth, less propagation paths superimpose, so that the IPDPs in a local area are increasingly stable. If all paths can be resolved, the calculated instantaneous TOA values of one channel observation are virtually identical to TOA values derived from the related APDP (corresponding to non-overlapping pulses in Section 3.6.2). If it can be shown, e.g. by geometric considerations, that at least the most relevant propagation paths can be resolved, IPDP-based TOA values can be seen as an approximation to the APDP-based parameters.

In general, however, it is important to note that IPDP-based values can be strongly influenced by small-scale fading and highly depend on the measurement bandwidth. This makes the comparison of values in the literature considerably more difficult.

The measurement parameters and involved estimation methods must be carefully considered.

3.6.3 Calculation of Channel Gain and Path Loss

In this work, the channel gain G_C is defined as the overall transmission gain induced by the radio channel. It is calculated from a measured CIR or CFR by

$$\begin{aligned} G_C &= \int_0^{\tau_{\max}} |h(\tau)|^2 \, d\tau \\ &= \frac{1}{B} \int_{-\frac{B}{2}}^{\frac{B}{2}} |H(f)|^2 \, d\tau. \end{aligned} \tag{3.53}$$

If the integration is performed over $P(\tau)$ instead of $|h(\tau)|^2$, the result is denoted as local area channel gain. According to [SC97] the normalized received power (NRP) is defined as the ratio of received to transmitted power, including the antenna gains. Assuming a calibrated measurement system that exhibits a flat frequency response over B, G_C and NRP are equal. They are therefore regarded as equivalent in this work and derived in the same way. The quantities are used instead of the PL to deliberately include the antenna gains in the evaluation. Based on the local area channel gain $\bar{G}_C$, the PL is calculated by

$$L_{\mathrm{PL|dB}} = -10 \log_{10} \bar{G}_C + G_{T|\mathrm{dBi}} + G_{R|\mathrm{dBi}} \,. \tag{3.54}$$

3.7 Comparison of Measurement Results

Statistically reliable measurement data is needed to develop stochastic channel models and to derive accurate model parameters. Associated measurement campaigns typically require expensive channel sounding equipment at mm-wave frequencies and involve a high effort. With regard to the validation and parametrization of 5G channel models, which need to support a huge frequency range, it is therefore increasingly important to compare and merge available measurement results. In the following, some fundamental related aspects are outlined. Although not explicitly mentioned, the considerations refer not only to measurement data, but also to data from deterministic or stochastic models with regard to mutual comparisons and comparisons with measurement data.

When comparing measurement results, it is first of utmost importance to consider whether the measurement antennas are included in the channel or not, hence if the results refer to the radio channel or the propagation channel. As reported in the

literature and as will be shown in Section 4.2, the characteristics of the radio channel may strongly depend on the measurement antenna, although the propagation environment remains unchanged. Path estimation and antenna deconvolution techniques may be used to remove the antenna effects [CSW02, FTH+99, SSKW05]. However, the results provided by different algorithms, may also differ.

Wideband channel measurement results can be compared at different abstraction levels, denoted as comparison levels (CL) in the following. A possible classification is:

- CL 1: single observations (CIR, CTF)
- CL 2: characteristic functions (e.g. APDP, FCF)
- CL 3: large-scale parameters (e.g. DS, coherence bandwidth, PL)
- CL 4: statistical metrics of large-scale parameters or specific parameters for their modeling (e.g. standard deviation of the DS, PL exponent)

From CL 1 to 4, the comparison typically requires an increasing amount of data and data processing.

A CL 1 comparison has been e. g. presented by Zwick et al. [ZBN05] to verify time-domain measurement results with a VNA-based system, using observations at identical Tx and Rx positions in the same environment. The exemplary CTFs and CIRs show a very good agreement—a result, which also well sustains theory, stating that a measurement result neither depends on the measurement principle nor a particular sounder implementation (see Section 3.1). Besides system calibration, CL 1 comparisons only involve processing steps that are essential for converting the data to the same representation, for example (inverse) Fourier transform, windowing and filtering. CL 2 comparisons are based on a coherent set of data rather than on single observations. They involve additional steps to estimate the characteristic functions, e. g. spatial averaging.

Both CL 1 and CL 2 comparisons are mainly useful to illustrate congruence of measurement results or singular deviations—incongruity is generally hard to quantify. In fact, a comparison of data acquired with different channel sounders in the same environment intends to indirectly confirm that the system outputs correct results rather than to show that they are identical. A direct approach for verification is to measure in an environment with predictable results, such as an anechoic chamber or a reverberation chamber. An exemplary result is presented in Section 3.8. Meaningful CL 1 and CL 2 comparisons require access to the data and convertibility to an

identical representation (e.g. illustration of the IPDP) with the same boundary conditions, e. g. the same bandwidth and frequency resolution.

In Section 5.5, the DS of the street canyon channel at different frequencies is compared in a statistical manner (CL 3/4 comparison). As can be expected from the analytical considerations in Section 3.6.2, the results show a clear dependence on the evaluation threshold. Although convertibility to an identical representation is not a prerequisite on CL 3 and CL 4, this illustrates that direct comparisons at least require consistent definitions of the respective quantities, which are applicable to measurement data and reflected in the post-processing. It is shown in Section 5.3 that consistent PL model parameters may be derived from measurement data irrespective of the evaluation bandwidth.

3.8 Characterization of Channel Sounders and Validation of Measurement Results

Verifying the correctness of measurement data is a prerequisite to derive reliable channel characteristics and allow meaningful comparisons of results. As a matter of principle, measurement data is always distorted by errors to a certain extent. The objective of channel sounder calibration as described in Section 3.4 is to minimize system-induced errors as far as possible. The remaining errors can be assessed by channel sounder characterization.

In the following publication, the characterization of channel sounders and the validation of measurement results are addressed, using exemplary data from different channel sounder setups at 28 and 82 GHz [PWK+16]. Metrics such as the dynamic range, maximum measurable path loss, amplitude error and phase stability are statistically evaluated. They provide information on the residual errors, which is valuable for the optimization of the channel sounder and for post-processing of the measurement data. Over-the-air validation measurements confirm that back-to-back calibration is a valid approach to remove system-intrinsic effects.

It should be noted that the paper addresses only a selection of metrics for the characterization of sounder setups. An overview of further criteria and related performance tests can e. g. be found in [Sal13].

Contribution

The characterization and validation measurements were conducted by my co-authors based on my suggestions. I analyzed the measurement data, derived the results and authored the publication. My co-authors provided support for the interpretation of the results, proof-reading and smaller corrections of the text.

Characterization of mm-Wave Channel Sounders up to W-Band and Validation of Measurement Results

Michael Peter*, Richard J. Weiler*, Wilhelm Keusgen*, Taro Eichler†, Meik Kottkamp† and Alexander Nähring‡
*Fraunhofer Heinrich Hertz Institute, Berlin, Germany, michael.peter@hhi.fraunhofer.de
†Rohde & Schwarz, Munich, Germany
‡RWTH Aachen University, Aachen, Germany

***Abstract*—In this paper, the characterization of mm-wave channel sounders and validation of measurement data are discussed. Suitable procedures and metrics like the dynamic range and the maximum measurable path loss are proposed for this purpose. They are illustrated by using measurement data at 28 and 82 GHz from back-to-back measurements in the laboratory as well as from over-the-air (OTA) measurements in an anechoic chamber.**

I. Introduction

Millimeter-wave channel sounding has recently gained increasing interest, since fifth generation (5G) generation mobile networks in the long term will need to make use of much higher frequencies to provide ultra-high data rates and capacity [1]. The targeted frequency bands cover a huge range from 6 up to 100 GHz. As for legacy frequencies, suitable channel models are required to enable simulations on link and system level [2], [3]. The ultimate target is to elaborate a flexible and comprehensive frequency-agile channel model, which covers the entire range up to 100 GHz for all relevant 5G scenarios.

However, the derivation of such a model and respective parameters poses a considerable challenge at mm-wave frequencies. Channel sounders that could provide statistically reliable measurement data [4] with directional information at multiple frequencies for time-variant channels and are not yet available. In order to establish a firm data basis, it is necessary to pool available channel measurement data. With regard to coherent evaluations and the optimization of measurement results, channel sounder characterization is of utmost importance.

In this paper, the characterization of mm-wave channel sounders as well as the validation of measurement data is discussed. Section II briefly outlines the background of measurement errors and introduces related terms. Two different channels sounder setups have been used to capture exemplary data for the subsequent investigations. They are introduced in Section III. In Section IV metrics and evaluations are proposed to characterize the performance of a setup, or more precise, the expectable quality of measurement data. The opportunities of noise reduction by averaging in post-processing are described in Section V. Finally, first results from OTA measurements for validation are presented in Section VI

II. Measurement Errors

Channel sounder characterization and validation is closely related to measurement errors – the difference between a measured value of quantity and its true value. Accuracy is usually associated with the closeness of the mean of a set of measurement results to the true value and is hence linked to systematic measurement errors. Precision denotes the closeness of agreement among a set of results. It is related to random errors and involves repeatability, reproducibility and measurement uncertainty. Measurement errors are e.g. caused by thermal noise, phase noise, I/Q imbalance, and nonlinearities. The target of channel sounder characterization is to assess the system-intrinsic limits of accuracy and precision to enable the correct interpretation of measurement data and usage of appropriate parameters (e.g. thresholds) for further evaluation. In the case that the parameters of the system are flexible, i.e. if the length of the sounding sequence or averaging factors can be set to different values, the characterization results will depend on these settings. In order to obtain applicable results, the characterization must hence be performed with the same setting as used for the measurements.

III. Channel Sounder Setups and Parameters

Exemplary characterization measurements were conducted in the laboratory at Fraunhofer HHI in Berlin with the HIRATE channel sounder setup [5] (Setup 1) incorporating additional external components according to Figure 1. The measurement frequency was 28 GHz. Transmitter (Tx) and receiver (Rx) have been directly connected via an adjustable attenuator. 10,000 channel impulse response (CIR) snapshots for statistical evaluations were acquired after back-to-back calibration. In the present case, a sounding sequence length of 1024 samples has been chosen, corresponding to a duration of 4.096 μs. The Rx supports real-time waveform averaging over multiple sequence periods (waveform averaging) to further improve the signal-to-noise ratio of the received signal. An averaging factor of 64 has been used.

Further measurements at 82 GHz were performed at Rohde & Schwarz (R&S) in Munich with a sounder setup mainly based on R&S test and measurement equipment (Setup 2). It is illustrated in Figure 2. Back-to-back calibration has been performed as for Setup 1 and sets of CIRs were recorded, in this case consisting of 1000 CIRs, with an adjustable attenuator. In addition, Setup 2 was used for the OTA measurements presented in Section VI. Real-time averaging has not been applied, but the sequence duration was much longer, namely 131.1 μs. The parameters of both channel sounder setups are summarized in Table I.

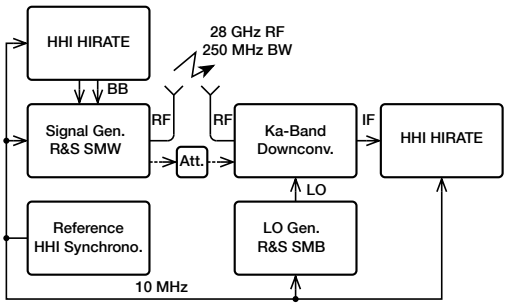

Figure 1. Channel sounder setup used for measurements at 28 GHz (Setup 1)

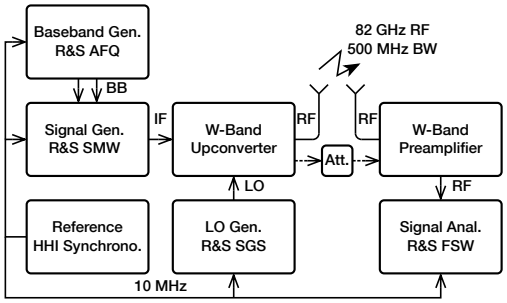

Figure 2. Channel sounder setup used for measurements at 82 GHz (Setup 2)

The (theoretical) processing gain G_{proc} results from the correlation gain and the averaging gain. Assuming a sequence with perfect autocorrelation properties, it can be calculated by

$$G_{\mathrm{proc|dB}} = 10 \cdot \log_{10}\left(BT_m\right), \tag{1}$$

where T_m is the measurement time, the duration of the signal segment processed by the Rx for obtaining one CIR, and B is the measurement bandwidth. The theoretical processing gain is 48.2 dB for both setups (see Table I).

It shall be noted that parameters like the Tx power, measurement frequency (or frequency range), bandwidth (related to theoretical delay resolution), maximum measurable delay (sounding sequence duration), measurement duration and maximum repetition/snapshot rate only describe the fundamental capabilities of a setup. They are given or can be calculated. However, the sounder performance and hence the expectable accuracy/precision, which is highly dependent on proper calibration, must be determined by tests.

Table I
FIGURES OF THE CHANNEL SOUNDER SETUPS AND PARAMETER SETTINGS

Parameter	Setup 1	Setup 2
Frequency	28 GHz	82 GHz
Bandwidth B	250 MHz	500 MHz
Power at Tx port	27 dBm	4.6 dBm
Sounding sequence duration	4.096 μs	131.1 μs
Number of real-time averages N_{avrg}	64	-
Measurement time T_m	262.1 μs	131.1 μs
Theoretical processing gain G_{proc}	48.2 dB	48.2 dB
Number of recorded CIRs per measurement run	10,000	1,000
Temporal spacing of CIRs	1.02 ms	1.31 ms

IV. EVALUATIONS

In the following sections, the collected data is used to illustrate the steps for performance characterization and typical results. Figure 3 shows two exemplary CIRs at 82 GHz for an attenuator setting of 72 dB. A Chebyshev window with 60 dB sidelobe suppression has been applied in the frequency domain. Besides the expected path at zero delay, no further distinct multipath components (MPCs) are visible. Below a level of −110 dB, the result is dominated by noise. For comparison, two CIRs for 80 dB attenuator setting are shown in Figure 4, which have been obtained with with Setup 1 at 28 GHz. The path also appears at zero delay with the expected

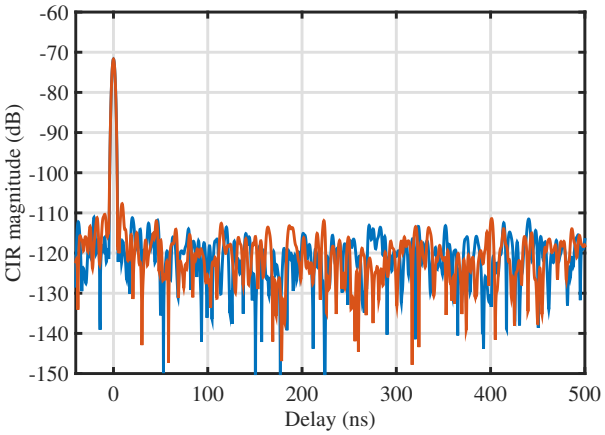

Figure 3. Exemplary CIRs at 82 GHz measured with Setup 2 for an attenuator setting of 72 dB

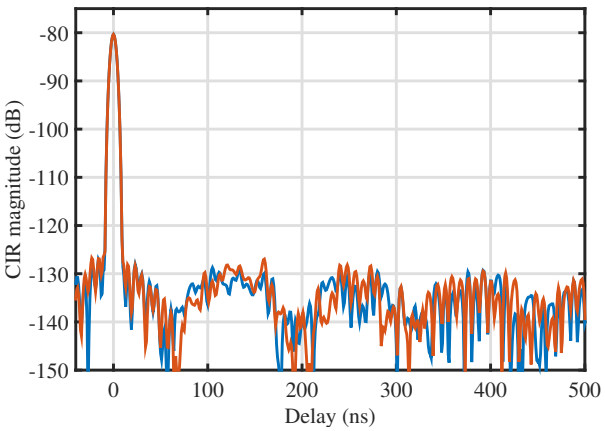

Figure 4. Exemplary CIRs at 28 GHz measured with Setup 2 for an attenuator setting of 80 dB.

gain. Around −130 dB and below, the result is dominated by error contributions. Compared to Figure 3 they show a regular structure, which indicates a systematic error. It may be caused be nonlinearities or errors during calibration and would be a starting point for further optimizing the setup, which, however, is not the focus of this work. In the present case, the effect is beneficial to illustrate how systematic errors affect the performance metrics.

A. Dynamic Range

In the following, the instantaneous dynamic range (IDR) is defined as the difference (in dB) between the strongest path (local maximum in the CIR) and the strongest error contribution (largest local maximum in the CIR, which is not related to a propagation path). In Figure 3 we see that the IDR is around 40 dB. However, to properly characterize the IDR, statistical evaluations are required. The solid lines in Figure 5 show the empirical cumulative distribution functions (CDFs) of the IDR at 82 GHz for three different settings of the adjustable attenuator, namely 71.7, 81.3 and 89.4 dB (determined by measurements with a vector network analyzer). As expected, the IDR decreases with increasing attenuation,

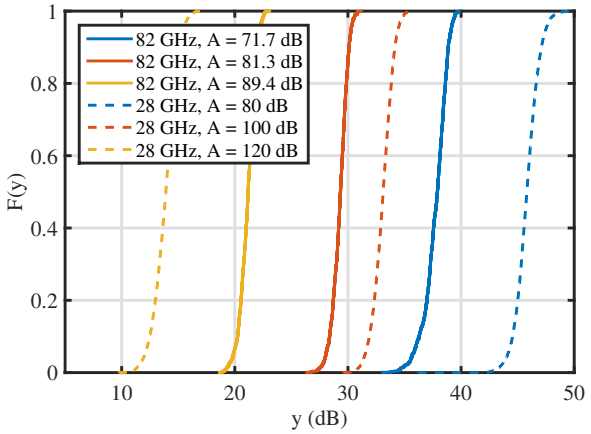

Figure 5. Empirical CDFs of instantaneous dynamic range (IDR).

since it is directly impacted by thermal noise. The CDF for $A = 81.3$ dB is shifted to the right by 8.1 dB (median value) compared to the one for $A = 89.4$ dB. The spacing of the CDFs for $A = 81.3$ dB and $A = 72$ dB is 8.6 dB, which is is only slightly smaller than expected. The dominant IDR-limiting factor is noise in all cases.

The dashed lines show the same evaluation for 28 GHz. Note that the attenuator settings have been different: 80, 100 and 120 dB. The spacing between the CDFs for $A = 100$ dB and $A = 120$ dB (19.3 dB) is almost as expected. However, the spacing for $A = 100$ dB and $A = 80$ dB turns out to be only 12.9 dB. This clearly shows that for $A = 80$ dB thermal noise is not the dominant limiting factor. Other system impairments become effective, resulting in an upper limit of the IDR in the higher SNR region.

In Table II the median, the standard deviation and the 1% quantile ($Q_{0.01}$: value, where the CDF takes 0.01) of the IDR are summarized. $Q_{0.01}$ can be seen as minimum requirement regarding a relative threshold for path estimation in CIRs measured with the same setup and settings.

B. Measureable Path Loss

The maximum measurable path loss (MMPL) is a practical measure to characterize the detectability of weak propagation paths in the CIR and the sounder performance in the low SNR region. It is hence useful to assess meaningful measuring distances and non-line-of-sight (NLOS) capabilities. Here, equivalent to the IDR, the instantaneous MMPL (IMMPL)

Table II
MEDIAN (MED.), STANDARD DEVIATION (STD.) AND 1% QUANTILE $Q_{0.01}$ OF IDR AND IMMPL

	Freq. (GHz)	28			82		
	Att. (dB)	80	100	120	71.7	81.3	89.4
IDR (dB)	med.	46.1	33.2	13.9	37.9	29.3	21.2
	$Q_{0.01}$	43.1	30.7	11.0	34.5	27.4	19.2
IMMPL (dB)	med.	126	133	134	110	111	111
	$Q_{0.01}$	124	131	132	106	109	109
IDR/IMMPL std. (dB)		1.02	0.91	1.05	0.70	0.69	1.04

is defined as the value of the largest local maximum in the CIR, which is not related to a propagation path, corrected by the amplitude error (see Section IV-C). The resulting values are listed in Table II. As expected, they converge for large attenuation, since thermal noise becomes the limiting factor. The 82 GHz values for $A = 81.3$ dB and $A = 89.4$ dB are identical. The values for $A = 71.7$ dB are slightly reduced. At 28 GHz the system-related limitations of the IDR strongly effect the IMMPL in the high SNR region.

C. Amplitude Error

Amplitude (gain) inaccuracies can e.g. be caused by improper calibration of the channel sounder or strong non-linearities. Imprecision mainly arises from thermal noise, phase noise and timing jitter. The evolution of the amplitude (of the CIR maximum) over time is shown in Figure 6 for 82 GHz. The median value and the standard deviation of the amplitude errors are listed in Table III. It reveals that the accuracy as well as the precision is very high in the present case for both setups.

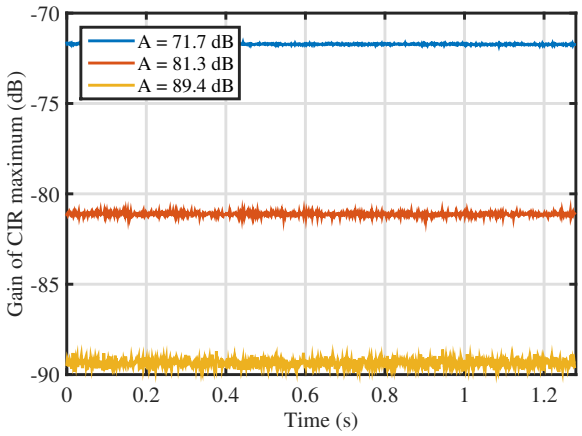

Figure 6. Evolution of the amplitude/gain of the CIR maximum over time.

D. Phase Stability

Methods to derive directional information from channel measurements with switched or virtual arrays are typically based on the signal phase. With this respect, phase stability can be very important. However, it also affects other post-processing procedures, which make use of the phase information, e.g. coherent averaging as described in Section V. The

Table III
MEDIAN (MED.) AND STANDARD DEVIATION (STD.) OF AMPLITUDE AND PHASE ERROR BASED ON THE EVALUATION OF THE CIR MAXIMUM

	Freq. (GHz)	28			82		
	Att. (dB)	80	100	120	71.7	81.3	89.4
Ampl. error (dB)	med.	−0.3	−0.1	0.0	0.0	0.2	0.1
	std.	0.0	0.1	0.5	0.0	0.1	0.2
Phase error, windowed (deg.)	std.	1.1	1.1	4.5	2.9	2.8	3.2

variation of the phase over time at 82 GHz is illustrated in Figure 7. It is visible that the phase may vary by several degrees between consecutive samples and there are also variations on a larger time scale.

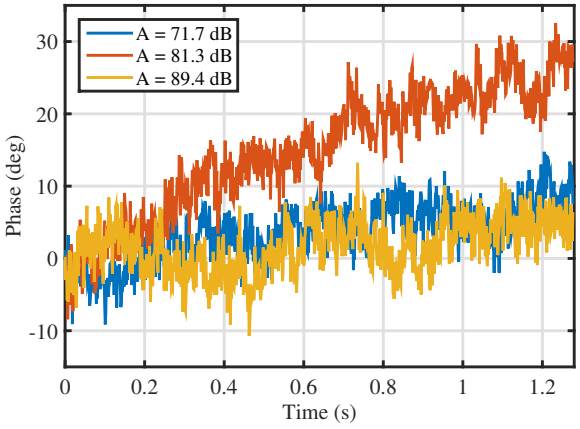

Figure 7. Evolution of the phase (CIR maximum) over time.

With respect to angle estimation, the phase variations within a short time interval, e.g. the time needed for switching between all antenna elements, affects the estimation accuracy. Therefore, it is meaningful to characterize the phase variation within a short time window. The standard deviation of the phase for a windowed evaluation (window size of approx. 10 ms) are given in Table III.

Errors of the delay are closely related to phase stability and frequency offset. An offset between the reference frequencies at Tx and Rx would be visible in Figure 7 as a linear decrease/increase of the phase, typically with a very large slope, and even result in a high standard deviation of the windowed phase error. Since the sample clock is based on the same reference, it would also translate into a continuous drift of the delay. Thus, a frequency offset (or drift) must be avoided or kept as small es possible. In the present case, Tx and Rx have been connected to the same reference clock. If this is not possible, an offset can only be achieved by making use of temperature-compensated rubidium atomic clocks with preceding back-to-back synchronization or GPS synchronization.

V. AVERAGING

Averaging might be one of the most fundamental initial steps for data post-processing. However, it can be highly beneficial in view of improving the dynamic range (DR) and the MMPL as well as reducing measurement errors. There are two different ways of averaging: coherent and non-coherent averaging. Coherent averaging is performed over complex CIRs, resulting in an "averaged CIR" (ACIR). In contrast, non-coherent averaging is performed over instantaneous power delay profiles (IPDPs), given by the squared-magnitude CIRs, leading to an averaged power delay profile (APDP). For coherent averaging, the phase must be sufficiently stable within the averaging window to avoid errors.

In Figure 8 the differences are exemplarily shown for the 82 GHz measurements and an averaging factor of $N_{\mathrm{avrg}} = 100$. As expected, coherent averaging shifts the noise con-

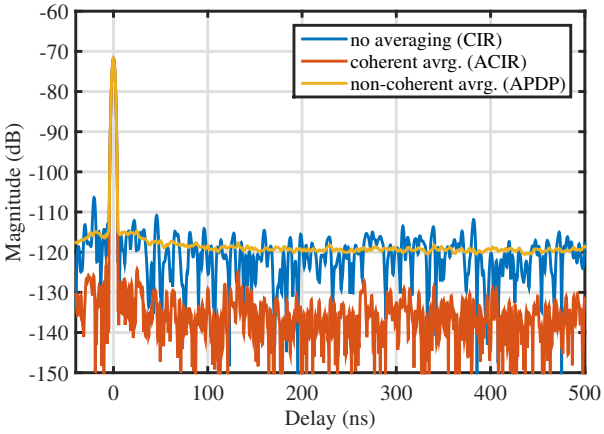

Figure 8. Influence of coherent and non-coherent averaging (example for .

tributions to a lower level. In the best case, as long as system-related systematic errors do not become effective, the improvement is given by the averaging gain $G_{\mathrm{avrg}} = 10 \cdot \log_{10} N_{\mathrm{avrg}}$. Differently, non-coherent averaging reduces the fluctuations/variance of the noise contributions – the noise tail in the APDP becomes very stable. This also results in an improvement of the performance metrics, but to a smaller extent. Moreover, it is clear that the achievable gain saturates with increasing N_{avrg} as a matter of principle. Nevertheless, non-coherent averaging can be very valuable for processing data of time variant channels, where the phase of the MPCs changes (related to the Doppler shift) within the observation time. To quantify the improvements for the measured examples, the median values of the DR and MMPL are summarized in Table IV. At 82 GHz with $A = 89.4$ dB and $A = 81.3$ dB, the improvements for coherent averaging are equal or close to the theoretical value of 20 dB. For $A = 71.7$ dB they reduce, indicating that systematic system impairments become effective that cannot be reduced by averaging. For 28 GHz, gains from averaging are much lower for all attenuator settings. This shows that after averaging system related effects are relevant in all cases. For $A = 80$ dB, improvements by averaging are almost negligible.

VI. OVER-THE-AIR VALIDATION MEASUREMENTS

The evaluations presented above were based on back-to-back measurements. They are useful to assess and characterize the performance of a channel sounder up to the front-ends. In view of real measurements, the adjustable attenuator is

Table IV
MEDIAN OF DR AND MMPL WITHOUT AND WITH AVERAGING

Freq. (GHz)	28			82		
Att. (dB)	80	100	120	71.7	81.3	89.4
IDR based on CIR (dB)	46.1	33.2	13.9	37.9	29.3	21.2
DR, coherent avrg. (dB)	47.3	40.5	24.3	52.1	48.3	41.2
DR, non-coh. avrg. (dB)	47.2	38.2	19.9	42.8	36.9	28.8
IMMPL (dB)	126	133	134	110	110	111
MMPL, coherent avrg. (dB)	128	141	144	124	129	131
MMPL, non-coh. avrg. (dB)	127	138	140	114	118	118

replaced by antennas. In order to investigate the influence of this modification, over-the-air measurements (OTA) were carried out in an anechoic chamber. Figure 9 shows the measurement setup. Self-built onmidirectional antennas of the

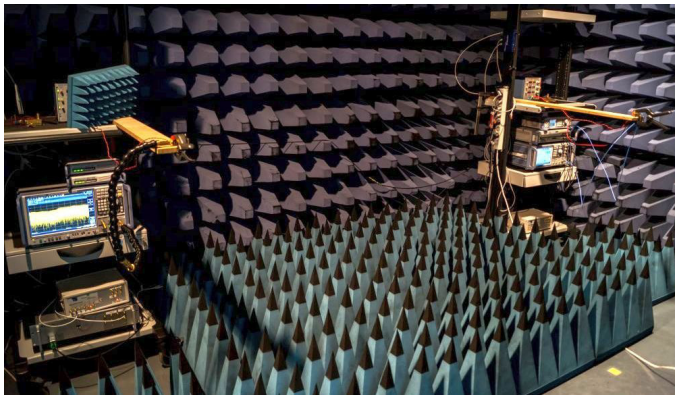

Figure 9. APDPs for OTA measurements with and without reflector.

same type ($\lambda/4$ monopoles with vertical polarization) were used at the Tx and the Rx with 2.7 m distance. They had been characterized via independent OTA measurements with a vector network analyzer – a gain of -1dBi had been determined. Two measurement runs were performed in the chamber. During the first one, the chamber was empty besides the equipment. For the second one, an aluminum plate was placed at one side parallel to the line of sight (LOS) with a lateral distance of 1.58 m. Figure 10 shows the APDPs of both measurements. Since the reference had been disconnected after back-to-back calibration, the absolute delay cannot be evaluated. Therefore, the APDP is plotted against the excess delay. The measured gain of the LOS path is -81.4 dB. Taking into account the antenna gain of -1 dB at both sides, this is in full accordance with the expectations, as the free-space loss at 2.7 m is 79.3 dB. A relatively strong additional peak is visible at 7.6 ns excess delay. It can be clearly attributed to a reflection at the side wall with a lateral distance of 2.1 m, where several absorbers showed irregularities.

In the measurement with the reflector, the second peak arrives at 4.8 ns excess delay, which equals the calculated value (4.85 ns based on 1.46 m excess travel distance). Its gain is -86.5 dB. This is slightly lower than the value resulting from free space propagation for 4.16 m travel distance (-85.1 dB including antenna gain). The difference might have been

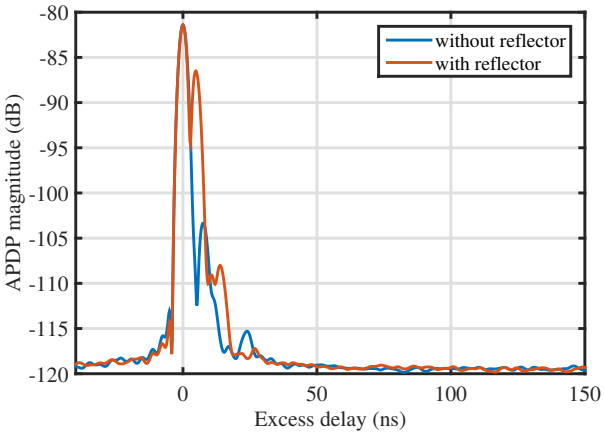

Figure 10. APDPs for OTA measurements without and with reflector.

caused by a small tilt of the reflector or even by deviations of the antenna pattern.

Though reflections in the chamber could not be fully avoided, the results point out that back-to-back calibration is a suitable approach. The measured path gains and delays agree well with the expected values. However, the observations also show that great care must be taken in OTA measurements (in particular regarding OTA calibration) to exclude any reflections within the dynamic range of the channel sounder.

VII. CONCLUSION

In this paper, procedures and metrics have been proposed to characterize the performance of channel sounders. They are based on back-to-back measurements with an adjustable attenuator and subsequent statistical evaluation of the dynamic range, maximum measurable path loss, amplitude error and phase stability. The methods have been illustrated on the basis of exemplary measurement data with two time-domain sounder setups. They can be used to for comparative investigations and optimization of channel sounder setups. Moreover, they provide valuable information for post-processing of measurement data, e.g. for determining evaluation thresholds and assessing expected errors. Over-the-air validation measurement results have confirmed that back-to-back calibration is a suitable preparatory procedure for OTA measurements.

REFERENCES

[1] F. Boccardi, R. Heath, A. Lozano, T. Marzetta, and P. Popovski, "Five disruptive technology directions for 5G," *Communications Magazine, IEEE*, vol. 52, no. 2, pp. 74–80, 2014.

[2] 3GPP TR 36.873 V12.0.0, "3rd generation partnership project; technical specification group radio access network; study on 3D channel model for LTE (release 12)," Tech. Rep., 2014.

[3] J. Medbo, K. Börner, K. Haneda, V. Hovinen, T. Imai, J. Järvelainen, T. Jämsä, A. Karttunen, K. Kusume, J. Kyröläinen, P. Kyösti, J. Meinilä, V. Nurmela, L. Raschkowski, A. Roivainen, and J. Ylitalo, "Channel modelling for the fifth generation mobile communications," in *Antennas and Propagation (EUCAP), 2014 8th European Conference on*, 2014.

[4] M. Peter, W. Keusgen, and R. J. Weiler, "On path loss measurement and modeling for millimeter-wave 5G," in *The 9th European Conference on Antennas and Propagation (EuCAP 2015)*, Lisbon, Portugal, Apr. 2015.

[5] W. Keusgen, A. Kortke, M. Peter, and R. Weiler, "A highly flexible digital radio testbed and 60 GHz application examples," in *Microwave Conference. EuMC 2013. 43rd European*, 2013.

4 Indoor and In-Vehicle Measurement Campaigns and Evaluations

In this chapter, the 60 GHz channel in rooms and vehicles is investigated with regard to applications such as ultra-high capacity wireless local area networks (WLANs) and short-range links between multimedia devices. The chapter is composed of six papers. In Section 4.1, measurements in a conference room are presented, which were performed at 5 GHz and 60 GHz with the same setup. The channel is characterized at both frequencies, and the results are compared. As an extension of the campaign, the measurements were repeated with different antenna configurations at 60 GHz. Their impact on the radio channel is analyzed in Section 4.2. In Section 4.3, measurements and evaluations for a passenger cabin of a wide-bodied aircraft are presented, based on the same channel sounder as used for the conference room. The in-car channel is investigated in Section 4.4. Since the small dimensions and application-specific antenna positions allowed only static measurements, a vector network analyzer (VNA) was used in this case to maximize the bandwidth. A dedicated measurement campaign was performed in the conference room to analyze human body shadowing (HBS). Its impact on the LOS path and suitable modeling approaches are addressed in Section 4.5. As a matter of principle, the considerations are not limited to the measurement environment.

4.1 Indoor Measurements at 5 and 60 GHz

As introduced in Section 2.1, wave propagation is frequency-dependent and mm-wave channels may significantly differ from channels at lower frequencies. The following publication presents results of an indoor measurement campaign at 60 GHz in a small conference room—a typical scenario where a mm-wave WLAN could be operated [PK09]. The channel is characterized by the path loss, the TOA parameters and the coherence bandwidth for LOS and OLOS. To assess the difference of the results

compared to the channel at lower frequencies, the measurements were repeated at 5 GHz in the same environment with the same setup (besides the radio front ends) and identical post-processing.

An almost constant offset of the PL shows up in the LOS results, which practically equals the expected value for free-space propagation. The 60 GHz indoor channel is significantly affected by multipath propagation. However, in the present scenario, multipath power clearly decays faster than at 5 GHz. The corresponding average RMS DS is less than half as large, which can be exploited by an appropriate system design to reduce overhead, e. g. by shortening the cyclic prefix in OFDM systems. Though the power loss caused by obstructing the LOS is slightly larger at 60 GHz, it is less than 10 dB in all cases. This in turn can be attributed to significant multipath power, which is only marginally affected by the obstruction. The results motivate to consider 60 GHz also for links without LOS.

Contribution

This paper was authored by me and I made the related preparations and investigations, which included the build-up, programming and testing of the channel sounder setup, planning and performance of the measurement campaign, as well as data post-processing and analysis. The co-author supported me by providing advice for the build-up of the setup, proof reading and several corrections.

Analysis and Comparison of Indoor Wideband Radio Channels at 5 and 60 GHz

Michael Peter [#1], Wilhelm Keusgen [#2]

[#] *Fraunhofer-Institut für Nachrichtentechnik, Heinrich-Hertz-Institut*
Einsteinufer 37, 10587 Berlin, Germany
[1] michael.peter@hhi.fraunhofer.de
[2] wilhelm.keusgen@hhi.fraunhofer.de

***Abstract*— In this paper we present measurement results for indoor wideband radio channels at 5 and 60 GHz. To ensure full comparability, the measurements were carried out under the same conditions by using mostly the same equipment. We analyze path loss, time dispersion, frequency selectivity and the impact of an obstructed line-of-sight at both frequencies. The results are compared and characteristic differences are pointed out.**

I. Introduction

During the last 10 years a considerable technological development has been taking place in the area of Wireless Local Area Networks (WLANs). The original IEEE 802.11 standard supported data rates up to 2 Mbit/s in the 2.4 GHz frequency band. Today, the majority of WLAN devices are based on the 802.11g extension, which supports rates up to 54 Mbit/s. However, the continuously growing demand for multimedia services and broadband data transmission gives rise to higher requirements on future indoor wireless networks, and it becomes more and more difficult to meet them. WLANs at 5 GHz according to 802.11a will probably gain in importance since up to 675 MHz bandwidth can be used, and therefore, a significantly larger number of users and networks are enabled to operate simultaneously.

However, even much higher carrier frequencies are considered for future short-range broadband transmission. A 60 GHz Very High Throughput (VHT) 802.11 variant is currently discussed as an extension of 802.11b, 802.11a and 802.11g. The basic idea is that a high compatibility with established WLAN systems could be achieved by the VHT extension, and the market introduction would be facilitated significantly as only minor modifications on network and link layer are necessary. Additionally, the IEEE 802.15.3 Task Group 3c (TG3c) is working towards an alternative 60 GHz Physical Layer (PHY) for the 802.15.3 Wireless Personal Area Network (WPAN) standard. Both systems are intended to operate in the unlicensed band from 57 to 64 GHz and are a candidate for indoor and in-cabin [1] high speed internet access as well as real-time video streaming and data synchronization.

With regard to a wireless 60 GHz network, one must take into account that – besides the differences in bandwidth – the millimeter wave radio channel differs from channels at lower frequencies, which involves essential modifications on the PHY. Hence, the investigation and the characterization of the underlying radio channel are pivotal elements in the design and the optimization of corresponding future wireless networks.

General investigations on the frequency dependence of propagation effects are presented in [2]. Several comparative investigations concerning wave propagation at 60 GHz and lower frequencies can be found in literature, where frequencies around 2 GHz are considered in the majority of cases [3], [4]. Swept frequency measurements with a bandwidth of 100 MHz at 5 and 60 GHz are presented in [5]. The latter contains exemplary measurement results, but no detailed analyses have been carried out.

In this paper we analyze wideband channel measurement results for both frequencies and point out characteristic disparities.

II. Indoor Wideband Channel Measurements

We carried out channel measurements in a conference room located on the ground floor of our institute building. Fig. 1 shows the floor plan of the separable room. The partition wall was closed, so that the room size was approximately 6.6 m × 5.9 m. There are four windows integrated in the ceiling and a glass door towards the corridor. The room was furnished with tables and chairs. The location of the transmitter (Tx), representing the access point, was fixed, whereas the receiver (Rx) was considered as a mobile terminal and placed at twelve different locations (Rx loc.) around the tables according to Fig. 1. The distance between Tx an Rx varied between approx. 2 and 5 m.

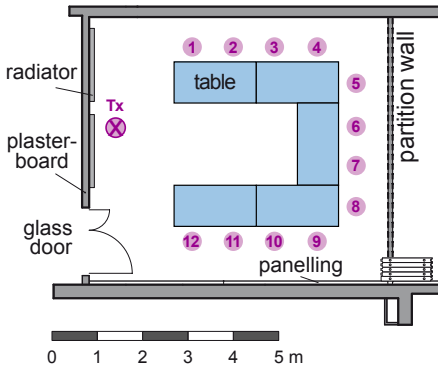

Fig. 1. Floor plan of the conference room. Rx locations are marked by numbered circles.

A time domain channel sounder (similar to the setup in [6]) with 1 GHz bandwidth around the center frequencies of 5 GHz and 61 GHz was used for the measurements. The bandwidth corresponds to a temporal multipath resolution of approximately 1 ns. For each Rx location a coherent small-scale measurement set of 100 Channel Impulse Responses (CIRs) has been acquired by moving the Rx antenna on a linear track over a distance of 10 cm by the help of a controllable positioning platform.

We used a commercial millimeter wave antenna for the 60 GHz measurements, whereas a self-built biconical antenna was employed at 5 GHz. Both wideband antennas have an almost constant, frequency-independent pattern in the azimuth plane and a gain of approx. 2 dBi. They were vertically polarized and mounted at a height of 130 cm. Both line-of-Sight (LOS) and Obstructed Line-of-Sight (OLOS) conditions have been taken into account. OLOS was achieved by blocking the Line-of-sight between Tx antenna and Rx antenna with an absorber mat of size 60 cm × 60 cm.

Fig. 2 and Fig. 3 show two exemplary small-scale sets of CIRs under LOS conditions measured at 60 and 5 GHz. A Kaiser window with parameter $\beta = 5$ has been applied in the frequency domain to reduce the sidelobes in the time domain. We see that the transmission is largely affected by multipath propagation in both cases. Expectedly, the power of arriving paths is significantly smaller at 60 GHz due to the larger free space attenuation. Differences in the fading structure of resolvable (distinguishable with respect to the delay) multipath components result from the differing wavelengths. As the Rx antenna covered a distance of 10 cm (approx. 20 wavelengths at 61 GHz and approx. 1.7 wavelengths at 5 GHz) in both cases, fading minimums and maximums occur approx. 12 times more frequent at 60 GHz compared to 5 GHz. However, besides this we already observe that the decay of multipath power is faster at 60 GHz. Significant multipaths arrive up to delays around 60 ns, whereas at 5 GHz, multipaths with delays of approx. 120 ns are visible within the illustrated magnitude range. In the following the differences in path loss, time dispersion and frequency selectivity are investigated in more detail.

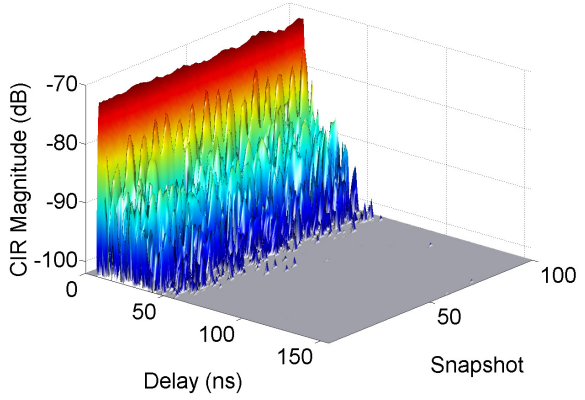

Fig. 2. Small-scale set of CIRs at 60 GHz under LOS conditions (Rx loc. 2).

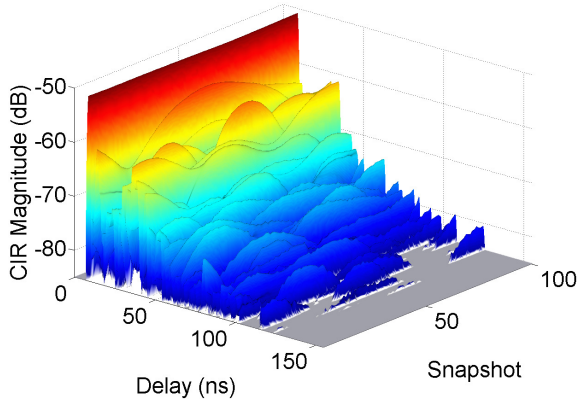

Fig. 3. Small-scale set of CIRs at 5 GHz under LOS conditions (Rx loc. 2).

III. Investigations

A. Path Loss

We investigate the Path Loss (PL), which is defined as the ratio of the effective transmitted power to the received power:

$$\begin{aligned} \mathrm{PL}\ (\mathrm{dB}) \quad &= \quad P_T\ (\mathrm{dBm}) + G_T\ (\mathrm{dBi}) + G_R\ (\mathrm{dBi}) \\ &\quad -P_R\ (\mathrm{dBm}), \end{aligned} \tag{1}$$

where P_T, P_R, G_T and G_R denote the transmitted power, the received power, the transmitter antenna gain and the receiver antenna gain, respectively. The mean path loss $\overline{\mathrm{PL}}$ over distance d can be approximated by the path loss exponent model (log-distance law), which is given by:

$$\overline{\mathrm{PL}}(d)\ (\mathrm{dB}) = \overline{\mathrm{PL}}(d_0)\ (\mathrm{dB}) + 10\, n_{\mathrm{PL}} \log_{10}\left(\frac{d}{d_0}\right), \tag{2}$$

where $\overline{\mathrm{PL}}(d_0)$ denotes the intercept point (average PL at reference distance d_0), and n_{PL} is the path loss exponent. Fig. 4 shows the scatter plots of the measured path losses at 60 and 5 GHz with respect to the Tx–Rx separation in logarithmic scale. Additionally, the result of a linear least-mean-square fit is plotted. The corresponding PL exponents, the intercept points, and the standard deviations of the approximations are

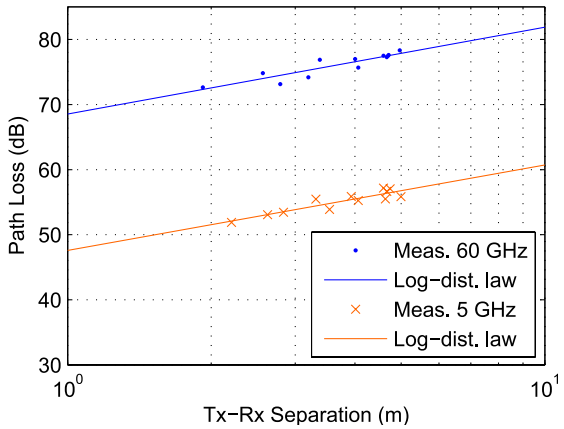

Fig. 4. Measured path loss and linear least-mean-square fit.

TABLE I

PATH LOSS MODEL PARAMETERS.

Frequency	$\mathrm{PL}(d_0 = 1\,\mathrm{m})$ (dB)	n_{PL}	σ_{PL} (dB)
60 GHz	68.6	1.33	0.79
5 GHz	47.6	1.31	0.68

summarized in Table I. Accordingly, $\mathrm{PL}(d_0 = 1\,\mathrm{m})$ is close to the theoretical values for free space propagation in both cases (68.1 dB at 60 GHz and 46.4 dB at 5 GHz). The PL exponents take quite low and almost identical values. Hence, there is an almost constant offset of 21 dB in mean path loss when changing the frequency from 5 to 60 GHz. The 60 GHz value is in accordance with the one determined in [7] for an office environment.

B. Time Dispersion and Frequency Selectivity

In this section we analyze the multipath structure and the frequency domain characteristics of the channel. The time domain analyses are based on the Averaged Power Delay Profiles (APDPs). An APDP $\overline{p}(\widetilde{\tau})$ is calculated by

$$\overline{p}(\widetilde{\tau}) = \frac{1}{K} \sum_{k=1}^{K} |h_k(\widetilde{\tau})|^2 \tag{3}$$

where $\widetilde{\tau}$ and $h_k(\widetilde{\tau})$ denote the delay and the (bandlimited) CIR of channel observation (snaphot) k at a particular Rx location. Fig. 5 shows the APDPs for 60 and 5 GHz resulting from the measurements at Rx loc. 2 under LOS conditions. They are quite characteristic for the whole measurement set. The APDPs have been normalized to the strongest multipath component to allow an illustrative comparison of the multipath structure. One the one hand, we can see clear similarities between the APDPs. After the LOS component, two conspicuous clusters at delays around 14 and 30 ns arrive at the receiver in both cases. On the other hand, differences in the strength of involved multipath components can be observed. Whereas the power of the first strong multipath at 14 ns delay is almost equivalent for both frequencies, the second cluster is significantly weaker

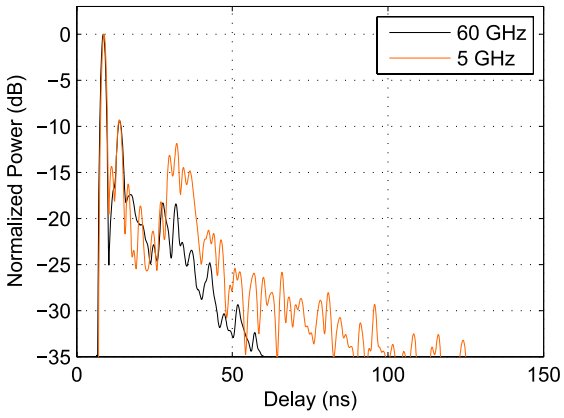

Fig. 5. Normalized APDPs at Rx location 2 under LOS conditions.

for 60 GHz, and in average the differences get larger with increasing propagation delay. Hence, the multipath power decays faster at 60 GHz. In the illustrated example, at 60 GHz the power falls permanently below −30 dB for delays above 52 ns, whereas at 5 GHz there are multipath components up to 96 ns exceeding this threshold.

Another interesting observation is that the APDP at 60 GHz appears smoother, especially for higher delays. (This effect is even more conspicuous at several other Rx locations.) Although the overall power decay of the 5 GHz result is slower with respect to the delay, the run of the APDP is continuously subjected to sharp declines. As small-scale fading of resolvable multipath components is clearly observable in Fig. 2 and Fig. 3, we can conclude that the temporal resolution is not sufficient to resolve each particular physical propagation path neither at 60 nor at 5 GHz. However, the sharp declines in the 5 GHz result indicate that the arrival of significant (with respect to adjacent resolvable multipath components) multipaths between two significant resolvable components is interrupted more frequently for more than 1–2 ns at the lower frequency. At 60 GHz the declines are less frequent and less severe. Therefore we conclude that the density of physical paths is higher in the millimeter wave band. It is lower at 5 GHz, whereas in this case stronger multipaths arise in general.

In order to quantify the time dispersion of the channel, we derived the Time-of-Arrival (TOA) parameters, including maximum excess delay, mean excess delay and Root-Mean-Square (RMS) delay spread from the APDPs at each Rx location. A threshold of −30 dB relative to the strongest component was used to differentiate between multipath contributions and noise. The excess delay is given by $\tau = \widetilde{\tau} - \widetilde{\tau}_0$, where $\widetilde{\tau}_0$ is defined by the delay at which the power exceeds the threshold for the first time. The maximum excess delay $\tau_{\max}$ defines the interval from $\widetilde{\tau}_0$ to the last time the power falls below the threshold (at delay $\widetilde{\tau}_{\max}$): $\tau_{\max} = \widetilde{\tau}_{\max} - \widetilde{\tau}_0$. The mean excess delay τ_{m} is calculated by

$$\tau_{\mathrm{m}} = \frac{\int_0^{\tau_{\max}} \tau \cdot \overline{p}(\tau)\, d\tau}{\int_0^{\tau_{\max}} \overline{p}(\tau)\, d\tau}, \tag{4}$$

and the RMS delay spread is given as

$$\tau_{\mathrm{rms}} = \sqrt{\frac{\int_0^{\tau_{\max}} \tau^2 \cdot \overline{p}(\tau)\, d\tau}{\int_0^{\tau_{\max}} \overline{p}(\tau)\, d\tau} - \tau_{\mathrm{m}}^2}. \tag{5}$$

The resulting values for LOS are summarized in Table II. We see that the TOA values for the 5 GHz channel are significantly higher than the values for the 60 GHz channel. The delay spread at 5 GHz is 11.2 to 17.9 ns, whereas values between approx. 5.5 and 7.0 ns arise at 5 GHz. The average delay spreads are 14.7 and 6.3 ns, repectively, which is a decline of factor 2.3. Very similar results can be observed for τ_{m} and $\tau_{\max}$, where the factors are 2.0.

The frequency coherence or selectivity is characterized by the Spaced-Frequency Correlation Function (FCF) $R_H(\Delta f)$. Since we assume Wide-Sense Stationary Uncorrelated Scattering (WSSUS) for each Rx loc., the FCF is given by the

TABLE II
TOA PARAMETERS FOR 60 GHZ AND (5 GHZ) UNDER LOS CONDITIONS.

Rx loc.	$\tau_{\max}$ (ns)	τ_{m} (ns)	τ_{rms} (ns)	$B_{\mathrm{coh},0.9}$ (MHz)	$B_{\mathrm{coh},0.5}$ (MHz)
1	46.1 (67.1)	3.66 (6.77)	5.59 (11.2)	14.6 (6.67)	412 (393)
2	45.5 (89.0)	4.49 (8.79)	6.38 (12.8)	11.5 (6.01)	367 (260)
3	48.6 (89.0)	5.41 (8.50)	6.93 (12.2)	9.72 (6.13)	253 (240)
4	50.6 (109)	5.91 (10.0)	6.99 (14.5)	9.78 (5.54)	188 (64.3)
5	46.5 (115)	5.13 (14.0)	5.92 (17.7)	11.2 (4.56)	251 (24.3)
6	53.1 (96.0)	6.11 (9.65)	6.92 (13.0)	9.86 (5.80)	122 (31.3)
7	52.2 (101)	5.66 (11.2)	6.41 (15.7)	10.3 (5.12)	42.4 (28.8)
8	51.4 (122)	6.00 (11.1)	6.43 (15.6)	10.8 (5.40)	48.0 (37.9)
9	48.5 (110)	5.90 (12.3)	6.62 (17.9)	9.70 (4.79)	89.0 (71.7)
10	50.5 (103)	4.67 (9.88)	6.11 (15.6)	12.2 (4.93)	145 (116)
11	49.1 (98.6)	4.23 (10.4)	5.59 (15.4)	14.8 (4.93)	175 (194)
12	44.7 (106)	4.35 (9.32)	5.60 (15.1)	13.3 (4.86)	202 (170)
min.	44.7 (67.1)	3.66 (6.77)	5.53 (11.2)	9.70 (4.56)	42.4 (24.3)
max.	53.1 (122)	6.11 (14.0)	6.99 (17.9)	14.8 (6.67)	412 (393)
avrg.	48.9 (100)	5.13 (10.2)	6.29 (14.7)	11.5 (5.40)	191 (136)

Fourier transform of the APDP [8]:

$$R_H(\Delta f) = \int_{-\infty}^{\infty} p(\widetilde{\tau})\, e^{-j2\pi\Delta f\widetilde{\tau}} d\widetilde{\tau}. \qquad (6)$$

Fig. 6 illustrates the FCF at Rx loc. 2 (corresponding to Figs. 3, 2 and 5). We can see that the run of the FCFs shows similarities, which results from the similar structure of the APDPs at short delays (see Fig. 5). However, the FCF for 60 GHz decays slower with respect to small frequency offsets. Furthermore, its run is smoother since the decay of the APDP is faster and a lower number of significant multipaths have an influence on $R_H(\Delta f)$. We define the coherence bandwidths $B_{\mathrm{coh},0.9}$ and $B_{\mathrm{coh},0.5}$ as the frequency shift where the correlation level falls (and remains) below 0.9 or 0.5, respectively. $B_{\mathrm{coh},0.9}$ can be interpreted as the range of frequencies over which two frequency points have a strong potential for correlation, whereas they are only weakly correlated for $\Delta f \geq B_{\mathrm{coh},0.5}$. The calculated LOS values are also given in Table II. As could be expected due to the time dispersion results, the coherence bandwidths are considerably larger for 60 GHz than for 5 GHz. $B_{\mathrm{coh},0.9}$ is between 9.7 and 14.8 MHz and between 4.6 and 6.7 MHz, respectively. The average values are 11.5 and 5.4 MHz, which means they differ by a factor of 2.1.

C. Obstructed Line-of-Sight

In practical scenarios, LOS conditions cannot be guaranteed, and it is an important aspect to investigate cases where the line-of-sight is limited or blocked. Therefore, the measurement procedure was carried out twice for each Rx location. During the second measurement the LOS between Tx and Rx antenna has been blocked (severe shadowing) by an absorber mat of size 60 × 60 cm nearby the Rx. The distance between the absorber and the Rx antenna was approximately 100 cm.

Figs. 7 and 8 illustrate the influence of an obstructed LOS on the APDPs. As expected, the impact on the LOS component is very severe. Its relative power drops below −110 dB in the 60 GHz APDP, so that the LOS component is not visible anymore. At 5 GHz its relative power declines by 20 dB (from −51 to −71 dB), but the component is still visible. This means that a small part of the power could penetrate the absorber or was diffracted around it. Nevertheless, the total received power is not substantially dependent on this component but on subsequent multipaths. Latter are only weakly influenced by the obstacle. This observation is applicable for both frequencies and all Rx locations.

Table III summarizes the loss of total received power for each Rx loc. when the conditions change from LOS to OLOS. For all Rx locations the loss is smaller at the lower frequency, which is due to the slower decay of multipath power at 5 GHz. Whereas losses between 4.2 and 8.7 dB arise at 60 GHz, they range from 3.2 to 6.1 dB at 5 GHz. The average values (Averaging was performed on the "linear" power values rather than on the dB values.) are 6.4 and 4.5 dB, respectively. Consequently, the loss is always larger at 60 GHz, but the difference is only 1.9 dB in average compared to 5 GHz.

As can be concluded from Figs. 7 and 8, the shadowing also has an impact on the TOA parameters since the strongest path is attenuated or blocked completely. The TOA values for OLOS are given in Table IV. The values increase without

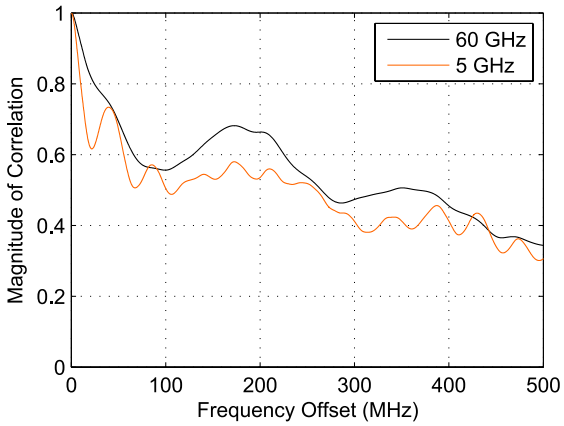

Fig. 6. Frequency correlation function for Rx loc. 2 under LOS conditions.

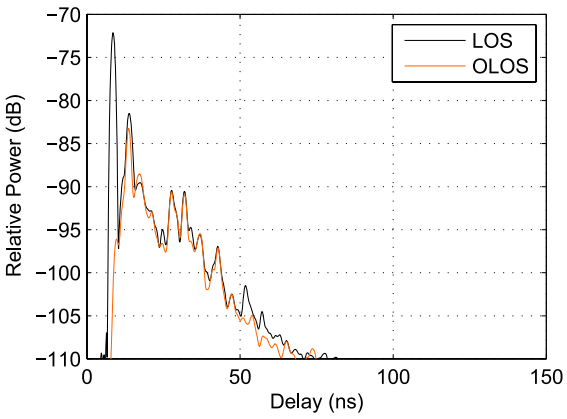

Fig. 7. APDPs at 60 GHz under LOS and OLOS conditions (Rx location 2).

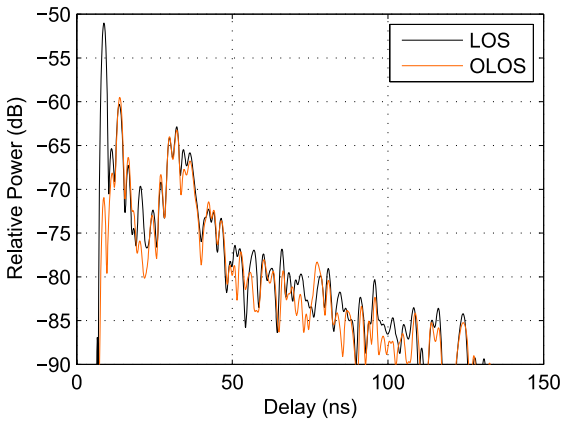

Fig. 8. APDPs at 5 GHz under LOS and OLOS conditions (Rx location 2).

TABLE III

LOSS OF POWER (dB) FOR TRANSITION FROM LOS TO OLOS.

Rx loc.	1	2	3	4	5	6	7	8	9	10	11	12
5 GHz	6.1	4.6	5.3	4.6	3.6	4.3	3.8	3.2	3.4	4.7	4.8	5.1
60 GHz	6.7	7.1	6.1	5.1	5.5	5.0	4.8	4.2	4.7	7.8	8.7	4.2
	min.	max.	avrg.									
5 GHz	3.2	6.1	4.5									
60 GHz	4.2	8.7	6.4									

exception. The averages of τ_{rms} become 8.8 and 18.1 ns for 60 and 5 GHz, respectively. This corresponds to an increase of factor 1.4 and 1.2 compared to the LOS results. The consequences on $B_{\mathrm{coh},0.9}$ and $B_{\mathrm{coh},0.5}$ can be seen in Table IV, too. The average values of $B_{\mathrm{coh},0.9}$ decrease by the factors 1.9 and 1.25 for 60 and 5 GHz, respectively. The corresponding factors for $B_{\mathrm{coh},0.5}$ are 5.1 and 6.8. Hence, severe shadowing has a strong impact on the coherence bandwidth, especially on $B_{\mathrm{coh},0.5}$, which means that most probably two frequency points are nearly uncorrelated even for relatively small frequency offsets of several tens of MHz.

IV. CONCLUSIONS

In this paper we analyzed wideband measurement results of 5 GHz and 60 GHz indoor radio channels. Since the PL exponents are very close to each other, there is an almost constant offset in mean PL of 21 dB when raising the frequency from 5 to 60 GHz. The 60 GHz channel is less dispersive than the 5 GHz channel since multipath power decays faster at the higher frequency. The average RMS delay spread is 14.7 at 5 GHz and 6.3 ns at 60 GHz for LOS, which is a difference of factor 2.3. This result is also reflected in the coherence bandwidths. Under OLOS conditions, the received power declines by 4.5 dB (at 5 GHz) and by 6.4 dB (at 60 GHz) in average. Although the loss is larger at 60 GHz, the difference of 1.9 dB turns out to be smaller than expected. The delay spreads are increased by 23% (at 5 GHz) and 39% (at 60 GHz).

Compared to a 5 GHz system, a 60 GHz device must cope with an extremely low signal-to-noise ratio. This implies to use robust low order modulation schemes. Although the power loss due to severe shadowing at 60 GHz is of the same order as the loss at 5 GHz, it must be taken into account that it will be significantly harder to provide a sufficient power reserve due to technological or regulatory limitations. Macroscopic diversity and multiple APs will be necessary to realize a reliable network. With regard to an efficient transmission, it should be taken into account that the time dispersion is remarkably smaller at 60 GHz. For example, the duration of a guard interval (cyclic prefix) in an OFDM system can be reduced by around 50% without affecting the protection against intersymbol interference and the separation of two OFDM carriers can approx. be doubled.

TABLE IV

TOA PARAMETERS FOR 60 GHZ AND (5 GHZ) FOR OLOS.

Rx loc.	$\tau_{\max}$ (ns)	τ_{m} (ns)	τ_{rms} (ns)	$B_{\mathrm{coh},0.9}$ (MHz)	$B_{\mathrm{coh},0.5}$ (MHz)
1	63.7 (148)	8.28 (20.5)	9.71 (18.6)	6.73 (4.33)	64.3 (14.1)
2	60.2 (116)	9.96 (16.4)	9.88 (16.2)	5.51 (4.83)	23.4 (15.2)
3	65.1 (141)	10.1 (19.7)	9.23 (17.8)	5.43 (4.40)	24.9 (16.0)
4	60.4 (165)	9.31 (21.8)	8.30 (18.5)	6.07 (4.61)	27.2 (17.5)
5	58.2 (142)	7.92 (18.0)	7.62 (16.6)	6.05 (4.86)	32.0 (24.8)
6	63.4 (146)	8.86 (17.2)	7.54 (15.5)	6.42 (5.05)	38.4 (25.5)
7	68.0 (118)	7.97 (17.9)	7.56 (16.4)	6.89 (5.19)	44.7 (26.9)
8	68.2 (120)	7.60 (14.3)	7.46 (15.9)	7.45 (4.97)	48.2 (34.4)
9	65.0 (153)	8.42 (19.0)	8.21 (20.2)	6.31 (3.96)	33.9 (23.1)
10	65.9 (156)	10.6 (20.8)	10.3 (20.7)	4.72 (4.27)	21.4 (15.0)
11	64.0 (164)	9.14 (23.6)	9.89 (20.4)	5.45 (4.16)	26.9 (15.0)
12	60.6 (140)	10.1 (24.0)	9.29 (19.9)	6.61 (4.15)	61.5 (12.1)
min.	58.2 (116)	7.60 (14.3)	7.46 (15.5)	4.72 (3.96)	21.4 (12.1)
max.	68.2 (165)	10.6 (24.0)	10.3 (20.7)	7.45 (5.19)	64.3 (34.4)
avrg.	63.5 (142)	9.02 (19.4)	8.75 (18.1)	6.14 (4.57)	37.2 (20.0)

REFERENCES

[1] M. Peter, W. Keusgen, and M. Schirrmacher, "Measurement and analysis of the 60 GHz in-vehicular broadband radio channel," in *Vehicular Technology Conference, 2007. VTC 2007-Fall. 2007 IEEE 66th*, Sept.–Oct. 2007.

[2] J. McDonnell, "Characteristics of the indoor wireless propagation environment at microwave and millimetre frequencies," in *Radio Communications at Microwave and Millimetre Wave Frequencies (Digest No. 1996/239), IEE Colloquium on*, 1996, pp. 13/1–13/6.

[3] R. Davies, M. Bensebti, M. A. Beach, and J. P. McGeehan, "Wireless propagation measurements in indoor multipath environments at 1.7 GHz and 60 GHz for small cell systems," in *Vehicular Technology Conference, 1991. 'Gateway to the Future Technology in Motion', 41st IEEE*, 1991, pp. 589–593.

[4] H. Yang, P. Smulders, and M. Herben, "Indoor channel measurements and analysis in the frequency bands 2 GHz and 60 GHz," in *Personal, Indoor and Mobile Radio Communications, 2005. PIMRC 2005. IEEE 16th International Symposium on*, vol. 1, 2005, pp. 579–583.

[5] A. Plattner, N. Prediger, and W. Herzig, "Indoor and outdoor propagation measurements at 5 and 60 GHz for radio LAN application," in *Microwave Symposium Digest, 1993., IEEE MTT-S International*, 1993, pp. 853–856 vol.2.

[6] M. Peter and W. Keusgen, "A component-based time domain wideband channel sounder and measurement results for the 60 GHz in-cabin radio channel," in *Antennas and Propagation, EuCAP 2007. The second European Conference on*, Nov. 2007.

[7] T. Zwick, T. J. Beukema, and H. Nam, "Wideband channel sounder with measurements and model for the 60 GHz indoor radio channel," *Vehicular Technology, IEEE Transactions on*, vol. 54, no. 4, pp. 1266–1277, 2005.

[8] R. Kattenbach, "Statistical modeling of small-scale fading in directional radio channels," *Selected Areas in Communications, IEEE Journal on*, vol. 20, no. 3, pp. 584–592, 2002.

4.2 Impact of the Antenna Configuration

The investigations in Section 4.1 support the usage of 60 GHz for ultra-high data rate short range links, even for scenarios without LOS. Nevertheless, the received normalized received power (NRP) is at least 21 dB smaller that at 5 GHz due to the larger free-space path loss. To cope with this problem, directional antennas can be used at the Tx and/or the Rx. Assuming free-space propagation and perfect alignment of the antennas, the received power, and thus the SNR of the received signal, is increased by the cumulative antenna gain. Under real-world conditions, however, perfect alignment might not be guaranteed. Furthermore, multipaths are spatially filtered out by the limited beamwidth of the antennas. Looking at the results in Section 4.1, this filtering can be expected to reduce the time dispersion of the radio channel, but also to suppress multipaths carrying valuable power when the LOS is blocked.

The impact of the antenna configuration—defined as a particular combination of a Tx and an Rx antenna—on the radio channel is addressed in the following publication [PK08]. The measurements were part of the same measurement campaign in the conference room as described in Section 4.1. The same equipment was used, but three different antenna configurations were considered, including directional Vivaldi antennas in addition to the omnidirectional ones. The investigations are based on the assumption that the Tx antenna (access point) is fixed, but the Rx antenna (portable device) is aligned towards the Tx in the horizontal plane.

The results reveal that the RMS delay spread for LOS can indeed be significantly reduced (to one third) by using a Vivaldi antenna at the Rx instead of the omnidirectional one. It can be further decreased by additionally applying a Vivaldi antenna at the Tx, but only for a good alignment. The obstruction of the LOS results in a distinct increase of the DS for all configurations. In this case, directional antennas at both sides yield the largest values. As expected, the received power is maximized with the latter configuration for LOS, though in practice the full antenna gain is not utilizable due to non-ideal alignment.

Dynamic measurements with a person or an absorber mat crossing the LOS revealed that the impact of human body shadowing (HBS) is significantly less severe than effects caused by the absorber. Since the attenuation of the LOS component is much lower, but mm-waves cannot penetrate the body, this shows that diffraction is a relevant propagation mechanism for HBS, even for short wavelengths. This aspect is addressed in Section 4.5 in detail. In addition to the LOS path, multipaths arriving with lager delays can be highly attenuated when directional antennas are included. Nevertheless, the NRP under OLOS conditions is very similar for all configurations.

Though this result is expected to be scenario-dependent, it can be concluded that a purely omnidirectional setup does not outperform configurations with moderately directional antennas in general. However, setups employing directional antennas must cope with much larger *relative* losses when the LOS is obstructed.

Contribution

This paper was authored by me and I made the related preparations and investigations, which included the build-up, programming and testing of the channel sounder setup, planning and performance of the measurement campaign, as well as data post-processing and analysis. The co-author supported me by providing advice for the build-up of the channel setup, proof reading and several corrections.

Impact of Antenna Configuration and Shadowing on the Characteristics of the 60 GHz Indoor Wideband Radio Channel

Michael Peter, Wilhelm Keusgen

Fraunhofer-Institut für Nachrichtentechnik, Heinrich-Hertz-Institut, Einsteinufer 37, 10587 Berlin, Germany
Phone: +49 30 31002-{583, 639}, e-mail: {michael.peter, wilhelm.keusgen}@hhi.fraunhofer.de

Abstract

In this paper, we present the results of an extensive measurement campaign concerning the 60 GHz indoor wideband radio channel. Three different antenna configurations are considered involving omnidirectional and directional antennas. We analyze the impact of the antenna configuration on the time dispersion and the normalized received power under line-of-sight (LOS) as well as under obstructed line-of-sight (OLOS) conditions.

1. Introduction

The growing demand for wireless broadband multimedia services gives rise to high requirements on systems for short-range radio data transmission and bears a considerable technical challenge [1]. Since future usage scenarios call for wireless systems with an aggregate capacity of up to several Gbit/s, great efforts are currently made with regard to new concepts and standards. A promising approach to achieve rates beyond 1 Gbit/s is the utilization of unused frequency resources within the millimeter wave band. The IEEE 802.15.3 Task Group 3c (TG3c) is working towards an alternative physical layer (PHY) for the 802.15.3 Wireless Personal Area Network (WPAN) standard. The systems are supposed to operate in the unlicensed band from 57 to 64 GHz and are a candidate for indoor and in-vehicular [2] high speed internet access as well as real-time video streaming. To provide a basis for system design and implementation, it is essential to characterize millimeter wave propagation in application-oriented environments [3]. We performed wideband channel measurements in a conference room to investigate the influence of the antenna configuration and shadowing on the characteristics of the 60 GHz indoor radio channel. The paper gives an overview over the measurement campaign and the investigations concerning the received power and the time dispersion of the channel.

2. Indoor Broadband Channel Measurements

The measurements were performed in a conference room located on the ground floor of the institute building. We used a measurement setup based on pulse compression covering a bandwidth of 1 GHz around the center frequency of 61 GHz. The system allows for taking snapshots of the channel impulse response (CIR) with an adjustable rate. Each measurement yields a coherent set of CIRs. More details of the setup can be found in [4]. Fig. 1 shows the floor plan of the separable conference room. The partition wall was closed, so that the room size was approximately 6.6 m $\times$ 5.9 m. The room is provided with four windows integrated in the ceiling and a glass door towards the corridor. It was furnished with tables and chairs. The location of the transmitter (Tx), representing the access point, was fixed, whereas the receiver (Rx) was considered as a mobile terminal and placed at twelve different locations around the tables according to Fig. 1. For each Rx location (Rx loc.) and each antenna configuration a spatial small-scale measurement set of 100 CIRs has been acquired. Three different antenna configurations have been considered: omnidirectional antennas at the Tx and the Rx (OO), an omnidirectional antenna at the Tx and a Vivaldi antenna at the Rx (OV) and Vivaldi antennas at both the Tx and the Rx (VV). The omnidirectional antennas have an almost constant pattern in the azimuth plane and an FWHM (full width at half maximum) of about $\Theta_{3\mathrm{dB}} = 70^\circ$ in elevation. This results in a maximum gain of 2 dBi. The Vivaldi antennas are directional antennas with a gain of approximately 12 dBi and an FWHM of $\Theta_{3\mathrm{dB}} = 33^\circ$ in both azimuth and elevation plane. All antennas were vertically polarized. The stationary Tx antenna was mounted at a height of 245 cm with a downtilt of 15°. Since the transmitter should represent a fixed access point, the antenna was not

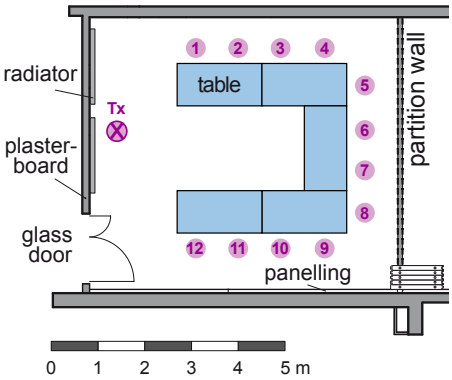

Fig. 1: Floor plan of the conference room, numbered circles mark the Rx locations.

moved or adjusted during the measurement, whereas the Rx antenna had always been aligned towards the Tx antenna in the horizontal plane. In order to be able to remove the effects of spatial small-scale fading, the Rx antenna (mounted at a height of 130 cm) was moved on a linear track over a distance of 10 cm by the help of a controllable positioning platform. This results in a spatial separation of 1 mm between two consecutive snapshots. LOS and OLOS conditions have been considered. OLOS was realized by blocking the line-of-sight between Tx antenna and Rx antenna with an absorber mat of size 60×60 cm. Additional measurements were performed to investigate the effects of temporary shadowing by a human body. The acquired data set comprises more than 10,000 complex-valued CIRs.

3. Normalized Received Power

The normalized received power (NRP) $P_{R,\mathrm{norm}}$ was calculated on the basis of the averaged power delay profiles (APDPs). An APDP is given by

$$\overline{p}(\tilde{\tau}) = \frac{1}{K}\sum_{k=1}^{K} p_k(\tilde{\tau}) = \frac{1}{K}\sum_{k=1}^{K} |h_{b,k}(\tilde{\tau})|^2, \qquad (1)$$

where $\tilde{\tau}$ is the delay, $p_k(\tilde{\tau})$ denotes the individual power delay profile (PDP) of channel observation (snaphot) k at a particular Rx location, and $h_{b,k}(\tilde{\tau})$ is the corresponding bandlimited CIR. $P_{R,\mathrm{norm}}$ can be calculated by integrating all multipath power above the noise floor:

$$P_{R,\mathrm{norm}} = \int_{\tilde{\tau}_0}^{\tilde{\tau}_{\max}} \overline{p}(\tilde{\tau})\, d\tilde{\tau}, \qquad (2)$$

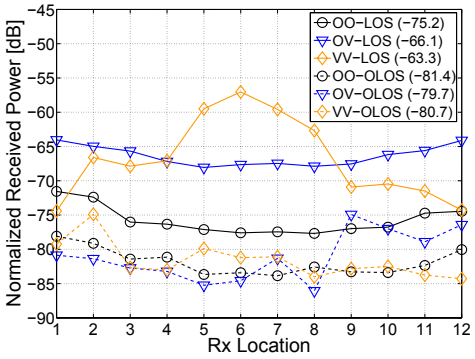

Fig. 2: NRP versus Rx loc., average values (dB) are given in brackets.

where $\tilde{\tau}_0$ and $\tilde{\tau}_{\max}$ were determined by applying a threshold of -30 dB with respect to the strongest component, resulting in a maximum value of approx. 125 ns for $\tilde{\tau}_{\max}$. Fig. 2 illustrates $P_{R,\mathrm{norm}}$ at the 12 Rx locations for all antenna configurations. Under LOS conditions (solid lines), the power is expected to decay when the Tx-Rx distance is increased and vice versa. This is true for the OO and the OV config. (see Fig. 1), but it is not the case for the VV config. The received power is smallest for the nearby locations and reaches its maximum at loc. 6, which is 4.6 m away from the transmitter. This effect becomes clear, when we bear in mind that the mounting height of the Tx antenna was 1.15 m above the height of the Rx antenna, and the Tx antenna pointed towards the back wall of the room. As a result, the alignment was poor for the nearby locations. At most of the Rx loc. the NRP is around 10 dB higher for the OV configuration with respect to the OO configuration. This is in accordance to the expected value due to the antenna gain of the Vivaldi antenna compared to the omnidirectional one. An additional gain of 10 dB can be achieved with the VV configuration, but only for Rx loc. 6. For seven of the twelve Rx loc. the NRP is smaller than for the OV case.

In general, millimeter wave systems are proposed for LOS transmission, but in practical scenarios intervisibility between Tx and Rx antenna might not be guaranteed. To investigate the impact of an obstructed line-of-sight, the measurement procedure was carried out twice for each Rx loc. During the second measurement, the LOS was blocked by an absorber mat. One would expect that the OO configuration performs best under OLOS conditions since multipath power can be collected from all directions. However, the measurement results did not comply with this expectation. The average OLOS values of $P_{R,\mathrm{norm}}$ (dashed lines) are almost identical, and the curves in Fig. 2 are quite close to each other. By inspecting the APDPs we could ensure that the (virtual) LOS-MPC did not penetrate the absorber mat. Indeed, there are MPCs whose powers sum up to values corresponding to an NRP of around -80 dB.

4. Temporary Shadowing

In order to further investigate the influence of an obstructed LOS, additional measurements were performed with temporary shadowing. Fig. 3 gives a vivid impression of the typical effects of shadowing by the absorber mat and a person crossing the LOS. In the shown example, the power of the first resolvable component (LOS-RMPC) drops about 32.2 dB. The loss in total power is 23.8 dB. We see that the impact of human shadowing is significantly less severe than effects caused by the absorber mat. The loss of total power is around 7.0 dB. Values up to 13 dB have been observed for other Rx locations. In contrast, values up to 5 dB arose for the OO configuration, but one must

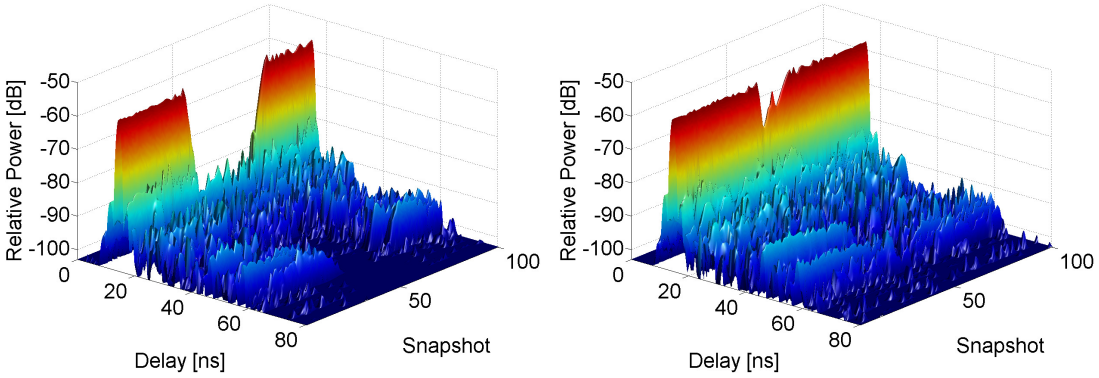

(a) Absorber (b) Human body

Fig. 3: Effects caused by temporary shadowing for the VV configuration at Rx loc. 6.

bear in mind that the reference (received LOS power) is much lower in this case. Frequently, OLOS measurement results are derived from the LOS CIRs by mathematical removal of the "direct ray" (LOS-MPC). Since MPCs cannot be resolved in general, this is only possible within the temporal resolution. In fact, not the distinct LOS-MPC but the LOS-RMPC is removed. Therefore, in [5] it is stated that this is a somewhat pessimistic approach since some part of the diffracted rays is removed, too. However, in realistic obstruction scenarios, not only the LOS-MPC might be eliminated, but also other MPCs arising from similar angles of departure or angles of arrival – depending on whether the obstructing object is situated nearby the Tx or the Rx antenna. This effect is clearly visible in Fig. 3. Consequently, the approach can also be too optimistic. The actual impact of shadowing strongly depends on the size, the material and the position of the obstructor as well as on the directivity of the antennas. Hence, one should carefully analyze if the "mathematical approach" for OLOS is adequate under the investigated conditions. The minimum power within the measurement set with human body shadowing is reached after three snapshot intervals corresponding to 150 ms, whereby the person crossed the line-of-sight with a speed of approximately $0.4\ \frac{\mathrm{m}}{\mathrm{s}}$. Assuming a maximum speed of $2.0\ \frac{\mathrm{m}}{\mathrm{s}}$, severe fluctuations of the channel state due to human body shadowing can occur within an interval of 30 ms.

5. Time Dispersion

Several publications deal with the time dispersion of the 60 GHz indoor channel. In [6] the channel has been measured by means of highly directional antennas, whereas in [7] omnidirectional antennas have been used. In [8] the influence of different antenna types is also investigated. In order to characterize the time dispersion of the channel, we derived the RMS delay spread from the APDPs for each antenna configuration and each Rx location:

$$\overline{\tau}_{\mathrm{rms}} = \sqrt{\frac{\int_0^{\overline{\tau}_{\max}} \tau^2 \cdot \overline{p}(\tau)\, d\tau}{\int_0^{\overline{\tau}_{\max}} \overline{p}(\tau)\, d\tau} - \overline{\tau}_{\mathrm{m}}^2} \tag{3}$$

with

$$\overline{\tau}_{\mathrm{m}} = \frac{\int_0^{\overline{\tau}_{\max}} \tau \cdot \overline{p}(\tau)\, d\tau}{\int_0^{\overline{\tau}_{\max}} \overline{p}(\tau)\, d\tau}, \tag{4}$$

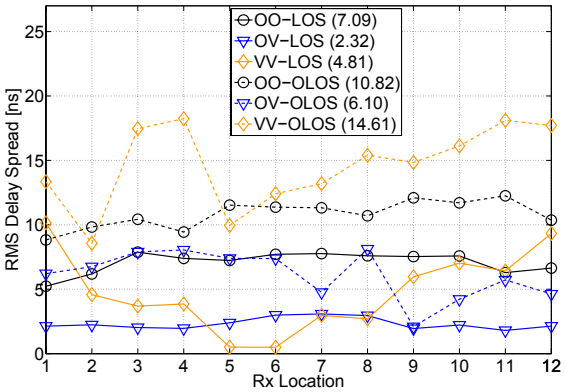

Fig. 4: RMS delay spread for different antenna configurations, average values (ns) are given in brackets.

where $\tau = \tilde{\tau} - \tilde{\tau}_0$, $\overline{\tau}_{\mathrm{m}}$ and $\overline{\tau}_{\max}$ denote the excess delay, the mean excess delay and the maximum excess delay, respectively. Again, a threshold of -30 dB relative to the strongest component was used to determine $\tilde{\tau}_0$ and $\overline{\tau}_{\max} = \tilde{\tau}_{\max} - \tilde{\tau}_0$. Fig. 4 shows the delay spread with respect to the Rx loc. 1–12 (see Fig. 1) for all considered antenna combinations. Solid lines refer to the LOS cases, dashed lines to OLOS conditions. The average RMS delay spread values are also given in Fig. 4. Comparing the LOS results, we see that the curves are quite flat for the OO and the OV configuration, which means that the RMS delay spread is only weakly related to the actual Rx loc. or

the distance between Tx and Rx. The values are 5.2–7.9 ns (OO) and 1.8–3.1 ns (OV), respectively. Applying the directional antenna at the Rx side reduces $\overline{\tau}_{\mathrm{rms}}$ to approximately one third on average in LOS scenarios – compared to the OO configuration. The VV curve shows a completely different behavior. The largest delay spread (10.2 ns) is observed at Rx loc. 1, whereas the lowest values of 0.5 ns (equivalent to the RMS delay spread of the sounding pulse) arises at loc. 5 and 6. Again, the impact of the antenna pointing error emerges. The transition from LOS to OLOS increases the mean delay spread significantly in all cases. The increase is around 50% for the OO, 160% for the OV and 204% for the VV configuration. While the OV value remains below the delay spread of the OO case, even compared to the LOS value, the average $\overline{\tau}_{\mathrm{rms}}$ of the VV configuation exceeds the OO value by 35%.

6. Conclusion

In this paper, we presented major results of a measurement campaign regarding the 60 GHz indoor channel. Three different antenna configurations have been investigated. As stated in [8], the patterns of the antennas have a great impact on the time dispersion of the channel. Under LOS conditions, the average RMS delay spread reduces to one third by applying a directional antenna with a gain of 12 dBi at the Rx side (OV). If at most one directive antenna is used, the variance of $\overline{\tau}_{\mathrm{rms}}$ is small with respect to different Rx locations. The delay spread can be decreased further by additionally using a directional antenna at the transmitter (VV), but only for a good alignment – which might not be guaranteed under realistic conditions. Obstructing the LOS significantly increases the delay spread. The VV configuration yields the largest values in the OLOS case. Under LOS conditions the received power reaches its maximum for the VV configuration, but the theoretical gain of 20 dB – compared to the OO configuration – is only achieved for a single Rx loc. In contrast, a gain of approximately 10 dB is achieved in the OV case for almost all Rx locations. Counter-intuitively, the average NRP is almost identical under OLOS conditions for all antenna combinations. This result might depend on the scenario, but we conclude that an OO configuration does not outperform configurations with moderately directive antennas in general. However, if a system with directive antennas is supposed to sustain a link even under OLOS conditions, it must not rely on the large received LOS power, but it must be capable to switch to another mode that allows for data transmission with a 20 dB lower SNR. In contrast, the gap between average LOS and OLOS received power is only around 6 dB for the OO case, and the fluctuations of power are much smaller with respect to the actual Rx loc. In any case, a high-rate millimeter wave wireless system is to be highly adaptive to the channel conditions and should involve mechanisms like macroscopic diversity in order to ensure a reliable transmission.

7. References

[1] P. Smulders. Exploiting the 60 GHz band for local wireless multimedia access: prospects and future directions. *Communications Magazine, IEEE*, 40(1):140–147, 2002.

[2] M. Peter, W. Keusgen, and M. Schirrmacher. Measurement and analysis of the 60 GHz in-vehicular broadband radio channel. In *Vehicular Technology Conference, 2007. VTC 2007-Fall. 2007 IEEE 66th*, Sept.–Oct. 2007.

[3] P. F. M. Smulders and L. M. Correia. Characterisation of propagation in 60 GHz radio channels. *Electronics & Communication Engineering Journal*, 9(2):73–80, 1997.

[4] M. Peter and W. Keusgen. A component-based time domain wideband channel sounder and measurement results for the 60 GHz in-cabin radio channel. In *Antennas and Propagation, EuCAP 2007. The second European Conference on*, Nov. 2007.

[5] P. F. M. Smulders. *Broadband Wireless LANs: A Feasibility Study*. PhD thesis, Eindhoven University of Technology, The Netherlands, 1995.

[6] R. Davies, M. Bensebti, M. A. Beach, and J. P. McGeehan. Wireless propagation measurements in indoor multipath environments at 1.7 GHz and 60 GHz for small cell systems. In *Vehicular Technology Conference, 1991. 'Gateway to the Future Technology in Motion', 41st IEEE*, pages 589–593, 1991.

[7] T. Zwick, T. J. Beukema, and H. Nam. Wideband channel sounder with measurements and model for the 60 GHz indoor radio channel. *Vehicular Technology, IEEE Transactions on*, 54(4):1266–1277, 2005.

[8] T. Manabe, Y. Miura, and T. Ihara. Effects of antenna directivity and polarization on indoor multipath propagation characteristics at 60 GHz. *Selected Areas in Communications, IEEE Journal on*, 14(3):441–448, 1996.

4.3 Aircraft In-Cabin Measurements

The usage of 60 GHz is particularly interesting for establishing WLANs that require a very high capacity due to the large number of connected users. A wireless inflight entertainment (IFE) system can be seen as an extreme example, since it provides access to multimedia content for hundreds of air travelers. The following publication was motivated by this use case. It presents channel measurements in an electromagnetic compatibility (EMC) mockup of a wide-bodied aircraft passenger cabin, performed with the same measurement setup as used for the investigations in the conference room (Sections 4.1–4.2). To the knowledge of the authors, it was the first 60 GHz measurement campaign in such an environment. In particular, it was unknown how lightweight and composite building materials in the cabin such as glass fiber reinforced plastic (GRP) and carbon fiber reinforced plastic (CRP) would affect the channel, and if an IFE connection could be maintained when the LOS is blocked by a passing passenger.

Overall, the evaluations show that the large-scale characteristics of the in-cabin channel are comparable to that of an indoor channel. The DS is only slightly larger than for the conference room (see Section 4.1) and e. g. very similar to the results for the office environment described by Zwick et al. [ZBN05]. However, in contrast to the conference room channel, very distinct clusters in the PDP can be observed with strong multipaths that are only weakly affected by small-scale fading. Such clustering in the delay domain has been reported by several authors, primarily at lower frequencies [SV87, CSW02] This is consistent with the observation in the conference room, where the clusters are more pronounced at 5 GHz. However, clustering cannot be observed in all measurements (see e.g. [CWM02]), indicating that the effect depends on the propagation environment. Complementing ray tracing simulations in [FKP08b] reveal that the strongest multipath components can be attributed to reflections at the metalized cabin windows, which foster the clustering effect.

OLOS conditions caused by human body shadowing (HBS) attenuated the LOS path by more than 30 dB, but the overall loss in the cabin only exhibited a median value of approx. 6 dB and was at most 12 dB. If a corresponding shadowing margin is considered, the IFE system can also cope with OLOS.

In close relation to these investigations, it is shown in [FKP08a] based on ray tracing that coverage can be achieved in an entire cabin with multiple access points and dynamic cell allocation. Aspects on system design and operation are addressed in [LKKP08a].

Contribution

This paper was authored by me. I planned the measurement campaign, analyzed the data and derived the results. Fig. 2 was provided by M. Schirrmacher and edited by W. Keusgen. The measurement campaign was conducted jointly by W. Keusgen and myself with the support of M. Schirrmacher. A. Kortke and W. Keusgen provided technical advice, proof reading and smaller corrections.

Measurement and Analysis of the 60 GHz In-Vehicular Broadband Radio Channel

Michael Peter, Wilhelm Keusgen, Andreas Kortke
Fraunhofer-Institut für Nachrichtentechnik,
Heinrich-Hertz-Institut
Einsteinufer 37, 10587 Berlin, Germany
E-mail: {Michael.Peter, Wilhelm.Keusgen,
Andreas.Kortke}@hhi.fraunhofer.de

Martin Schirrmacher
Airbus Deutschland GmbH
Airbus Buxtehude – BCEKET (Pre-development)
Lüneburger Schanze 30, 21614 Buxtehude, Germany
E-mail: martin.schirrmacher@airbus.com

***Abstract*— In this paper, we present the results of a measurement campaign regarding the 60 GHz in-vehicular wireless channel. The measurements have been performed inside an aircraft passenger cabin by the use of a modular setup covering a bandwidth of 1 GHz. We consider path loss aspects and investigate the time-dispersive nature of the channel. Additionally the influence of an obstructed line-of-sight is analyzed.**

I. Introduction

Due to the growing demand for broadband services in the area of passenger transport, several technical approaches are currently discussed. A wireless in-vehicular network shall provide access to travel-based information and multimedia contents for entertainment in buses, trains or aircrafts. Suchlike systems require downlink data rates of about 10 Mbit/s per user, in order to support high definition video standards. As a result of an extremely high user density, sum rates of up to several Gbit/s are to be considered.

A promising approach to meet the requirements, is the development of unused frequency resources within the millimeter wave band. So far, little work has been done concerning the investigation and the characterization of the in-vehicular radio channel although this is important to provide a basis for the design of 60 GHz transmission systems. Due to reflections at the vehicle structure and at objects within the propagation environment, the transmission is largely affected by multipath propagation. Since involved materials are different from those used in buildings, the characteristics of an in-vehicular radio channel might differ from that of typical indoor-channels. In the case of the in-cabin environment many composite materials are in use because lightweight design is an important issue in aircraft construction.

II. Broadband Channel Measurements

A. Measurement Setup

With regard to 60 GHz indoor and in-vehicular channel measurements and related analysis, a modular time-domain measurement setup was built up based on laboratory components. Its schematic is illustrated in Fig. 1. An arbitrary waveform generator (AWG) serves as source for the baseband signal. It results from a maximum length binary sequence which is repeated periodically. A dual sideband mixer is used to convert the signal to an IF of 8 GHz. Since both sidebands are used for the measurements, the system covers a bandwidth of 1 GHz and provides a temporal multipath resolution of about 1 ns. Finally the signal is mixed to the RF of 61 GHz. The received signal is sampled in the IF domain by a digital sampling oscilloscope (DSO) with a resolution of eight bits. In this way, the whole system works without an IQ modulator and demodulator. Synchronization of the equipment is realized

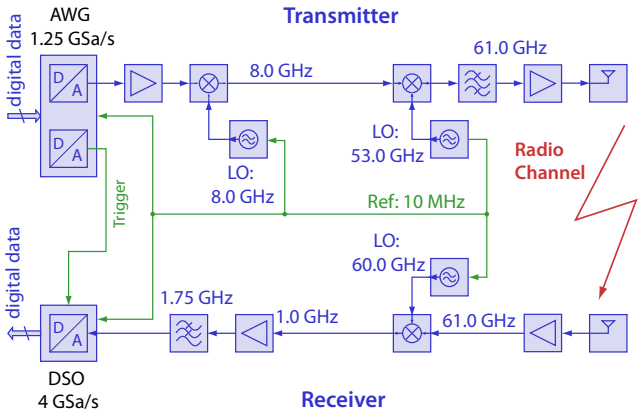

Fig. 1. Schematic of the channel sounder setup.

by connecting the 10 MHz reference clocks of the AWG, the DSO and the LO synthesizers.

An open-ended rectangular waveguide with a gain of approximately 5 dBi served as transmit antenna at a height of 168 cm. At the receiver side an omnidirectional antenna (omnidirectional in azimuth, approximately 100° 3 dB beamwidth in elevation, height: 130 cm) with a gain of 2 dBi was applied. Both antennas were vertically polarized. In order to be able to capture the small-scale variations of the channel, the receive antenna was mounted on a controllable positioning device.

B. Measurement Procedure and Data Processing

By the use of the positioning device the receive antenna was moved on a linear track over a distance of $d_m = 10$ cm $\approx 20\lambda$ in order to obtain a small-scale data set for each receiver location, which consists of 100 snapshots

of the complex channel impulse response (CIR). It can be captured during the continuous motion without affecting the accuracy of measurement because, for the chosen settings, the system only needs about 123 μs to acquire one snapshot. The total measurement duration needed for one set, which was 5 s in our case, is mainly determined by a suitable moving speed of the positioner. All postprocessing operations, including complex down conversion, averaging, noise filtering, correlation and pulse shaping are performed off-line in the digital domain. Additionally, the impulse response of the measurement system is calibrated out. The overall processing gain of $G_{\mathrm{proc}} = G_{\mathrm{corr}} + G_{\mathrm{avrg}} = 50.9$ dB results from the correlation gain and an additional gain due to averaging over 60 signal periods. Outband noise is eliminated in the frequency domain by setting corresponding components to zero. Depending on further analysis, a Kaiser window with $\beta = 5$ has been applied to restrict sidelobes in the time domain to a level of -37 dB with respect to the main lobe.

C. In-cabin Scenario

The system has been used to perform measurements inside an EMC mockup of the wide-bodied aircraft passenger cabin illustrated in Fig. 2. As implied by red circles, the channel has been measured at 17 application-oriented receiver locations at the back of the seats under line-of-sight (LOS) conditions. Each (large scale) receiver location is characterized by a small-scale set of 100 channel impulse responses. By the way of illustration, Fig. 3 shows the resulting small-scale set at Rx location 3.

Obstructed line-of-sight (OLOS) conditions were taken into account by considering the same locations, whereas a person was blocking intervisibility between transmitter and receiver. The positions of the person with regard to the receiver locations are pictured by ellipses in Fig. 2. It shall be mentioned that a real blockage of the line-of-sight was not achieved in some cases. To come to meaningful results, this data is discarded when referring to OLOS and with regard to any comparisons between LOS and OLOS results.

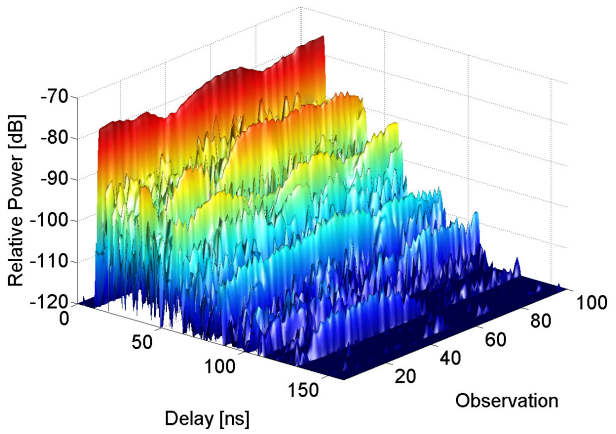

Fig. 3. Measured small-scale set of CIRs at Rx location 3 under LOS conditions.

III. Investigations

A. Channel Description

Under multipath propagation conditions, the received signal $x(t)$ results from a summation of echoes of the transmitted signal $s(t)$. The input-output relation for the time-invariant channel is given by

$$x(t) = \int_{-\infty}^{\infty} s(t-\tau)h(\tau)d\tau, \tag{1}$$

where $h(\tau)$ is the equivalent lowpass CIR. It can be modeled as a sum of time-shifted complex-weighted Diracs $\delta(\tau)$:

$$h(\tau) = \sum_{l=1}^{L} h_l \cdot \delta(\tau - \tau_l), \tag{2}$$

where τ_l, h_l denote the delay and the complex weight of the l-th channel tap, respectively. It shall be noted that practical systems have a limited bandwidth B, and it is commonly assumed that physical multipath components (MCPs) arriving within an interval smaller than $\frac{1}{B}$ cannot be resolved. Each channel tap may result from a superposition of multiple MPCs, and the channel is subjected to small-scale fading. This effect is clearly recognizable in Fig. 3.

B. Averaged Power Delay Profiles

By averaging over all power delay profiles (PDPs) within a small-scale set we obtain the averaged power delay profile (APDP):

$$\overline{p}(\tau) = \frac{1}{K}\sum_{k=1}^{K} p^{(k)}(\tau), \tag{3}$$

where $p^{(k)}(\tau) = |h^{(k)}(\tau)|^2$ denotes the PDP of channel observation k. The APDP indicates the decay of arriving multipath power with respect to the delay, discounting the small-scale fading effects. Fig. 4 shows four characteristic APDPs that

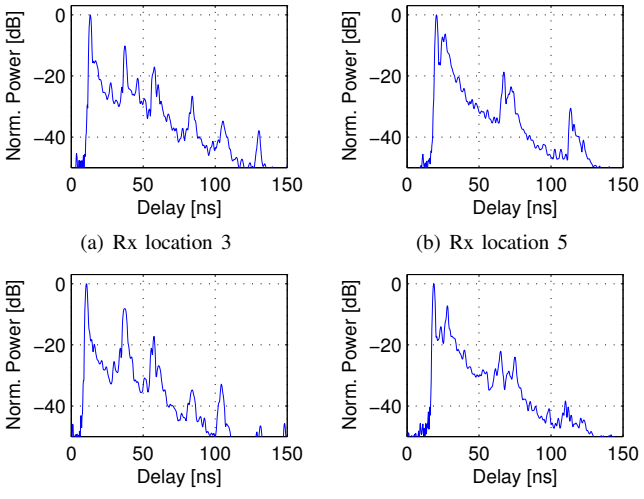

(a) Rx location 3 (b) Rx location 5

(c) Rx location 8 (d) Rx location 17

Fig. 4. Characteristic APDPs (normalized) at 4 different Rx locations under LOS conditions.

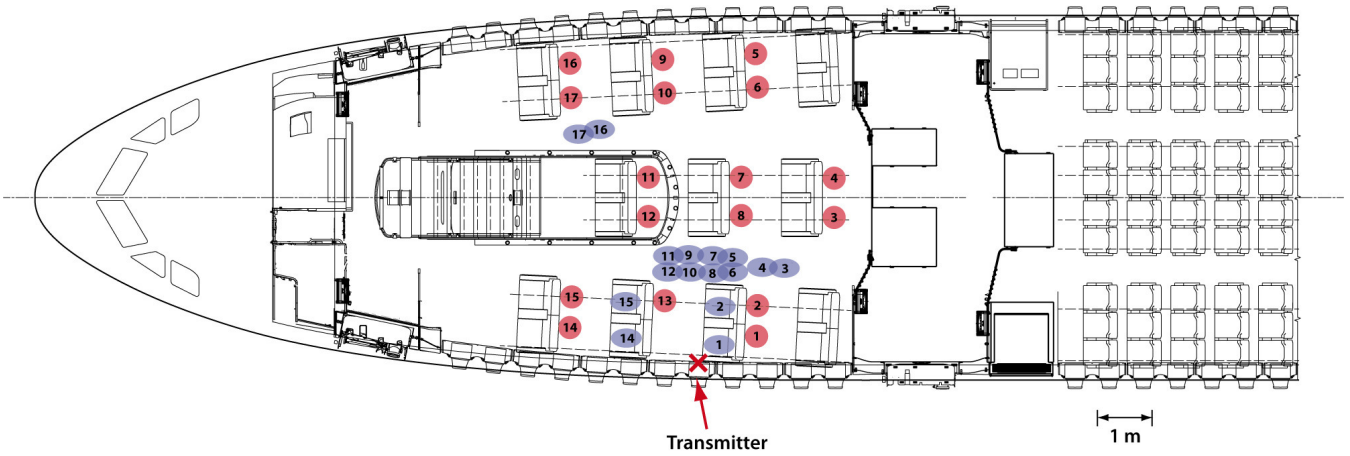

Fig. 2. In-cabin measurement scenario. Circles and ellipses mark the locations of the receiver and the person, respectively.

result from different Rx locations under line-of-sight. We see that the power does not decay continuously, but at certain delays, it increases abruptly. This is in accordance with Fig. 3, where several strong components of the impulse response show similar properties as the LOS component. They are only weakly affected by fading and appear as conspicuous "walls" within the illustrated small-scale set. Several authors refer to this clustering phenomenon in their measurement results ([1], [2]), whereas others did not observe or consider clustering ([3]). Although it is not quite clear, under which conditions clustering effects are to be taken into account, comparisons with indoor measurements indicate that building materials and the room size as well as the antenna configuration play an important role. In the in-cabin scenario the number of visible clusters varies between 3 and 7 within all measurement sets.

C. Path Loss

Path loss (PL) is defined as the ratio of the effective transmitted power to the received power:

$$\begin{aligned} \mathrm{PL}\ [\mathrm{dB}] \quad &= \quad P_T\ [\mathrm{dBm}] + G_T\ [\mathrm{dBi}] + G_R\ [\mathrm{dBi}] \\ &\quad -P_R\ [\mathrm{dBm}], \end{aligned} \tag{4}$$

where P_T, P_R, G_T and G_R denote the transmitted power, the received power, the transmitter antenna gain and the receiver antenna gain, respectively.

According to the frequently used *exponent model* (also referred to as *log-distance law*) the average path loss over the distance d is given by the path loss to a reference distance d_0 plus the additional path loss as follows [4]:

$$\overline{\mathrm{PL}}(d)\ [\mathrm{dB}] = \mathrm{PL}(d_0)\ [\mathrm{dB}] + 10n \log_{10}\left(\frac{d}{d_0}\right), \tag{5}$$

where $\mathrm{PL}(d_0)$ is called *intercept point*, and n is the *path loss exponent*, which characterizes how fast the path loss increases with respect to Tx-Rx separation. For free space propagation n equals 2, but it changes for multipath environments.

Fig. 5 shows the scatter plot of the measured path loss with respect to the transmitter-receiver separation in logarithmic scale. P_R has been determined on the basis of the averaged power delay profiles by summing up all multipath power above the noise floor. Additionally, the linear regression line, resulting from a minimum mean square error (MMSE) analysis, is shown. The corresponding path loss exponent is $n = 1.65$ with a standard deviation of $\sigma = 1.76$. Accordingly, n is slightly smaller than for free space propagation and lies in the range of values found for indoor millimeter wave propagation in office environments [5], [6]. The low value

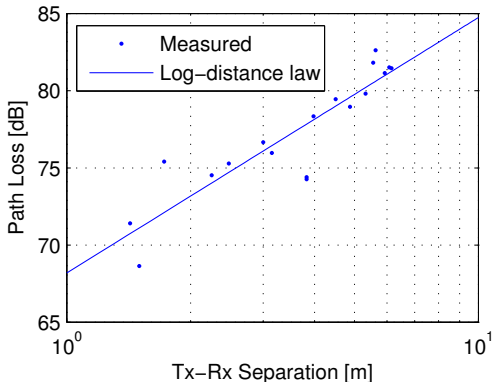

Fig. 5. Path loss versus Tx-Rx separation with linear regression MMSE curve fit.

of the standard deviation shows that the actual path loss at a certain receiver location follows the log-distance law quite accurately. The MMSE regression results in an intercept point of $\mathrm{PL}(d_0 = 1\ \mathrm{m}) = 68.2$ dB. It is very close to the theoretical value for 61 GHz free space propagation of 68.1 dB.

D. Obstructed Line-of-Sight

In general, millimeter wave systems are proposed for LOS applications. However, in practical scenarios intervisibility between transmit and receive antenna might not be guaranteed

without interruption due to persons moving inside the propagation environment. Hence, we also considered the OLOS case, whereas a person was blocking intervisibility between transmitter and receiver. As an example, Fig. 6 shows the APDP at Rx location 3 under LOS as well as under OLOS conditions. As expected, the impact on the LOS component of

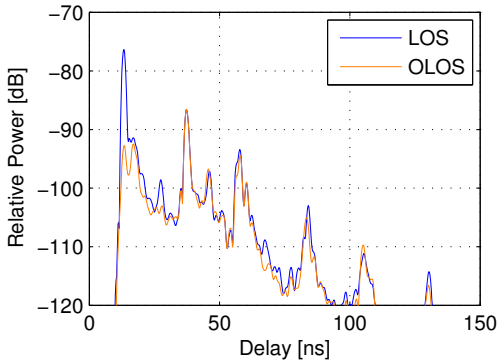

Fig. 6. APDPs at Rx location 3 under LOS and OLOS conditions.

the CIR is severe and its average power (corresponding to the first peak of the APDPs in Fig. 6) drops about 16.4 dB. An influence on other strong components is hardly recognizable in the present case. Although they can also be affected in principle, this effect is less important as long as non-directional antennas are involved. Consequently the loss in total power is approximately 6.7 dB, only. Detailed investigations of the whole data set lead to the cumulative distribution illustrated in Fig. 7. We see that the drop of power of the LOS component can exceed values of 30 dB, whereas the maximum loss of total power is about 12 dB and below 5.8 dB in 50% of all cases.

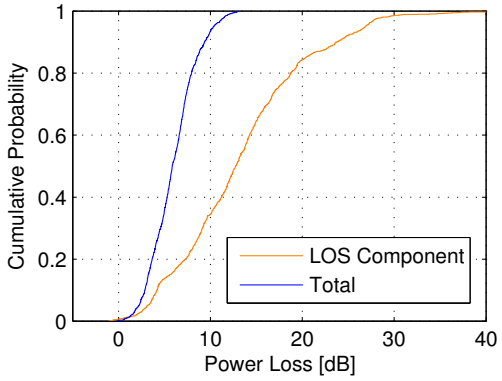

Fig. 7. Cumulative distribution of power loss due to obstruction.

E. Time Dispersion

The time-of-arrival (TOA) parameters including maximum excess delay $\tau_{\max}$, mean excess delay τ_{m} and RMS delay spread τ_{rms} are used to characterize the time dispersion of a multipath channel [7]. Under the assumption that $\tau_1 = 0$ these parameters are given as:

$$\tau_{\max} = \max_{1 \le l \le L} \tau_l \tag{6}$$

$$\tau_{\mathrm{m}} = \frac{\sum_{l=1}^{L} p_l \tau_l}{\sum_{l=1}^{L} p_l} \tag{7}$$

$$\tau_{\mathrm{rms}} = \sqrt{\overline{\tau^2} - \tau_{\mathrm{m}}^2}, \quad \text{where} \quad \overline{\tau^2} = \frac{\sum_{l=1}^{L} p_l \tau_l^2}{\sum_{l=1}^{L} p_l} \tag{8}$$

and $p_l = |h_l|^2$ is the power of the l-th channel tap. The TOA parameters were calculated for each small-scale set, whereas a threshold of -30 dB with respect to the strongest component was used to terminate the PDPs. The average values, determined from the particular APDPs, are summarized in Table I. $\overline{\tau}_{\mathrm{rms}}$ lies between 3.4 ns and 12.5 ns for LOS,

Loc.	d [m]	PL [dB]	$\overline{\tau}_{\max}$ [ns]	$\overline{\tau}_{\mathrm{m}}$ [ns]	$\overline{\tau}_{\mathrm{rms}}$ [ns]
1	1.43	71.4	53.8 (95.8)	5.6 (12.4)	9.3 (16.5)
2	1.73	75.4	53.3 (*52.5*)	6.2 (*5.8*)	10.3 (*9.8*)
3	3.98	78.3	73.8 (98.3)	7.2 (23.8)	11.5 (15.5)
4	4.50	79.5	95.0 (96.0)	5.5 (15.6)	12.4 (16.8)
5	6.15	81.5	56.3 (96.3)	5.4 (9.4)	7.2 (10.0)
6	5.55	81.8	96.3 (98.0)	7.8 (11.1)	9.5 (10.2)
7	3.83	74.4	50.0 (70.3)	6.7 (19.4)	9.3 (8.0)
8	3.15	76.0	53.3 (97.0)	8.8 (15.8)	12.5 (14.3)
9	5.93	81.1	56.8 (*56.5*)	5.1 (*4.8*)	6.8 (*6.0*)
10	5.32	79.8	59.8 (58.3)	5.0 (5.8)	7.7 (7.2)
11	3.83	74.3	69.3 (*28.8*)	3.5 (*3.1*)	6.5 (*5.0*)
12	3.00	76.7	48.5 (78.3)	3.7 (20.5)	6.7 (12.3)
13	1.50	68.6	38.8 (n/a)	2.4 (n/a)	3.4 (n/a)
14	2.25	74.5	51.8 (89.5)	6.0 (12.6)	10.7 (15.9)
15	2.48	75.3	52.8 (*47.5*)	5.0 (*4.7*)	8.5 (*7.7*)
16	6.08	81.5	58.5 (55.3)	6.4 (8.3)	6.4 (5.9)
17	5.63	82.6	59.3 (61.3)	5.4 (11.8)	7.9 (8.9)
avrg.	–	–	60.4 (82.9)	5.6 (13.9)	8.6 (11.8)

TABLE I

TX-RX DISTANCE d, PATH LOSS PL AND TOA PARAMETERS FOR RX LOCATIONS 1-17, LOS AND (OLOS). ITALICIZED OLOS VALUES ARE DISCARDED (SEE SECTION II-C).

and varies within 5.9 ns and 16.8 ns for the OLOS case. The overall average value of $\overline{\tau}_{\mathrm{rms}}$ moderately increases from 8.6 to 11.8 ns (corresponding to a relative increase of 37%) when the line-of-sight is obstructed. A relationship between $\overline{\tau}_{\mathrm{rms}}$ and d or PL could not be observed. Fig. 8 shows the cumulative distribution of τ_{rms} and τ_{m} for LOS and OLOS. We see that values of up to 24 ns and 30 ns can arise for the delay spread and the mean excess delay, respectively. One has to be careful when comparing investigated TOA parameters with values in other publications. In many cases, the 60 GHz channel has been measured by means of highly directional antennas [8], [5]. But it is well-known that the radiation patterns and polarizations of the applied antennas have a significant influence on these channel characteristics in the millimeter wave band [9]. In [6], 60 GHz indoor propagation has been investigated in different rooms and buildings with vertically polarized omnidirectional antennas. The delay spread values

determined for the office environment are comparable to our results for in-cabin propagation. This is in accordance with [10], where wideband measurements results for a short haul aircraft are analyzed. As the used frequency was 2150 MHz, the delay spread values cannot be compared to the 60 GHz results. However, the authors conclude that τ_{rms} in an aircraft cabin behaves similar as in an office environment.

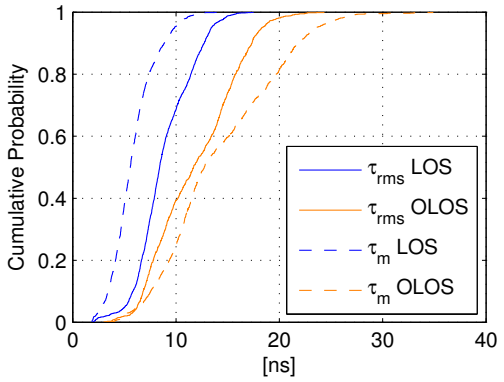

Fig. 8. Cumulative distribution of RMS delay spread and mean excess delay for line-of-sight and obstructed line-of-sight.

F. Coherence Bandwidth

An important measure to characterize the time-dispersive channel in the frequency domain is the frequency correlation function (FCF) $\Phi(\Delta f)$. We derived $\Phi(\Delta f)$ from the frequency response $H(f)$ (Fourier transform of $h(\tau)$) as

$$\Phi(\Delta f) = \int_{-\infty}^{\infty} H(f)H^*(f+\Delta f)df, \qquad (9)$$

where Δf is the frequency shift, and we define the coherence bandwidth $B_{\mathrm{coh},0.9}$ as the frequency shift for which the correlation level of the averaged FCF (average of the FCFs of a small-scale set) falls below 0.9. Related investigations result in the following approximate relationship between coherence bandwidth and the average delay spread, which is valid for the LOS as well as for the OLOS case:

$$B_{\mathrm{coh},0.9} \approx \frac{1}{\alpha_{\mathrm{coh}} \cdot \overline{\tau}_{\mathrm{rms}}} \quad \text{with} \quad \alpha_{\mathrm{coh}} = 13.5. \qquad (10)$$

In literature also other correlation thresholds like $\frac{1}{e}$, 0.5 or 0.7 are used to define the coherence bandwidth. It shall be mentioned that a relationship like (10) could not be found for those lower-value definitions.

IV. Conclusion

In this paper, the results of a measurement campaign regarding the 60 GHz short range in-cabin channel have been presented. A strong clustering phenomenon could be observed and the characteristics of the channel vary significantly within the propagation environment.

The utilization of highly directional antennas and circular polarization are effective methods to reduce multipath propagation [9]. This might be important with regard to the design of simple transmission systems, but suchlike systems fail under OLOS conditions. The usage of omnidirectional or low directional antennas seems to be more promising for practical purposes, because such a system can take advantage of multipath propagation. In the investigated scenario, arriving multipath power limits the total power loss due to obstruction to 12 dB, whereas the value is below 5.8 dB in 50% of the cases. Concerning the delay spread, the in-cabin channel seems to behave similar to indoor-channels in office environments. In order to avoid degradations due to intersymbol interference, an in-cabin system is to cope with delay spreads of up to 24 ns. Mean excess delays of up to 30 ns are to be considered.

In view of the extreme average values in Table I (Rx loc. 4, OLOS and Rx loc. 13, LOS) together with (10), the carrier separation of a multicarrier transmission system is to be below $(13.5 \cdot 16.8\ \mathrm{ns})^{-1} \approx 4.4$ MHz to obtain nearly frequency-flat parallel channels. On the other hand, frequency diversity can be exploited by involving carriers with a separation much greater than $(13.5 \cdot 3.4\ \mathrm{ns})^{-1} \approx 21.8$ MHz. A pass loss exponent of $n = 1.65$ has been derived, which is also to be considered with regard to interference in a cellular system architecture.

Acknowledgment

The authors would like to thank the Airbus Deutschland GmbH for friendly supporting the in-cabin channel measurements.

References

[1] A. Saleh and R. Valenzuela, "A statistical model for indoor multipath propagation," *Selected Areas in Communications, IEEE Journal on*, vol. 5, no. 2, pp. 128–137, 1987.

[2] R.-M. Cramer, R. Scholtz, and M. Win, "Evaluation of an ultra-wide-band propagation channel," *Antennas and Propagation, IEEE Transactions on*, vol. 50, no. 5, pp. 561–570, 2002.

[3] D. Cassioli, M. Win, and A. Molisch, "The ultra-wide bandwidth indoor channel: from statistical model to simulations," *Selected Areas in Communications, IEEE Journal on*, vol. 20, no. 6, pp. 1247–1257, 2002.

[4] M. Feuerstein, K. Blackard, T. Rappaport, S. Seidel, and H. Xia, "Path loss, delay spread, and outage models as functions of antenna height for microcellular system design," *Vehicular Technology, IEEE Transactions on*, vol. 43, no. 3, pp. 487–498, 1994.

[5] C. Anderson and T. Rappaport, "In-building wideband partition loss measurements at 2.5 and 60 ghz," *Wireless Communications, IEEE Transactions on*, vol. 3, no. 3, pp. 922–928, 2004.

[6] T. Zwick, T. Beukema, and H. Nam, "Wideband channel sounder with measurements and model for the 60 ghz indoor radio channel," *Vehicular Technology, IEEE Transactions on*, vol. 54, no. 4, pp. 1266–1277, 2005.

[7] H. Xu, V. Kukshya, and T. Rappaport, "Spatial and temporal characteristics of 60-ghz indoor channels," *Selected Areas in Communications, IEEE Journal on*, vol. 20, no. 3, pp. 620–630, 2002.

[8] R. Davies, M. Bensebti, M. Beach, and J. McGeehan, "Wireless propagation measurements in indoor multipath environments at 1.7 ghz and 60 ghz for small cell systems," in *Vehicular Technology Conference, 1991. 'Gateway to the Future Technology in Motion', 41st IEEE*, 1991, pp. 589–593.

[9] T. Manabe, Y. Miura, and T. Ihara, "Effects of antenna directivity and polarization on indoor multipath propagation characteristics at 60 ghz," *Selected Areas in Communications, IEEE Journal on*, vol. 14, no. 3, pp. 441–448, 1996.

[10] N. Diaz and J. Esquitino, "Wideband channel characterization for wireless communications inside a short haul aircraft," in *Vehicular Technology Conference, 2004. VTC 2004-Spring. 2004 IEEE 59th*, vol. 1, 2004, pp. 223–228 Vol.1.

4.4 In-Car Measurements

In this Section, the suitability of 60 GHz transmission is investigated for a further in-vehicle use case, namely for wireless distribution of multi-media content inside a car. Compared to the conference room and the aircraft in-cabin environment investigated in the previous sections, the car cabin represents a very small enclosed space, and the required link distance does not exceed 2 m. In the measurement campaign, different antenna arrangements were considered, related to rear seat entertainment, ceiling-mounted display, front-seat passenger display and consumer electronic devices communication. Moreover, various propagation conditions with and without passengers, closed and open doors, outside and inside a garage were taken into account.

The results show that the in-car channel declines significantly faster than a typical indoor channel and the DS is much lower. Neither the surrounding environment nor the conditions of the doors have a relevant influence on the channel. Passengers only affect the channel if they obstruct the LOS. An arrangement with aligned antennas always outperforms an indirect transmission relying on multipaths only.

Based on quite conservative assumptions, a sufficiently large SNR can be achieved to support a high data rate link, even under the poorest channel conditions that occurred during the measurement campaign. Interference from other cars (using a comparable system in the same band) is noncritical under relaxed traffic conditions, but can become a limiting factor for crowded urban scenarios.

To the authors' knowledge, the following work was the first publication that addressed mm-wave transmission in a car based on measurements.

Contribution

The in-car measurement campaign was planned by me, based on background information provided by J. Hillebrand, and conducted jointly by R. Felbecker and myself. I analyzed the data and derived the results. The text of this paper was authored by me. I created Fig. 4–7. Fig. 1–3 and Fig. 8 were provided by J. Hillebrand and edited by W. Keusgen based on my suggestions.

Measurement-Based Investigation of 60 GHz Broadband Transmission for Wireless In-Car Communication

Michael Peter, Robert Felbecker and Wilhelm Keusgen
Fraunhofer-Institut für Nachrichtentechnik,
Heinrich-Hertz-Institut
Einsteinufer 37, 10587 Berlin, Germany
E-mail: michael.peter@hhi.fraunhofer.de

Joachim Hillebrand
BMW Group Research and Technology
Hanauer Straße 46, 80788 Munich, Germany
E-mail: Joachim.Hillebrand@bmw.de

***Abstract*—In this paper we investigate the 60 GHz in-car wideband radio channel to assess the feasibility of 60 GHz high bit rate radio communication inside a car. The investigations are based on a measurement campaign comprising different application-oriented transmission scenarios and propagation conditions. We analyze the channel gain, time dispersion and frequency selectivity. Finally, we derive the achievable signal-to-noise ratio and cover interference aspects.**

I. Introduction

Today, premium class cars are equipped with a multitude of electronic entertainment and infotainment devices like DVD players, in-car-TV, navigation systems, cameras etc. Those devices are typically connected to each other via the automotive cable harness consisting of wires for various bus systems and point-to-point links. The cable harness in current vehicles has a significant weight that may exceed 30 kg. In particular, when utilizing higher bit rates for the data communication, this figure would even grow further due to necessary cable shielding and bulkier connectors. It becomes evident that a reduction of CO_2 emissions in cars can also be achieved by utilizing alternative ways of data communication within the vehicle.

Future broadband 60 GHz systems are supposed to operate in the unlicensed band from 57 to 64 GHz and are a candidate for wireless indoor [1] and in-cabin [2] high speed internet access as well as real-time video streaming. It is well known that the channel characteristics strongly depend on the propagation environment [3]. Results in the literature mostly refer to 60 GHz indoor channels [4]. Very few results are available for more specific scenarios like aircraft cabins [2]. To the authors' knowledge the millimeter wave in-car channel has not been considered yet. In this paper we thoroughly investigate the 60 GHz in-car wideband radio channel on the basis of measurement results for a Sport Utility Vehicle (SUV) to assess the feasibility of 60 GHz high bit rate radio communication inside a car.

II. Channel Measurement Campaign

The Head Unit (HU) is the central communication platform in a car comprising functions like radio tuner, MP3 player, navigation system, DVD drive, telephone etc. and would be the most promising component to integrate the 60 GHz wireless system as well. It is typically located behind the front panel. Therefore, the transmit antenna was mounted perpendicularly to the front panel for the measurements (see Figs. 1–3). Since various application scenarios are of interest for in-car communication, several arrangements of the receive antenna have been considered according to Figs. 1–3. The arrows and the silhouettes indicate the orientation and the pattern of the antennas, respectively. Open-ended waveguides served as antennas at both sides. Their gain of approx. 8 dBi and their pattern are quite representative for a planar antenna which would be well suited for the in-car usage case. Scenario A/B, C, D and E refer to Rear Seat Entertainment (RSE), ceiling-mounted display, front-seat passenger display and consumer electronic devices communication, respectively. It should be noted that the antennas were not supposed to be perfectly aligned. The orientation of the Tx antenna was not changed for different Rx antenna positions, and realistic losses due to misalignment and polarization mismatch arise. In the presented cases, the polarization was (more or less) vertical. There is a direct Line-of-Sight (LOS) between the Tx and the Rx antenna for Scenario A, C and D if the car is empty (no passengers are present). If the LOS is blocked by a person or an object, this is denoted as Obstructed-Line-of-Sight (OLOS) in the following. An alternative antenna configuration to Scenario A for RSE is considered by Scenario B. In this case, the Rx

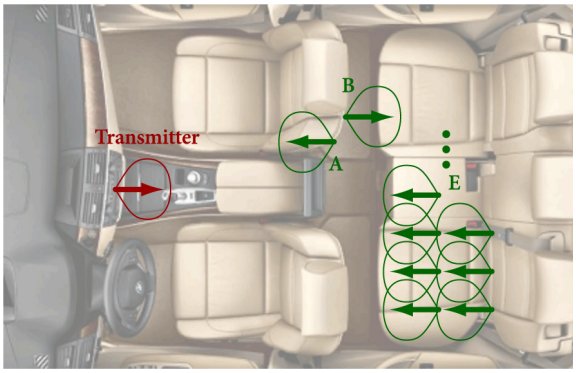

Fig. 1. Antenna arrangement for Scenario A, B and E – top view.

Fig. 2. Antenna arrangement for Scenario A and C – side view.

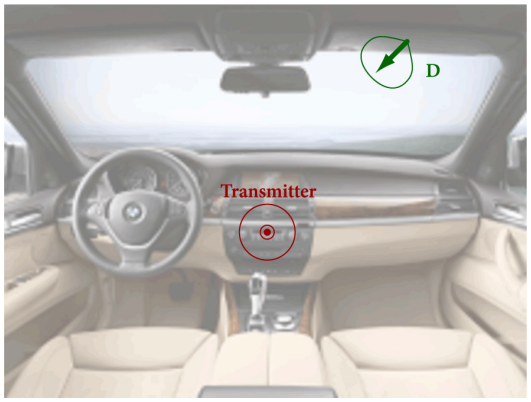

Fig. 3. Antenna arrangement for Scenario D – front panel view.

antenna points in the opposite direction of the HU to the rear window resulting in non-line-of-sight-like propagation conditions (denoted with NLOS). A transmission based on this antenna arrangement, relies on multipath power only.

In order to analyze the influence of varying propagation conditions and the environment, we carried out measurements with and without passengers, closed and open doors, outside and inside a garage for different scenarios. The outside measurements were carried out at center of a 18 m×9 m parking yard surrounded by buildings on three sides. Additional meausurements were performed to investigate the influence of interference from a 60 GHz wireless system in another car.

A Rohde & Schwarz ZVA24 vector network analyzer with self-developed frequency extension modules was used to gather bandpass Channel Frequency Responses (CFRs) from $f_{\min} = 50$ GHz to $f_{\max} = 72$ GHz at 5501 sampling points.

III. In-Car Channel Investigations

A. Channel Gain

Fig. 4 shows an exemplary bandpass CFR $H_{\mathrm{BP}}(f)$ (solid line) referring to Scenario A together with the channel gain G_C (dashed line). G_C is calculated on the basis of the equivalent

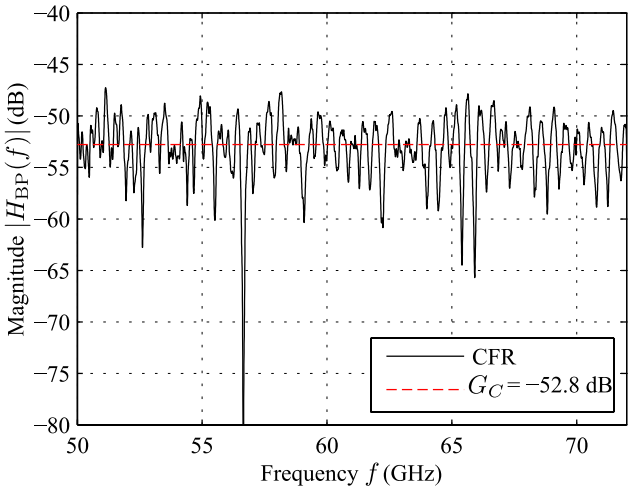

Fig. 4. CFR for Scenario A ($f > 0$).

lowpass CFR $H(f)$ as

$$G_C = \frac{1}{B} \int_{-\frac{B}{2}}^{\frac{B}{2}} |H(f)|^2 \, df, \tag{1}$$

where $B = f_{\max} - f_{\min} = 22$ GHz. The equivalent lowpass Channel Impulse Response (CIR) $h(\tau)$ is obtained by inverse Fourier transform of $H(f)$. For the following illustrations and evaluations, Kaiser-windowing with parameter $\beta = 6$ was performed in the frequency domain to reduce the sidelobes in the time domain. The resulting CIR is denoted by $h_w(\tau)$. Fig. 5 shows the CIR corresponding to the CFR in Fig. 4.

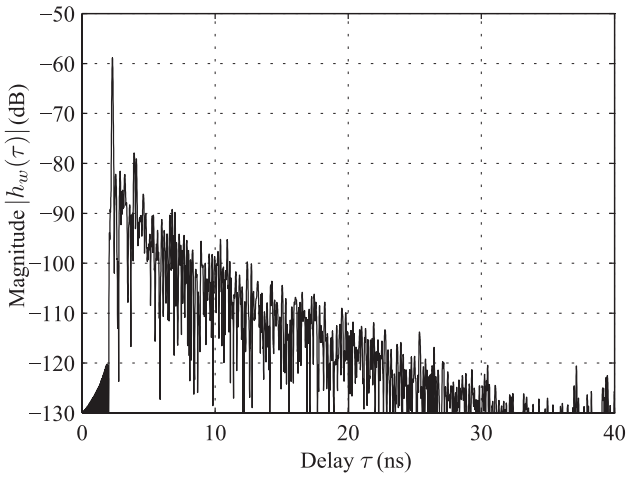

Fig. 5. CIR for Scenario A2

B. Time Dispersion and Frequency Selectivity

It reveals that the transmission is affected by multipath propagation due to reflections at the vehicle structure and the interior. At a delay of 2.3 ns the LOS path is visible with a magnitude of approx. −59 dB. It is followed by a large number of multipath components. However, their strength declines quickly with respect to the delay. After 27 ns they

already fall below −60 dB relative to the LOS component. This comparatively small time dispersion results in moderate frequency selectivity of the channel (see Fig. 4). However, there is also a very deep fade at 56.7 GHz in this case.

To quantify the time dispersion of the channel, we derive the Root-Mean-Square (RMS) delay spread from each CIR as

$$\tau'_{\mathrm{rms}} = \sqrt{\frac{\int_0^{\tau'_{\max}} \tau_e^2 \cdot |h_w(\tau_e)|^2 \, d\tau_e}{\int_0^{\tau'_{\max}} |h_w(\tau_e)|^2 \, d\tau_e} - (\tau'_{\mathrm{m}})^2} \tag{2}$$

with

$$\tau'_{\mathrm{m}} = \frac{\int_0^{\tau'_{\max}} \tau_e \cdot |h_w(\tau_e)|^2 \, d\tau_e}{\int_0^{\tau'_{\max}} |h_w(\tau_e)|^2 \, d\tau_e}. \tag{3}$$

τ_e, τ'_{m} and $\tau'_{\max}$ denote excess delay (delay at which the CIR exceeds a threshold of −40 dB relative to the strongest component for the first time), mean excess delay and maximum excess delay, respectively. Multipath components beneath the threshold were discarded.

The characterization of frequency coherence/selectivity is based on the Frequency Correlation Function (FCF)

$$R'_H(\Delta f) = \int_{-\frac{B}{2}}^{\frac{B}{2}} H(f) H^*(f + \Delta f) \, df. \tag{4}$$

We define the coherence bandwidth $B'_{\mathrm{coh},0.9}$ as the frequency shift where $\frac{|R'_H(\Delta f)|}{|H(f)|^2}$ falls below 0.9 (for the first time). Similarly $B'_{\mathrm{coh},0.5}$ is defined as the shift where the level falls (and remains) below 0.5.[1]

The values for G_C, τ'_{rms}, $B'_{\mathrm{coh},0.9}$ and $B'_{\mathrm{coh},0.5}$ are given in Table I. The channel gain is −52.8 dB for Scenario A (w/o passengers, LOS). As expected, the G_C is much smaller for Scenario B since the Rx antenna is not aligned to the Tx. Since, according to Fig. 5 (Scenario A), the strength of the LOS component in the CIR is significantly larger than subsequent multipaths, and as the power decays quickly with respect to the delay, τ'_{rms} is very low compared to indoor and in-cabin measurement results, where delay spreads between 5 and 30 ns typically occur for LOS channels in small environments [4], [2]. Even for Scenario B only a value of 3.5 ns arises. The low time dispersion is also reflected in the coherence bandwith values. $B'_{\mathrm{coh},0.9}$ and $B'_{\mathrm{coh},0.5}$ are 255 MHz and 5.66 GHz, respectively.

C. Influence of Passengers

In order to investigate the impact of passengers on in-car wave propagation, the measurements were repeated with an occupied car (4 passengers). Fig. 6 shows the comparison of the CIRs without and with passengers for Scenario A. We see that the strength of the LOS path is considerably decreased in this case. Although not intended, the front-seat passenger had an impact on the LOS path in a normal sitting position, since his shoulder was very close to the Rx antenna. Furthermore, additional attenuation of multipaths occurs, resulting in a slightly faster decay of the CIR. The channel gain drops from −53 to −60 dB. $B'_{\mathrm{coh},0.9}$ and $B'_{\mathrm{coh},0.5}$ decrease by a factor of approx. 3.2 and 1.5, respectively. The influence of passengers on the channel gain is less severe for Scenario B: G_C decreases from −69.1 to −71.2 dB. There is no influence on the channel gain for Scenario C and D at all. Only small variations of τ'_{rms}, $B'_{\mathrm{coh},0.9}$ and $B'_{\mathrm{coh},0.5}$ can be observed. These results show that passengers only have a significant impact on in-car wave propagation if they reduce the quality of the LOS or if an indirect tranmission is considered, solely relying on multipath contributions.

Although millimeter wave systems are usually proposed for LOS transmission, it is obvious that severe blockage of the LOS can occur quite frequently. In view of this problem, it is essential to investigate the OLOS case to assess the consequences on the received signal. The values in Table I

[1]We would like to remark that we derive an FCF for a static channel from a single measurement by calculating the autocorrelation function of $H(f)$. Referring to [5], this departs from the frequency correlation definition and the FCF of randomly time-varying channels. A static channel is fully described by its CIR or its CFR, and a correlation function is not needed in principle. However, a coherence bandwith definition based on $R'(\Delta f)$ is still a useful measure to quantify the frequency selectivity of a channel for comparison reasons.

TABLE I
CHANNEL GAIN, DELAY SPREAD AND COHERENCE BANDWIDTH WITHOUT AND WITH PASSENGERS FOR SCENARIOS A, B, C AND D.

Scenario	G_C (dB)	τ'_{rms} (ns)	$B'_{\mathrm{coh},0.9}$ (MHz)	$B'_{\mathrm{coh},0.5}$ (GHz)
A w/o passengers, LOS	−52.8	0.57	255	5.66
A with passengers, LOS	−59.9	1.18	79.4	3.77
A with passengers, OLOS	−68.9	1.33	52.3	2.19
B w/o passengers, NLOS	−69.1	3.50	21.4	0.0619
B with passengers, NLOS	−71.2	2.91	26.1	0.0854
C w/o passengers, LOS	−51.6	0.58	407	4.67
C with passengers, LOS	−51.8	0.34	558	4.98
C with passengers, OLOS	−70.5	1.88	39.7	0.239
D w/o passengers, LOS	−52.5	0.75	864	5.15
D with passengers, LOS	−52.6	0.65	831	5.34
D with passengers, OLOS	−65.7	1.68	53.4	0.448

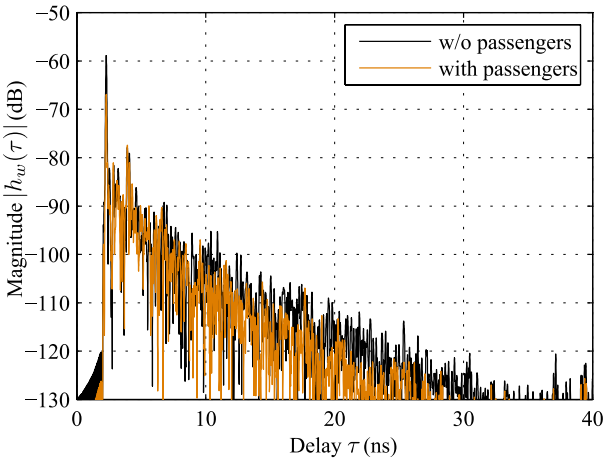

Fig. 6. CIRs for Scenario A with and without passengers, outside garage, closed doors.

(OLOS) reveal a severe impact of human body shadowing on the channel gain, time dispersion and frequency selectivity. G_C additionally decreases by 9 dB compared to the case with already limited LOS. The losses for Scenario C and D are approx. 19 and 13 dB, respectively.

Fig. 7 shows a comparison of the CIR for Scenario A under OLOS conditions and the CIR for Scenario B (with passengers). Early arriving multipaths are highly attenuated in both cases. Besides an offset in the delay, the CIRs are quite similar. However, since there is a stronger path for Scenario A CIR at 4 ns delay, G_C is still more than 2 dB larger (-68.9 dB compared to -71.2 dB). We conclude that an arrangement with aligned antennas outperforms an indirect transmission relying on multipaths, even if the LOS is obstructed. Moreover, when there is LOS between Tx and Rx antenna, which is assumed to be the normal case, the receiver can utilize a 11–16 dB higher power.

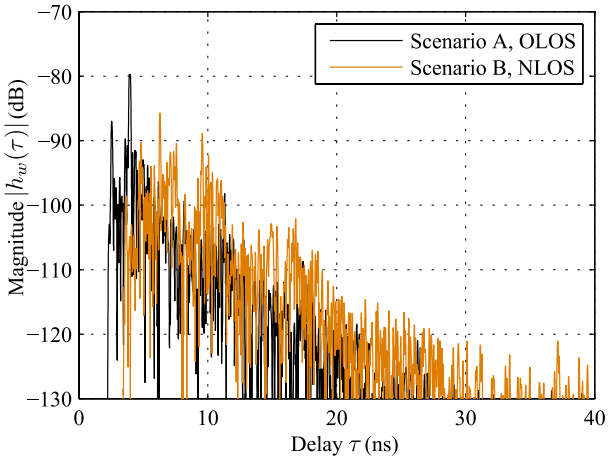

Fig. 7. CIR for Scenario A, OLOS compared to CIR for Scenario B (NLOS).

D. Influence of the Environment

Multipath components can arise from reflections at the car body, the interior, the windows and the outer environment. To analyze the influence of the surrounding, we performed additional measurements for Scenario B inside a 5.9 m×5.5 m×2.2 m garage with a steel wall cupboard at the rear of the car. Since there is no direct path for this scenario, we expect the impact to be most significant compared to the other scenarios. Further, we repeated the measurements with all four car doors open, which can be assumed to be the extreme case for one or more open windows or doors. The influence of the doors was also considered for Scenario C and D. The results are summarized in Table II. It is clearly evident from all the measures that neither the environment nor the conditions of the doors have a significant influence for the considered antenna arrangements. G_C remains practically constant. Only slight changes occur for τ'_{rms}, $B'_{\mathrm{coh},0.9}$ and $B'_{\mathrm{coh},0.5}$.

TABLE II
CHANNEL GAIN, DELAY SPREAD AND COHERENCE BANDWIDTH: COMPARISON OUTSIDE AND INSIDE GARAGE / CLOSED AND OPEN DOORS.

Scenario	G_C (dB)	τ'_{rms} (ns)	$B'_{\mathrm{coh},0.9}$ (MHz)	$B'_{\mathrm{coh},0.5}$ (GHz)
B inside, closed doors	−69.7	4.07	18.7	0.0526
B outside, closed doors	−69.7	3.67	20.4	0.0586
B inside, open doors	−69.7	4.05	18.8	0.0536
B outside, open doors	−69.9	3.49	21.4	0.0619
C outside, closed doors	−51.6	0.58	407	4.67
C outside, open doors	−51.6	0.52	394	4.73
D outside, closed doors	−52.5	0.75	864	5.15
D outside, open doors	−52.5	0.62	888	5.19

E. Scenario E: Consumer Electronic Devices

The motivation for Scenario E is to establish a wireless connection to consumer electronic devices like laptops or MP3 players. To investigate the achievable coverage of the rear seats, 20 Rx measurement positions at a height of approx. 30 cm above the seat have been considered. In all cases, the antenna pointed towards the front of the car (perpendicular to the seat back). Thus realistic propagation conditions have been achieved. Fig. 8 illustrates the results for the channel gain. High values arise at some locations near the middle of the seat with LOS conditions. However, in most of the cases the LOS was obstructed by the driver's, the front passenger seat or by the screen on the center console (see Fig. 8). Although the scenario is symmetric, the channel gain values are not. The reason is that there are only small gaps of few centimeters between the seats and the screen. Therefore, slight differences in the antenna position and orientation could cause completely different propagation conditions. G_C varies from -72.6 dB to -51.3 dB. These values also define the extreme values for all considered scenarios.

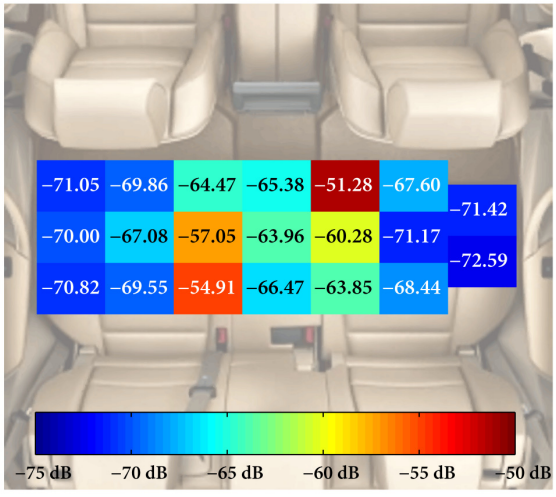

Fig. 8. Scenario E – Back seat coverage analysis: Color-coded values for the channel gain G_C at 20 Rx positions.

IV. Signal-to-Noise Ratio

As the in-car channel has been found to be only little up to moderately frequency selective, the achievable mean Signal-to-Noise Ratio (SNR) can serve as a simple initial measure to evaluate the feasibility and the performance of a 60 GHz in-car broadband link. We estimate the SNR on the basis of the channel gains as

$$\mathrm{SNR}_{|\mathrm{dB}} = P_{T|\mathrm{dBm}} + G_{C|\mathrm{dB}} - P_{\mathrm{th}|\mathrm{dBm}} - \mathrm{NF}_{|\mathrm{dB}}, \quad (5)$$

where P_T, P_{th} and NF denote transmit power, thermal noise power and receiver noise figure, respectively. With regard to a future broadband system, we assume P_T to be 10 dBm (according to regulations for worldwide operation), P_{th} to be -83.9 dBm (based on 1 GHz system bandwidth and a temperature of 293 K) and NF to be 6 dB. The investigations in Section III revealed that a channel gain between -72.6 dB and -51.3 dB can be expected, taking account of all considered scenarios and propagation conditions. With (5) and the above assumptions, these values transform to an SNR in the range from 15.3 dB (worst case with severe shadowing) to 36.6 dB (best case with free LOS). Even if degradations due to analog frontend imperfections (nonlinearities, phase noise) and implementation losses are to be considered for a practical system, the achievable mean SNR and the low time dispersion are a promising basis for 60 GHz high data rate in-car communication. Nevertheless, with regard to a wideband system utilizing a bandwidth of several hundreds of MHz or even more, we note that it is indispensable to compensate even for the low dispersion by channel equalization. Otherwise an error floor due to intersymbol interference will arise.

V. Interference

As a bandwidth of up to 7 GHz is available in the millimeter wave band, spectral efficiency is not a crucial design aspect in general. It is more important to find specific solutions taking account of power consumption and production costs. The consequence is that several GHz of bandwidth could be allocated by an in-car system. Since situations can occur, where numerous cars are located inside a small area (junctions, parking areas, traffic jams), interference could become a crucial issue. Therefore, we carried out interference measurements for two different car arrangements: cars side by side (Interference Scenario 1 – IS 1) and one behind the other (IS 2). The setup was always arranged in such a way that the transmitter (interferer) radiated into the direction of the car with the receiver. In Table III the results for the interference channel gain G_I and the Signal-to-Interference Ratio (SIR) estimated by

$$\mathrm{SIR} = 10 \cdot \log\left(\frac{G_C}{G_I}\right) \quad (6)$$

are summarized. It reveals that the SIR is highly dependent on the considered scenario. It varies between 23.5 and 47 dB for the measured cases. It is important to note that only one interferer is considered in these calculations. In extreme situations, a couple of relevant interferers could give rise to significantly lower values of the SIR. We conclude that in most usual cases the performance of a 60 GHz wireless system will mainly depend on the condition of the in-car channel (SNR, frequency selectivity) rather than on the interference. However, if numerous cars equipped with similar systems are located close to each other, the transmission might be interference-limited.

TABLE III
Interference channel gain G_I and SIR for IS 1 and IS 2 (no passengers, outside garage, closed doors).

	G_I (dB)		SIR (dB)	
Scenario	IS 1	IS 2	IS 1	IS 2
A w/o passengers, LOS	−99.8	−89.8	47.0	37.0
B w/o passengers, LOS	−93.2	−99.6	23.5	29.9
C w/o passengers, LOS	−98.3	−91.4	46.6	39.7
D w/o passengers, LOS	−90.1	−95.5	37.7	43.0

VI. Conclusion

In this paper, we presented major results of a measurement campaign in an upper class SUV regarding the 60 GHz in-car radio channel. It revealed that the time dispersion is low ($0.57\ \mathrm{ns} \leq \tau'_{\mathrm{rms}} \leq 4.1\ \mathrm{ns}$) compared to indoor channels and that neither the environment nor the conditions of the doors have a significant influence on the in-car wave propagation. Passengers do not have a relevant impact as long as they do not obstruct the LOS. An antenna arrangement with aligned antennas outperforms an indirect transmission relying on multipaths, even if the LOS is obstructed. The channel gain is high enough to achieve a mean SNR of approx. 15 dB in worst case situations (OLOS). Even more than 36 dB can be utilized under best-case LOS conditions. We conclude that 60 GHz is a promising approach for broadband wireless in-car communication and that a reliable indoor system will also work for the in-car environment. Interference is not an issue for relaxed traffic conditions, but might be a limiting factor for crowded urban scenarios.

References

[1] P. Smulders, "Exploiting the 60 GHz band for local wireless multimedia access: prospects and future directions," *Communications Magazine, IEEE*, vol. 40, no. 1, pp. 140–147, 2002.

[2] M. Peter, W. Keusgen, and M. Schirrmacher, "Measurement and analysis of the 60 GHz in-vehicular broadband radio channel," in *Vehicular Technology Conference, 2007. VTC 2007-Fall. 2007 IEEE 66th*, Sep.–Oct. 2007.

[3] H. Yang, M. Herben, and P. Smulders, "Impact of antenna pattern and reflective environment on 60 GHz indoor radio channel characteristics," *Antennas and Wireless Propagation Letters*, vol. 4, pp. 300–303, 2005.

[4] H. Xu, V. Kukshya, and T. Rappaport, "Spatial and temporal characteristics of 60-GHz indoor channels," *Selected Areas in Communications, IEEE Journal on*, vol. 20, no. 3, pp. 620–630, 2002.

[5] R. Bultitude, "Estimating frequency correlation functions from propagation measurements on fading radio channels: a critical review," *Selected Areas in Communications, IEEE Journal on*, vol. 20, no. 6, pp. 1133–1143, 2002.

4.5 Human Body Shadowing Analysis and Modeling

Besides the evaluation of LOS channels, several investigations were carried out in the previous sections, which refer to OLOS conditions. As shown in Section 4.1, multipath power can limit the power loss caused by an absorber mat to a value of around 10 dB, so that the loss is only slightly larger than at 5 GHz. Similarly, the attenuation caused by HBS did not exceed 12 dB in the aircraft cabin (see Section 4.3). The influence on the LOS component is typically much more severe. The conference room measurements revealed that the attenuation caused by an absorber mat is significantly larger than that caused by a human body. Since both are impenetrable for mm-waves, the difference can only be explained by diffraction effects.

In this Section, the influence of HBS on the LOS component and related diffraction phenomena are analyzed in detail based on dedicated measurements. Different modeling approaches are assessed with respect to their accuracy to match and predict the measured behavior. The results clearly show that—on a fine time scale—the power of the LOS path does not disappear abruptly, but diffraction around a person is significant, resulting in a continuous increase in attenuation during the transition from LOS to OLOS. The superposition of diffracted waves from both edges of the body leads to strong oscillations during the shadowing event. Characteristic oscillations can even be observed before the person reaches the geometric LOS connecting line. This can be highly valuable to predict a shadowing event and prepare the system for an imminent drop of power or to take suitable countermeasures in time.

As shown in the paper, a distance-dependent piecewise linear model can be used to match the measured attenuation curves in a large-scale sense, but it does not account for the oscillations. All effects can be modeled by a double knife-edge (DKE) model or a (more complex) UTD model. In the latter case, the body is represented by a perfectly conducting cylinder-–an assumption, which is supported by the findings in [JPK+13b]. Quantitative comparisons in the following publication show that the DKE model tends to underestimate the HBS-induced attenuation, whereas the UTD model tends to overestimate. However, all three approaches are principally suitable for expanding existing channel models (deterministic or stochastic) by time-variant HBS effects.

Though the measurements were conducted in a conference room, it is important to note that the results are not environment-specific, since the investigations are related to an individual propagation path (here: the LOS path). Making use of the measurement results and conclusions from [JPK+13b], an extension and a holistic validation of the IEEE 802.11ad 60 GHz human blockage model has been presented by Jacob et al. [JPK+13a]. It is based on a multiple knife-edge model and takes into

account interactions with multiple persons. In [WPK+16b], the DKE model has also recently been confirmed to provide a good prediction of shadowing events caused by pedestrians in an outdoor access scenario at 28 GHz.

Contribution

This paper was authored by me. I planned the measurement campaign, processed the data and made the overall analysis. The measurements were conducted jointly by M. Wisotzki and myself. Under my supervision, M. Raceala-Motoc derived the parameters for the piecewise linear model, implemented the UTD model and generated the simulation data. The co-authors from Technische Universität Braunschweig supported the work by providing initial UTD simulation data and their own UTD implementation, which has been used to validate the results.

Analyzing Human Body Shadowing at 60 GHz: Systematic Wideband MIMO Measurements and Modeling Approaches

Michael Peter, Mike Wisotzki, Miruna Raceala-Motoc, Wilhelm Keusgen and Robert Felbecker
Fraunhofer Heinrich Hertz Institute
Berlin, Germany
michael.peter@hhi.fraunhofer.de

Martin Jacob, Sebastian Priebe and Thomas Kürner
Technische Universität Braunschweig
Braunschweig, Germany
jacob@ifn.ing.tu-bs.de

***Abstract*—This paper presents results of a systematic 2×2 MIMO channel measurement campaign, which has been carried out in order to analyze the impact of human body shadowing (HBS) on the 60 GHz wideband channel. A piecewise linear and two analytical models, namely the double knife-edge (DKE) model and a cylinder approach incorporating the uniform theory of diffraction (UTD), are used to approximate and to predict the measurement curves. We propose measures to quantify the degree of match between attenuation curves in the millimeter wave frequency band and use them to evaluate the model results with respect to different scenario groups. The presented results are beneficial to refine existing diffraction models regarding the prediction of HBS effects.**

I. Introduction

Millimeter wave transmission in the unlicensed 60 GHz band is the most promising approach to meet the requirements of next generation multi-Gbps Wireless Local Area Networks (WLANs). Despite promising progress in technology, the propagation characteristics at 60 GHz still pose a challenge with regard to marketable solutions for end-user devices. Whereas point-to-point links for high-capacity backhaul connectivity can rely on Line-of-Sight (LOS) conditions and make use of huge antenna gains in order to overcome the high path loss and limited transmit power, this is not the case for indoor systems.

It is well known that HBS at 60 GHz has a significant impact on the received power level. The effect is most severe if the direct path (LOS path) is blocked. An exemplary measurement result is presented in [1], revealing a mean attenuation of about 20 dB for HBS. The focus in [1] is to derive a model for path visibility rather than for the Shadowing Event (SE) itself. In [2] SEs as well as their occurrence are investigated. They are characterized by means of their duration, amplitude and rising time. A similar approach is presented in [3] to model the dynamics of distinct propagation paths. In [4] a modified double knife-edge model is proposed in order to approximate diffraction around a person at ultra-wideband frequencies, whereas multiple knife-edges are used in [5] at 60 GHz.

Despite available publications, HBS at 60 GHz is not fully explored yet. A closer look at the measurement results reveals significant differences. Furthermore, comparisons are difficult, since conditions, and evaluation methods differ widely. Our objective is to gain a detailed insight into the dynamics of the LOS path caused by HBS with regard to analytical models.

II. 60 GHz MIMO Measurements

A. Measurement Environment and Setup

To obtain an evaluation basis, we carried out a comprehensive systematic measurement campaign in a $11.22\,\mathrm{m} \times 5.9\,\mathrm{m}$ conference room located on the ground floor of the Fraunhofer Heinrich Hertz Institute building. Its floorplan is shown in Figure 1. A self-developed component-based 2×2 MIMO

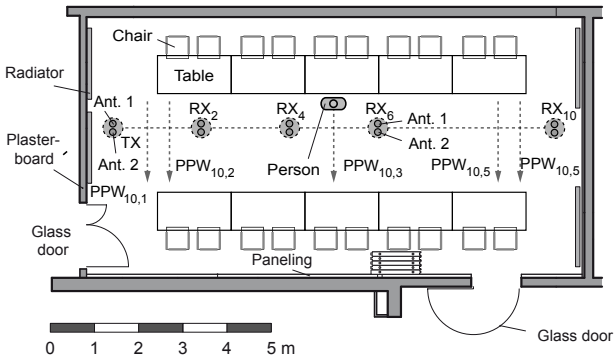

Figure 1. Floor plan of the conference room and positions of TX and RX measurement setup.

wideband channel sounder setup was used to acquire the time-varying channel on $B = 3\,\mathrm{GHz}$ bandwidth. It is a further development of the 1 GHz SISO system presented in [6].

During each measurement, a well defined SE was caused by a person walking through the LOS with a walking speed of approximately $0.5\,\frac{\mathrm{m}}{\mathrm{s}}$. To obtain reproducible results, markers had been fixed on the floor as orientation, and the movements have been synchronized with a clocking sound generated by the control laptop. The body breadth (across the shoulders) and the depth were $b_{\mathrm{body}} = 0.56\,\mathrm{m}$ and $a_{\mathrm{body}} = 0.27\,\mathrm{m}$. At the TX, omnidirectional antennas (O) ($G \approx 2\,\mathrm{dBi}$) as well as open-ended waveguides (W) ($G \approx 8\,\mathrm{dBi}$) with vertical polarization were applied in consecutive measurement runs. To investigate the dependence of shadowing effects on the transmission distance, we repeated the procedure for TX–RX distances of $d = 2$, 4, 6 and 10 m by repositioning

the RX. All antennas were fixed at a height of 1.2 m at both sides. The person inducing shadowing crossed the LOS at 5 well defined intersection points (3 points for the 2 m distance): at 0.5 and 1.0 m distance from the TX, in the middle of TX and the RX and at 1.0 and 0.5 m from the RX. These "perpendicular walks" (PPWs) are illustrated in Figure 1 regarding RX placement 10. The time between two successive CIR snapshots was approx. 9 ms for the PPWs.

The antenna spacing at the transmitter has been kept fixed at 15 cm, whereas the spacing at the RX was varied (5 cm, 15 cm and 30 cm) to collect data for evaluations on spatial/antenna diversity and correlations among the four channels. In total, 152 measurement sets are available. Each PPW set contains 512 CIRs for each channel. After each setup modification (change of the antenna and/or spacing) the system has been recalibrated to ensure maximum accuracy. The whole campaign has been documented by photos and video recordings to facilitate the interpretation of results.

B. Data Preprocessing and Result

In this paper, we focus on attenuation effects that are related to shadowing of the LOS path (direct path) during the PPWs. Hence we performed a preprocessing of the corresponding CIR data sets. The delay τ_0 and the attenuation of the LOS path without shadowing L_0 were determined on the basis of maximum search in CIRs before and after the SE.

The normalized attenuation of the LOS path in dB was then calculated as $L_{\mathrm{norm}}(t) = L(t) - L_0$, where the determination of $L(t)$ has been based on the delay window $\left[\tau_0, \tau_0 + \frac{1}{B}\right]$. By using this window, diffraction components up to excess propagation distances of 10 cm are fully taken into account. Multipath components caused by reflections at surrounding objects, walls, the floor and the ceiling are neglected, as they arrive with significantly higher excess delays.

Figure 2 shows an exemplary measurement result. Each

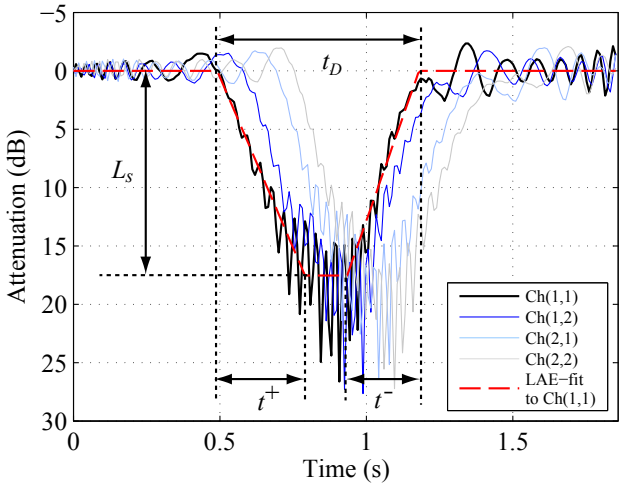

Figure 2. Attenuation of the LOS path for PP$W_{4,3}$ with OW antenna configuration and 5 cm antenna spacing at the RX.

attenuation curve corresponds to a MIMO channel. We clearly see that diffraction around the person is significant, preventing a total loss of the path and leading to oscillations within the shadowing gap, which result from superposition of diffracted waves from both sides of the body. Furthermore, characteristic oscillations are visible before and after the actual shadowing gap. The curves are not fully symmetric – an effect which has also been observed by Kunisch and Pamp [4]. The dashed lines represent a piecewise linear fit (least absolute errors in dB scale) to the attenuation curve of Ch(1,1) (channel from TX antenna 1 to RX antenna 1). The fit is useful in order to derive tangible shadowing parameters like decay time/rate, rising time/rate, duration of the shadowing event and the attenuation level in the deep shadow region. At the same time, the piecewise linear approximation represents a very simple model for the time-variant shadowing effects. More details can be modeled having regard to double knife-edge diffraction [4] or by applying the uniform theory of diffraction [7], [8]. These three approaches are considered in Section III.

III. Modeling Approaches and Evaluations

A. Piecewise Linear Model and Parameters

The piecewise linear (PWL) approximation illustrated in Figure 2 represents a simple model for the shadowing effects [3], though it is not related to a physical interpretation. The approximation has been determined by least absolute errors fitting. The attenuation in dB scale is modeled by a period with linear increase (slope r^+), a period with a constant level L_s and a period with linear attenuation decrease (slope r^-). Setting $t_0 = 0$, it can be described by

$$L_{\mathrm{PWL}}(t)\,|_{\mathrm{dB}} = \begin{cases} r^+ \cdot t & \text{for } 0 < t \le \frac{L_s}{r^+} \\ L_s & \text{for } \frac{L_s}{r^+} < t \le t_D - \frac{L_s}{r^-} \\ L_s - r^- \cdot t & \text{for } t_D - \frac{L_s}{r^-} < t \le t_D \\ 0 & \text{else.} \end{cases} \quad (1)$$

Note that this model does not consider fluctuations in the deep shadow region.

We conducted a systematic analysis to identify deterministic dependencies by separating/grouping the data with respect to the measured scenarios. It revealed that neither the antenna type nor the TX antenna spacing has a recognizable impact on the parameter statistics. For a fixed TX–RX distance it is irrelevant whether the person crosses the LOS at a certain distance from the TX or from the RX (reciprocity). However, in accordance to diffraction models the parameters (apart from t_D) depend on the TX–RX distance and the shadowing distance. Table I summarizes the PWL model parameters with respect to each scenario group (SG), which have been determined by averaging over the values within each SG. Note that the values $r^{+/-}$ are based on L_s and the mean of the corresponding time values: $r^{+/-} = \frac{L_s}{\frac{1}{K}\sum_{k=1}^{K} t_k^{+/-}}$. L_s decreases with increasing TX–RX distance and shadowing distance. r^+ can significantly differ from r^-, meaning that the shadowing curves show an asymmetric behavior. As expected, a tendential decrease of r^+ and r^- can be observed with increasing TX–RX distance and shadowing distance.

Table I
PWL MODEL PARAMETERS WITH RESPECT TO SCENARIO GROUPS.

d (m)	Shadowing distance	Label of scenario group	t_D (s)	r^+ (dB/s)	r^- (dB/s)	L_s (dB)
2	0.5 m	SG-0205	0.57	109	119	25.4
	$\frac{(d-b_{\mathrm{body}})}{2}$	SG-02M	0.60	88.4	103	25.1
4	0.5 m	SG-0405	0.57	94.3	115	20.7
	1.0 m	SG-0410	0.63	78.8	75.4	19.4
	$\frac{(d-b_{\mathrm{body}})}{2}$	SG-04M	0.63	75.3	69.7	18.0
6	0.5 m	SG-0605	0.59	82.5	113	21.8
	1.0 m	SG-0610	0.63	71.9	66.2	17.8
	$\frac{(d-b_{\mathrm{body}})}{2}$	SG-06M	0.69	59.8	47.9	15.2
10	0.5 m	SG-1005	0.58	93.8	113	21.2
	1.0 m	SG-1010	0.61	71.8	72.6	18.7
	$\frac{(d-b_{\mathrm{body}})}{2}$	SG-10M	0.76	44.8	33.9	12.4

B. Double Knife-Edge Model

The double knife-edge (DKE) model as described in e. g. [4] regards the human body as a stripe of width w and infinite height. The total diffracted field results from the superposition of the two knife-edge fields around the stripe edges, each of them calculated separately from the field of the non-obstructed half-plane according to the Fresnel-Huygens principle. For an obstructing half-plane the resulting diffraction gain can be computed as a function of the obstruction depth and the distance to the transmitter, respectively to the receiver, on the basis of a Fresnel integral. Note that in [4] the stripe is aligned with the main body axes. Since we apply the model on the PPWs, the width of the stripe is related to the body depth (see Figure 1).

C. UTD Cylinder Model

Besides the double knife-edge model, the uniform theory of diffraction (UTD) has already been used to model human body shadowing before. In [7], [8], the UTD for a conducting circular cylinder has been proven valid for modeling the presence of a human body at 10.5 GHz. Nevertheless, the theory has not been applied to the 60 GHz range yet. Compared to the double knife-edge model, the cylinder is a better physical representation of the human body and the UTD provides a solution for both hard and soft polarization. The theory is mainly derived by Pathak et al. [9], [10]. In the shadow region, where the LOS path is blocked by the cylinder, the total field is modeled as a superposition of two so-called surface diffracted rays. One is travelling clockwise and the other one counterclockwise around the cylinder. The field strength for each of these rays can be calculated by generalized diffraction coefficients depending on the actual geometry of the problem. In the lit region, the field is composed by contributions from one reflected ray and one surface diffracted ray travelling around the cylinder. The reflected field is calculated by a generalized reflection coefficient. The solution for the diffraction and reflection coefficients is given in terms of certain special functions, namely Fock and Fresnel functions.

D. Determination of DKE and UTD Model Parameters

In our case, both the DKE model as well as the UTD have three degrees of freedom, namely the starting point y_0 of the person, the walking speed v and the depth a of the person. Though the person crossed the LOS with an approximate speed of 0.5 $\frac{\mathrm{m}}{\mathrm{s}}$, it is clear that some deviation from this value could not be avoided. Therefore, both parameters have been extracted from the measurements of the four MIMO channels for each PPW taking into consideration the geometry parameters of the measurement scenario. Here, the person is assumed as a DKE.

The time where one knife-edge reaches the direct path between TX and RX corresponds to an attenuation of 6 dB, because approximately half of the electromagnetic wave is shadowed by the person. This holds true for the 6 dB level crossings of the falling edge as well as the rising edge of the the SE. In a first step, these times have been extracted from the measurements for all four channels. The walking speed $v = \frac{\Delta y_v}{\Delta t_v}$ is then determined by the difference Δt_v between the 6 dB level crossings from Ch(1,1) and Ch(2,2) and the distance Δy_v covered by the person. This distance can be determined from the positions of the TX and RX antennas and the location of the walking path. In this case, the average walking speed over both edges has been taken.

With the knowledge of v, the depth a of the person is calculated as $a = v \cdot \Delta t_a$, where Δt_a is the mean duration of the four SEs with respect to the 6 dB level crossings. The starting point y_0 can then be determined from the 6 dB level crossings, from the parameters a and v and the scenario geometry. Here, the average over the falling edges has been used. The statistical parameters of the extracted values are summarized in Table II .

Table II
EXTRACTED PARAMETERS USED FOR DKE AND UTD CYLINDER MODEL

	mean	min	max	std
v $\left(\frac{\mathrm{m}}{\mathrm{s}}\right)$	0.51	0.41	0.61	0.046
a (m)	0.23	0.20	0.27	0.015

In average, the walking speed is practically identical to the target value and its variation is fairly low. The (effective) depth of the person a (mean value) is slightly below the actual body depth of $a_{\mathrm{body}} = 0.27\,\mathrm{m}$.

E. Results and Evaluations

Figure 3 shows a exemplary measurement result of SG-1010 together with the corresponding curves of the DKE and the UTD model. The measurement bandwidth has been considered within the models by superimposing the results for ten equidistant frequency points from 58.5 to 61.5 GHz. The DKE model slightly underestimates the attenuation, whereas the UTD yields values that are larger than the measurement result. Though the number and the position of the attenuation maxima is not perfectly predicted, the model curves show a good agreement with the measurement.

Another comparative example is illustrated in Figure 4. Similar to the first example, some deviation of both model

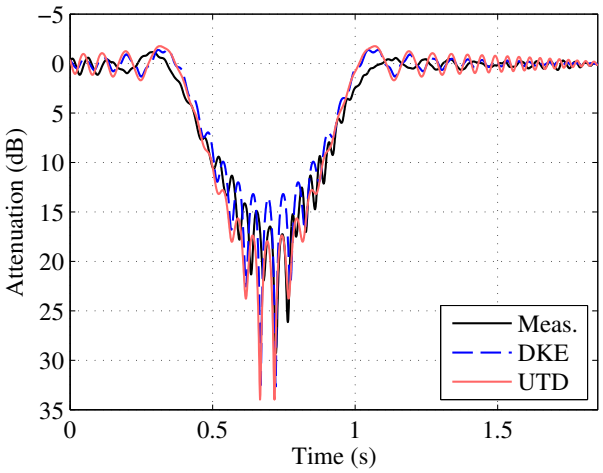

Figure 3. Measured attenuation of LOS for path for PA$W_{10,2}$ (SG-1010) together with DKE and UTD model results.

curves can be observed, especially with respect to the numer of attenuation maxima. In order to be able to make quantitative

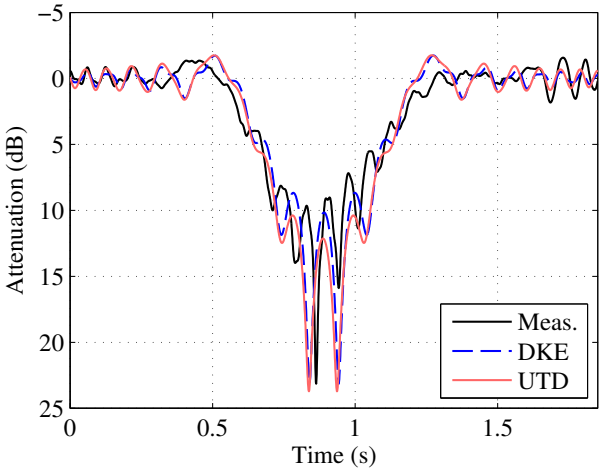

Figure 4. Measured attenuation of LOS for path for PA$W_{4,3}$ (SG-04M) together with DKE and UTD model results.

comparisons, suitable measures are needed. It is clear that it is hardly possible to achieve a full match between model and measurement curves, since both models rely on more or less coarse approximations of the human body. Furthermore, the results at 60 GHz are extremely sensitive to the actual position of the person and antenna displacements due to the small wavelength. Keeping this in mind, we evaluated various measures concerning their suitability. Some of them rely on smoothed attenuation curves (denoted by $\overline{L}(t)$) in order to disregard small deviations of the attenuation maximum positions. The measures delivering the most meaningful results are listed in Table III.

Smoothing has been performed by calculating the weighted moving average (filtering) of the original measurement/model data (linear scale) over a time interval of 72 ms using a Kaiser window with parameter $\beta = 5$. Only the data range of the

Table III
USED MEASURES FOR COMPARISON OF MODEL AND MEASUREMENT DATA

Measure	Symbol	Base data
deviation max. attenuation	DMA	smoothed
mean squared error	MSE	smoothed
deviation of pseudo period	DPP	original

shadow region itself (between the 6 dB level crossings) is used to calculate the values. We define the deviation of maximum attenuation as $\mathrm{DMA} = \max\left(\overline{L}_{\mathrm{model}}(t)\right) - \max\left(\overline{L}_{\mathrm{meas}}(t)\right)$. DMA and MSE assess the matching of the attenuation values, whereas the deviation of the pseudo period DPP quantifies the temporal evolution of the model relative to the measurement curve. It is calculated as $\mathrm{DPP} = 10\log\left(T_{P,\mathrm{model}}\right) - 10\log\left(T_{P,\mathrm{meas}}\right)$, where T_P is defined as the mean time between two adjacent attenuation maxima. We applied these measures to evaluate the "goodness of fit" with respect to the scenario groups defined in Table I and to compare the two models.

The empirical cumulative distribution functions (CDFs) of the DMA are illustrated in Figure 5. They reveal that DKE model tendentially underestimates the HBS-induced attenuation. In contrary, the UTD model clearly tends to overestimate.

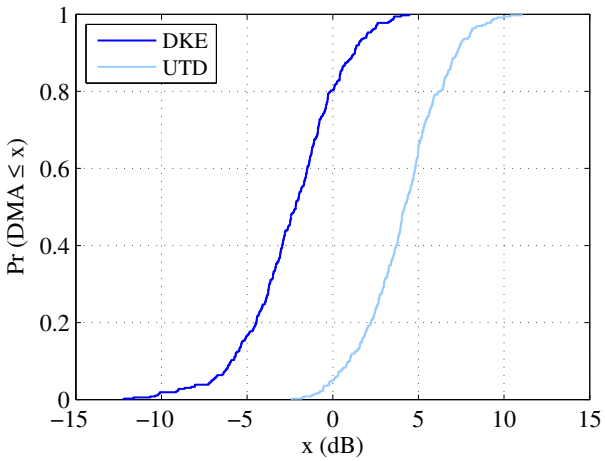

Figure 5. Empirical CDF of the DMA for DKE and UTD model.

Figure 6 illustrates the dependency on the scenario group. Whereas the DKE mean DMA is nearly −6 dB for SG-0205, the values tend to 0 dB for increasing distance and become positive for SG-06M and SG-10M (overestimation of the attenuation). Small shadowing distances result in larger deviations from the optimum value (0 dB). The UTD model yields positive values for all SGs and a clear deterministic dependence on TX–RX distance or the shadowing distance cannot be identified. It shall be noted that the mean MSE shows a very similar behavior with respect to the SGs. However, since the DMA not only provides the level of deviation, but also signed information, it is to be preferred in most cases.

The results of the DPP evaluations are illustrated in Figure 7. Again, a dependence on the SG is visible. For a TX–RX distance of 2 m (SG-0205 and SG-02M), the DKE model

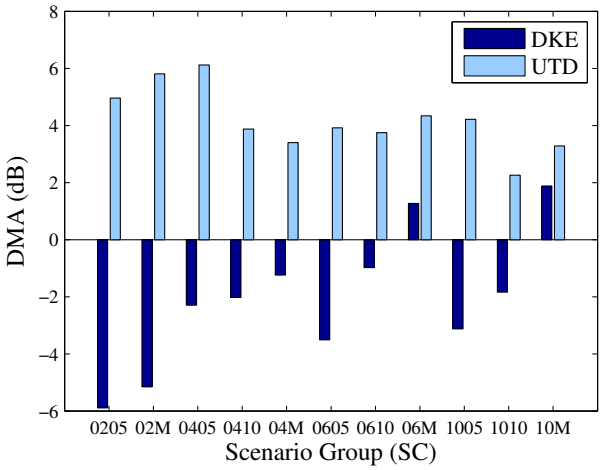

Figure 6. Mean DMA values for DKE and UTD model with respect to SGs.

delivers values above, the UTD slightly below 0 dB. For all other SGs, the pseudoperiod is overestimated. Contrary to the DMA, the DPP is tendentially better for smaller TX–RX and shadowing distances.

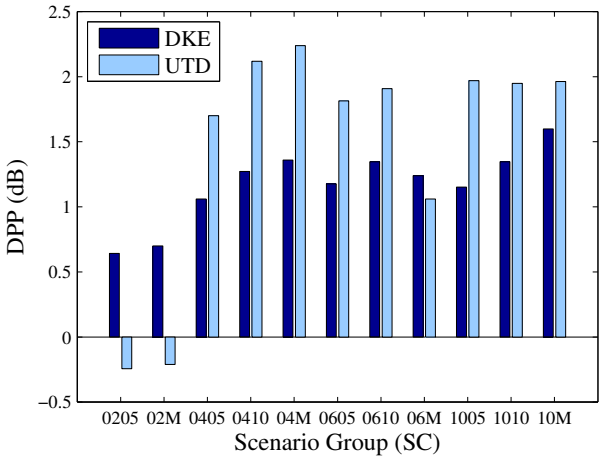

Figure 7. Mean DPP values for DKE and UTD model with respect to SGs.

It shall be mentioned that the results and statements are strongly related to the determination of the DKE and UTD model parameters. The approach described in Section III-D allowed us to determine the walking speed of the person on the basis of the MIMO channels without the need for making a pre-assumption with respect to the effective depth of the body. Therefore, both parameters could be separated and the approach enables to relate the results to the actual speed. By determining a on the basis of the 6 dB level crossings, the duration of the SE of the model is fitted to that of the measurements. However, the measures given in Table III and the presented methods may not only be used to compare results for given model parameters, but also to perform parameter and model fitting/modification in the future.

IV. Conclusion

In this paper, we have presented analyses on human body shadowing effects at 60 GHz, which have been based on systematic wideband channel measurements with a 2×2 MIMO setup. We have given parameters for a simple piecewise linear model and proposed measures suited to evaluate the degree of match between attenuation curves at millimeter wave frequencies.

Using parameters that are related to match the shadowing duration (6 dB level crossings), it reveals that the double-knife edge DKE model tendentially underestimates HBS-induced attenuation, whereas the UTD model clearly tends to overestimate. The DMA and the MSE results improve with increasing TX–RX distance and shadowing distance. However, the performance concerning the DPP tends to decrease, meaning that the temporal fluctuations are not fully reproduced by the models. On the one hand, the comparative measures can be used to contrast the measurement results with each other, assess the performance of different models and perform model fitting. On the other hand, the presented results are beneficial to predict the impact of HBS on the power level of the LOS path and may be applied to existing channel models (stochastic as well as deterministic) to extend them by shadowing effects. The latter are essential in order to evaluate the performance of system concepts and algorithms with regard to beamforming, macro/antenna diversity and MIMO.

References

[1] K. Sato and T. Manabe, "Estimation of propagation-path visibility for indoor wireless LAN systems under shadowing condition by human bodies," in *48th IEEE Vehicular Technology Conference, VTC'98*, vol. 3, 1998, pp. 2109–2113.

[2] S. Collonge, G. Zaharia, and E. Zein, G. "Influence of the human activity on wide-band characteristics of the 60 GHz indoor radio channel," *IEEE Transactions on Wireless Communications*, vol. 3, no. 6, pp. 2396–2406, 2004.

[3] M. Jacob, C. Mbianke, and T. Kürner, "A dynamic 60 GHz radio channel model for system level simulations with MAC protocols for IEEE 802.11ad," in *2010 IEEE 14th International Symposium on Consumer Electronics (ISCE)*, 2010, pp. 1–5.

[4] J. Kunisch and J. Pamp, "Ultra-wideband double vertical knife-edge model for obstruction of a ray by a person," in *IEEE International Conference on Ultra-Wideband, ICUWB 2008*, vol. 2, 2008, pp. 17–20.

[5] M. Jacob, S. Priebe, A. Maltsev, V. Erceg, and T. Kürner, "A ray tracing based stochastic human blockage model for the IEEE 802.11ad 60 GHz channel model," in *5th European Conference on Antennas and Propagation, EuCAP 2011*, 2011.

[6] M. Peter and W. Keusgen, "A component-based time domain wideband channel sounder and measurement results for the 60 GHz in-cabin radio channel," in *2nd European Conference on Antennas and Propagation, EuCAP 2007*, Nov. 2007.

[7] M. Ghaddar, L. Talbi, and T. Denidni, "Human body modelling for prediction of effect of people on indoor propagation channel," *Electronics Letters*, vol. 40, no. 25, pp. 1592 – 1594, dec. 2004.

[8] M. Ghaddar, L. Talbi, T. Denidni, and A. Sebak, "A conducting cylinder for modeling human body presence in indoor propagation channel," *Antennas and Propagation, IEEE Transactions on*, vol. 55, no. 11, pp. 3099 –3103, nov. 2007.

[9] D. McNamara, C. Pistorius, and J. Malherbe, *Introduction to the Uniform Geometrical Theory of Diffraction*. Artech House, 1990.

[10] P. Pathak, W. Burnside, and R. Marhefka, "A Uniform GTD Analysis of the Diffraction of Electromagnetic Waves by a Smooth Convex Surface," *IEEE Transactions on Antennas and Propagation*, vol. 28, no. 5, pp. 631–642, 1980.

5 Outdoor Measurement Campaigns and Evaluations on mm-Wave Backhaul and Access

Utilizing spectrum at mm-wave frequencies is seen as a crucial aspect to meet the capacity requirements of future 5G networks [BHL+14]. The potential of mm-wave transmission in cellular networks has already been assessed in e.g. [RRE14, WKNP14, STS+15], and the Radiocommunication Sector of the International Telecommunication Union (ITU-R) has published a study on the technical feasibility of International Mobile Telecommunication (IMT) in bands above 6 GHz [Int15c]. During the latest World Radiocommunication Conference in 2015 (WRC-15), seven candidate frequency bands for 5G mobile services were agreed to be studied in view of WRC-19 [Int15d]. They lie between 24 GHz and 86 GHz. Furthermore, several national regulatory bodies have issued consultations. In the US, the FCC released a Notice of Inquiry on "Use of Spectrum Bands above 24 GHz for Mobile Radio Services" [Fed14]. In the UK, OFCOM delivered a report with identification of preliminary frequency ranges between [Off15]. Though standardization activities for 5G have just recently been kicked off in ITU-R [Int15b] and the 3rd Generation Partnership Project (3GPP) [3rd16b], they are assumed to advance quickly due to a high interest and commitment.

Since accurate channel models are an indispensable basis for investigations on system design, performance assessment and deployment, considerable effort is currently put into channel measurements and model refinement. In relation to these activities, this chapter presents channel measurement campaigns and modeling aspects for microcellular outdoor scenarios at frequencies above 6 GHz. The propagation conditions significantly differ from those in indoor and in-cabin scenarios that were addressed in Chapter 4. At first, the environment is no longer an enclosed space. Besides the absence of a ceiling or a roof, it may be open in one or more directions. Power, which is transmitted, reflected, diffracted, or scattered into these directions, is lost for the transmission. Secondly, the dimensions of the setting and required

link ranges are scaled by at least one order of magnitude. Thirdly, the materials and surface conditions of building walls and scatterers in an outdoor environment typically deviate from those dominating indoors.

This chapter is composed of five publications. Overall, they include results from five independent measurement campaigns in just as many environments. In Section 5.1, the 60 GHz small-cell backhaul channel investigated in a residential area and fundamental conclusions on deployment and system design are derived. Based on three measurement campaigns and comparative ray tracing simulations, Section 5.2 presents results for the urban access channel in street canyons and on an open square. The comparability and accuracy of path loss parameters are discussed in Section 3.7. Section 5.4 contains additional aspects on model refinement and a different beamsteering-centric path loss modeling approach. The most recent street canyon measurement campaign was performed with a multi-frequency channel sounder setup and four frequency bands between 10 and 82 GHz were measured simultaneously. A statistical analysis of the delay spread is presented in Section 5.5.

5.1 Small-Cell Backhaul Measurements and Considerations on Street-Level Deployment

Due to its multi-Gbps capabilities, wireless mm-wave backhaul is seen as a key enabler for further network densification and the massive deployment of 5G small cells or micro cells [BLM+14]. Whereas macro cell backhaul links are installed above rooftop level, mm-wave links for connecting small cells may be deployed on street level and be affected by multipath propagation.

Preceding measurements on a tarmac runway of a former airport (open area scenario) revealed that the ground reflection has a very dominant impact on the channel [WPK+15a]. It superimposes with the direct path and results in a distinct and regular distance-dependent fading structure. As intended, buildings and other possible reflectors have did not contribute to the channel because they were too far away or beyond the beam width of the antennas.

In this Section, a follow-up measurement campaign in a residential area is presented [PWK+15]. It was conducted with the same setup to investigate how the presence of buildings affects the propagation. It reveals that only one resolvable multipath component is visible in the CIR for 250 MHz sounding bandwidth. It is subject to distance-dependent fading. Though the structure is less regular than observed for the airport [WPK+15a], the channel is still dominated by the interaction of the direct and the ground-reflected path. Besides that, the urban/sub-urban environment

with small detached houses yields only a few week reflection paths that fall into the beamwidth of the directional antennas. Hence, in the first approximation, the channel can be predicted by a two-ray model.

Based on this assumption, power-limited and frequency-selective regions are derived. They indicate whether a given setup is limited by flat fading or frequency selectivity, or if the system operates in the "clear region", which means that it is not significantly influenced by these effects. The results are used to illustrate the interdependence of link distance, antenna height, system bandwidth and antenna gain, and to draw conclusions on system design and deployment.

Contribution

This paper was authored by me. I planned the measurement campaign, analyzed the measurement data and derived the results. The preparation of the measurement setup was supported by R. J. Weiler, W. Keusgen and T. Kühne. The measurements were conducted jointly by T. Kühne, F. Undi and myself. Under my supervision, J. Serafimoska performed the post-processing of the meta data (position information) and created Figure 2. B. Göktepe provided support with the refinement of the two-ray model. W. Keusgen proofread the submission.

Millimeter-Wave Small-Cell Backhaul Measurements and Considerations on Street-Level Deployment

Michael Peter*, Richard J. Weiler*, Thomas Kühne†, Barış Göktepe*, Jasminka Serafimoska*, Wilhelm Keusgen*,
*Fraunhofer Heinrich Hertz Institute, Berlin, Germany
†Communications and Information Theory Chair, TU Berlin, Berlin, Germany

***Abstract*—In this paper a measurement campaign related to the 60 GHz small-cell backhaul channel in a residential area is described, and evaluations on its time dispersion and channel gain (normalized received power) are presented. They reveal that the channel is constituted by the direct path, the ground reflection and a few additional reflections with less power. Hence, in the first approximation, its behavior can be predicted by a simple two-ray model. It is used as basis for investigations on frequency selectivity and fading-induced power limitations as a function of distance, antenna height, system bandwidth and antenna gain. The illustrative results are helpful to understand the interdependence of these parameters and can be taken into account for system design and deployment.**

I. Introduction

Mobile networks of the fifth generation (5G) will make use of higher frequency bands (above 6 GHz) in order to enable the use of much higher transmission bandwidth. The network capacity will be vastly increased by network densification, hence by deploying a large number of additional base stations, which cover only a small area. They are denoted as small cells or micro cells [1]. As wired access to the core network cannot be accomplished in many cases, wireless millimeter-wave backhaul links are seen as a key enabler for this development. Due to the large available bandwidth, they can support the required data rates up to multiple Gbps. However, in contrast to conventional point-to-point microwave links, millimeter-wave backhaul links may be deployed on street level in urban environments. It can no longer be assumed that the there is pure line-of-sight (LOS) propagation, but reflections on the street or buildings and street furniture may give rise to multipath contributions, leading to fading and a frequency-selective channel. It is important to measure and characterize these effects to enable proper system design and deployment.

In [2], measurements on a former airport (open area) have been presented focusing the impact of the ground reflection on asphalt. As the excess traveling distance of the reflected path was very small, it could not be resolved by the channel sounder and superimposed with the direct path. Further paths have not been observed, since buildings and other potential reflectors were far away or beyond the visibility (beamwidth) of the directional antennas. In order to investigate the influence of development/houses, a follow-up measurement campaign was carried out in a residential area in Berlin with the same setup. This paper briefly describes the measurement campaign in Section II. Measurement results and evaluations on the channel gain are presented in Section III. Motivated by the findings, a simple two-ray propagation model is used to assess the fading behavior. It is further used as basis for considerations on deployment and system design in Section IV-B, which underpin and generalize the measurement results.

II. Measurement Campaign

A. Channel Sounder

The measurements were performed with the in-house digital radio testbed "HIRATE" [3]. Each device contains a commercial FPGA board, a self-developed converter board and several plug-on modules like filters, clocks and modulators. For measurements at 60 GHz, the devices have been used in combination with external front-ends.

The device at the transmitter side generates a periodic baseband sounding signal, which is based on a Frank sequence of length 256. It exhibits a flat spectrum and hence perfect periodic autocorrelation properties. The signal is up-converted to an intermediate frequency (IF) of 2.4 GHz. An external mixer is used to convert it to 60 GHz – the lower sideband is removed by a band-pass filter. The signal is finally fed into two parallelized power amplifiers and radiated via the transmit antenna.

At the Rx, the received signal is amplified with a low noise amplifier, down-converted to IF and fed into the second HIRATE device. An automatic gain control (AGC) ensures that the signal level is always in a suitable range for the subsequent amplifier chain and – after down-conversion – for the analog-to-digital converter. An internal trigger allows capturing snapshots of the received signal with a high repetition rate and hence measuring time-variant channels. Most of the processing to compute the channel impulse response (CIR) is done via off-line post-processing, besides a real-time averaging procedure. It performs an N_{avrg}-times waveform averaging before writing the received sounding sequence to the memory. This improves the signal-to-noise ratio (SNR) by $(10{\cdot}\log_{10} N_{\mathrm{avrg}})$ dB without allocating additional memory space.

Synchronization between Tx and Rx is established via temperature-controlled rubidium clocks. They are calibrated to each other before the measurement campaign to further

improve their relative accuracy. This enables fully coherent measurements and measuring the absolute delay of propagation paths without limiting mobility. Moreover, the setup is always calibrated on site via back-to-back measurement for each AGC setting using an adjustable attenuator. Its attenuation (and possible frequency response) for each setting in known from measurements with the vector network analyzer and taken into account during the post-processing. In this way, the system frequency response is subtracted out and the post-processed data directly yields the CIR of the radio channel, which (by definition) is independent from the Tx power.

The whole system can be controlled via a graphical user interface (GUI) running on a laptop, which also allows displaying samples of the measurement results during the procedure.

B. Measurement Site and Procedure

The measurement campaign was performed in a residential area in Berlin, Germany, with small detached houses. Figure 1 illustrates the suburban-like environment. The channel sounder

(a) Tx 1 location (see Figure 2) with Tx setup (right) and Rx setup (left)

(b) View from the Rx towards the Tx on Rx track 3 at 200 m distance

Figure 1: Measurement setup and environment.

equipment was placed on the bed of two pick-up trucks. The front-ends and antennas were mounted on two tripods allowing an easy adjustment of the height. For the backhaul measurements, standard gain horns with a gain of 20 dBi were used at the Tx and the Rx at a height of 4.0 m, simulating lamp-post deployment. Further figures and parameters related to the measurements are summarized in Table I.

Table I: Measurement and environmental parameters

Type	Value
Center frequency	60 GHz
Bandwidth	250 MHz
Transmit power	15 dBm
Antenna (Tx and Rx)	20 dBi rectangular standard gain horn
Half-power beamwidth	19.5 ° E-plane, horizontal
	18.1 ° H-plane, vertical
Polarization (Tx/Rx)	vertical/vertical and horizontal/horizontal
Antenna height (Tx/Rx)	4.0 m/4.0 m
Rx speed	1.87 m/s
Sequence duration	1.024 µs
N_{avrg}, waveform averaging	64
Snapshot meas. duration	65.5 µs
Snapshot repetition rate	1.87 kHz
Distance range	20–380 m
Length of segment per run	60 m
Number of snapsots per run	60,000
Number of runs	70
Conditions	mainly LOS, partly OLOS/nLOS

The Tx was placed at two fixed positions according to Figure 2, whereas the Rx was moved away from the Tx with a constant speed of 1.87 m/s on the Rx tracks. During each measurement run, which covered a track segment of 60 m, 60,000 CIR snapshots have been taken. This procedure has been chosen to achieve a sampling of the channel in space, rather than considering a mobile station. Naturally, both stations of a backhaul link will be fixed and hence are subject to one (quasi-)random realization of the channel, which arises at the respective position on the measurement track. The snapshot repetition rate corresponds to a spatial sampling with 1.0 mm spacing. Depending on the length of the street, the Tx-Rx distance was up to 380 m. As the duration of the sounding sequence only enables for observing a unique range of 300 m, additional reference measurements were made at known distances under LOS conditions and saved as calibration data. They allow for resolving the ambiguity in the post-processing.

To enable the investigation of the polarization impact, the measurements were carried out for vertical and horizontal polarization (same polarization at Tx and Rx) by inserting a 90° twister on both sides. The collected data set comprises 70 measurement runs, hence 4.2 million CIRs. The whole measurement campaign has been recorded using two cameras at the Rx and one camera at the Tx. Based on time stamps, the videos can be attributed to the measurement runs and highly facilitate the interpretation of the measurement results.

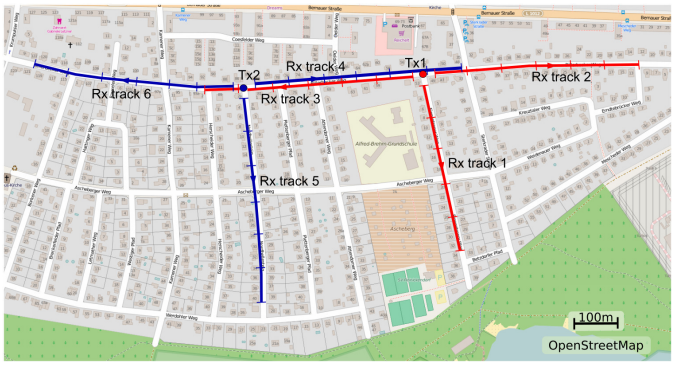

Figure 2: Map of measurement location with Tx positions and Rx tracks.

III. Measurement Results and Evaluations

A. Power Delay Profiles

As explained above, channel snapshots have been taken at equidistant Rx positions with 1 mm spacing. Figure 3 shows a typical result of one measurement run in the form of an averaged power delay profile (APDP) evolving over time.

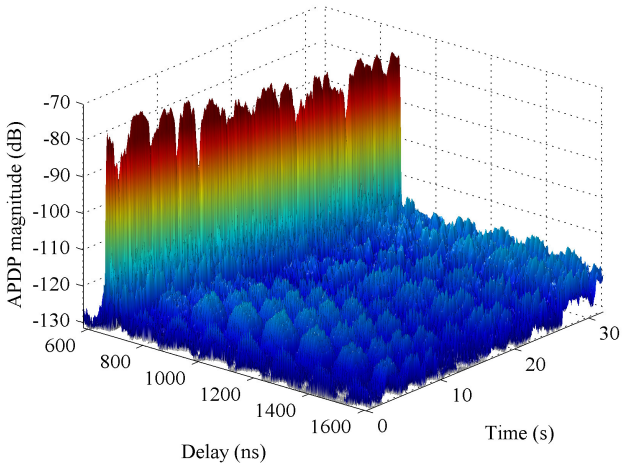

Figure 3: Exemplary measurement result: sequence of APDPs on Rx track 3 (distance: 200–260 m, horizontal polarization).

It is related to the fourth measurement run on Rx track 3 with horizontal polarization. Each APDP has been obtained by averaging over $K_{\mathrm{avrg}} = 100$ "instantaneous power delay profiles" $|h_k(t)|^2$ at consecutive Rx points, corresponding to a spatial averaging over 10 cm. For the given setup with directional antennas, this mainly reduces noise effects rather than averaging out fading.

It is visible that the first resolvable multipath component (MPC) is subject to significant fading. The distinct periodicity can be attributed to the superposition of the direct path and the ground reflection. The irregularities lead to the conclusion that there are a few additional paths which superimpose within the first MPC.

Apart from the first MPC, no other MPCs can be observed. As can be seen in Figure 3, due to the high overall antenna gain, the evaluable dynamic range at this distance is still limited by the instantaneous dynamic range of the system (approx. 40 dB) rather then by thermal noise. However, within a range of 40 dB relative to the first MPC, the environment does not yield propagation paths, which could be resolved with 250 MHz bandwidth. (Possibly occurring paths below this level can be regarded as insignificant for a transmission system.) This applies to all measurement runs.

B. Channel Gain

Since only one resolvable MPC can be observed, the main information is included in the channel gain (normalized received wideband power). It can be calculated on the basis of CIRs or APDPs by adding up all multipath power. In the present case, it is practically equivalent with the gain of the first resolvable MPC. Figure 4a illustrates the channel gain versus distance for Rx track 3 and horizontal polarization. The curve is a concatenation of the results from six individual

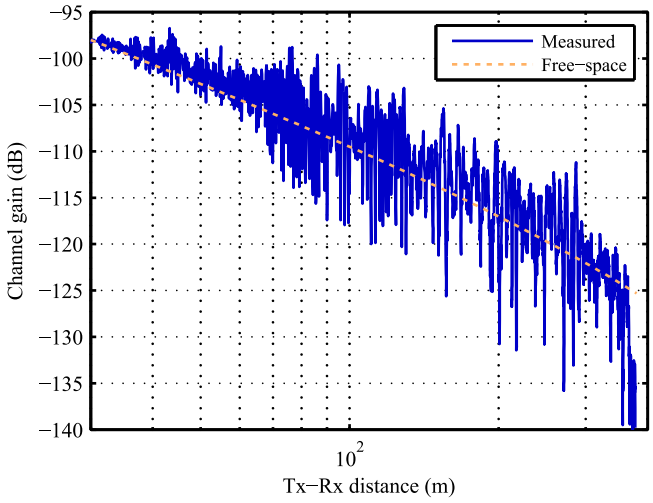

(a) Horizontal polarization

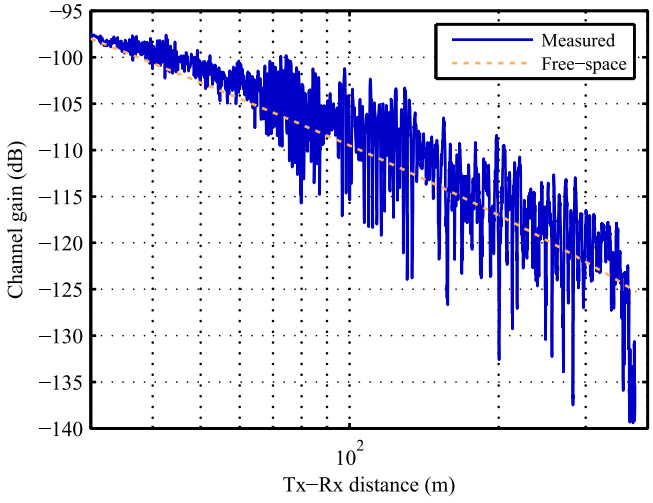

(b) Vertical polarization

Figure 4: Channel gain versus distance for Rx track 3.

measurement runs. Antenna gains have been subtracted, so that the result can be directly compared with the free-space loss, which is also plotted in the figure. In the present case, an additional attenuation has been added to account for oxygen absorption, which already has a visible effect for distances above 200 m. A specific absorption rate of 15 $^{\mathrm{dB}}/_{\mathrm{km}}$ has been assumed [4].

The channel gain is subject to fading, which clearly increases with distance. This behavior arises from a superposition of the following effects: 1) At close-by distances the system bandwidth is almost large enough to resolve the reflected paths, so that they may not interfere fully constructively or destructively. 2) At small distances the reflected paths are suppressed by the antenna pattern: up to 45–50 m they are outside the half-power beamwidth (HPBW). 3) The magnitude of the Fresnel reflection coefficients reach a maximum for grazing angle of incidence with respect to the surface. The reflected paths can become almost as strong as the direct path for large distances, even for rough surfaces.

Over the whole distance range, the distinct fading period (distance of the minimums or maximums) can be attributed to the ground-reflected path. It has the most significant effect on the variation of the channel gain. At a distance of 365 m the channel gain drops severely, since the propagation conditions change from LOS to near-LOS (nLOS). This effect is further investigated in Section III-C.

Figure 4b shows the same evaluation, but for vertical polarization. The result is very similar. A detailed comparison reveals that the position of the minimums and maximums is fully aligned for distances above 150 m and partly the curves are practically congruent. This principle result can be observed for all Rx tracks. Thus, the channel characteristics cannot be influenced by changing the polarization from horizontal to vertical for the given setup and environment. However, it shall be noted that this finding applies to the co-polar channels and does not allow drawing conclusions on cross-polar characteristics.

C. Obstructed LOS and Near-LOS

The effect of loosing LOS conditions has already been partly visible at the end of Rx track 3 in Section III-B. In order to investigate the impact in more detail, a measurement track on a curved section of the street has been considered, namely Rx track 6 (see Figure 2). The channel gain is illustrated in Figure 5. It significantly drops below the free-space loss beyond 86 m. At this distance, leafed branches of a birch tree and a fir tree started to impair the direct path. At the end of the track (above 250 m), it is even blocked by houses and the received power can only arise from reflections. In this distance range, the average channel gain is around 15 dB smaller than the theoretical value from free-space propagation with oxygen absorption. This result confirms that the environment yields reflections, but that they are significantly weaker than the ground-reflected path.

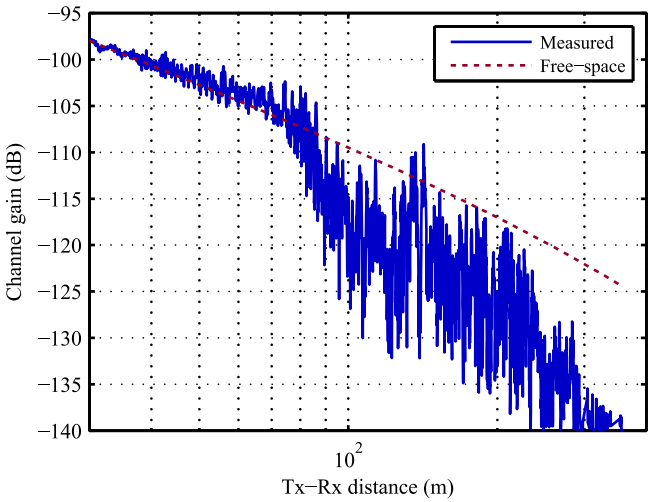

Figure 5: Channel gain versus distance for Rx track 6 (vertical polarization).

IV. Two-Ray Model and Further Considerations

A. Comparison with Two-Ray Model

Motivated by the fact that the channel is mainly constituted by the superposition of the direct and a ground-reflected path, the results are directly compared with a two-ray model in this section.

The discrete channel impulse response of the two-ray channel can be expressed as

$$h(t) = \sum_{i=1}^{2} G_i \, e^{\frac{-2\pi j l_i}{\lambda}} \, \delta\left(t - \frac{l_i}{c_0}\right), \tag{1}$$

where $i = 1$ is attributed to the LOS path and $i = 2$ to the reflected path. λ, l_i and c_0 are the wavelength, the traveling distance and the speed of light, respectively. $G_i = G_{Tx}(\theta_{i,Tx}) \cdot G_{Rx}(\theta_{i,Rx}) \cdot \frac{\lambda}{4\pi l_i} 10^{-\frac{l_i l_{Ox}}{1000 \cdot 20}} R_i$ is the path gain with the angle-dependent antenna gains G_{Tx} and G_{Rx} (normalized in this case), the oxygen absorption rate l_{Ox} in $^{\mathrm{dB}}/_{\mathrm{km}}$ and the reflection coefficient R_i, which can be calculated according to the Fresnel reflection laws [5]. The discrete CIR can then be binned and translated into a band-limited version to compute the (wideband) channel gain. Figure 6 shows the result for the parameters of the measurement setup. The angle-dependent gain was calculated using the formulas for a rectangular aperture antenna [6]. The effective dielectric constant was set to $\varepsilon_r = 3.18$ – the value for asphalt given in [7]. It can be seen that the position of the fading maximums (local minimums of the curve) are predicted quite accurately with the simple two-ray approach. Their amplitude is not fully reproduced, since the other multipaths are neglected. However, at those positions, where the fading maximums are very distinct in the measurement curve, also the amplitude is in very good agreement with the model. This leads to the conclusion that the two-ray model is well suited to assess the lower bound of the received power and hence covers worst case scenarios (positions).

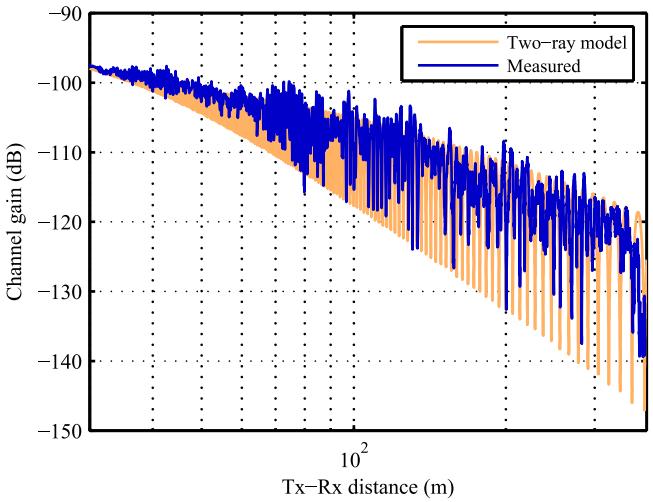

Figure 6: Channel gain versus distance for Rx track 6 (vertical polarization).

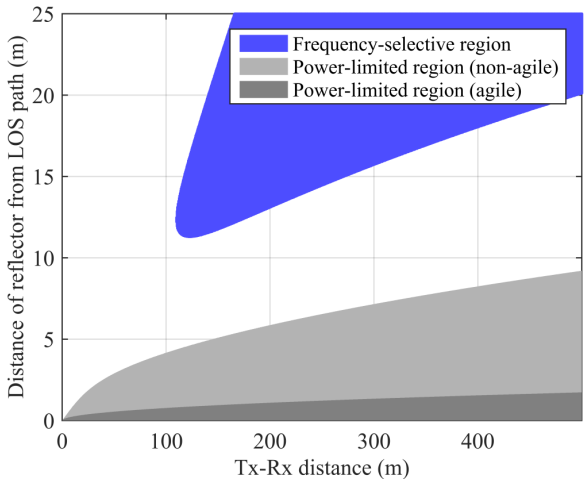

Figure 7: Power-limited, frequency selective and clear regions of a two-ray small-cell backhaul channel (20 dBi antennas, 250 MHz bandwidth, usable band for frequency-agile system: 7 GHz).

B. Considerations on Deployment and System Design

The measurement results presented in Section III reveal that for the given environment, antenna setup and bandwidth, the multipaths cannot be resolved, but superimpose with the direct path. They cause flat fading rather than a time-dispersive channel. In this section, these observations are substantiated in more detail. The investigations are based on the two-ray model presented in Section IV-A. It is assumed that a fading margin of 6 dB is reserved to account for fading losses. If the loss exceeds 6 dB (with respect to the power of the LOS path), the system is said to be power-limited. The coherence bandwidth of the channel is calculated as [8]

$$B_{\mathrm{coh},0.5} = \frac{1}{6 \cdot \tau_{\mathrm{rms}}}, \tag{2}$$

where τ_{rms} is the root-mean-square (RMS) delay spread derived from (1). If the condition $B \geq 4 \cdot B_{\mathrm{coh},0.5}$ holds, the channel is interpreted as beeing frequency-selective with respect to the system bandwidth.

Figure 7 shows the resulting frequency-selective and power-limited regions as a function of the Tx-Rx distance and the distance of the reflector from the LOS path. A bandwidth of 250 MHz has been assumed in conformity with the measurements. With the assumptions above, a (symmetric) backhaul setup with an antenna height of 4 m can become power limited, when the distance exceeds 92 m (non-agile). Fading-induced power-limitation can be avoided by increasing the antenna height. However, at larger distances the channel can become frequency-selective if a certain antenna height is exceeded. In this region, the system needs to apply channel equalization to enable a performant transmission. In order to maximize the link capacity, carrier-adaptive power allocation and modulation can be used. The region, which is neither frequency-selective nor power-limited is denoted as “clear region”. In this region it is tendentially possible to operate simple, non-adaptive systems without equalization.

An alternative approach to avoid power limitations, namely frequency agility, can be pursued if the usable frequency band is much larger than the system bandwidth. As the unlicensed band at 60 GHz comprises 7 GHz, a frequency-agile system can adjust its carrier frequency in order to maximize the received power. The effect on the power-limited region is also visible in Figure 7 (agile) – it shrinks significantly. Even at a link distance of 500 m, the distance of the antennas from the ground (or from a reflecting building) could be as low as 1.7 m, compared to 9.2 m for the non-agile system.

Figure 8 illustrates the results if the antenna gain at both sides of the link is increased to 30 dBi. In this case, there

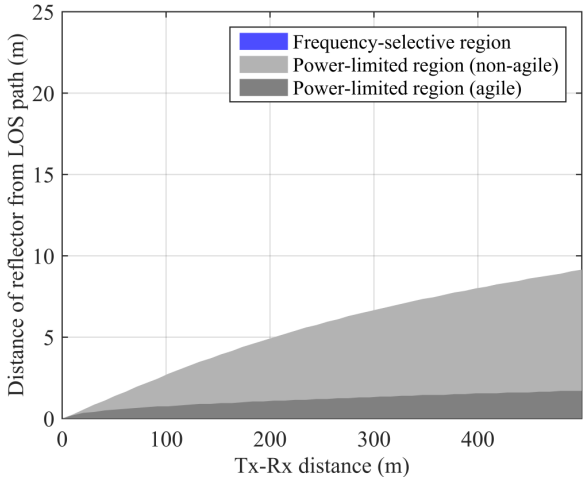

Figure 8: Power-limited, frequency selective and clear regions of a two-ray small-cell backhaul channel (30 dBi antennas, 250 MHz bandwidth, usable band for frequency-agile system: 7 GHz).

is no frequency-selective region in the considered distance range anymore. The power-limited region shrinks, but only for smaller distances. Consequently, increasing the antenna

gain is an effective way to reduce frequency selectivity and of course to improve the overall link budget and reduce potential interference. However, it does not automatically translate to lower fading and might come along with increasing issues on proper alignment.

Link capacity can be increased by enlarging the transmission bandwidth – as mentioned above, a sufficiently large band is available at least at 60 GHz. The effect on allocating 2 GHz bandwidth in combination with 30 dBi antennas is visible in Figure 9. As expected, the size of the power-limited region is

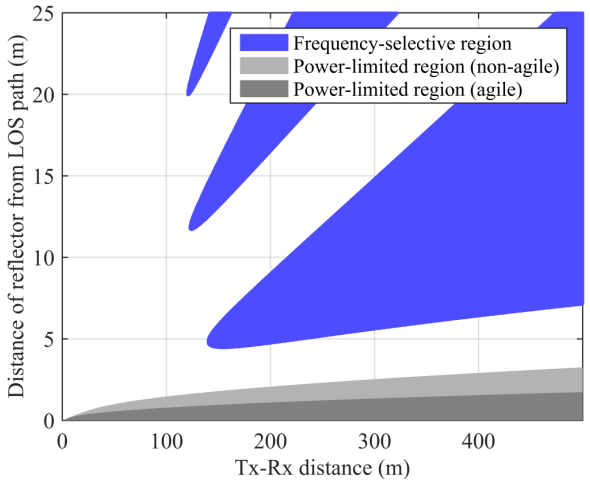

Figure 9: Power-limited, frequency selective and clear regions of a two-ray small-cell backhaul channel (30 dBi antennas, 2 GHz bandwidth, usable band for frequency-agile system: 7 GHz).

reduced significantly. On the other hand, frequency selectivity becomes a major issue. In addition to reflected paths falling in the main lobe of the antennas, paths excited/collected from the side lobes may take effect. Channel equalization is obligatory to ensure proper operation.

V. Conclusions

In this paper, a measurement campaign on the small-cell backhaul channel has been presented which was performed with the in-house digital radio testbed. The results show that the urban/sub-urban environment with small detached houses did not yield reflected propagation paths, which could be resolved with the sounder bandwidth of 250 MHz. Instead, all (significant) reflected paths superimpose with the direct (LOS) path and induce fading on the first resolvable MPC. From the structure of the fading it can be concluded that it comprises several reflected paths (it is less regular compared to the results obtained for an open area [2]), but the ground reflection has the most dominant impact. A simple two-ray model may be used to assess the channel behavior, especially for the worst-case positions.

The findings have been substantiated and generalized by deriving power-limited and frequency-selective regions, which illustrate whether a given setup is limited by flat fading or frequency selectivity, or if the system operates in the "clear region", which means that it is not influenced by these effects significantly. It reveals that frequency-agility is a very effective way to decrease the size of the power-limited region. Increasing the antenna gain first of all reduces/prevents frequency selectivity, but does not automatically reduce fading. Backhaul links relying on a very large bandwidth (e.g. 2 GHz) require channel equalization techniques if the are deployed on street level – at least, if they make use of antennas with a moderate gain, which facilitates mounting and alignment.

Acknowlegment

Part of the research leading to these results has received funding from the EU's FP7 Program (FP7-ICT-2013-EU-Japan) under grant agreement number 608637 (MiWEBA).

References

[1] N. Bhushan, J. Li, D. Malladi, R. Gilmore, D. Brenner, A. Damnjanovic, R. Sukhavasi, C. Patel, and S. Geirhofer, "Network densification: the dominant theme for wireless evolution into 5G," *Communications Magazine, IEEE*, vol. 52, no. 2, pp. 82–89, February 2014.

[2] R. J. Weiler, M. Peter, W. Keusgen, A. Kortke, and M. Wisotzki, "Millimeter-wave channel sounding of outdoor ground reflections," in *IEEE Radio Wireless Symposium, San Diego, USA*, Jan. 2015.

[3] W. Keusgen, A. Kortke, M. Peter, and R. Weiler, "A highly flexible digital radio testbed and 60 GHz application examples," in *Microwave Conference (EuMC), 2013 European*, 2013, pp. 740–743.

[4] H. J. Liebe, "MPM-An atmospheric millimeter-wave propagation model," *International Journal of Infrared and Millimeter Waves*, vol. 10, no. 6, pp. 631–650, 1989.

[5] B. Langen, G. Lober, and W. Herzig, "Reflection and transmission behaviour of building materials at 60 GHz," in *Personal, Indoor and Mobile Radio Communications, 1994. Wireless Networks - Catching the Mobile Future., 5th IEEE International Symposium on*, 1994, pp. 505–509 vol.2.

[6] C. A. Balanis, *Antenna Theory: Analysis and Design*, 3rd ed. Wiley, 2005.

[7] K. Sarabandi, E. Li, and A. Nashashibi, "Modeling and measurements of scattering from road surfaces at millimeter-wave frequencies," *Antennas and Propagation, IEEE Transactions on*, vol. 45, no. 11, pp. 1679–1688, Nov 1997.

[8] A. F. Molisch and M. Steinbauer, "Condensed parameters for characterizing wideband mobile radio channels," *International Journal of Wireless Information Networks*, vol. 6, no. 3, pp. 133–154, 1999.

5.2 Measurements and Modeling for UMi Access Scenarios

Driven by the bandwidth shortage in the traditional cellular bands, frequencies above 6 GHz are supposed to be utilized also for access in 5G networks and related channel models are being developed [3rd16a, ICT16b, Aal16, JPS+16]. In the following publication, channel measurement results and modeling aspects for 5G urban access scenarios are presented [PWG+16], aiming to support the validation of emerging models and proposed extensions.

The investigations build on three measurement campaigns in the city center and in a residential area in Berlin, Germany. Like the backhaul measurements in Section 5.1, they were conducted with the HIRATE channel sounder setup (see CS 3 in Section 3.5.1), however, omnidirectional antennas were used at both sides instead of horn antennas. The mobile Rx was moved during the measurement runs and CIR snapshots were recorded with 0.4 mm spacing between adjacent Rx positions. In total, more than 15 million CIRs were collected for statistical evaluations in this way. In addition, ray tracing simulations were performed for the city center scenarios to assess their accuracy in terms of predicting the large-scale and small-scale characteristics of the channel. In this context, great care has been taken to take into account the influence of street furniture and tree trunks [GPWK16, GPWK15].

It reveals that the ground reflection has a considerable impact on the LOS channel. This has already been observed for the backhaul scenario in Section 5.1. It can be confirmed that similar fading effects caused by the superposition of the LOS path and the ground-reflected path also occur in urban access scenarios. At traditional cellular frequencies below 6 GHz, the distance of the user to the base station in a microcellular scenario is typically beyond the breakpoint distance (see e.g. dual-slope path loss model 3GPP-3D UMi in [3rd15]). In this case, any potential impact of the ground reflection is fully considered by the slope of the path loss model. However, at mm-wave frequencies, links will be shorter than the breakpoint distance. For a mobile user, the ground reflection can cause distinct quasi-periodic flat fading or, for small link distances and large bandwidths, frequency selectivity of the channel. Since these effects decisively determine the conditions of a mm-wave LOS link and can occur in any UMi scenario, almost regardless of the specific development, the ground reflection should be considered in mm-wave 5G channel models.

In contrast to the backhaul results, further MPCs besides the first resolvable component can be observed in the PDPs, which are caused by reflections on buildings, street furniture and trees. Compared to typical indoor channels, e.g. in the conference

room as presented in Section 4.1, emerging excess delays are increased by one order of magnitude, which is in line with the scaling of the propagation environment. The MPCs are subject to small-scale fading, indicating that multiple propagation paths superimpose within one delay bin for 250 MHz measurement bandwidth. Since the number of strong MPCs is quite limited, however, the channel appears relatively sparse on the delay axis.

A path loss analysis reveals that the PL exponent for LOS is close to free-space propagation at 60 GHz and slightly smaller at 10 GHz. The delay spread (DS) shows a clear dependence on the scenario and strong distance dependence for the open square and the wide street canyon in the city center. This behavior can be well reproduced by ray tracing simulations. Nevertheless, the ray tracer tends to overestimate the DS. Furthermore, it is not able to accurately reflect the small-scale fading behavior of the channel, which means that intra-cluster paths cannot be predicted. The latter result is in accordance with observations for the indoor conference room, which was investigated in Section 4.1 and 4.2 by means of measurements [PKF07]. They indicate that beyond a certain point, the simulation results may not be further improved by increasing the number of interactions and the modeling granularity of the environment—at least if diffraction and diffuse scattering are not considered. From [FRKP12] and [MIPGR+13] it can be concluded that this finding is not limited to the ray tracer and the specific environment. Overall, the ray tracing results show that such tools on the one hand are very valuable to gain information about site-specific channels. On the other hand, it is important to substantiate the findings by measurements.

Contribution

The measurement campaigns were primarily planned by me and carried out jointly by my co-authors and myself. I made the overall data analysis and wrote the paper. The preparation of the measurement setup was supported by R. Weiler and W. Keusgen. B. Göktepe performed the ray tracing simulations, pre-processed the simulation data and provided input to Section 3. K. Sakaguchi provided input to Section 1 and proofread the paper.

sensors

MDPI

Article

Channel Measurement and Modeling for 5G Urban Microcellular Scenarios

Michael Peter [1,*], Richard J. Weiler [1], Barış Göktepe [1], Wilhelm Keusgen [1] and Kei Sakaguchi [1,2]

[1] Department of Wireless Communications and Networks, Fraunhofer Heinrich Hertz Institute, Berlin 10587, Germany; richard.weiler@hhi.fraunhofer.de (R.J.W.); baris.goektepe@hhi.fraunhofer.de (B.G.); wilhelm.keusgen@hhi.fraunhofer.de (W.K.); kei.sakaguchi@hhi.fraunhofer.de (K.S.)

[2] Department of Electrical and Electronic Engineering, Tokyo Institute of Technology, Tokyo 152-8552, Japan

* Correspondence: michael.peter@hhi.fraunhofer.de; Tel.: +49-30-3100-2583

Academic Editor: Leonhard M. Reindl

Received: 1 June 2016; Accepted: 15 August 2016; Published: 20 August 2016

Abstract: In order to support the development of channel models for higher frequency bands, multiple urban microcellular measurement campaigns have been carried out in Berlin, Germany, at 60 and 10 GHz. In this paper, the collected data is uniformly analyzed with focus on the path loss (PL) and the delay spread (DS). It reveals that the ground reflection has a dominant impact on the fading behavior. For line-of-sight conditions, the PL exponents are close to free space propagation at 60 GHz, but slightly smaller (1.62) for the street canyon at 10 GHz. The DS shows a clear dependence on the scenario (median values between 16 and 38 ns) and a strong distance dependence for the open square and the wide street canyon. The dependence is less distinct for the narrow street canyon with residential buildings. This behavior is consistent with complementary ray tracing simulations, though the simplified model tends to overestimate the DS.

Keywords: millimeter-wave propagation; channel sounding; urban micro; 60 GHz channel; 5G channel model; ray tracing

1. Introduction

Fifth generation (5G) mobile networks will need to make use of frequencies above 6 GHz to provide multi-Gbps data rates and realize ultra-high capacity for various deployment scenarios [1–3]. The targeted frequency bands range up to 100 GHz [4]. Early stage studies have shown the feasibility of millimeter waves for cellular networks [5–7], and standardization activities for 5G have been kicked off in the Radiocommunication Sector of the International Telecommunication Union (ITU-R) [8] and the 3rd Generation Partnership Project (3GPP) [9]. Considerable effort is currently put into the refinement of channel models, since they are essential for accurately assessing the performance of future deployments. Most relevant work builds upon state-of-the-art three-dimensional (3D) geometry-based stochastic channel models (GSCMs) that have been developed recently for lower frequency bands. New model features and extended parameter tables have been proposed to fulfill the requirements for 5G millimeter-wave (mm-wave) channel models, which have to support a much wider frequency range, large antenna arrays, large bandwidth and high mobility [10–15].

Providing measurement data for their validation that is both statistically reliable [16] and including full directional information is very challenging as long as high performance electronically steerable antennas for various mm-wave frequency bands are not available at reasonable expense. Multiple channel sounding campaigns have been reported in the literature for cellular access scenarios above 10 GHz, e.g., at 11 GHz [17], 28 GHz [18,19], 38 and 73 GHz [20] and 60 GHz [21]. The amount of available data, however, is still not sufficient to fully substantiate and reliably parameterize the models. Currently, directional information is mainly obtained by successively scanning all (relevant) angles

with mechanically steerable directional antennas [21]. Since the scanning takes a long time, the number of observation points is limited in practice. A different measurement approach, which is also pursued in this work, is to use a channel sounder with a high measurement repetition rate in conjunction with omnidirectional antennas and a mobile receiver (RX). It allows for collecting large data sets and capturing all multipaths even for time-variant channels and aims to support the parameterization and validation of channel models on a reliable statistical basis. Omnidirectional path loss (PL) models can be derived directly from such data, and it is well suited for assessing results from ray tracing (RT) tools, which become increasingly important for channel modeling at higher frequencies [22,23]. They are capable of generating large data sets with unlimited dynamic range and can provide directional information to complement the measurements.

In this paper, data from three recent urban microcellular (UMi) measurement campaigns at 60 and 10 GHz is analyzed with focus on the PL and delay spread (DS). The frequencies were chosen since they represent sample points in the lower and the upper part of the range 6–100 GHz and hence are well suited to investigate frequency dependence. Moreover, a radio license could be obtained with sufficient bandwidth at 10 GHz, 60 GHz is an unlicensed band, and suitable measurement equipment was available. In view of complementing the measurements with validated simulation data, the results are compared with predictions from an in-house RT tool for the same environments. The findings provide valuable insight into the dependence of channel characteristics on the propagation scenario, distance and frequency. The presented modeling approaches and parameters were derived from several million channel observations for each scenario and can be used to refine 5G channel models and for comparative investigations. To the knowledge of the authors, a comparable unified analysis for the UMi channel at 60 and 10 GHz based on such large data sets has not been reported in the literature so far.

The measurement campaigns are briefly described in Section 2. Section 3 introduces the RT environment. The investigations on the PL and DS are presented in Section 4, including the comparison between simulation and measurement results. Conclusions are provided in Section 5.

2. Urban Microcellular Measurement Campaigns

To provide a data basis for model refinement, several measurement campaigns have been performed in Berlin at 60 GHz and 10 GHz. Two of them are related to UMi street canyon scenarios, namely "street canyon, city center" (SC-CC) [24] and "street canyon, residential area" (SC-RA) [24,25]. The third UMi scenario is "open square, city center" (OS-CC). Table 1 summarizes information on the environments and the collected data. The OS-CC measurement campaign is briefly described in Section 2.2.

2.1. Channel Sounder

All measurements were performed with the same setup, namely the in-house "High Performance Digital Radio Testbed" (HIRATE). Each device contains a commercial field-programmable gate array (FPGA) board, a self-developed converter board and several plug-on modules like filters, clocks and modulators. Two fully parallel signal chains allow dual-channel/frequency measurements [25].

The transmitter (TX) device generates a periodic baseband sounding signal based on a Frank sequence of length 256. The signal is up-converted to an intermediate frequency (IF) of 2.4 GHz. External mixers and filters are used to convert the IF signal to 10 and 60 GHz, respectively. The signal is finally fed into power amplifiers and radiated via the transmit antenna. The RX amplifies the received signal with a low noise amplifier. It is down-converted to IF and fed into the second HIRATE device, where it is converted to baseband. An internal trigger allows capturing snapshots of the signal with a high repetition rate. Most of the processing to compute the channel impulse response (CIR) is done via off-line post-processing, besides a real-time averaging procedure. It performs an N_{avrg}-times waveform averaging before storing the digitized signal, improving the signal-to-noise ratio by an averaging gain of $G_{\mathrm{avrg|dB}} = 10 \cdot \log_{10} N_{\mathrm{avrg}}$. Synchronization between TX and RX is established via

temperature-controlled rubidium clocks. The setup is calibrated on site via back-to-back measurement. Details on the HIRATE can be found in [26].

Table 1. Summary of measured urban microcellular (UMi) scenarios and main parameters.

Scenario	**OS-CC**	**SC-CC** [24]	SC-RA [25]
Site	Berlin city center, Leipziger Platz	Berlin city center, Potsdamer Str.	Berlin residential area Kreuzberg
Dimensions	Square diameter: ≈150 m	Street canyon width: ≈52 m	Street canyon width: 15–20 m
Frequency	60.0 GHz	60.0 GHz	60.4 GHz and 10.0 GHz
Bandwidth	250 MHz	250 MHz	250 MHz
Antenna type (TX and RX)	omni, vertical pol.	omni, vertical pol.	omni, vertical pol.
HPBW in elevation	≈80 deg	≈80 deg	≈80 deg at 60.4 GHz, ≈60 deg at 10.0 GHz
Antenna height (TX/RX)	3.5 m/1.5 m	3.5 m/1.5 m	5.0/1.5 m
Conditions	mainly LOS	mainly LOS	LOS/NLOS
Distance	2–50 m	2–50 m	4–210 m
Spacing between meas. points for mobile RX	0.4 mm	0.4 mm	0.4 mm
Number of collected CIRs	2.4 million	6.4 million	6.3 million

2.2. Open Square Measurements

The OS-CC measurements at 60 GHz were performed on "Leipziger Platz", which is an open square of octagonal shape and a diameter of approx. 150 m in the city center of Berlin. It is bordered by modern multi-story buildings, as can be seen in Figure 1a.

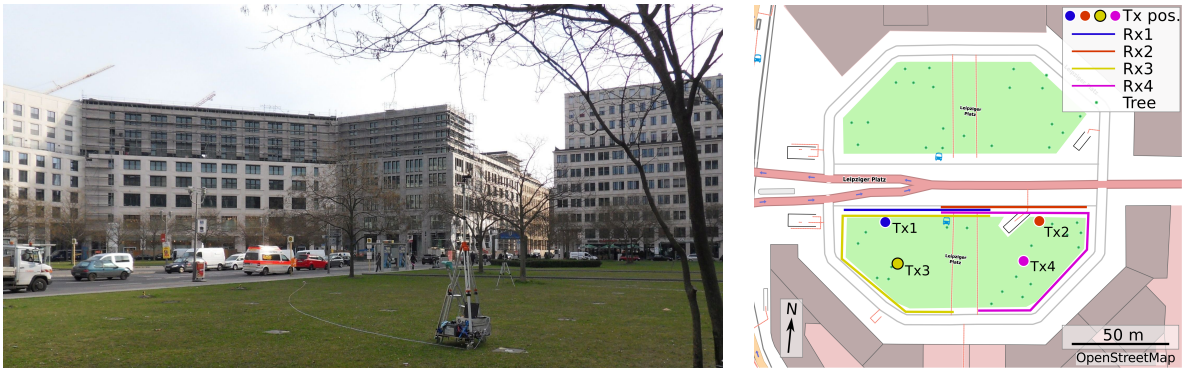

(**a**) (**b**)

Figure 1. Measurement environment "open square, city center" (OS-CC): (**a**) photo with transmitter (TX) pole at position Tx3 and (**b**) map with TX positions and receiver (RX) tracks.

The TX of the channel sounder was placed at four different positions on the square. The antenna was mounted on a pole of 3.5 m height to simulate street furniture deployment. In accordance with the SC-CC and SC-RA measurements, the RX was mounted on a trolley at a height of 1.5 m and moved along the sidewalk at constant speed of 0.5 m/s. Figure 1b shows a map of the square with the TX positions and the RX tracks. For the majority of the RX positions, there was line-of-sight (LOS) between the TX and RX antenna. The measurement bandwidth was 250 MHz and a transmit power of 15 dBm could be achieved. Vertically polarized antennas with omnidirectional pattern in azimuth and 2 dBi gain were used at the TX and RX. A CIR snapshot took 65.5 µs and was recorded every 800 µs, corresponding to 0.4 mm spacing between adjacent RX positions. The overall data set acquired for the OS-CC scenario comprises 2.4 million CIRs.

3. Ray Tracing Simulations

As support for the UMi measurements, RT simulations were performed for the OS-CC and SC-CC environments. The polarimetric RT tool, which has been developed by the Fraunhofer Heinrich Hertz Institute (Berlin, Germany) based on NVIDIA's OptiX engine, makes use of parallelized processing on the graphics processing unit (GPU) [27]. It applies geometrical optics (GO) and the uniform theory of diffraction (UTD) for reflections on convex surfaces. The measurement environments are incorporated in form of 3D models from Leipziger Platz (Figure 2a) and Potsdamer Strasse (Figure 2b). They were manually extended to include street furniture and tree trunks [28].

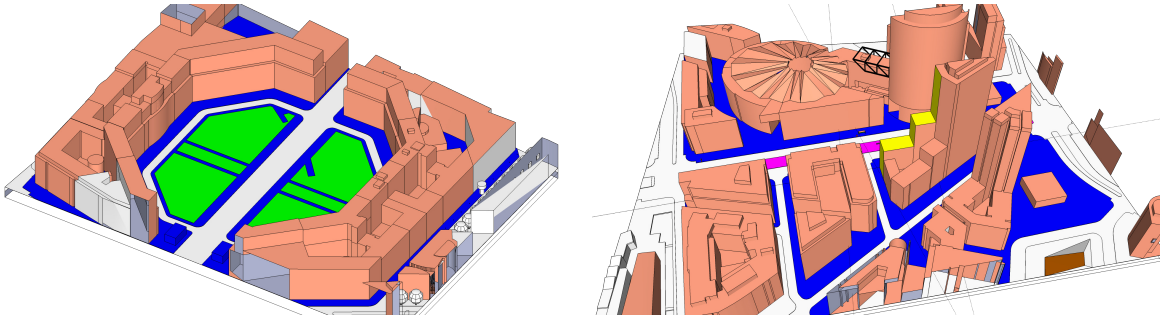

(**a**) (**b**)

Figure 2. Top view of 3D models used for ray tracing. (**a**) OS-CC scenario; (**b**) "street canyon, city center" (SC-CC) scenario.

All building surfaces were assumed to be glass with relative permittivity $\varepsilon_r = 8.9 - j0.13$ [29], where j is the imaginary unit. The ground was modeled with $\varepsilon_r = 6.14 - j0.30$, the value defined for concrete in [30], since the sidewalk is paved with concrete setts. The trees were assumed to be smooth, dielectric cylinders with $\varepsilon_r = 1.57 - j0.096$, the value for wood in [30]. The lamp posts were modeled as smooth and perfectly electrically conducting cylinders. Up to one transmission and four reflections were admitted. Isotropic, vertically polarized antennas were used, which has been found to well reflect the omnidirectional measurement antennas as long as only distances above 5 m are considered and their gain is subtracted. The RX measurement tracks with 0.4 mm spacing were fully re-simulated with the ray tracer. For each simulated RX point, a discrete equivalent baseband CIR was composed from the simulated rays based on their complex amplitude and propagation delay by binning (small bin size of 0.4 ns). Rays falling in one delay bin were added coherently. To provide fully comparable results, the simulated CIRs were band limited to the measurement bandwidth of 250 MHz, and the same post-processing was applied.

4. Evaluations

4.1. Power Delay Profiles

Figure 3a shows a typical result of one measurement run on Track Rx1 in the form of averaged power delay profiles (APDPs) evolving over time. During the measurement run, the RX moved away from the TX, starting at 25 m distance and ending at 50 m. Each APDP has been obtained by averaging over $K = 250$ "instantaneous power delay profiles" $|h_k(t)|^2$ at consecutive RX points according to

$$P(\tau) = \frac{1}{K} \sum_{k=1}^{K} |h_k(\tau)|^2 , \tag{1}$$

where $P(\tau)$ denotes the APDP and $h_k(\tau)$ is the kth CIR. $K = 250$ corresponds to a spatial averaging over 10 cm or 20 wavelengths. Comparative investigations with different factors have shown that the dominant effect of this kind of averaging on the given data is the reduction of thermal noise

and phase noise. It is clearly visible that the first resolvable multipath component (MPC) is subject to strong fading. Based on geometric considerations, the distinct regular structure can clearly be attributed to the superposition of the direct path and the ground reflection, which cannot be resolved with 250 MHz bandwidth for larger distances. Further MPCs can be observed up to 800 ns delay. They are also subject to fading on a scale above 50 cm. However, overall, the APDP is relatively sparse. The MPCs will lead to time dispersion on the one hand. On the other hand, the related propagation paths can be very beneficial if the LOS path is blocked.

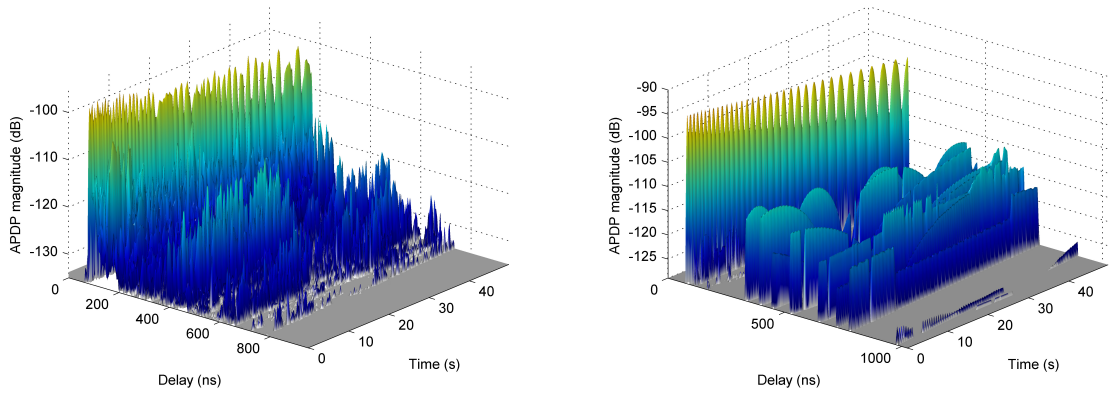

(**a**) (**b**)

Figure 3. Evolution of averaged power delay profiles (APDPs) over time for TX position Tx1 and mobile RX on Track Rx1 from (**a**) measurement and (**b**) simulation.

Figure 3b illustrates the corresponding simulated APDPs. The first MPC and its fading structure are well reproduced by the ray tracer and further strong MPCs are identified. However, in the measurements, they underlie a stronger fading on a time scale of several seconds. This indicates that the ray tracer is able to predict arriving path clusters, but not potential intra-cluster paths from a structured surface, e.g., outer walls with windows inwards. The granularity of the 3D model is of the order of 1 m and does not account for such structures. Furthermore, scattering, blockage and dynamic changes of the environment caused by cars and pedestrians cannot be considered. The ray tracer also tends to overestimate the strength of MPCs arriving with long delays, which gives rise to further investigations. The reason may be partially diffuse rather than ideal specular reflections. However, it is important to note that the results have been achieved without calibration of the ray tracer, but based on the simple assumptions mentioned above.

4.2. Path Loss

In this section, the local area PL is analyzed. To mitigate the strong fading of the first MPC as observed in Figure 3 and to eliminate a bandwidth dependence of the PL, a spatial averaging over at least one fading period must be performed [16]. In the present case, this could be achieved by choosing $K = 3125$, which corresponds to 1.25 m RX movement. The local area channel gain G_C was calculated by integrating over the entire APDP and subtracting the estimated noise power P_N. For omnidirectional antennas, the antenna-deconvolved local area PL is then given by

$$L_{\mathrm{PL|dB}} = -10 \log_{10} G_C + G_{\mathrm{TX|dB}} + G_{\mathrm{RX|dB}}, \tag{2}$$

where G_{TX} and G_{RX} are the antenna gains at the TX and the RX. Figure 4a illustrates the PL for the measurement runs with LOS (no blockage). As explained above, each data point results from 3125 CIRs. Data from distances below 5 m has been discarded, since the received power was significantly reduced by the elevation beamwidth of the antennas (at $d = 2$ m, the RX antenna was directly below the

TX antenna). In addition to the calculated PL, the log-distance least-squares (LS) fit is shown. It relates to the well-known PL exponent model with a floating intercept point (IP) [31]:

$$L_{\mathrm{PL}}(d)_{|\mathrm{dB}} = \overline{L}_{\mathrm{PL}}(d_0)_{|\mathrm{dB}} + 10n\log_{10}\left(\frac{d}{d_0}\right) + X_\sigma, \tag{3}$$

where d denotes the TX–RX distance. The IP $\overline{L}_{\mathrm{PL}}(d_0)_{|\mathrm{dB}}$ is the mean PL at the reference distance d_0, n is the PL exponent and X_σ is a zero-mean Gaussian random variable (in dB) with standard deviation σ, which accounts for shadow fading.

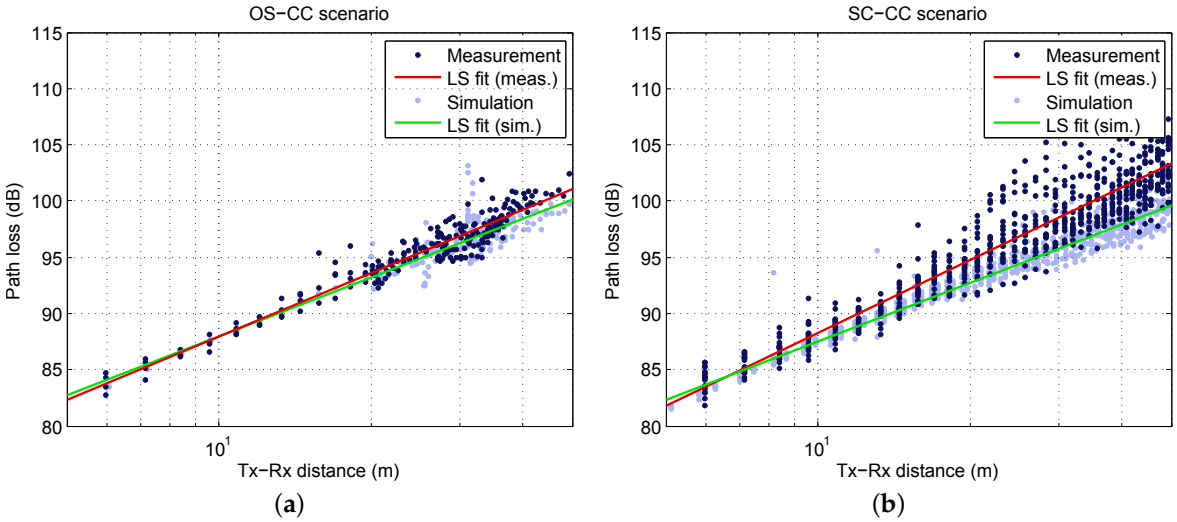

Figure 4. Measured and simulated path loss (PL) versus distance with linear regression line; (**a**) OS-CC scenario; (**b**) SC-CC scenario.

The linear regression yields $\overline{L}_{\mathrm{PL}}(d_0) = 82.3\,\mathrm{dB}$ for $d_0 = 5\,\mathrm{m}$, $n = 1.88$ and $\sigma = 1.03\,\mathrm{dB}$. Hence, the IP is very close to free space propagation (82.0 dB) and n is slightly below. The same evaluation is shown for the SC-CC scenario in Figure 4b. In this case, the IP is $\overline{L}_{\mathrm{PL}}(d_0) = 81.9\,\mathrm{dB}$ for $d_0 = 5\,\mathrm{m}$, and a PL exponent of $n = 2.13$ is obtained. The shadow fading standard deviation is slightly higher, namely $\sigma = 2.03\,\mathrm{dB}$.

Table 2 summarizes the PL parameters for all measured UMi scenarios. The IP is given for the reference distance of $d_0 = 1\,\mathrm{m}$ to be comparable with most of the literature values. Nevertheless, the models should not be applied outside the distance range, which has been used for the LS fit, namely the range where reliable measurement data is available without outage. It is denoted as validity range in Table 2. If for comparison reasons a different reference distance $\tilde{d}_0$ shall be used, the new IP can simply be derived from the model itself by calculating $\overline{L}_{\mathrm{PL}}(\tilde{d}_0)_{|\mathrm{dB}} = \overline{L}_{\mathrm{PL}}(d_0)_{|\mathrm{dB}} + 10n\log_{10}\left(\frac{\tilde{d}_0}{d_0}\right)$. n and σ are not affected as a matter of principle.

Under LOS conditions, n is basically close free-space propagation. A significantly smaller value ($n = 1.62$) only occurs in the street canyon at 10 GHz. It can be caused by a waveguiding effect, which is not significant at 60 GHz. With 57.7 dB, the IP at $d_0 = 1\,\mathrm{m}$ is significantly higher than the theoretical PL in free space (52.4 dB), which is an effect of the LS fit in connection with $n < 2$. (Note that $d = 1\,\mathrm{m}$ is beyond the validity range.)

As expected, the IP is larger for non-line-of-sight (NLOS), since the transition from LOS to NLOS results in a significant drop of the received power [16,32]. It is noteworthy that the NLOS scenario yields surprisingly low PL exponents. This, of course, is related to the scenario, but also because the LS fit has been limited to the distance range 5–80 m (propagation around one building corner only) to avoid outage at both 10 and 60 GHz to maintain full comparability. For the measured RA scenario, the PL exponent is higher for 60 GHz.

Table 2. Path loss (PL) parameters derived from measurements for all UMi scenarios and values from ray tracing simulations for "open square, city center" (OS-CC) and "street canyon, city center" (SC-CC) scenario.

Scenario	Freq. (GHz)	Conditions	Measurement			Simulation			Valid. Range (m)
			$\overline{L}_{PL}$ (1 m)	n (dB)	σ (dB)	$\overline{L}_{PL}$ (1 m) (dB)	n	σ (dB)	
OS-CC	60.0	LOS	69.2	1.88	1.03	69.2	1.74	1.17	5–50
SC-CC	60.0	LOS	67.0	2.13	2.03	69.2	1.72	0.97	5–50
SC-RA	60.4	LOS	67.0	2.07	2.53	-	-	-	10–210
		NLOS	69.7	2.67	4.93	-	-	-	10–80
	10.0	LOS	57.7	1.62	2.95	-	-	-	10–210
		NLOS	61.7	2.10	7.36	-	-	-	10–80

Figure 4 shows the simulated PL in addition to the measured results. For OS-CC, the simulation shows a good agreement with the measurement: the regression lines are very close to each other and the standard deviation is predicted very well (see Table 2). Discrepancies arise for the SC-CC scenario at larger distances: the simulations yield a lower PL exponent and a smaller σ. Making use of recorded videos during the measurements, investigations revealed that the LOS was temporarily obstructed by persons with increasing occurrence for increasing distance. Since pedestrians have not been included in the simulations, these effects cannot be reproduced. For the OS-CC scenario, obstruction was unlikely due to the TX positions on the lawn and the much lower density of pedestrians.

4.3. Delay Spread Statistics

To characterize the temporal spread of the channel, the root mean square (RMS) DS τ_{rms} was calculated on the basis of APDPs according to

$$\tau_{\mathrm{rms}} = \sqrt{\frac{\int_0^{\tau_{\max}} \tau^2 P(\tau)\, d\tau}{\int_0^{\tau_{\max}} P(\tau)\, d\tau} - \tau_{\mathrm{m}}^2}, \quad \tau_{\mathrm{m}} = \frac{\int_0^{\tau_{\max}} \tau P(\tau)\, d\tau}{\int_0^{\tau_{\max}} P(\tau)\, d\tau}, \tag{4}$$

where τ_{m} and $\tau_{\max}$ denote the mean and the maximum excess delay, respectively. A 25 dB threshold relative to the strongest MPC was used to exclude thermal noise and make the results fully comparable [32,33].

The empirical complementary cumulative distribution functions (CCDFs) of all measured and simulated UMi LOS scenarios are illustrated in Figure 5. They show a clear trend towards smaller DS for the SC-RA scenario. This is most probably related to the street canyon width, which is much smaller than for SC-CC environment and compared to the dimensions of the square (OS-CC). In addition, glass façades are dominant in the city center (OS-CC and SC-CC), which are more reflective than the plastered walls in the residential area (SC-RA). The difference in DS is more distinct for the peak values, which occur with lower probability. Table 3 summarizes the statistical parameters.

The 95%-quantile ($Q_{\mathrm{DS},0.95}$) is almost twice as large for SC-CC compared to SC-RA. Furthermore, it can be noticed that the SC-RA channel is slightly more dispersive at 10 GHz, which can be related to relative surface roughness and oxygen absorption at 60 GHz. The latter may already take effect, since the excess traveling distance of reflected paths can easily exceed 100 m. On the other hand, the DS for OS-CC and SC-CC is very similar—μ_{DS} is almost equal. The slightly deformed shape of the CCDF for OS-CC might be due to the fact that—in contrast to SC-CC—the measurement points are not equally distributed over the distance range and overall less DS values are available.

In this context, it is noteworthy that the empirical statistical distribution of the DS (and other channel metrics) depends on the distribution of the measurement points over distances as long as a correlation between the respective metric and distance cannot be excluded. Simulations on system level might assume an equal distribution of users within a cell [10], resulting in a linear increase of the probability with respect to distance. It is therefore advisable to investigate a possible distance dependence and, if applicable, consider it in the channel model (see Section 4.4).

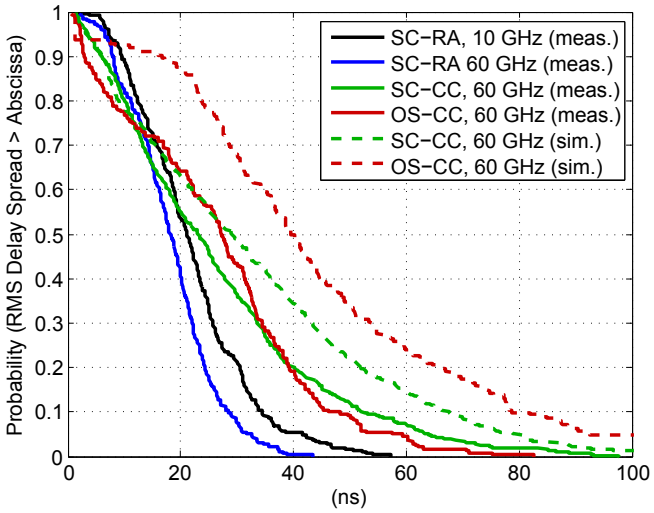

Figure 5. Empirical complementary cumulative distribution functions (CCDFs) of the root mean square (RMS) delay spread (DS) for all measured and simulated UMi line-of-sight (LOS) scenarios.

Table 3. Statistical parameters of the root mean square (RMS) delay spread (DS): mean μ_{DS}, standard deviation σ_{DS}, median m_{DS} and 95%-quantile $Q_{\mathrm{DS},0.95}$.

Scenario	Frequency (GHz)	Conditions	μ_{DS} (ns)	m_{DS} (ns)	σ_{DS} (ns)	$Q_{\mathrm{DS},0.95}$ (ns)
OS-CC	60.0	LOS	26.5	27.3	16.9	59.5
SC-CC	60.0	LOS	26.6	23.2	19.1	63.9
SC-RA	60.4	LOS	18.3	18.2	7.84	32.5
		NLOS	20.9	15.9	13.4	43.8
	10.0	LOS	21.9	21.1	10.2	42.2
		NLOS	37.7	38.2	17.4	67.9

Equivalent evaluations were made with the RT data, available for SC-CC and OS-CC. To ensure full comparability, the CIRs were limited to 250 MHz bandwidth and the RMS DS τ_{rms} was calculated on the basis of APDPs with the same threshold. The CCDFs are also shown in Figure 5. It can be seen that the ray tracer tends to overestimate the DS. The curves of the SC-CC scenario are still fairly close to each other, and the maximum DS is around 100 ns for the measurement as well as for the simulation. However, the deviation is larger for the OS-CC scenario. More detailed comparisons revealed that the RT predicts paths with relatively large delays, which do not exist in the measurement results, or whose power is larger (see also exemplary comparison in Figure 3).

It is important to note that the DS observed by an operational mm-wave system using directional antennas or antenna arrays with analog beamforming will be different from the reported values measured with omnidirectional antennas, since only a subset of propagation paths will be illuminated. However, the purpose of the presented evaluations is to quantitatively investigate the characteristics of the (antenna-decoupled) propagation channel on a fully comparable statistical basis. The results are valuable to parameterize and validate stochastic models and deterministic prediction tools, taking in turn into account directional information from the latter and from measurements e.g., with mechanical antenna steering. A directional channel model is then able to incorporate arbitrary antenna patters and multi-antenna configurations [14].

4.4. Distance Dependence of the Delay Spread

In this section, the dependence of the DS on distance is investigated in more detail. In Figure 6, the DS for the OS-CC and SC-CC scenarios is plotted (in logarithmic) scale against the distance. A distinct increase can be observed for the OS-CC scenario, which motivates the use of a linear regression model. It is expressed by

$$\log_{10}\left(\frac{\tau_{\mathrm{rms}}}{1\,\mathrm{s}}\right)(d) = \alpha + \beta d + \Gamma_{\epsilon}, \tag{5}$$

where α is the IP at $d = 0\,\mathrm{m}$, β is the slope and Γ_{ϵ} is a zero-mean random variable with standard deviation ϵ. The values obtained by LS fitting are given in Table 4.

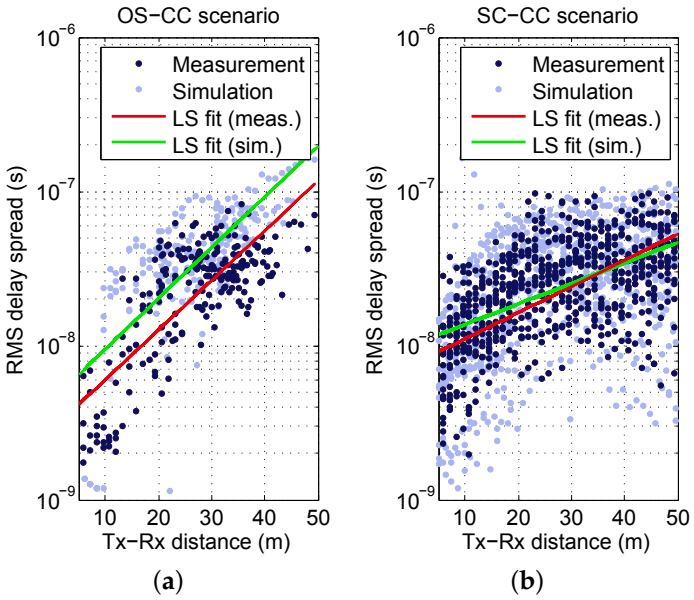

Figure 6. Measured and simulated DS as a function of distance with linear least-squares (LS) fit: (**a**) OS-CC scenario; (**b**) SC-CC scenario.

Figure 6b illustrates the same evaluation for the SC-CC environment, where more samples are available. The DS values similarly increase as a function of distance, though the slope is less steep and a saturation effect can be observed at around 20 m. Hence, the model should not be extrapolated to distances beyond the validity range. It shall be noted that the saturation is not related to an exclusion of values due to an insufficient dynamic range of the APDPs, but the evaluable dynamic range is always large enough.

Figure 6 also includes the DS derived from simulations—the corresponding parameters for the distance-dependent model are given in Table 4. As already seen in Section 4.3, the prediction yields a noticeably higher DS than the measurement for the OS-CC scenario. However, according to Figure 6a, the behavior of the DS over distance is very similar and the linear regressions are parallel. This is also reflected by the model parameters. Whereas the slope β of the simulations fits the measurements, the IP α has a slight difference that matches the offset between the regressions. The larger standard deviation is mainly caused by some data points close to 10^{-9}, where no significant multipaths were predicted. For the SC-CC scenario, see Figure 6b, the simulated DS matches the measured DS very well. The ray tracer reproduces the behavior over a distance in a good manner, and also saturates around 100 ns. Smaller DS in the simulation are caused by non-predicted paths, which increases the standard deviation in Table 4. α is in agreement with the measurements. The slope β varies slightly, which is also obvious in Figure 6.

The measurement results for the SC-RA scenario are depicted in Figure 7. The gradient for 60 GHz is moderate (compared to OS-CC and SC-CC). Nevertheless, it is clear that limiting the set to DS values attributed to distances below 50 m and calculating the empirical CCDF on this basis, would further increase the difference to the OS CC and SC-CC curves in Figure 5. For 10 GHz, the gradient is very small—the calculated DS is almost independent from distance.

Table 4. Parameters for distance-dependent DS model for line-of-sight (LOS): intercept point α, slope β and standard deviation ϵ.

Scenario	Freq. (GHz)	Measurement			Simulation			Valid. Range (m)
		α	β	ϵ	α	β	ϵ	
OS-CC	60.0	−8.54	0.0322	0.262	−8.35	0.0329	0.306	5–50
SC-CC	60.0	−8.13	0.0170	0.287	−8.06	0.0135	0.371	5–50
SC-RA	60.4	−8.05	0.0055	0.185	-	-	-	5–50
	10.0	−7.84	0.0024	0.216	-	-	-	5–50

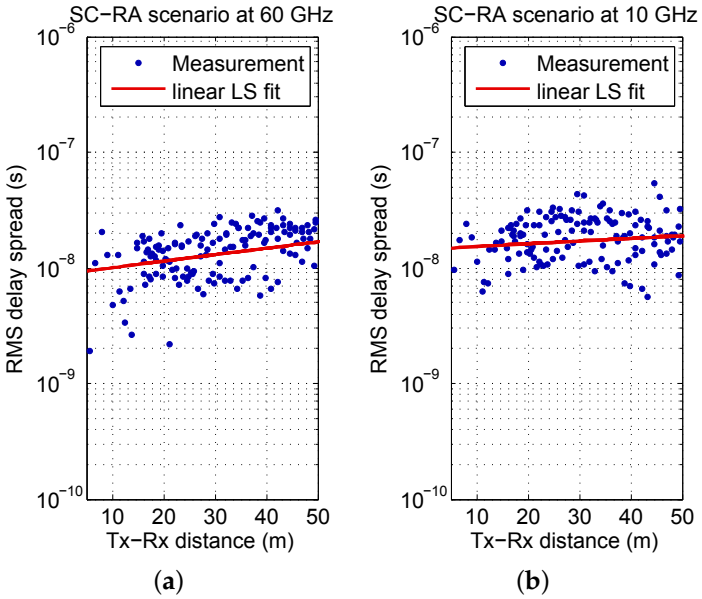

Figure 7. Measured DS as a function of distance with linear LS fit for "street canyon, residential area" (SC-RA) scenario: (**a**) at 60 GHz; (**b**) at 10 GHz.

Overall, it can be concluded that the RMS DS tendentially increases with distance for all measured UMi scenarios and the distance dependence is well predicted by the ray tracer. The potential of a steeper gradient is increased for propagation environments that yield high DS values.

5. Conclusions

The availability of reliable and accurate channel models is one of the crucial aspects for supporting the deployment of ultra-high capacity 5G networks. Proposed models that target a frequency range between 0.5 and 100 GHz and corresponding parameter tables still require further refinement and substantiation by statistically reliable measurement data in multiple frequency bands and various key scenarios.

In this paper, the results of three UMi measurement campaigns performed in Berlin, Germany, have been presented, focusing on the PL and DS of the UMi access channel at 60 and 10 GHz. The evaluations are based on several million channel observations for each scenario, and full comparability has been ensured by uniform data processing. The findings aim to support the validation and improvement of current 5G channel models above 6 GHz. It revealed that the ground reflection has a strong impact on the LOS channel. Since its superposition with the LOS path results in a distinct regular fading of the first resolvable MPC, it will largely affect the instantaneous received power and channel conditions for a mobile user in a quasi-deterministic manner. State-of-the-art GSCMs do not consider this behavior, and it is strongly recommended to further investigate and incorporate this effect.

At 60 GHz, the PL exponents under LOS conditions were found to be close to free-space propagation. A smaller value, namely 1.62, has been observed for 10 GHz in the narrow street canyon. The RMS DS shows a clear dependence on the scenario and its dimensions. Under LOS conditions, it is largest for the open square, and the values for the wide street canyon with modern buildings exceed the results obtained in the residential area. The DS is slightly larger at 10 GHz (data for narrow street canyon only) compared to 60 GHz for LOS, indicating only a weak frequency dependence. For NLOS, however, the difference is significant for the given scenario (median values are 38 and 16 ns for 10 and 60 GHz, respectively). The DS tendentially increases with distance for all measured UMi scenarios, but saturates around 100 ns. The distance dependence is strong for the open square scenario and the wide street in the city center, but less distinct in the narrow street canyon with residential buildings. It is well predicted by complementary RT simulations, although not all channel characteristics could be reproduced with satisfying accuracy. It is important to underpin such simulation results by measurements and to further improve the prediction tools.

Acknowledgments: The research leading to these results has received funding from the European Union's Seventh Framework Programme FP7-ICT-2013-EU-Japan MiWEBA (Millimetre-Wave Evolution for Backhaul and Access) under grant agreement number 608637 and ICT-317669 METIS (Mobile and Wireless Communications Enablers for the Twenty-twenty Information Society).

Author Contributions: Michael Peter, Richard J. Weiler and Wilhelm Keusgen planned and performed the channel measurement campaigns; Barış Göktepe performed the ray tracing simulations and pre-processed the simulation data; Michael Peter analyzed the data and wrote the paper; Barış Göktepe and Kei Sakaguchi supported the writing by providing material to Sections 1 and 3, respectively.

Conflicts of Interest: The authors declare no conflict of interest.

Abbreviations

The following abbreviations are used in this manuscript:

3D	three-dimensional
3GPP	3rd Generation Partnership Project
5G	fifth generation
APDP	averaged power delay profile
CCDF	complementary cumulative distribution function
CIR	channel impulse response
deg	angular degree
DS	delay spread
FPGA	field-programmable gate array
GO	geometrical optics
GPU	graphics processing unit
GSCM	geometry-based stochastic channel model
HIRATE	High Performance Digital Radio Testbed
HPBW	half-power beamwidth
IF	intermediate frequency
IP	intercept point
ITU-R	International Telecommunication Union Radiocommunication Sector
LOS	line-of-sight
LS	least-squares
METIS	Mobile and Wireless Communications Enablers for the Twenty-twenty Information Society
MiWEBA	Millimetre-Wave Evolution for Backhaul and Access
mm-wave	millimeter-wave
MPC	multipath component
NLOS	non-line-of-sight
omni	omnidirectional
OS-CC	open square, city center
PL	path loss
pol.	polarization
RMS	root mean square
RT	ray tracing
RX	receiver
SC-CC	street canyon, city center
SC-RA	street canyon, residential area

TX	transmitter
UMi	urban microcellular
UTD	uniform theory of diffraction

References

1. Boccardi, F.; Heath, R.; Lozano, A.; Marzetta, T.; Popovski, P. Five disruptive technology directions for 5G. *IEEE Commun. Mag.* **2014**, *52*, 74–80.
2. International Telecommunication Union Radiocommunication Sector (ITU-R). *Future Spectrum Requirements Estimate for Terrestrial IMT*; Report ITU-R M.2290-0; December 2013. Available online: http://www.itu.int/pub/R-REP-M.2290-2014 (accessed on 18 August 2016).
3. Ai, B.; Guan, K.; Rupp, M.; Kurner, T.; Cheng, X.; Yin, X.F.; Wang, Q.; Ma, G.Y.; Li, Y.; Xiong, L.; et al. Future railway services-oriented mobile communications network. *IEEE Commun. Mag.* **2015**, *53*, 78–85.
4. ICT-671650 mmMAGIC Project. *Use Case Characterization, KPIs and Preferred Suitable Frequency Ranges for Future 5G Systems between 6 GHz and 100 GHz*; Deliverable D1.1; November 2015. Available online: https://5g-mmmagic.eu/results/ (accessed on 18 August 2016).
5. Rangan, S.; Rappaport, T.S.; Erkip, E. Millimeter-wave cellular wireless networks: Potentials and challenges. *Proc. IEEE* **2014**, *102*, 366–385.
6. Sakaguchi, K.; Tran, G.; Shimodaira, H.; Nanba, S.; Sakurai, T.; Takinami, K.; Siaud, I.; Strinati, E.; Capone, A.; Karls, I.; et al. Millimeter-wave evolution for 5G cellular networks. *IEICE Trans. Commun.* **2015**, *E98-B*, 388–402.
7. International Telecommunication Union Radiocommunication Sector (ITU-R). *Technical Feasibility of IMT in Bands above 6 GHz*; Report ITU-R M.2376; July 2015. Available online: http://www.itu.int/pub/R-REP-M.2376-2015 (accessed on 18 August 2016).
8. International Telecommunication Union Radiocommunication Sector (ITU-R). *Framework and Overall Objectives of the Future Development of IMT for 2020 and Beyond*; Recommendation ITU-R M.2083-0; September 2015. Available online: http://www.itu.int/rec/R-REC-M.2083-0-201509-I (accessed on 18 August 2016).
9. 3rd Generation Partnership Project (3GPP). *Scenarios and Requirements for Next Generation Access Technologies*; Technical Report 3GPP TR 38.913 V0.2.0; February 2016. Available online: http://www.3gpp.org/ftp/Specs/archive/38_series/38.913/38913-020.zip (accessed on 18 August 2016).
10. 3rd Generation Partnership Project (3GPP). *Study on 3D Channel Model for LTE (Release 12)*; Technical Report 3GPP TR 36.873 V12.2.0; July 2015. Available online: http://www.3gpp.org/ftp/Specs/archive/36_series/36.873/36873-c20.zip (accessed on 18 August 2016).
11. ICT-671650 mmMAGIC Project. *Measurement Campaigns and Initial Channel Models for Preferred Suitable Frequency Ranges*; Deliverable D2.1; March 2016. Available online: https://5g-mmmagic.eu/results/ (accessed on 18 August 2016).
12. Aalto University, BUPT, CMCC, Nokia, NTT DOCOMO, New York University, Ericsson, Qualcomm, Huawei, Samsung, Intel, University of Bristol, KT Corporation, University of Southern California. 5G *Channel Model for Bands up to 100 GHz*; 5GCM White Paper; March 2016. Available online: http://www.5gworkshops.com/5GCM.html (accessed on 18 August 2016).
13. ICT-317669 METIS Project. *METIS Channel Models*; Deliverable D1.4, Version 3; July 2015. Available online: https://www.metis2020.com/documents/deliverables/ (accessed on 18 August 2016).
14. Jaeckel, S.; Raschkowski, L.; Borner, K.; Thiele, L. QuaDRiGa: A 3-D multi-cell channel model with time evolution for enabling virtual field trials. *IEEE Trans. Antennas Propag.* **2014**, *62*, 3242–3256.
15. Ai, B.; Cheng, X.; Kürner, T.; Zhong, Z.D.; Guan, K.; He, R.S.; Xiong, L.; Matolak, D.W.; Michelson, D.G.; Briso-Rodriguez, C. Challenges toward wireless communications for high-speed railway. *IEEE Trans. Intell. Transp. Syst.* **2014**, *15*, 2143–2158.
16. Peter, M.; Keusgen, W.; Weiler, R.J. On path loss measurement and modeling for millimeter-wave 5G. In Proceedings of the 9th European Conference on Antennas and Propagation (EuCAP 2015), Lisbon, Portugal, 12–17 April 2015; pp. 1–5.
17. Kim, M.; Takada, J.I.; Chang, Y.; Shen, J.; Oda, Y. Large scale characteristics of urban cellular wideband channels at 11 GHz. In Proceedings of the 9th European Conference on Antennas and Propagation (EuCAP 2015), Lisbon, Portugal, 12–17 April 2015; pp. 1–4.

18. Rappaport, T.S.; MacCartney, G.R.; Samimi, M.K.; Sun, S. Wideband millimeter-wave propagation measurements and channel models for future wireless communication system design. *IEEE Trans. Commun.* **2015**, *63*, 3029–3056.
19. Hur, S.; Cho, Y.J.; Kim, T.; Park, J.; Molisch, A.F.; Haneda, K.; Peter, M. Wideband spatial channel model in an urban cellular environments at 28 GHz. In Proceedings of the 9th European Conference on Antennas and Propagation (EuCAP 2015), Lisbon, Portugal, 12–17 April 2015; pp. 1–5.
20. MacCartney, G.R.; Zhang, J.; Nie, S.; Rappaport, T.S. Path loss models for 5G millimeter wave propagation channels in urban microcells. In Proceedings of the IEEE Global Telecommunications Conference (GLOBECOM), Atlanta, GA, USA, 9–13 December 2013; pp. 3948–3953.
21. Ben-Dor, E.; Rappaport, T.S.; Qiao, Y.; Lauffenburger, S.J. Millimeter-wave 60 GHz outdoor and vehicle AOA propagation measurements using a broadband channel sounder. In Proceedings of the IEEE Global Telecommunications Conference (GLOBECOM), Houston, TX, USA, 5–9 December 2011; pp. 1–6.
22. Hur, S.; Baek, S.; Kim, B.; Chang, Y.; Molisch, A.F.; Rappaport, T.S.; Haneda, K.; Park, J. Proposal on millimeter-wave channel modeling for 5G cellular system. *IEEE J. Sel. Top. Signal Process.* **2016**, *10*, 454–469.
23. Oestges, C.; Hennaux, G.; Gueuning, Q. Centimeter- and millimeter-wave channel modeling using ray-tracing for 5G communications. In Proceedings of the IEEE 82nd Vehicular Technology Conference (VTC2015-Fall), Boston, MA, USA, 6–9 September 2015; pp. 1–5.
24. Weiler, R.J.; Peter, M.; Keusgen, W.; Wisotzki, M. Measuring the busy urban 60 GHz outdoor access radio channel. In Proceedings of the IEEE International Conference on Ultra-Wideband (ICUWB), Paris, France, 1–3 September 2014; pp. 166–170.
25. Weiler, R.J.; Peter, M.; Kühne, T.; Wisotzki, M.; Keusgen, W. Simultaneous millimeter-wave multi-band channel sounding in an urban access scenario. In Proceedings of the 9th European Conference on Antennas and Propagation (EuCAP 2015), Lisbon, Portugal, 12–17 April 2015; pp. 1–5.
26. Keusgen, W.; Kortke, A.; Peter, M.; Weiler, R.J. A highly flexible digital radio testbed and 60 GHz application examples. In Proceedings of the 43rd European Microwave Conference (EuMC 2013), Nuremberg, Germany, 6–11 October 2013; pp. 740–743.
27. Felbecker, R.; Raschkowski, L.; Keusgen, W.; Peter, M. Electromagnetic wave propagation in the millimeter wave band using the NVIDIA OptiX GPU ray tracing engine. In Proceedings of the 6th European Conference on Antennas and Propagation (EuCAP 2012), Prague, Czech Republic, 26–30 March 2012; pp. 488–492.
28. Göktepe, B.; Peter, M.; Weiler, R.J.; Keusgen, W. The influence of street furniture and tree trunks in urban scenarios on ray tracing simulations in the millimeter wave band. In Proceedings of the 46th European Microwave Conference (EuMC 2015), Paris, France, 3–7 September 2015; pp. 195–198.
29. Cuinas, I.; Pugliese, J.P.; Hammoudeh, A.; Sanchez, M. Comparison of the electromagnetic properties of building materials at 5.8 GHz and 62.4 GHz. In Proceedings of the IEEE 52nd Vehicular Technology Conference (VTC2000-Fall), Boston, MA, USA, 24–28 September 2000; Volume 2, pp. 780–785.
30. Correia, L.M.; Frances, P.O. Estimation of materials characteristics from power measurements at 60 GHz. In Proceedings of the IEEE International Symposium on Personal, Indoor and Mobile Radio Communications (PIMRC), The Hague, The Netherlands, 18–23 September 1994; Volume 2, pp. 510–513.
31. Feuerstein, M.; Blackard, K.; Rappaport, T.; Seidel, S.; Xia, H. Path loss, delay spread, and outage models as functions of antenna height for microcellular system design. *IEEE Trans. Veh. Technol.* **1994**, *43*, 487–498.
32. International Telecommunication Union Radiocommunication Sector (ITU-R). *Propagation Data and Prediction Methods for the Planning of Short-Range Outdoor Radiocommunication Systems and Radio Local Area Networks in the Frequency Range 300 MHz to 100 GHz*; Recommendation ITU-R P.1411-8; July 2015. Available online: https://www.itu.int/rec/R-REC-P.1411-8-201507-I/en (accessed on 18 August 2016).
33. International Telecommunication Union Radiocommunication Sector (ITU-R). *Multipath Propagation and Parameterization of Its Characteristics*; Recommendation ITU-R P.1407-5; September 2013. Available online: https://www.itu.int/rec/R-REC-P.1407-5-201309-I/en (accessed on 18 August 2016).

This reprint is the published version of the article. The article is available under https://doi.org/10.3390/s16081330 and was reprinted without changes.

5.3 Comparability of UMi Path Loss Results

It has already been pointed out that it is increasingly important to pool and combine available measurement results to provide a strong basis for frequency-agile 5G channel models. In this context, a quite fundamental question arises, namely to what extent results from independent measurement campaigns of different researchers can be compared in general. The data may have been collected with different channel sounders and subjected to different post-processing.

As introduced in Section 3.7, CL 1 and CL 2 comparisons require the data to be convertible to an identical representation with the same boundary conditions. This implies, for example, that CIRs must be compared using the same bandwidth, unless the bandwidth itself is the comparison criterion. Formally, this is not needed for evaluations at higher levels. For example, the PL or the DS can be derived from measurement results that exhibit a different bandwidth. However, care must be taken to use the same quantity definitions and ensure a corresponding processing/estimation.

The investigations in Section 5.2 revealed that the mm-wave outdoor access channel is subject to strong spatial fading. Its distinctiveness depends on the measurement bandwidth. Nevertheless, it is shown in the following publication that consistent PL model parameters can be derived by appropriate spatial averaging irrespective of the bandwidth. On the other hand, the sample size of PL values and their distribution over distance can heavily affect the estimation results. This underlines the fact that a large amount of data is typically required to derive statistically reliable model parameters, but an aligned post-processing contributes to making results comparable.

Contribution

This paper was authored by me and I made the related evaluations. The sample measurements were taken from a campaign, which was carried out jointly by my colleagues and myself. The co-authors supported the work by taking part in discussions and provided proof-reading.

On Path Loss Measurement and Modeling for Millimeter-wave 5G

Michael Peter*, Wilhelm Keusgen*, Richard J. Weiler*
*Fraunhofer Heinrich Hertz Institute, Berlin, Germany, michael.peter@hhi.fraunhofer.de

***Abstract*—This paper addresses the derivation of path loss models and model parameters based on measurement data, in particular with a view to current modeling work for 5G millimeter-wave systems. In order to ensure accurate and comparable results, which are independent from the measurement hardware, it is of utmost importance to incorporate a sufficiently large data set and use a coherent data processing including spatial averaging.**

I. Introduction

In order to assess the performance of wireless communication systems, it is a fundamental issue to properly predict the signal power arriving at the receiver, since it decisively determines the achievable data rate on the links. Rather than modeling the received power directly, it is typically calculated via the path loss (PL) – the loss of power from the transmitter to the receiver [1]. PL models and parameters are derived from channel measurement data. They are bound to a certain propagation environment, antenna arrangement, carrier frequency and distance range. In view of the development of comprehensive channel models for future millimeter-wave (mm-wave) 5G systems, the harmonization of PL models is an important step [2].

Crucial aspects with regard to the comparability of results are related to the measurement hardware, the measurement procedure and data processing. Common models describe the local mean PL as a function of the distance [1]. It is frequently disregarded that the estimation of model parameters hence must be based on locally averaged power values. If averaging is omitted, the values are subject to small-scale fading and the model parameters will depend on the measurement bandwidth. As a consequence, results from campaigns performed with different bandwidth cannot be compared.

In this paper, the above mentioned issues with regard accuracy and comparability of PL models are investigated. Guidelines for related measurements and spatial averaging are derived in view of estimating accurate, comparable parameters. The impact of the sample size is addressed as well as the choice of the PL model reference value. Though the considerations are not confined to a specific frequency, they are in particular relevant for current work on mm-wave 5G channel modeling.

II. Fundamental Considerations and Definitions

A. Large-scale and Small-scale Fading

In this paper, PL is defined as the loss of power (density) of a wave as it propagates from the transmit to the receive antenna. The PL at distance d for pure line-of-sight (LOS) transmission is equivalent with the free-space loss L_{fs}, which can be calculated with the well-known Friis equation [3]. However, under multipath and non-line-of-sight (NLOS) conditions, the PL will deviate from L_{fs}.

The equivalent baseband channel impulse response (CIR) of the propagation channel at a certain receive point can be described by a superposition of N paths or "rays":

$$\widetilde{h}(\tau) = \sum_{n=1}^{N} a_n \delta(\tau - \tau_n), \quad \tau_n = \frac{l_n}{c}, \tag{1}$$

where a_n and τ_n denote the complex weight and the delay (arrival time) of the n^{th} path, respectively, c is the speed of light in vacuum and l_n the traveling distance of the n^{th} path. The path weights a_n depend on several parameters related to the setup geometry and the propagation environment. It is assumed that the amplitudes $|a_n|$ as well as the number N of paths are constant when e.g. the receiver (RX) is moving within a local area. Any changes of $|a_n|$ and N are attributed to large-scale (slow) fading.

Channel measurements only yield a bandlimited version $h(\tau)$ of $\widetilde{h}(\tau)$. In $h(\tau)$, paths do no longer appear as Diracs, but as pulses with a certain width, which overlap when they are close to each other. Since the phases $\angle a_n$ of superimposing paths change even for small displacements of the transmitter (TX) or the RX, $|h(\tau)|$ fluctuates, though the amplitudes $|a_n|$ are constant. This effect is denoted as small-scale (fast) fading.

PL models typically aim to predict the mean of the received power in a local area. This means that, in the presence of small-scale fading, spatial averaging (or some kind of statistical processing, see Section V-C) must be applied to measurement data prior to calculating PL values and estimating model parameters. Assuming that wideband channel measurement data is available in form of K bandlimited CIRs $h_k(\tau)$ at the receive points k in a wide-sense stationary (WSS) region, the local mean PL can be derived by

$$L_{\mathrm{PL|dB}} = -10 \log_{10} \frac{1}{K} \sum_{k=1}^{K} G_{C,k}, \tag{2}$$

where $G_{C,k}$ is the channel gain (normalized received signal power) at the k^{th} receive point:

$$G_{C,k} = \int_0^{\tau_{\max}} |h_k(\tau)|^2 \, d\tau, \tag{3}$$

where $\tau_{\max}$ denotes the maximum (relevant) delay. Omitting the averaging in (2) (setting $K = 1$) yields the "instantaneous path loss" L'_{PL}. Without bandwidth limitation L'_{PL} equals L_{PL} due to the absence of small-scale fading. However, for

evaluations based on bandlimited data, appropriate averaging must be applied in general.

It shall be mentioned that we assume in this paper that the influence of noise is negligible. Noise may lead to biased or incomplete data, which is to be taken into account for parameter estimation [4].

B. Path Loss Model

In the following, the established (single-slope) path loss exponent model is used, also referred to as log-distance law. It is given by

$$L_{\mathrm{PL}}(d)_{|\mathrm{dB}} = \overline{L}_{\mathrm{PL}}(d_0)_{|\mathrm{dB}} + 10n\log_{10}\left(\frac{d}{d_0}\right) + X_\sigma, \quad (4)$$

where $\overline{L}_{\mathrm{PL}}(d_0)$ is the intercept/reference point (overall mean path loss at the reference distance d_0), n is the path loss exponent and X_σ is a zero-mean Gaussian random variable (in dB) with standard deviation σ. The log-normal distribution takes (large-scale) shadowing effects of propagation paths into account which occur over a large number of measurement locations at the same distance. The parameters n, $\overline{L}_{\mathrm{PL}}(d_0)$ and σ are usually estimated by linear fitting of measurement data in the least squares (LS) sense. Frequently, $\overline{L}_{\mathrm{PL}}(d_0)$ is set to the free-space value $L_{\mathrm{fs}}(d_0)$ rather than estimating it (free-space vs. floating-point reference value). It seems natural to do so for LOS scenarios, because multipath power at the close-by reference distance d_0 is expected to be very small compared to the power of the direct path. However, care should be taken with respect to NLOS scenarios. This will be illustrated in Sections V-A and V-B.

C. Bandwidth and Resolution

In principle, small-scale fading may be avoided if B is sufficiently large to resolve every propagation path, which corresponds to the condition

$$B \geq \left[\min_{n=1\ldots N-1}(\Delta\tau)_n\right]^{-1}, \quad (5)$$

where $(\Delta\tau)_n = \tau_{n+1} - \tau_n$ is the inter-arrival time (IAT) between the n^{th} and the $(n+1)^{\text{th}}$ path. Since the delays τ_n are directly related to the traveling distances l_n via $\tau_n = \frac{l_n}{c}$, the minimum IAT is linked to the geometry of the propagation environment and the locations of the TX and RX. Measurements have shown that, in contrast to lower frequencies, the mm-wave mobile channel is mainly constituted by a limited number of most relevant propagation paths, e.g. the direct (LOS) path and several single-reflected paths [5]. In the simplest case, severe fading can be caused by the superposition of the LOS path and a ground-reflected path – it will be denoted as "two-ray case". The difference of the rays' traveling distance can be calculated by

$$\Delta l = \sqrt{d^2 + (h_{\mathrm{TX}} + h_{\mathrm{RX}})^2} - \sqrt{d^2 + (h_{\mathrm{TX}} - h_{\mathrm{RX}})^2} \quad (6)$$

with h_{TX} and h_{RX} being the height of the TX and RX antenna above the ground. Small values of Δl are critical in sense of fulfilling (5), as they result in small IATs. They occur when d is large compared to h_{TX} and h_{RX}, e.g. for larger distances in an access scenario with street level deployment of small-cell base stations. For $d \gg h_{\mathrm{TX}} + h_{\mathrm{RX}}$, Δl can be approximated by

$$\Delta l \approx \frac{2h_{\mathrm{TX}}h_{\mathrm{RX}}}{d}. \quad (7)$$

For fixed antenna heights we then obtain

$$B \geq \frac{d_{\max}c}{2h_{\mathrm{TX}}h_{\mathrm{RX}}}, \quad (8)$$

where $d_{\max}$ is the largest occurring distance between TX and RX in the scenario. (8) is a simple criterion to assess, whether small-scale fading in the two-ray case can be avoided for a given system bandwidth. If we e.g. assume a small-cell access scenario with $h_{\mathrm{TX}} = 3.5\,\mathrm{m}$, $h_{\mathrm{RX}} = 1.5\,\mathrm{m}$ and $d_{\max} = 100\,\mathrm{m}$, (8) demands $B \geq 2.86\,\mathrm{GHz}$.

The considerations equally apply to reflections at large objects like walls and buildings. In this case, h_{TX} and h_{RX} define the distance of the TX and the RX antenna to the reflecting surface. In a LOS multipath scenario, criterion (8) must be fulfilled for each single-reflected path individually, but this is only a necessary condition compared to (5). However, if there is at least one strong reflection in a LOS scenario for which (8) is not fulfilled, small-scale fading has to be taken into account. It is obvious that excessive bandwidth would needed for positions close to reflecting walls (e.g. $B \geq 15\,\mathrm{GHz}$ for $h_{\mathrm{TX}} = h_{\mathrm{RX}} = 1\,\mathrm{m}$ and $d_{\max} = 100\,\mathrm{m}$), which can hardly be realized. .

It shall be mentioned that, principally, small-scale fading can also be prevented by using directive antennas. However, the half-angle beamwidth must be smaller than the angular separation of arriving paths, which is hard to fulfill for larger distances unless pencil beam antennas are applied.

III. Spatial Averaging

Spatial averaging is used to estimate the local mean PL in the presence of small-scale fading. For the sake of simplicity, the two-ray case with $|a_1| = |a_2| = \frac{1}{\sqrt{2}}$ and $\tau_1 \neq \tau_2$ is used as basis for evaluations. We expect to obtain a local mean PL of 0 dB. However, a narrowband system will see an "effective channel" with a maximum weight of $|a_{\max}| = 2$ and a minimum weight of $|a_{\min}| = 0$. Hence taking a channel snapshot at a random position, will result in an instantaneous PL between $-3\,\mathrm{dB}$ and $\infty\,\mathrm{dB}$.

Figure 1 depicts the standard deviation σ_{PL} of the estimated PL as a function of the "normalized averaging range" R_{avrg}. It is defined as the ratio between the segment size used for averaging (with equidistant spatial sampling) and the "spatial fading period", the separation of two spatial nulls or maxima (in general multipath cases related to the minimum IAT) in the respective dimension. Without averaging, σ_{PL} converges to approx. 8.0 dB. Even small averaging ranges significantly reduce the error. It goes to 0 at $R_{\mathrm{avrg}} = 1$. The first "error sidelobe" reaches 0.68 dB at $R_{\mathrm{avrg}} \approx 1.4$. These results for the two-ray narrowband case show that it would be desirable to choose $R_{\mathrm{avrg}} = 1$ (or an integer) for averaging. However, this would require knowledge of the particular spatial fading period at each location and is not applicable to general multipath conditions. Based on the results above, $R_{\mathrm{avrg}} \geq 1$ (without violating the WSS condition) can be seen as rule of thumb.

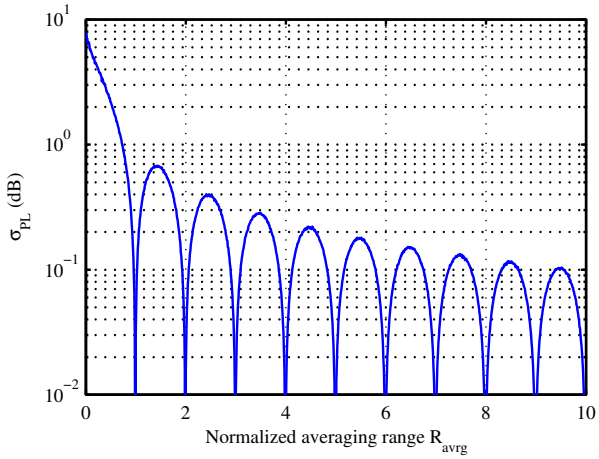

Figure 1. Standard deviation of the estimated PL as a function of the normalized averaging range.

The spatial fading period with respect to the variation of d, h_{TX}, or h_{RX} in the two-ray case with approximation (7) can be calculated as

$$d_{\mathrm{fp}} = \frac{\lambda d^2}{2h_{\mathrm{TX}}h_{\mathrm{RX}} - \lambda d} \quad \text{and} \quad h_{\mathrm{fp,TX/RX}} = \frac{\lambda d}{2h_{\mathrm{RX/TX}}}, \qquad (9)$$

respectively. Applying this to the small-cell access example ($h_{\mathrm{TX}} = 3.5\,\mathrm{m}$, $h_{\mathrm{RX}} = 1.5\,\mathrm{m}$ and $d_{\max} = 100\,\mathrm{m}$) and limiting to the variation of one variable, $R_{\mathrm{avrg}} = 1$ is e.g. achieved for segment sizes of $\Delta d \approx 5.0\,\mathrm{m}$, $\Delta h_{\mathrm{TX}} \approx 17\,\mathrm{cm}$ or $\Delta h_{\mathrm{RX}} \approx 7.1\,\mathrm{cm}$.

If wideband results are available, increasing the bandwidth has the same effect as increasing the spatial averaging range. The equivalent to the normalized spatial averaging range with respect to bandwidth is given by

$$R_B = B\left[\min_{n=1\ldots N-1}(\Delta\tau)_n\right], \qquad (10)$$

which can be regarded as a kind of channel oversampling factor. With wideband data, the rule of thumb relaxes to

$$R_{\mathrm{avrg}} + R_B \geq 1 \qquad (11)$$

and hence allows a trade-off between bandwidth and spatial averaging requirements. For the two-ray example with approximation (7), the fading period f_{fp} in the frequency domain is

$$f_{\mathrm{fp}} = \frac{dc}{2h_{\mathrm{TX}}h_{\mathrm{RX}}} \quad \text{and} \quad R_B = \frac{2Bh_{\mathrm{TX}}h_{\mathrm{RX}}}{dc}. \qquad (12)$$

E.g. assuming $B = 250\,\mathrm{MHz}$ for the small-cell example, however, results in a rather small $R_B = 0.0875$ at $d = 100\,\mathrm{m}$.

IV. Evaluations with 60 GHz Measurement Data

In this section, the impact of the measurement bandwidth and spatial averaging is illustrated based on measurement data from a 60 GHz channel measurement campaign in a street canyon environment related to the access channel for small-cell lamp post deployment [6]. CIR snapshots with 250 MHz bandwidth were taken with a fine spacing of 0.4 mm, so that small-scale fading effects can be investigated and sufficient data is available for spatial averaging. Figure 2 shows the instantaneous PL for an exemplary LOS measurement run calculated on a narrowband (NB) basis (equivalent to CW measurements) as well as on a wideband (WB) basis for $B = 250\,\mathrm{MHz}$.

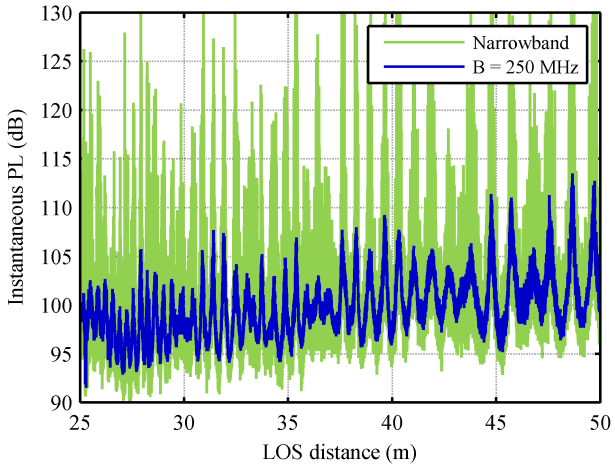

Figure 2. Evolution of instantaneous PL for exemplary measurement run.

The instantaneous narrowband PL is subjected to very large fluctuations due to small-scale fading. They drastically reduce in the wideband case. However, the periodic fading, which is mainly constituted by the superposition of the direct and the ground-reflected path, is still considerable. With $R_B \approx 0.35$ at $d = 25\,\mathrm{m}$ and $R_B \approx 0.18$ at $d = 50\,\mathrm{m}$ (two-ray assumptions), R_B is too small in view of estimating local mean PL values.

Figure 3a shows the scatter plot of the (instantaneous) PL versus distance, incorporating all measurement runs for LOS-dominant propagation together with the LS fit. The corresponding PL model values are given in Table I. As expected from Figure 3a, the estimated σ is much larger for the NB case, which means that the estimated value does not reflect (large-scale) shadow fading only, but also includes unwanted small-scale fading effects.

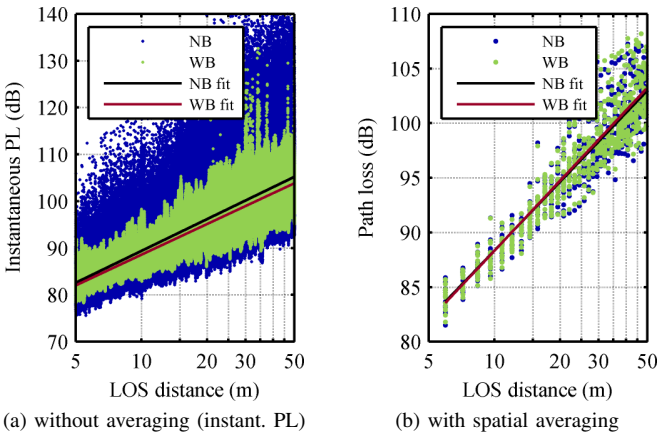

(a) without averaging (instant. PL) (b) with spatial averaging

Figure 3. Path loss versus distance together with least square fit; wideband (WB) and narrowband (NB) evaluation.

Figure 3 shows the equivalent evaluation with preceding spatial averaging. Averaging has been performed over 3125

adjacent snapshots, which corresponds to an RX movement of $\Delta d = 1.25\,\text{m}$ and guarantees $R_{\text{avrg}} \geq 1$ for the two-ray assumption. In contrast to the case without averaging, the NB and WB PL values in Figure 3 are nearly congruent. The PL model parameters are given in Table I. They are practically identical for the NB and the WB case – including σ. This highlights that proper spatial averaging yields accurate and comparable results, even though the measurement bandwidth differs.

Table I
COMPARISON OF ESTIMATED PARAMETERS FOR SINGLE-SLOPE PL MODEL

Bandwidth	Spatial averaging	$\overline{L}_{\text{PL}}(d_0)$ (dB)	n	σ (dB)
NB	-	82.6	2.26	5.08
WB	-	82.0	2.18	2.85
NB	1.25 m	82.1	2.09	2.05
WB	1.25 m	81.9	2.13	2.04

It shall be stressed that the parameters were estimated by free LS fitting to a large data set (more than two million CIRs nearly equally distributed over the distance range, resulting in 760 averaged values). Using the free-space reference value in this LOS-dominant case would yield almost the same results, since the free-space PL at 5 m is 82.0 dB. However, this does not apply to arbitrary measurement scenarios (see Sections V-A and V-B).

V. FURTHER CONSIDERATIONS

A. Limited Sample Size

So far, it is has been assumed that a large amount of PL data in the entire distance range is available for model fitting. In this section, some basic considerations will be made to assess the consequences on estimated model parameters when the sample size is limited. It is assumed that the PL actually follows (4). The sample size is limited to K PL values related to the distances d_k. The PL samples are ideal – in the sense that they are not subjected to small-scale fading or noise – and the parameters of the model (4) are estimated by linear regression in the LS sense. We exemplarily analyze the estimated PL exponent $\hat{n}$. The theory related to linear regression and LS estimation tells us that $\hat{n}$ is normally distributed with the variance

$$\operatorname{Var}\hat{n} = \frac{\sigma^2}{100}\left(\frac{1}{K} + \frac{\overline{x}^2}{(K-1)\,s_x^2}\right), \tag{13}$$

where

$$\overline{x} = \frac{1}{K}\sum_{k=1}^{K} x_k \quad \text{and} \quad s_x^2 = \frac{1}{K-1}\sum_{k=1}^{K}(x_k - \overline{x})^2 \tag{14}$$

with

$$x_k = \log_{10}\left(\frac{d_k}{d_{\text{ref}}}\right) \tag{15}$$

It is obvious that $\operatorname{Var}\hat{n}$ increases when σ increases, but σ is fixed for a given propagation scenario and cannot be influenced. In general, there are three possibilities to minimize estimation errors: 1) increase the sample size K, 2) increase the measurement range, 3) optimize the spatial distribution of the samples. From (14) it can be concluded that, in principal, it is optimal to maximize $x_k - \overline{x}$, hence to measure only at the minimum and the maximum distance. However, this must be viewed with caution, since such data does not provide any hint, whether (4) is an appropriate model. In practice, samples for many different distances should be available to motivate either (4) or another PL model, e.g. the dual-slope model. However, it is clear that samples at x_k-values, which are close to the mean $\overline{x}$, only contribute little to estimation accuracy. It is very important to involve large and especially small distances d_k, since $x_k - \overline{x}$ is calculated in logarithmic scale.

In order to further assess the estimation error in a practical case, we assume that PL model parameters for $d_{\text{ref}} = 5\,\text{m}$ shall be derived based on equally spaced "ideal" PL measurement samples with $\sigma = 4$ in the range $d_{\text{min,m}}$ to $d_{\text{max}} = 100\,\text{m}$. Figure 4a shows the standard deviation $\sigma_{\hat{n}}$ (square root of (13)) of the estimation error as a function of the sample size K for two different cases. In the first case, the samples are distributed over the whole range ($d_{\text{min,m}} = d_{\text{ref}} = 5\,\text{m}$), whereas the values are concentrated in the upper part in the second case ($d_{\text{min,m}} = 50\,\text{m}$). It is obvious that the distance range of the samples has

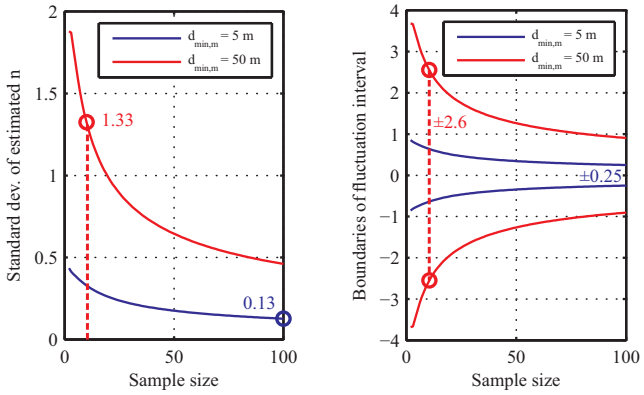

(a) standard deviation (b) central fluctuation interval

Figure 4. Standard deviation and central fluctuation interval of $\hat{n}$ as a function of the sample size for two different sampling ranges $[d_{\text{min,m}}, d_{\text{max}}]$.

a big impact: for $K = 2$ (first value in Figure 4a), $\sigma_{\hat{n}}$ is more that four times as large for $d_{\text{min,m}} = 50\,\text{m}$ compared to $d_{\text{min,m}} = 5\,\text{m}$ (1.88 vs. 0.45). In order to achieve the same error as for $K = 2$ and $d_{\text{min,meas}} = 5\,\text{m}$, $K > 100$ would be required for $d_{\text{min,m}} = 50\,\text{m}$. If we denote $d_{\text{min,m}} = 5\,\text{m}$ in combination with $K = 100$ as "good" Case 1 and $d_{\text{min,m}} = 50\,\text{m}$ with $K = 10$ as "bad" Case 2, $\sigma_{\hat{n}}$ is approx. 10 times larger for Case 2 compared to Case 1 (1.33 vs. 0.13, see Figure 4a).

The central fluctuation interval of $\hat{n}$ with respect to a confidence level of 95% is shown in Figure 4b. The interval is proportional to $\sigma_{\hat{n}}$, and consequently, approx. 10 times larger for Case 2 (± 2.6) compared to Case 1 (± 0.25). It shall be stressed that a fluctuation interval of ± 2.6 means that, assuming e.g. $n = 2$, the linear regression may yield values in the range $\hat{n} = -0.6 \ldots 4.6$. Such large estimation errors, of course, are not acceptable.

These results show that it is crucial to base path loss evalu-

ations on a proper data basis involving sufficient samples with a appropriate spatial distribution. The considerations focus on the PL exponent. However, similar evaluations can also be made for the intercept point. In particular, the estimation error drastically increases if $d_{\text{min,m}}$ is much larger than d_{ref} or if only a small number of samples close to d_{ref} is available.

B. Path Loss Model Reference Point

In the current literature on mm-wave outdoor PL modeling, the intercept point in (4) is often set to the free-space value (free-space reference point, FSRP), instead of determining it by a free fit of measurement data (floating reference point, FRP). This is reasonable and helpful for LOS scenarios, especially if only few measurement samples close to d_{ref} available. However, it must be ensured that the setup is well calibrated and that the antenna gains are properly taken into account.

In the same way, the FSRP model is frequently also used for NLOS scenarios, though it can hardly provide a good fit as we will illustrate in the following. Figure 5 shows a characteristic example of the measured path loss at 60 GHz as the RX moves behind a building. The propagation conditions change from LOS to NLOS between $d = 5.8$ m and 6.0 m. As expected, the PL increases abruptly, by approx. 17 dB in the shown example. For illustration it is assumed that the NLOS part of the data should be modeled by the FRP or the FSRP model. Figure 5 shows the corresponding LS fits to the averaged samples (1 m averaging) with $d_{\text{ref}} = 5$ m. It is obvious that they largely differ.

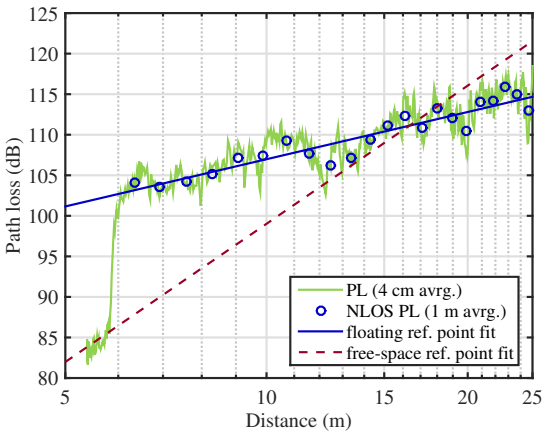

Figure 5. Measured 60 GHz path loss for transition from LOS to NLOS.

The estimated FRP parameters are $\overline{L}_{\text{PL}}(d_0) = 101$ dB and $n = 1.93$, compared to $\overline{L}_{\text{PL}}(d_0) = L_{\text{fs}}(d_0) = 82.0$ dB and $n = 5.66$ for the FSRP approach. Since the FSRP model (with respect to NLOS) presumes LOS at d_{ref} and NLOS at greater distances, it implies that a transition takes place in between. However, the transition leads to a steep increase of the PL, which largely deviates from the log-distance law. It can be summarized that 1) using the FSRP for NLOS data actually is a mixed LOS/NLOS modeling approach, 2) the FSRP model is ill-suited for fitting pure NLOS data – it may significantly underestimate the PL at small distances – and 3) NLOS PL exponents of the FRP and the FSRP model cannot be compared. It is hence highly recommended to use the FRP for NLOS modeling. Of course, according to Section V-A, sufficient measurement samples close to d_{ref} are required to keep estimation errors low.

C. Median Path Loss

In order to estimate the local path loss, we focused on mitigating small-scale effects by averaging over a wide-sense stationary region. In [7] it is emphasized that calculating the arithmetic mean can be problematic and using the median value instead, has several advantages. Indeed, the median is more robust against measurement errors and may considerably increase the accuracy of the estimation close to the noise floor. Nevertheless, the findings in this paper also apply to median values in an analogous manner. For linear regression, it makes no difference, whether it is applied to mean or median values. Moreover, all considerations related to system bandwidth and averaging range are valid in principle, though "averaging" is to be substituted by "determination of the median".

VI. Conclusion

In this paper, we illustrated that it is crucial to involve a proper data basis as well as proper pre-processing of measurement data to derive accurate path loss values and model parameters. To mitigate small-scale fading, the local PL is to be estimated via averaging of channel gain (power) values within an appropriately chosen local area/segment. In order to motivate a particular PL model and to determine precise parameters, the sample size of PL values for each propagation scenario must be large enough and the samples should be distributed over the whole distance range.

Acknowledgment

The research leading to these results has received funding from the European Union's Seventh Framework Programme (FP7-ICT-2013-EU-Japan) under grant agreement number 608637.

References

[1] J. Salo, L. Vuokko, H. El-Sallabi, and P. Vainikainen, "Shadow fading revisited," in *Vehicular Technology Conference, 2006. VTC 2006-Spring. IEEE 63rd*, vol. 6, 2006, pp. 2843–2847.

[2] T. Jämsä and T. S. Rappaport, "Harmonization of 5G path loss models," in *COST IC1004 10th Management Committee and Scientific Meeting*, 2014.

[3] H. Friis, "A note on a simple transmission formula," *Proceedings of the IRE*, vol. 34, no. 5, pp. 254–256, 1946.

[4] T. Abbas, C. Gustafson, and F. Tufvesson, "Pathloss estimation techniques for incomplete channel measurement data," in *COST IC1004 10th Management Committee and Scientific Meeting*, 2014.

[5] W. Keusgen, R. J. Weiler, M. Peter, and M. Wisotzki, "Propagation measurements and simulations for millimeter-wave mobile access in a busy urban environment," in *9th International Conference on Infrared, Millimeter, and Terahertz Waves, IRMMW-THz 2014, Sep 14–19, Tucson, USA*, 2014.

[6] R. J. Weiler, M. Peter, W. Keusgen, and M. Wisotzki, "Measuring the busy urban 60 GHz outdoor access radio channel (invited)," in *IEEE International Conference on Ultra-Wideband, ICUWB 2014, Sep 1–3, Paris, France*, 2014.

[7] H. Bühler, M. Christoph, R. Zelenka, and T. Gyoergyfalvay, "On measuring fast fading signals for channel modelling," in *COST IC1004 11th Management Committee and Scientific Meeting*, 2014.

5.4 Distance-Dependent Shadow Fading and MPC-Centric Path Loss

In Section 5.2, a coherent analysis of the PL and the DS in UMi scenarios has been presented. The estimated PL parameters are associated with the well-known PL exponent model with log-normal shadowing (standard deviation σ). In the following publication, additional investigations on the PL are presented for the street canyon scenario in the city center (SC-CC scenario in Section 5.2) [KWPW14]. As alternative to a fixed σ, it is proposed to model the parameter as a function of distance to better reflect the behavior of the measurement data. Furthermore, an MPC-centric path loss analysis is proposed that models dominant MPCs individually. In the first approximation, it can be used to assess the performance of a beamsteering system for LOS and OLOS.

Contribution

The street canyon measurement campaign was primarily planned by me and carried out jointly by my colleagues and myself. I analyzed the data, derived the models and wrote most of the manuscript. R. J. Weiler provided Figure 1. B. Göktepe performed the initial ray tracing simulations and provided input to Section III C. The co-authors further provided proof-reading.

Propagation Measurements and Simulations for Millimeter-Wave Mobile Access in a Busy Urban Environment

Wilhelm Keusgen, Richard J. Weiler, Michael Peter, Mike Wisotzki and Barış Göktepe
Fraunhofer Heinrich Hertz Institute, Berlin, Germany

***Abstract*—The authors have performed 60 GHz wideband channel measurements in Berlin to gain knowledge on millimeter-wave outdoor propagation in dense urban environments. In this paper first results for a street canyon are presented, focusing on path loss analysis of the line-of-sight-dominant small-cell access channel. They reveal that the local area path loss is very close to free-space propagation. Reflected paths do not contribute significantly to the received power as long as the line of sight (LOS) is unobstructed. However, they are usually strong enough to maintain a link if the LOS is blocked. The dominant multipath contributions can also be predicted by ray tracing simulations, though further calibration is needed to accurately determine their strength.**

I. Introduction

The trend in mobile radio access networks points toward ever increasing amounts of data over the next years. Evolution of the access technologies beyond the current worldwide adopted LTE-A standard are discussed under the term 5G. Within 5G, mobile millimeter-wave radio access is seen as a key enabling technology to improve the network capacity in dense urban environments [1], [2]. Successful design of such new systems will rely on profound knowledge of the outdoor radio channel. Comparing to the legacy frequency bands, the knowledge at millimeter-wave frequencies is still very limited [3]. We have performed channel measurements and accompanying ray tracing simulations in a dense urban environment at 60 GHz with a typical small-cell access setup and present initial results focusing on path loss evaluations.

II. Outdoor Channel Measurements

To provide a data basis for investigations, a measurement campaign related to outdoor small-cell access has been performed in Berlin. The Potsdamer Straße was selected as measurement site, representing a typical busy city street, where millimeter-wave small-cell base stations are expected to be deployed first. Figure 1 shows the scenario. The street canyon has a width of 51.5 m and is bordered by modern high-rise buildings. The transmitter (TX) of the channel sounder was placed at the 12 positions marked with red stars in Figure 1. It was mounted on a pole of 3.5 m height to simulate a typical small-cell deployment on street furniture. The receiver (RX) – representing the mobile terminal – was mounted on a trolley at a height of 1.5 m and moved along the sidewalk at constant speed of 0.5 m/s from 50 m to one side of the TX positions to 50 m to the other side, as indicated by the colored lines. On the sidewalks there are typical objects such as trees, bus stops, trash cans and bicycle stands. However, at the great majority of receiver positions there was an unobstructed LOS to the transmit antenna.

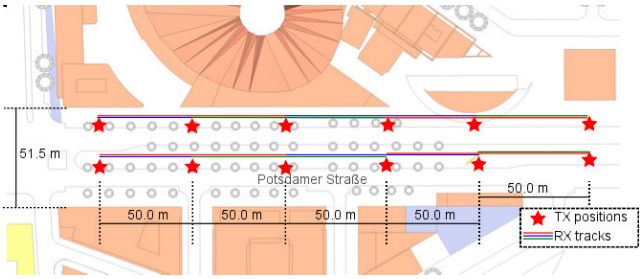

Figure 1. Street canyon measurement scenario.

The utilized channel sounder is based on a self-developed, flexible FPGA-based hardware platform [4]. The center frequency of the signal was 60 GHz and the measurement bandwidth 250 MHz. The transmit power was 15 dBm. Vertically polarized antennas with omnidirectional pattern in azimuth and 2 dBi gain were used at both the TX and RX. A measurement snapshot was taken every 800 µs, corresponding to 0.4 mm displacement between adjacent RX positions. Each snapshot took 65.5 µs and contains a channel impulse response (CIR). Using these settings, multipath components (MPCs) with up to 130 dB attenuation can be identified. The overall data set acquired for this scenario comprises 2.5 million CIRs.

III. Evaluations

Initial evaluations have been made to characterize the path loss (PL) and to gain information on the strength of the MPCs. Section III-A is related to the "classical" PL model, whereas in Section III-B an MPC-centered approach is presented.

A. Local Area Path Loss

In this section we characterize the PL as a function of the TX-RX distance. The aim is to derive a model that enables the prediction of the average received power in a local area. In the present case, we focus on the LOS-dominant street canyon access channel. The measurement results reveal that, besides the LOS path, the ground reflected path is of particular importance. Especially for larger distances, the its of incidence with respect to the street surface becomes quite small. The magnitude of the Fresnel reflection coefficients hence increase and the impact of the surface roughness diminishes. The same applies to reflections at close-by facades. As the excess delays of these reflected paths become small, they may not be

resolved by the measurement system. Consequently, in view of evaluating the mean PL, it is not sufficient to consider wideband power at a single receive point, but local averaging is obligatory. The local area is to be chosen large enough to compensate for the fluctuations of these dominant MPCs.

In the present case, the ground-reflected path already coincides with the direct one when the horizontal TX-RX distance exceeds 7.9 m. Averaging has been performed over $K_{\mathrm{avrg}} = 3125$ snapshots, which corresponds to an RX movement of 1.25 m. This ensures averaging over at least one fading period of the first MPC (LOS path and ground reflection) without introducing excessive errors for small distances due to distance-dependent power contributions of the paths within the local area. Fast fading due to moving cars is also averaged out. Figure 2 shows a scatter plot of the local average PL derived in this manner, together with the linear least-squares (LS) fit (log-log scale). Antenna gains have been subtracted. As expected

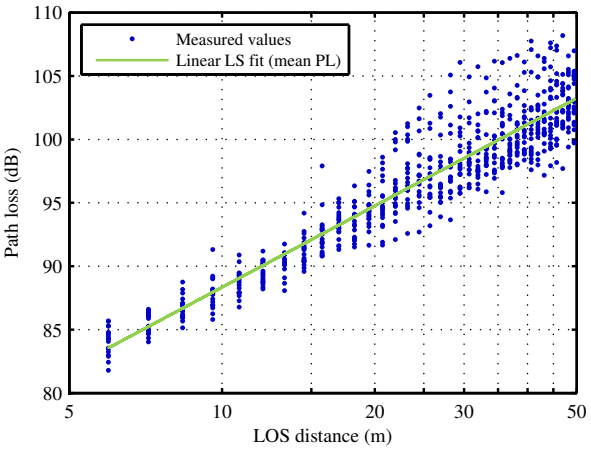

Figure 2. Measured local average path loss and linear LS fit.

for the LOS-dominant case, the result motivates the usage of the well-known path loss exponent model according to:

$$L_{\mathrm{PL}}(d)_{|\mathrm{dB}} = \overline{L}_{\mathrm{PL}}(d_0)_{|\mathrm{dB}} + 10n\log_{10}\left(\frac{d}{d_0}\right) + X_\sigma, \quad (1)$$

where d_0 is the close-by reference distance, $\overline{L}_{\mathrm{PL}}(d_0)$ is the intercept point (mean PL at the reference distance) and n is the path loss exponent. X_σ represents a zero-mean Gaussian random variable (in dB) with standard deviation σ. The model parameters are summarized in Table I. n is only slightly higher

Table I
PARAMETERS FOR LOCAL AREA PATH LOSS MODEL

$\bar{L}_{\mathrm{PL}}(d_0 = 5\,\mathrm{m})$	n	σ	α	β	d_σ
81.9 dB	2.13	2.04 dB	0.17 dB	0.08 dB/m	18.0 m

than 2 and the standard deviation σ is quite small. Overall, the path loss is very close to free space propagation, especially up to 15 m distance. However, Figure 2 reveals that the spread of the measured values increases with distance. A deeper analysis shows that σ first increases, but saturates at a certain point. Therefore, we introduce the following model for the distance-dependent standard deviation $\sigma(d)$:

$$\sigma(d) = \begin{cases} \alpha + \beta d, & d_0 \le d < d_\sigma \\ \alpha + \beta d_\sigma, & d \ge d_\sigma. \end{cases} \quad (2)$$

$\sigma(d)$ may be used alternatively to the fixed value σ to achieve a better accuracy (LS fit values see Table I).

We would like to emphasize again that the evaluations are based on omnidirectional measurements. Having subtracted the antenna gains, the PL model is related to the propagation channel without the antennas. One could claim that such a model is not relevant for millimeter wave mobile links, since they will most probably make use of electronically steerable antennas to achieve a sufficient link budget. However, by incorporating the adaptive antenna gain at the TX (G_T) and the RX (G_R), the calculation $P_{R|\mathrm{dBm}} = G_{T|\mathrm{dBi}} + G_{T|\mathrm{dBi}} + P_{T|\mathrm{dBm}} - L_{\mathrm{PL}}(d)_{|\mathrm{dB}}$, where $P_{R|\mathrm{dBm}}$ is the received and $P_{T|\mathrm{dBm}}$ is the transmit power, can be seen as an upper bound for the local received power. The more the power is concentrated in one propagation path, the closer this bound will be to the received power that can be achieved by a beamsteering system. In contrast, if the channel is constituted by numerous diffuse components of similar power, the predicted RX power will be much higher than the achievable one. However the measurement results indicate that the channel power is mainly spread over a limited number of dominant paths. A closer view on this issue is presented in Section III-B.

B. Individual Path Loss

As mentioned before, the "classical" PL model can be used to predict the received power for the omnidirectional case and provides an upper bound in view of beamsteering systems. In this section we present a slightly different beamsteering-oriented PL model, which is related to the power of strong MPCs rather than to the total power. Figure 3 shows a scatter plot of the individual PL of the five strongest MPCs. The latter have been derived by peak search in averaged power delay profiles (APDPs). In this case an averaging factor of $K_{\mathrm{avrg}} = 250$ has been used (0.2 s, 10 cm RX displacement), which mainly averages out fast fading due to cars and small-scale fading due to interfering paths, which arrive from substantially different directions. The idea behind this kind of averaging is that these fluctuations would not occur in combination with adaptive antennas, which form a sufficiently narrow beam. Table II summarizes the PL model parameters derived by the same linear LS fitting procedure as used in Section III-A, but applied individually for each of the strongest MPCs. In average, the 2nd strongest MPC (MPC_2) is approximately 15 dB weaker than the strongest one at 5 m. However, as n_2 is smaller than n_1, the difference reduces to 7.9 dB at 50 m. MPC_3 is 6.9 dB and 4.3 dB weaker than MPC_2 at 5 m and 50 m, respectively. According to Table II, $\sigma_1(d)$ increases with distance up to 29.2 m, the reverse tendency can be observed for the other MPCs. (2) simplifies to a single slope approximation within the validity range.

C. Ray Tracing Simulations

To support the omnidirectional measurements and to attain a comprehensive understanding of the spatial channel properties,

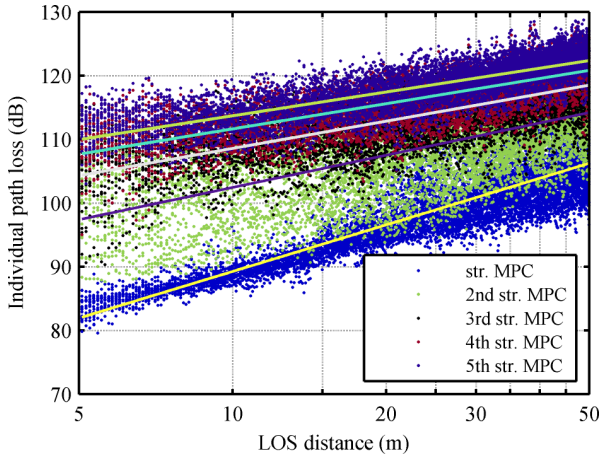

Figure 3. Path loss of the strongest five multipath components (MPCs) for distances from 5 to 50 m.

Table II
PARAMETERS FOR INDIVIDUAL PATH LOSS MODEL

Parameter	$k=1$	$k=2$	$k=3$	$k=4$	$k=5$
$\bar{L}_{\mathrm{PL},k}(d_0)$ (dB)	82.2	97.4	104.3	107.7	110.0
n_k	2.41	1.68	1.42	1.31	1.24
σ_k (dB)	3.49	5.01	3.37	2.73	2.42
α_k (dB)	-0.15	6.40	3.78	3.10	2.71
β_k (dB/m)	0.15	-0.053	-0.017	-0.016	-0.013
$d_{\sigma,k}$ (m)	29.2	>50	>50	>50	>50

ray tracing simulations have been set up. The ray tracing tool is an own development, basing on hardware accelerated operation on the graphics board (GPU) [5]. The measurement environment is incorporated in form of a 3D computer model (Figure 1 is a top view). For initial simulations, all building surfaces have been assumed to be glass with $\varepsilon_r = 8.9 - j0.13$ [6]. The ground has been modeled with $\varepsilon_r = 6.14 - j0.30$, the value defined for concrete in [7], since the sidewalk was paved with concrete setts, and the trees with $\varepsilon_r = 1.57 - j0.096$, the value for wood [7]. Up to two transmissions and two reflections have been admitted. Figure 4 shows an exemplary comparison of a measured and a simulated APDP with $K_{\mathrm{avrg}} = 3125$ at a LOS distance of 7.2 m. Overall, they show a good agreement. However, not all relevant MPCs can be found – at least with the correct strength. Further evaluations are needed to identify the origin of the related reflections – possible are light poles or even trash cans, which have not yet been included in the 3D model. The power of the first MPC is slighly overestimated. Such behavior is symptomatic and more distinct for greater distances. The reason for this is that the ground-reflected ray is not yet well modeled. Path loss evaluations based on the simulated data performed with exactly the same processing as used for the measurement data (see Section III-A) yield a path loss exponent of $n = 1.6$. Thus, the dielectric parameters as well as the angle-dependent reflection behavior need a closer look, especially related to the ground-reflected ray.

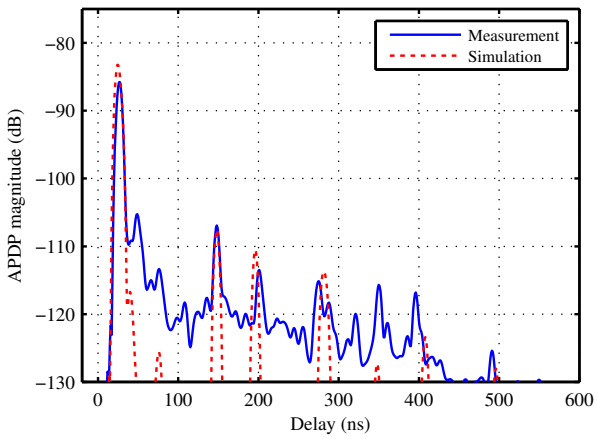

Figure 4. Exemplary comparison of measurement and ray tracing APDP.

IV. CONCLUSION

In this paper a measurement campaign on the 60 GHz outdoor access channel and related path loss evaluations have been presented. The total path loss is mainly determined by the LOS path, but reflected paths carry sufficient power to profit from them when the LOS is temporarily blocked. Initial ray tracing simulations yield promising results, but the material properties and the origin of missing relevant MPCs need a closer look to further improve the prediction accuary.

ACKNOWLEDGMENT

The research leading to these results has received funding from the European Union's Seventh Framework Programme (FP7-ICT-2013-EU-Japan) under grant agreement number 608637.

REFERENCES

[1] F. Boccardi, R. Heath, A. Lozano, T. Marzetta, and P. Popovski, "Five disruptive technology directions for 5G," *Communications Magazine, IEEE*, vol. 52, no. 2, pp. 74–80, 2014.

[2] R. J. Weiler, M. Peter, W. Keusgen, E. Calvanese-Strinati, A. De Domenico, I. Filippini, A. Capone, I. Siaud, A.-M. Ulmer-Moll, A. Maltsev, T. Haustein, and K. Sakaguchi, "Enabling 5G backhaul and access with millimeter-waves," in *European Conference on Networks and Communications, EuCNC 2014*, 2014.

[3] T. Rappaport, F. Gutierrez, E. Ben-Dor, J. Murdock, Y. Qiao, and J. Tamir, "Broadband millimeter-wave propagation measurements and models using adaptive-beam antennas for outdoor urban cellular communications," *Antennas and Propagation, IEEE Transactions on*, vol. 61, no. 4, pp. 1850–1859, 2013.

[4] W. Keusgen, A. Kortke, M. Peter, and R. Weiler, "A highly flexible digital radio testbed and 60 GHz application examples," in *Microwave Conference. EuMC 2013. 43rd European*, 2013.

[5] R. Felbecker, L. Raschkowski, W. Keusgen, and M. Peter, "Electromagnetic wave propagation in the millimeter wave band using the NVIDIA OptiX GPU ray tracing engine," in *6th European Conference on Antennas and Propagation, EuCAP 2012*, 2012.

[6] I. Cuinas, J.-P. Pugliese, A. Hammoudeh, and M. Sanchez, "Comparison of the electromagnetic properties of building materials at 5.8 GHz and 62.4 GHz," in *Vehicular Technology Conference, 2000. IEEE VTS-Fall VTC 2000. 52nd*, vol. 2, 2000, pp. 780–785 vol.2.

[7] L. Correia and P. Frances, "Estimation of materials characteristics from power measurements at 60 GHz," in *Personal, Indoor and Mobile Radio Communications, 1994. Wireless Networks - Catching the Mobile Future., 5th IEEE International Symposium on*, 1994, pp. 510–513 vol.2.

5.5 Frequency Dependence of the Delay Spread

The most striking, but also most challenging feature of a comprehensive 5G channel model is its applicability to a huge frequency range, ideally from below 1 GHz to 100 GHz. Even assuming that the model can reproduce all relevant propagation effects in principle, it is still a major task to determine accurate parameters. It is obvious that the path loss of the model must increase with frequency. However, for most of the other model components, the tendency is not yet clear, and it is under discussion if they should be modeled as a function of frequency or not. This also applies to the delay spread (DS).

In [JPS+16, ICT16b], an initial 5G channel model 10–80 GHz is proposed with associated parameter tables that have been derived from literature values. Based on the latter, the DS is modeled to decline with frequency, where the slope depends on the propagation scenario. This trend is line with the observations for the conference room presented in Section 4.1, where the average DS at 60 GHz was less than half the value at 5 GHz for LOS as well as for OLOS. The evaluations for the street canyon in the residential area at 60 and 10 GHz, see Section 5.2, yield a similar ratio for NLOS (slightly above 0.5). For LOS, however, the difference is much less distinct (14% lower median values). Medbo et al. [MSA16] could not observe an obvious frequency trend of the DS in measurement results for an indoor office environment between 6 and 60 GHz .

In the following publication, a statistical analysis of the DS is presented, based on data from a multi-frequency measurement campaign in an urban street canyon [PWU+16]. The four bands with the center frequencies 10.25, 28.5, 41.5 and 82.5 GHz were measured simultaneously and the data is therefore ideally suited to investigate frequency-dependent effects. Distortions by a limited repeatability of the measurements that could easily be caused by a dynamic environment, for example by varying occupancy of parking space, moving cars and pedestrians, are excluded.

It reveals that the largest DS values occur for 10.25 GHz when a high relative evaluation threshold is used. An evaluation based on a reduced data set for the distance range 10–60 m shows that the DS is lowest at 82.5 GHz in comparison to the other frequencies. Nevertheless, a pronounced frequency dependence can not be identified for the present scenario taking into account the results for all frequencies, evaluation thresholds and distance ranges. In conjunction with the aforementioned findings, this indicates that frequency dependence of the DS is a scenario-dependent phenomenon. Note that the distance-dependence of the DS has also been found to be scenario-dependent. It also reveals, however, that the results are very sensitive to data selection and processing—a fact that significantly complicates the comparison

and fusion of published values. The measurement and evaluation conditions should always be considered carefully.

Contribution

The multi-frequency measurement campaign was planned and conducted jointly by R. Weiler, F. Undi, W. Keusgen and myself. F. El-Kanawati pre-processed the measurement data under my supervision. I analyzed the data, derived the results and wrote the manuscript. S. Jaeckel helped to abridge the manuscript. The other co-authors proofread the paper and suggested smaller changes.

Investigations on the Frequency Dependence of the Delay Spread in an UMi Street Canyon Scenario

Michael Peter, Richard J. Weiler, Fabian Undi, Farouk El-Kanawati, Stephan Jaeckel,
Leszek Raschkowski, Lars Thiele, Kei Sakaguchi, and Wilhelm Keusgen
Fraunhofer Heinrich Hertz Institute, Einsteinufer 37, 10551 Berlin, Germany

Abstract - **A channel measurement campaign was carried out in Berlin, Germany, aiming to provide multi-frequency data for the urban microcellular (UMi) access channel in the street canyon. Four bands (10.25, 28.5, 41.5 and 82.5 GHz) were measured simultaneously. In this paper, statistical evaluations on the frequency dependence of the root-mean-square delay spread (DS) under line of sight (LOS) conditions are presented. The largest values occur for 10.25 GHz when a high relative evaluation threshold is used, and the values are smallest for 82.5 GHz. However, a distinct and clear frequency dependence cannot be observed for the measured scenario. The estimated DS is very sensitive to data selection and processing.**

Index Terms — Channel measurements, mm-wave propagation, delay spread, frequency dependence

1. Introduction

Fifth generation (5G) mobile networks will need to make use of much higher frequencies to provide ultra-high data rates and capacity [1]. The targeted frequency bands comprise a huge range up to 100 GHz. Since the provision of an accurate reference channel model is essential for enabling link and system level simulations at these high frequencies, there are strong related activities in the research community and standardization bodies like 3GPP and ITU-R. Most of the work strongly builds upon state-of-the-art three-dimensional (3D) geometry-based stochastic channel models (GSCMs) that have been developed in recent years for the lower frequency bands [2], [3], [4], [5]. The ultimate target is to elaborate a flexible and comprehensive frequency-agile channel model that covers the entire range up to 100 GHz for targeted 5G scenarios rather than providing a model for specific bands only. With this respect, the question arises to what extend the large-scale parameters (LSPs), like DS and the angular spreads, depend on frequency.

2. Channel Sounder Setup

The measurements were carried out with a multi-frequency wideband channel sounder based on dedicated hardware. The schematics and photos are shown in [2]. The sounder consists of four parallel transmit/receive chains, which were used at the carrier frequencies 10.25, 28.5, 41.5 and 82.5 GHz. The same baseband signal with 1.5 GHz bandwidth was feed into the 28, 41 and 82 GHz transmit chains. Due to regulatory reasons, the bandwidth at 10 GHz was limited to 500 MHz. The signal generators periodically repeated a PAPR-optimized 2.56 µs long sounding sequence. A transmit power of 30 dBm could be achieved at 10 and 28 GHz. It was lower for 41 GHz (20 dBm) and 82 GHz (11 dBm). Self-built omnidirectional antennas with vertical polarization at both, the transmitter (Tx) and the receiver (Rx) were used. Synchronization between Tx and Rx is ensured via temperature-controlled rubidium clocks and the system is calibrated on site via back-to-back measurements. At the receiver, the signals are amplified, down-converted, filtered and sampled at IF stage. Real-time averaging (averaging factor of 100) over multiple sequence periods further improves the signal-to-noise ratio of the received signal. Post-processing, e.g. down-conversion to baseband, and further averaging, is performed offline.

3. Measurement Scenario and Procedure

The measurement campaign was performed in a busy shopping street in downtown Berlin, Germany. The uniform street canyon is 2 km long, has a width of approximately 20 m and is bordered by 7–8-storey buildings. The Tx was placed on the sidewalk close to an intersection with 10 m distance from the building corner and at 5 m height. The Rx was mounted on a camera dolly at a height of 1.5 m and moved along the sidewalk on seven measurement tracks with a constant speed of 0.5 m/s. In conjunction with a snapshot separation of 2 ms, this corresponds to a spacing of 1 mm between adjacent channel observations. Three of the tracks were measured in LOS condition. Each started at 10 m distance from the Tx and consisted of six consecutive 50 m segments, adding up to 300 m total track length with a maximum distance of 310 m. Details can be found in [2].

4. Delay Spread Analysis

For each segment of 50 m length, 50,000 channel impulse responses (CIRs) are available. In a first processing step the CIRs were reduced to 500 MHz bandwidth and a Kaiser window (parameter $\beta = 6$) was applied in the frequency domain to reduce the sidelobes in the delay domain. Lowpass-interpolated versions (upsampling factor 4) of the CIRs were used for further processing. The DS was calculated based on averaged power delay profiles (APDPs). Each APDP was obtained by averaging over K successive CIRs according to

$$P(\tau) = \frac{1}{K}\sum_{k=1}^{K} |h_k(\tau)|^2,$$

This paper [PWU+16] was published by the same authors in the Proceedings of the 2016 International Symposium on Antennas and Propagation (ISAP 2016) and is reused under the permission of the IEICE. INSPEC Accession Number: 16602061. Available online: http://ieeexplore.ieee.org/document/7821230 [07/2017]. This reprint is the publisher's version of the paper.

where $P(\tau)$ denotes the APDP and $h_k(\tau)$ is the k^{th} CIR. An averaging factor of $K = 100$ was used, which corresponds to a spatial averaging over 10 cm. A relative threshold Γ with respect to the maximum in $P(\tau)$ was applied and contributions below the threshold were discarded [6]. Great care has been taken to ensure that the dynamic range of the APDPs was always large enough to support the respective threshold in order to exclude distortions of the estimated values by noise. In cases where the evaluation threshold was not supported by an APDP of at least one band, the data of all bands was discarded for the comparison.

Figure 1 shows the empirical cumulative distribution functions (CDFs) of the DS for three different thresholds, namely 15, 20 and 25 dB at a Tx-Rx distance of up to 110 m. These are based on 3000 APDPs for each frequency band. As expected, increasing the threshold yields higher values and the CDFs shift to the right. The results for the three frequencies are very similar for $\Gamma = 15$dB and $\Gamma = 20$ dB. There is only a small trend towards larger spreads for 10 GHz, which occurs with lower probability. However, for $\Gamma = 25$ dB this trend becomes more distinct, whereas the curves for 28.5 and 41.5 GHz are still practically congruent.

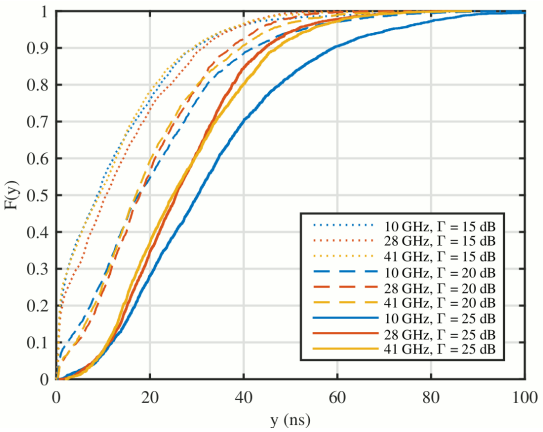

Figure 1. Empirical CDFs of RMS delay spread for 10–110 m distance range and relative thresholds of 15, 20 and 25 dB.

Results on the comparison of all four frequencies are illustrated in Figure 2. In this case, a threshold of 15 dB was chosen and the evaluated distance range was limited to 10–60 m. Compared to the results based on the distance range 10–110 m lower DSs occur with higher probability. The CDFs are less smooth as only 600 APDPs for each frequency are available that exhibit the required dynamic range at the respective Rx position for each measured band (after bandwidth limitation of the upper bands), including 82 GHz. The DS for 82 GHz is clearly smaller than for the lower bands. However, for the lower bands a trend of a potential frequency dependence cannot be identified based on this subset of data samples. Figure 2 shows that the considered distance range can impact the results and that a large sample size is beneficial to enable clear conclusions. Preliminary investigations on the dependence of the DS on Tx-Rx distance indicate that lower values and lower variations occur for very small distances (10–20 m). Both tend to increase with distance, but saturate at distances between 30 and 50 m.

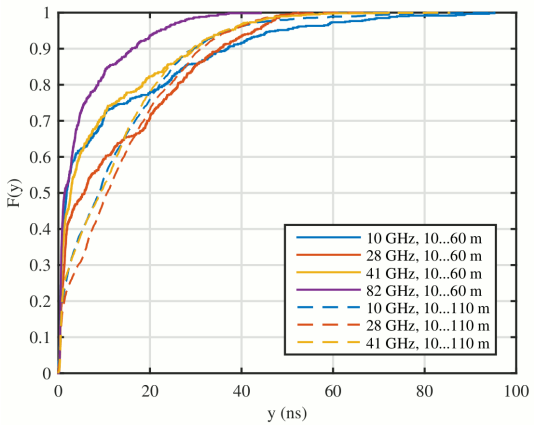

Figure 2. Empirical CDFs of RMS delay spread for 10–60 m Tx-Rx distance and relative threshold of 15 dB.

5. Conclusion

An initial statistical analysis of the DS based on LOS data of a multi-frequency channel measurement campaign in an UMi street canyon scenario has been presented. In order to ensure the greatest comparability, the data for the higher bands was reduced to the same bandwidth as used for 10.25 GHz, namely 500 MHz. The same relative evaluation threshold was applied to the power delay profiles for all bands. Based on the data for distances between 10 and 110 m, it can be shown that the distribution of the DS for the lower bands (10, 28, 41 GHz) is very similar for evaluation thresholds of 15 and 20 dB. For a threshold of 25 dB, there is a trend to higher values for 10 GHz. A statistical analysis based on a reduced data set for the distance range 10–60 m shows that the DS is tendentially lower at 82 GHz in comparison to the other frequencies. However, taking into account all results, a distinct and clear frequency dependence cannot be identified. In conjunction with findings in the literature, these results indicate that the frequency dependence is scenario-specific and may e.g. differ for indoor and outdoor environments.

Acknowledgment

The research leading to these results received funding from the European Commission H2020 programme under grant agreement n°671650 (5G PPP mmMAGIC project).

References

[1] F. Boccardi, R. Heath, A. Lozano, T. Marzetta, and P. Popovski, "Five disruptive technology directions for 5G," Communications Magazine, IEEE, vol. 52, no. 2, pp. 74–80, 2014.

[2] ICT-671650 mmMAGIC D2.1, "Measurement Campaigns and Initial Channel Models for Preferred Suitable Frequency Ranges," Mar. 2016.

[3] 3GPP TR 36.873 V12.2.0, "Study on 3D channel model for LTE," Tech.Rep., 2015.

[4] ICT-317669 METIS D1.4, "METIS Channel Models," Jul. 2015.

[5] S. Jaeckel, L. Raschkowski, K. B¨orner, and L. Thiele, "QuaDRiGa: A 3-D Multi-Cell Channel Model with Time Evolution for Enabling Virtual Field Trials," IEEE Trans. Antennas Propag., vol. 62, pp. 3242–3256, 2014.

[6] ITU-R P.1411-8, "Propagation data and prediction methods for the planning of short-range outdoor radiocommunication systems and radio local area networks in the frequency range 300 MHz to 100 GHz," Tech. Rep., 2015.

6 Conclusions

In this thesis, I presented channel measurement campaigns in indoor, in-vehicle and outdoor environments. They were conducted to investigate the characteristics of millimeter-wave wireless channels in the context of future wireless local area networks as well as 5G mobile backhaul and access. For this purpose, I built up and utilized modular channel sounder setups that allowed to acquire wideband channel impulse responses at numerous receive points. The measurement results were evaluated with focus on the path loss, shadowing and time dispersion.

Comparative measurements at 5 and 60 GHz showed an almost constant offset of the path loss for line-of-sight in the conference room environment in line with the difference of the free-space loss. The average delay spread in this scenario was found to be less than half that at 5 GHz. Investigations with different antenna configurations lead to the conclusion that time dispersion for LOS scenarios can be reduced by applying directional antennas, but a reduction for arbitrary propagation conditions, in particular obstructed line-of-sight (OLOS) cannot be guaranteed. Contrary to expectations, an omnidirectional configuration does not necessarily outperform configurations with moderately directional antennas, though a larger relative loss must be considered in the latter case when the LOS is obstructed.

Measurements in a mockup of a wide-bodied aircraft passenger cabin revealed that the large-scale characteristics of the 60 GHz in-cabin channel are similar to that of an indoor channel. However, very distinct clusters in the power delay profile were observed with strong multipaths. They could be attributed to reflections at the metalized cabin windows. The 60 GHz in-car channel is much less time dispersive. The small link distances guarantee a sufficient signal-to-noise ratio even for OLOS. Interference from other cars using the same frequency band is uncritical under relaxed traffic conditions, but can become a limiting factor for crowded urban scenarios.

Specific investigations on human body shadowing (HBS) confirmed that diffraction around a person is significant. It results in a continuous transition of the received power from LOS to OLOS and in distinct oscillations during the shadowing event. Characteristic oscillations can even be observed before the person reaches the geometric LOS. This fact can be exploited to predict shadowing events and to make

suitable preparations. The effects can be well reproduced by a double knife-edge model and a uniform theory of diffraction model, with the body being approximated by a perfectly conducing stripe or cylinder, respectively.

The 60 GHz small-cell backhaul channel in a residential area is clearly dominated by the superposition of the direct and the ground-reflected path. It can be approximated by a two-ray model. Flat fading can be an crucial issue for deployments on street level and is to be considered for system design and mounting. Frequency agility is an effective way to mitigate related losses. The increase of the antenna gains does not automatically translate to lower fading, but primarily reduces frequency selectivity.

The ground reflection also has a significant influence on the urban microcellular (UMi) access channel. In contrast to transmission at sub-6 GHz frequencies, mm-wave links will be typically shorter than the breakpoint distance. As a result, the ground reflection can cause distinct quasi-periodic flat fading or, for small distances and large bandwidths, frequency selectivity.

Compared to typical indoor channels, excess delays of occurring multipaths are increased by one order of magnitude, which is in line with the scaling of the propagation environment. The channel is relatively sparse on the delay axis. For LOS, the path loss exponents are close to two. However, a path loss analysis on individual multipath components (MPCs) for the wide street canyon confirmed that significant multipath power is utilizable by beamsteering systems if the direct path is blocked.

The delay spread shows a clear dependence on the scenario and a pronounced distance dependence for the open square and the wide street canyon in the city center. For the latter case, the shadow fading increases with distance. Comparative ray tracing simulations support these dependencies. However, not all the channel characteristics could be reproduced with satisfactory accuracy, indicating that prediction tools should be used as complement for measurements rather than as stand-alone approach to gain channel-related information. A statistical analysis of street canyon measurement data between 10 and 82 GHz did not yield a clear trend of the delay spread as a function of frequency. In conjunction with the findings in the conference room and results in the literature, this indicates that its frequency dependence is a scenario-dependent phenomenon.

As pointed out in this work, evaluation results and conclusions can be very sensitive to data selection and processing. Therefore, when comparing and combining results, it is important to ensure that they are based on equivalent definitions. Using the example of the path loss, it was shown that consistent model parameters can be derived from measurement data by appropriate spatial averaging, irrespective of the bandwidth. Since the sample size can heavily impact the estimation results, a

large amount of data is needed to derive reliable model parameters. To analyze the dependence of the channel on certain parameters like frequency or distance range, the other parameters and boundary conditions need to be fixed. This especially applies if the dependency is only weak or not existent at all and underlines the importance of examining such aspects within the same measurement campaign.

Planned future activities include measurements with the multi-frequency channel sounder in further microcellular environments. In collaboration with other researchers, first steps based on virtual array analysis have been taken to derive directional information from the spatially sampled channels [NMP+16, MPK+16]. The results are promising, but further studies need to be undertaken in order to better understand dominant sources of error and to enable a largely automatic data processing. In order to resolve the ambiguity in the determination of the azimuth angle caused by the limitation to a one-dimensional virtual array, alternative antenna setups are being investigated for expansion to several dimensions. In this thesis, the transmitter and the receiver were either fixed or moved slower than walking speed. Future measurements will also consider higher mobility, with at least one station moving at vehicle speed. Such scenarios are exceptionally challenging for millimeter-wave channel sounding because they yield highly time-varying channels, which can come close to the practical limits of measurability.

Bibliography

[3rd03] 3rd Generation Partnership Project (3GPP). 3GPP TR 25.996, V6.1.0: Spatial channel model for multiple input multiple output (MIMO) simulations, December 2003.

[3rd15] 3rd Generation Partnership Project (3GPP). 3GPP TR 36.873 V12.2.0: Study on 3D channel model for LTE (Release 12), July 2015.

[3rd16a] 3rd Generation Partnership Project (3GPP). 3GPP TR 38.900 V14.1.0: Study on channel model for frequency spectrum above 6 GHz (Release 14), September 2016.

[3rd16b] 3rd Generation Partnership Project (3GPP). 3GPP TR 38.913: Scenarios and requirements for next generation access technologies, February 2016.

[Aal15] Aalto University, BUPT, CMCC, Ericsson, Huawei, INTEL, KT Corporation, Nokia, NTT DOCOMO, New York University, Qualcomm, Samsung, University of Bristol, University of Southern California. 5G channel model for bands up to 100 GHz, December 2015.

[Aal16] Aalto University, AT&T, BUBT, CMCC, Ericsson, Huawei, INTEL, KT Corporation, Nokia, NTT DOCOMO, New York University, Qualcomm, Samsung, University of Bristol, University of Southern California. 5G channel model for bands up to 100 GHz, revised version 2.2, September 2016.

[Ake88] D. Akerberg. Properties of a TDMA pico cellular office communication system. In *IEEE Global Telecommunications Conference and (GLOBECOM '88)*, volume 3, pages 1343–1349, November–December 1988.

[AMH04] H. Artés, G. Matz, and F. Hlawatsch. Unbiased scattering function estimators for underspread channels and extension to data-driven

operation. *IEEE Transactions on Signal Processing*, 52(5):1387–1402, 2004.

[ANS02] M. Al-Nuaimi and A. Siamarou. Coherence bandwidth characterisation and estimation for indoor rician multipath wireless channels using measurements at 62.4 GHz. *IEE Proceedings on Microwaves, Antennas and Propagation*, 149(3):181–187, 2002.

[AR04] C. Anderson and T. Rappaport. In-building wideband partition loss measurements at 2.5 and 60 GHz. *IEEE Transactions on Wireless Communications*, 3(3):922–928, 2004.

[ARY95] J. Andersen, T. Rappaport, and S. Yoshida. Propagation measurements and models for wireless communications channels. *IEEE Communications Magazine*, 33(1):42–49, 1995.

[BC13] S. Banerji and R. S. Chowdhury. On IEEE 802.11: Wireless LAN technology. *International Journal of Mobile Network Communications & Telematics (IJMNCT)*, 3(4), August 2013.

[BDRQL11] E. Ben-Dor, T. Rappaport, Y. Qiao, and S. Lauffenburger. Millimeter-wave 60 GHz outdoor and vehicle AOA propagation measurements using a broadband channel sounder. In *2011 IEEE Global Telecommunications Conference (GLOBECOM 2011)*, 2011.

[Bel63] P. Bello. Characterization of randomly time-variant linear channels. *IEEE Transactions on Communications, [legacy, pre - 1988]*, 11(4):360–393, 1963.

[Bel69] P. Bello. Measurement of random time-variant linear channels. *IEEE Transactions on Information Theory*, 15(4):469–475, 1969.

[BHL+14] F. Boccardi, R. Heath, A. Lozano, T. Marzetta, and P. Popovski. Five disruptive technology directions for 5G. *Communications Magazine, IEEE*, 52(2):74–80, 2014.

[BHS05] D. Baum, J. Hansen, and J. Salo. An interim channel model for beyond-3G systems: extending the 3GPP spatial channel model (SCM). In *IEEE 61st Vehicular Technology Conference (VTC 2005-Spring)*, 2005.

[BLM+14] N. Bhushan, J. Li, D. Malladi, R. Gilmore, D. Brenner, A. Damnjanovic, R. Sukhavasi, C. Patel, and S. Geirhofer. Network densification: the dominant theme for wireless evolution into 5G. *IEEE Communications Magazine*, 52(2):82–89, February 2014.

[BS94] H. Bischl and W. Schäfer. The 60 GHz mobile-to-mobile radio channel-fading statistics and estimated packet error rates. In *IEEE 44th Vehicular Technology Conference (VTC 1994)*, 1994.

[Bul02] R. J. C. Bultitude. Estimating frequency correlation functions from propagation measurements on fading radio channels: a critical review. *IEEE Journal on Selected Areas in Communications*, 20(6):1133–1143, 2002.

[CBH+14] Y. Chang, S. Baek, S. Hur, Y. Mok, and Y. Lee. A novel two-slope mmwave channel model based on 3D ray-tracing in urban environments. In *IEEE International Symposium on Personal, Indoor and Mobile Radio Communications (PIMRC)*, 2014.

[CE09] M. Cheffena and T. Ekman. Dynamic model of signal fading due to swaying vegetation. *EURASIP Journal on Wireless Communications and Networking*, 2009:1–11, 2009.

[CFM93] P. J. Cullen, P. C. Fannin, and A. Molina. Wide-band measurement and analysis techniques for the mobile radio channel. *IEEE Transactions on Vehicular Technology*, 42(4):589–603, 1993.

[Chu72] D. Chu. Polyphase codes with good periodic correlation properties (corresp.). *IEEE Transactions on Information Theory*, 18(4):531–532, 1972.

[Cis17] Cisco. Cisco visual networking index: global mobile data traffic forecast update, 2016–2021, white paper, February 2017. Available online: http://www.cisco.com/c/en/us/solutions/collateral/service-provider/visual-networking-index-vni/mobile-white-paper-c11-520862.pdf.

[CLW69] J. Cooley, P. Lewis, and P. Welch. The finite fourier transform. *IEEE Transactions on Audio and Electroacoustics*, 17(2):77–85, 1969.

[Cor95] A. M. C. Correia. Spread-spectrum to combat multipath induced intersymbol interference. In *Sixth IEEE International Symposium on*

Personal, Indoor and Mobile Radio Communications (PIMRC'95), 1995.

[Cor06] L. M. Correia, editor. *Towards Mobile Broadband Multimedia Networks, ch. 6.8: The COST 273 MIMO Channel Model*. Elsevier, 2006.

[Cox72] D. Cox. Delay doppler characteristics of multipath propagation at 910 MHz in a suburban mobile radio environment. *IEEE Transactions on Antennas and Propagation, [legacy, pre - 1988]*, 20(5):625–635, 1972.

[CR96] L. M. Correia and J. R. Reis. Wideband characterisation of the propagation channel for outdoors at 60 GHz. In *Seventh IEEE International Symposium on Personal, Indoor and Mobile Radio Communications (PIMRC'96)*, 1996.

[CRB+07] N. Czink, A. Richter, E. Bonek, J. P. Nuutinen, and J. Ylitalo. Including diffuse multipath parameters in MIMO channel models. In *IEEE 66th Vehicular Technology Conference (VTC 2007-Fall)*, September–October 2007.

[CSW02] R. J.-M. Cramer, R. A. Scholtz, and M. Z. Win. Evaluation of an ultra-wide-band propagation channel. *IEEE Transactions on Antennas and Propagation*, 50(5):561–570, 2002.

[CWM02] D. Cassioli, M. Z. Win, and A. F. Molisch. The ultra-wide bandwidth indoor channel: from statistical model to simulations. *IEEE Journal on Selected Areas in Communications*, 20(6):1247–1257, 2002.

[DFM+14] D. Dupleich, F. Fuschini, R. Mueller, E. Vitucci, C. Schneider, V. Degli Esposti, and R. Thomä. Directional characterization of the 60 GHz indoor-office channel. In *2014 XXXIth URSI General Assembly and Scientific Symposium (URSI GASS)*, August 2014.

[DK95] H. Droste and G. Kadel. Measurement and analysis of wide band indoor propagation characteristics at 17 GHz and 60 GHz. In *Ninth International Conference on Antennas and Propagation*, volume 2, pages 288–291, 1995.

[DL95] I. Dilworth and B. L'Ebraly. Propagation effects due to foliage and building scatter at millimetre wavelengths. In *Ninth International Conference on Antennas and Propagation*, volume 2, pages 51–53, 1995.

[DR00] G. D. Durgin and T. S. Rappaport. Theory of multipath shape factors for small-scale fading wireless channels. *IEEE Transactions on Antennas and Propagation*, 48(5):682–693, 2000.

[DRX98] G. Durgin, T. S. Rappaport, and H. Xu. Measurements and models for radio path loss and penetration loss in and around homes and trees at 5.85 GHz. *IEEE Transactions on Communications*, 46(11):1484–1496, 1998.

[DSA99] J. E. Dalley, M. S. Smith, and D. N. Adams. Propagation losses due to foliage at various frequencies. In *IEE National Conference on Antennas and Propagation*, pages 267–270, 1999.

[Dur00] G. D. Durgin. *Theory of Stochastical Local Area Channel Modeling for Wireless Communications*. PhD thesis, Faculty of the Virginia Polytechnic Institute and State University, 2000.

[EAS] EASY-A project: Enablers for Ambient Services & Systems Part A—60 GHz Broadband Links. Project website: http://www.easy-a.de.

[FBR+94] M. J. Feuerstein, K. L. Blackard, T. S. Rappaport, S. Y. Seidel, and H. H. Xia. Path loss, delay spread, and outage models as functions of antenna height for microcellular system design. *IEEE Transactions on Vehicular Technology*, 43(3):487–498, 1994.

[Fed14] Federal Communications Commission. NOI to examine use of bands above 24 GHz for mobile broadband, October 2014.

[FHZ13] W. Fu, J. Hu, and S. Zhang. Frequency-domain measurement of 60 GHz indoor channels: a measurement setup, literature data, and analysis. *IEEE Instrumentation & Measurement Magazine*, 16(2):34–40, 2013.

[FKKP09] R. Felbecker, W. Keusgen, A. Kortke, and M. Peter. Estimation of effective permittivity and effective thickness of inhomogeneous materials at 52–70 GHz. In *The third European Conference on Antennas and Propagation (EuCAP 2009)*, March 2009.

[FKP08a] R. Felbecker, W. Keusgen, and M. Peter. Incabin millimeter wave propagation simulation in a wide-bodied aircraft using ray-tracing. In *IEEE 68th Vehicular Technology Conference, 2008 (VTC 2008-Fall)*, September 2008.

[FKP08b] R. Felbecker, W. Keusgen, and M. Peter. Ray-tracing simulations of the 60 GHz incabin radio channel. In *XXIXth General Assembly of the International Union of Radio Science (URSI GA 2008)*, August 2008.

[FKP11] R. Felbecker, W. Keusgen, and M. Peter. Estimation of permittivity and loss tangent of high frequency materials in the millimeter wave band using a hemispherical open resonator. In *2011 IEEE International Conference on Microwaves, Communications, Antennas and Electronics Systems (COMCAS)*, November 2011.

[FM91] P. C. Fannin and A. Molina. Accuracy and dynamic range improvement of bandpass impulse response measurements using pseudorandom noise. *Electronics Letters*, 27(19):1755–1756, 1991.

[Foe02] J. Foerster. Channel modeling sub-committee report final. Technical report, IEEE P802.15 Working Group for Wireless Area Networks (WPANSs), November 2002.

[Fri46] H. T. Friis. A note on a simple transmission formula. *Proceedings of the IRE*, 34(5):254–256, 1946.

[Fri97] M. Friese. Multitone signals with low crest factor. *IEEE Transactions on Communications*, 45(10):1338–1344, 1997.

[FRKP12] R. Felbecker, L. Raschkowski, W. Keusgen, and M. Peter. Electromagnetic wave propagation in the millimeter wave band using the NVIDIA OptiX GPU ray tracing engine. In *6th European Conference on Antennas and Propagation (EuCAP 2012)*, March 2012.

[FTH+99] B. H. Fleury, M. Tschudin, R. Heddergott, D. Dahlhaus, and K. Ingeman Pedersen. Channel parameter estimation in mobile radio environments using the SAGE algorithm. *IEEE Journal on Selected Areas in Communications*, 17(3):434–450, 1999.

[FZH62] R. Frank, S. Zadoff, and R. Heimiller. Phase shift pulse codes with good periodic correlation properties. *IRE Transactions on Information Theory (Corresp.)*, 8(6):381–382, 1962.

[Gar12] L. Garber. Wi-Fi races into a faster future. *Computer*, 45(3):13–16, March 2012.

[GATM+11] A. P. Garcia Ariza, U. Trautwein, R. Müller, F. Wollenschläger, R. S. Thomä, J. Kunisch, I. de la Torre, R. Felbecker, M. Peter, and W. Keusgen. 60 GHz short-range communications: channel measurements, analysis, and modeling. *International Journal of Microwave and Wireless Technologies*, 2:201–211, March 2011.

[GGS+05] S. S. Ghassemzadeh, L. J. Greenstein, T. Sveinsson, A. Kavcic, and V. Tarokh. UWB delay profile models for residential and commercial indoor environments. *IEEE Transactions on Vehicular Technology*, 54(4):1235–1244, 2005.

[GKT+09] A. P. Garcia, W. Kotterman, R. S. Thoma, U. Trautwein, D. Bruckner, W. Wirnitzer, and J. Kunisch. 60 GHz in-cabin real-time channel sounding. In *Fourth International Conference on Communications and Networking in China (ChinaCOM 2009)*, 2009.

[GKT+10] A. P. Garcia, W. Kotterman, U. Trautwein, D. Bruckner, J. Kunisch, and R. S. Thoma. 60 GHz time-variant shadowing characterization within an Airbus 340. In *4th European Conference on Antennas and Propagation (EuCAP 2010)*, April 2010.

[Gol92] S. W. Golomb. Two-valued sequences with perfect periodic autocorrelation. *IEEE Transactions on Aerospace and Electronic Systems*, 28(2):383–386, 1992.

[GPA+15] O. Galinina, A. Pyattaev, S. Andreev, M. Dohler, and Y. Koucheryavy. 5G multi-RAT LTE-WiFi ultra-dense small cells: Performance dynamics, architecture, and trends. *IEEE Journal on Selected Areas in Communications*, 33(6):1224–1240, 2015.

[GPWK15] B. Göktepe, M. Peter, R. J. Weiler, and W. Keusgen. The influence of street furniture and tree trunks in urban scenarios on ray tracing simulations in the millimeter wave band. In *2015 European Microwave Conference (EuMC)*, pages 195–198, September 2015.

[GPWK16] B. Göktepe, M. Peter, R. J. Weiler, and W. Keusgen. The influence of street furniture, tree trunks, and traffic in urban scenarios on ray tracing simulations in the millimeter wave band. *International Journal of Microwave and Wireless Technologies*, 8:785–793, 6 2016.

[GTW+11] C. Gustafson, F. Tufvesson, S. Wyne, K. Haneda, and A. Molisch. Directional analysis of measured 60 GHz indoor radio channels using

SAGE. In *IEEE 73rd Vehicular Technology Conference (VTC 2011-Spring)*, May 2011.

[Gus14] C. Gustafson. 60 GHz wireless propagation channels: Characterization, modeling and evaluation, 2014.

[Han15] K. Haneda. Channel models and beamforming at millimeter-wave frequency bands. *IEICE Transactions on Communications*, E98-B(5):755–772, 2015.

[Has93] H. Hashemi. The indoor radio propagation channel. *Proceedings of the IEEE*, 81(7):943–968, 1993.

[HBK+15] S. Hur, S. Baek, B. Kim, J. Park, A. F. Molisch, K. Haneda, and M. Peter. 28 GHz channel modeling using 3D ray-tracing in urban environments. In *9th European Conference on Antennas and Propagation (EuCAP 2015)*, pages 1–5, May 2015.

[HBK+16] S. Hur, S. Baek, B. Kim, Y. Chang, A. F. Molisch, T. S. Rappaport, K. Haneda, and J. Park. Proposal on millimeter-wave channel modeling for 5G cellular system. *IEEE Journal of Selected Topics in Signal Processing*, 10(3):454–469, 2016.

[HCK+15] S. Hur, Y.-J. Cho, T. Kim, J. Park, A. Molisch, K. Haneda, and M. Peter. Wideband spatial channel model in an urban cellular environments at 28 GHz. In *9th European Conference on Antennas and Propagation (EuCAP 2015)*, April 2015.

[HCKP14] S. Hur, Y.-J. Cho, T. Kim, and J. Park. Millimeter-wave channel modeling based on measurements in in-building, campus and urban environments at 28 GHz. TD(14)11029, COST IC 1004, 11th MC and Scientific Meeting, Krakow, Poland, September 2014.

[HCL+14] S. Hur, Y.-J. Cho, J. A. Lee, N.-G. Kang, J. Park, and H. Benn. Synchronous channel sounder using horn antenna and indoor measurements on 28 GHz. In *2014 IEEE International Black Sea Conference on Communications and Networking (BlackSeaCom)*, pages 83–87, 2014.

[HOI+16] K. Haneda, N. Omaki, T. Imai, L. Raschkowski, M. Peter, and A. Roivainen. Frequency-agile pathloss models for urban street canyons.

IEEE Transactions on Antennas and Propagation, 64(5):1941–1951, May 2016.

[HPM+16] K. Haneda, M. Peter, J. Medbo, M. Beach, R. D'Errico, S. Wu, and J.-M. Conrat. Radio channel sounding campaigns in EU H2020 mmMAGIC project for 5G channel modeling. In *2016 International Symposium on Antennas and Propagation (ISAP)*, October 2016.

[Hus94] T. Huschka. Ray tracing models for indoor environments and their computational complexity. In *5th IEEE International Symposium on Personal, Indoor and Mobile Radio Communications (PIMRC'94)*, volume 2, pages 486–490, September 1994.

[HZK+97] J. Hubner, S. Zeisberg, K. Koora, J. Borowski, and A. Finger. Simple channel model for 60 GHz indoor wireless LAN design based on complex wideband measurements. In *IEEE 47th Vehicular Technology Conference (VTC 1997)*, volume 2, pages 1004–1008, 1997.

[ICTa] ICT-2013-EU-Japan MiWEBA project. Website: http://www.miweba.eu/.

[ICTb] ICT-317669 METIS project. Website: https://www.metis2020.com/.

[ICTc] ICT-67650 mmMAGIC project. Website: https://5g-mmmagic.eu/.

[ICT14] ICT-2013-EU-Japan MiWEBA project. Channel modeling and characterization. Deliverable 5.1, June 2014.

[ICT15a] ICT-317669 METIS project. METIS channel models. Deliverable 1.4, version 3, July 2015.

[ICT15b] ICT-671650 mmMAGIC project. Use case characterization, KPIs and preferred suitable frequency ranges for future 5G systems between 6 GHz and 100 GHz. Deliverable 1.1, November 2015.

[ICT16a] ICT-671650 mmMAGIC project. 6–100 GHz channel modelling for 5G: Measurement and modelling plans in mmMAGIC. mmMAGIC White Paper 2.1, February 2016. Available online: https://5g-mmmagic.eu/results/.

[ICT16b] ICT-671650 mmMAGIC project. Measurement campaigns and initial channel models for preferred suitable frequency ranges. Deliverable 2.1, March 2016.

[Int09] International Telecommunication Union, Recommendation ITU-R M.2135. Guidelines for evaluation of radio interface technologies for IMT-advanced, December 2009.

[Int15a] International Telecommunication Union, Recommendation ITU-R P.2040-1. Effects of building materials and structures on radiowave propagation above about 100 MHz, July 2015.

[Int15b] International Telecommunication Union, Report ITU-R M.2083-0. Framework and overall objectives of the future development of IMT for 2020 and beyond, September 2015.

[Int15c] International Telecommunication Union, Report ITU-R M.2376. Technical feasibility of IMT in bands above 6 GHz, July 2015.

[Int15d] International Telecommunication Union, Resolution COM6/20 (WRC-15). Studies on frequency-related matters for international mobile telecommunications identification including possible additional allocations to the mobile services on a primary basis in portion(s) of the frequency range between 24.25 and 86 GHz for the future development of international mobile telecommunications for 2020 and beyond, 2015. Available online: https://www.itu.int/oth/R0A0600006C/en.

[IST05] IST-2003-507581 WINNER project, . Final report on link level and system level channel models. Deliverable 5.4, v.1.4, November 2005.

[IST07] IST-4-027756 WINNER II project. WINNER II channel models. Deliverable 1.1.2, version 1.1, September 2007.

[IY02] M. F. Iskander and Z. Yun. Propagation prediction models for wireless communication systems. *IEEE Transactions on Microwave Theory and Techniques*, 50(3):662–673, 2002.

[JBTJ12] S. Jaeckel, K. Börner, L. Thiele, and V. Jungnickel. A geometric polarization rotation model for the 3-D spatial channel model. *IEEE Transactions on Antennas and Propagation*, 60(12):5966–5977, 2012.

[JMP+16] A. Jafari, T. Mavridis, L. Petrillo, J. Sarrazin, M. Peter, W. Keusgen, P. D. Doncker, and A. Benlarbi-Delai. UWB interferometry TDOA estimation for 60-GHz OFDM communication systems. *IEEE Antennas and Wireless Propagation Letters*, 15:1438–1441, 2016.

[JPK+13a] M. Jacob, S. Priebe, T. Kürner, M. Peter, M. Wisotzki, R. Felbecker, and W. Keusgen. Extension and validation of the IEEE 802.11ad 60 GHz human blockage model. In *7th European Conference on Antennas and Propagation (EuCAP 2013)*, pages 2806–2810, April 2013.

[JPK+13b] M. Jacob, S. Priebe, T. Kürner, M. Peter, M. Wisotzki, R. Felbecker, and W. Keusgen. Fundamental analyses of 60 GHz human blockage. In *7th European Conference on Antennas and Propagation (EuCAP 2013)*, pages 117–121, April 2013.

[JPS+16] S. Jaeckel, M. Peter, K. Sakaguchi, W. Keusgen, and J. Medbo. 5G channel models in mm-wave frequency bands. In *22th European Wireless (EW) Conference*, May 2016.

[JRBT14] S. Jaeckel, L. Raschkowski, K. Börner, and L. Thiele. QuaDRiGa: A 3-D multi-cell channel model with time evolution for enabling virtual field trials. *IEEE Transactions on Antennas and Propagation*, 62(6):3242–3256, 2014.

[Kai74] J. F. Kaiser. Nonrecursive digital filter design using the I0-sinh window function. In *IEEE International Symposium on Circuits and Systems (ISCAS'74)*, pages 20–23, April 1974.

[Kat97] R. Kattenbach. *Characterisation of time-variant indoor radio channels my means of their system and correlation functions (in German)*. PhD thesis, Universität Kassel, 1997.

[Kat02] R. Kattenbach. Statistical modeling of small-scale fading in directional radio channels. *IEEE Journal on Selected Areas in Communications*, 20(3):584–592, 2002.

[KGF+11] S. Krone, F. Guderian, G. Fettweis, M. Petri, M. Piz, M. Marinkovic, M. Peter, R. Felbecker, and W. Keusgen. Physical layer design, link budget analysis, and digital baseband implementation for 60 GHz short-range applications. *International Journal of Microwave and Wireless Technologies*, 2:189–200, March 2011.

[KKK+11] W. Keusgen, A. Kortke, L. Koschel, M. Peter, R. Weiler, H. Zirath, M. Gavell, and Z. He. An NLOS-capable 60 GHz MIMO demonstrator: System concept & performance. In *IEEE 9th International New Circuits and Systems Conference (NEWCAS)*, pages 265–268, June 2011.

[KKPW13] W. Keusgen, A. Kortke, M. Peter, and R. Weiler. A highly flexible digital radio testbed and 60 GHz application examples. In *43rd European Microwave Conference (EuMC 2013)*, 2013.

[KKV12] M. Kyro, V. Kolmonen, and P. Vainikainen. Experimental propagation channel characterization of mm-wave radio links in urban scenarios. *IEEE Antennas and Wireless Propagation Letters*, 11:865–868, 2012.

[Koz97] W. Kozek. On the transfer function calculus for underspread LTV channels. *IEEE Transactions on Signal Processing*, 45(1):219–223, 1997.

[KP74] R. G. Kouyoumjian and P. H. Pathak. A uniform geometrical theory of diffraction for an edge in a perfectly conducting surface. *Proceedings of the IEEE*, 62(11):1448–1461, 1974.

[KP05] W. Kozek and G. E. Pfander. Identification of operators with bandlimited symbols. *SIAM Journal on Mathematical Analysis*, 37(3):867–888, 2005.

[KUW+15] M. Kim, K. Umeki, K. Wangchuk, J. i. Takada, and S. Sasaki. Polarimetric mm-wave channel measurement and characterization in a small office. In *IEEE 26th Annual International Symposium on Personal, Indoor, and Mobile Radio Communications (PIMRC)*, pages 764–768, August-September 2015.

[KWA+07] J. Karedal, S. Wyne, P. Almers, F. Tufvesson, and A. F. Molisch. A measurement-based statistical model for industrial ultra-wideband channels. *IEEE Transactions on Wireless Communications*, 6(8):3028–3037, 2007.

[KWPW14] W. Keusgen, R. J. Weiler, M. Peter, and M. Wisotzki. Propagation measurements and simulations for millimeter-wave mobile access in a busy urban environment. In *9th International Conference on Infrared, Millimeter, and Terahertz Waves (IRMMW-THz 2014)*, September 2014.

[KZPW99] J. Kunisch, E. Zollinger, J. Pamp, and A. Winkelmann. MEDIAN 60 GHz wideband indoor radio channel measurements and model. In *IEEE 50th Vehicular Technology Conference (VTC 1999-Fall)*, volume 4, pages 2393–2397, 1999.

[Lü92] H. D. Lüke. *Korrelationssignale*. Springer-Verlag, Berlin-Heidelberg, 1992.

[LFR96] O. Landron, M. J. Feuerstein, and T. S. Rappaport. A comparison of theoretical and empirical reflection coefficients for typical exterior wall surfaces in a mobile radio environment. *IEEE Transactions on Antennas and Propagation*, 44(3):341–351, 1996.

[Lia88] S. Y. Liao. *Engineering Applications of Electromagnetic Theory*. West Publishing Company, 1988.

[Lie89] H. J. Liebe. MPM—an atmospheric millimeter wave propagation model. *International Journal of Infrared and Millimeter Waves*, 10:631–650, 1989.

[LKKP08a] J. Luo, W. Keusgen, A. Kortke, and M. Peter. A design concept for a 60 GHz wireless in-flight entertainment system. In *IEEE 68th Vehicular Technology Conference (VTC 2008-Fall)*, 2008.

[LKKP08b] J. Luo, A. Kortke, W. Keusgen, and M. Peter. 60 GHz broadband wireless transmission experiments in a NLOS indoor environment. In *2008 Asia-Pacific Microwave Conference*, December 2008.

[LLH94] B. Langen, G. Lober, and W. Herzig. Reflection and transmission behaviour of building materials at 60 GHz. In *5th IEEE International Symposium on Personal, Indoor and Mobile Radio Communications (PIMRC)*, volume 2, pages 505–509, 1994.

[LOP+12] L. Liu, C. Oestges, J. Poutanen, K. Haneda, P. Vainikainen, F. Quitin, F. Tufvesson, and P. D. Doncker. The COST 2100 MIMO channel model. *IEEE Wireless Communications*, 19(6):92–99, December 2012.

[LR01] J. C. Liberti and T. S. Rappaport. *Smart Antennas for Wireless Communications: IS-95 and Third Generation CDM Applications*. Prentice Hall, 2001.

[MAB15] J. Medbo, H. Asplund, and J. E. Berg. 60 GHz channel directional characterization using extreme size virtual antenna array. In *IEEE 26th Annual International Symposium on Personal, Indoor, and Mobile Radio Communications (PIMRC)*, pages 176–180, August-September 2015.

[McD96] J. T. E. McDonnell. Characteristics of the indoor wireless propagation environment at microwave and millimetre frequencies. In *IEE Colloquium on Radio Communications at Microwave and Millimetre Wave Frequencies (Digest No. 1996/239)*, pages 13/1–13/6, 1996.

[MEP+10] A. Maltsev, V. Erceg, E. Perahia, C. Hansen, R. Maslennikov, A. Lomayev, A. Sevastyanov, A. Khoryaev, G. Morozov, M. Jacob, S. Priebe, T. Kürner, S. Kato, H. Sawada, K. Sato, and H. Harada. Channel models for 60 GHz WLAN systems. Technical report, IEEE P802.11 Wireless LANs, doc.: IEEE 802.11-09/0334r8, 2010.

[MF93] A. Molina and P. C. Fannin. Application of mismatched filter theory to bandpass impulse response measurements. *Electronics Letters*, 29(2):162–163, 1993.

[MHP98] D. M. Matic, H. Harada, and R. Prasad. Indoor and outdoor frequency measurements for mm-waves in the range of 60 GHz. In *IEEE 48th Vehicular Technology Conference, 1998 (VTC'98)*, volume 1, pages 567–571, 1998.

[MIPGR+13] M. T. Martinez-Ingles, J. Pascual-García, J. V. Rodríguez, J. M. M. Garcia-Pardo, L. Juan-Llácer, D. P. Gaillot, M. Liénard, and P. Degauque. Indoor radio channel characterization at 60 GHz. In *7th European Conference on Antennas and Propagation (EuCAP 2013)*, pages 2796–2799, April 2013.

[MMI96] T. Manabe, Y. Miura, and T. Ihara. Effects of antenna directivity and polarization on indoor multipath propagation characteristics at 60 GHz. *IEEE Journal on Selected Areas in Communications*, 14(3):441–448, 1996.

[MMS+09] A. Maltsev, R. Maslennikov, A. Sevastyanov, A. Khoryaev, and A. Lomayev. Experimental investigations of 60 GHz WLAN systems in office environment. *IEEE Journal on Selected Areas in Communications*, 27(8):1488–1499, October 2009.

[MMS+10a] A. Maltsev, R. Maslennikov, A. Sevastyanov, A. Lomayev, and A. Khoryaev. Statistical channel model for 60 GHz WLAN systems in conference room environment. In *Fourth European Conference on Antennas and Propagation (EuCAP 2010)*, April 2010.

[MMS+10b] A. Maltsev, R. Maslennikov, A. Sevastyanov, A. Lomayev, A. Khoryaev, A. Davydov, and V. Ssorin. Characteristics of indoor millimeter-wave channel at 60 GHz in application to perspective WLAN system. In *Fourth European Conference on Antennas and Propagation (EuCAP 2010)*, April 2010.

[MPK+13] K. Mahler, P. Paschalidis, A. Kortke, M. Peter, and W. Keusgen. Realistic IEEE 802.11p transmission simulations based on channel sounder measurement data. In *IEEE 78th Vehicular Technology Conference (VTC Fall-2013)*, 2013.

[MPK+16] A. Maltsev, A. Pudeyev, W. Keusgen, R. J. Weiler, M. Peter, and I. Bolotin. Virtual antenna arrays methodology for outdoor millimeter-wave channel measurements. In *2016 IEEE Globecom Workshops (GC Wkshps)*, December 2016.

[MSA16] J. Medbo, N. Seifi, and H. Asplund. Frequency dependency of measured highly resolved directional propagation channel characteristics. In *22th European Wireless Conference (EW 2016)*, May 2016.

[MSS92] U. Martin, H. W. Schüssler, and K. Schwarz. Ein System zur Messung der Eigenschaften von Mobilfunkkanälen und ein Verfahren zur Nachverarbeitung der Messdaten. *Frequenz*, 46:178–188, 1992.

[MTS+94] T. Manabe, K. Taira, K. Sato, T. Ihara, Y. Kasashima, and K. Yamaki. Multipath measurement at 60 GHz for indoor wireless communication systems. In *IEEE 44th Vehicular Technology Conference (VTC 1994)*, pages 905–909 vol.2, 1994.

[NGM15] NGMN Alliance. NGMN 5G White Paper, February 2015. Available online: https://www.ngmn.org/uploads/media/NGMN_5G_White_Paper_V1_0.pdf.

[NK12] R. Nakamura and A. Kajiwara. Empirical study on 60 GHz in-vehicle radio channel. In *2012 IEEE Radio and Wireless Symposium (RWS)*, pages 327–330, 2012.

[NMP+16] H. A. Nguyen, K. Mahler, M. Peter, W. Keusgen, T. Eichler, and H. Mellein. Estimation of DoA based on large-scale virtual array data. In *10th European Conference on Antennas and Propagation (EuCAP 2016)*, April 2016.

[NvWF+15] M. Nekovee, P. von Wrycza, M. Fresia, M. Peter, J. Gora, J. Luo, and M. Tesanovic. Millimetre-wave based mobile radio access network for fifth generation integrated communications (mmMAGIC). In *European Conference on Networks and Communications (EuCNC)*, 2015.

[Off15] Office of Communications (OFCOM). Laying the foundations for next generation mobile services, update on bands above 6 GHz, April 2015.

[OHG15] C. Oestges, G. Hennaux, and Q. Gueuning. Centimeter- and millimeter-wave channel modeling using ray-tracing for 5G communications. In *IEEE 82nd Vehicular Technology Conference (VTC 2015-Fall)*, September 2015.

[OHI04] I. Oppermann, M. Hamalainen, and J. Iinatti, editors. *UWB Theory and Applications*. John Wiley and Sons Ltd, 2004.

[OKI09] H. Okamoto, K. Kitao, and S. Ichitsubo. Outdoor-to-indoor propagation loss prediction in 800-MHz to 8-GHz band for an urban area. *IEEE Transactions on Vehicular Technology*, 58(3):1059–1067, 2009.

[Par00] J. D. Parsons. *The Mobile Radio Propagation Channel*. John Wiley & Sons Ltd, 2nd edition, 2000.

[PFKH09] M. Peter, R. Felbecker, W. Keusgen, and J. Hillebrand. Measurement-based investigation of 60 GHz broadband transmission for wireless in-car communication. In *IEEE 70th Vehicular Technology Conference (VTC 2009-Fall)*, September 2009.

[PGP06] M. Piz, E. Grass, and M. Peter. A simple OFDM physical layer for short-range high data rate transmission at 60 GHz. In *International OFDM-Workshop (InOWo)*, 2006.

[PJK12] S. Priebe, M. Jacob, and T. Kürner. Calibrated broadband ray tracing for the simulation of wave propagation in mm and sub-mm wave indoor communication channels. In *18th European Wireless Conference (EW 2012)*, April 2012.

[PK07] M. Peter and W. Keusgen. A component-based time domain wideband channel sounder and measurement results for the 60 GHz in-cabin radio channel. In *2nd European Conference on Antennas and Propagation (EuCAP 2007)*, November 2007.

[PK08] M. Peter and W. Keusgen. Impact of antenna configuration and shadowing on the characteristics of the 60 GHz indoor wideband radio channel. In *XXIXth General Assembly of the International Union of Radio Science (URSI GA 2008)*, August 2008.

[PK09] M. Peter and W. Keusgen. Analysis and comparison of indoor wideband radio channels at 5 and 60 GHz. In *3rd European Conference on Antennas and Propagation (EuCAP 2009)*, March 2009.

[PKB08] M. Peter, W. Keusgen, and G. Böck. Kleine Wellen ganz groß – neue alte Technik für den drahtlosen Datenhighway. *NET – Zeitschrift für Kommunikationsmanagement*, 11:28–29, November 2008.

[PKF07] M. Peter, W. Keusgen, and R. Felbecker. Measurement and ray-tracing simulation of the 60 GHz indoor broadband channel: Model accuracy and parameterization. In *Second European Conference on Antennas and Propagation (EuCAP 2007)*, November 2007.

[PKH+98] J.-H. Park, Y. Kim, Y.-S. Hur, K. Lim, and K.-H. Kim. Analysis of 60 GHz band indoor wireless channels with channel configurations. In *Ninth IEEE International Symposium on Personal, Indoor and Mobile Radio Communications (PIMRC 1998)*, volume 2, pages 617–620, 1998.

[PKK07] M. Peter, W. Keusgen, and A. Kortke. Temporal structure of the 60 GHz wireless channel. In *2nd International ITG Conference on Antennas (INICA '07)*, pages 10–14, 2007.

[PKL08] M. Peter, W. Keusgen, and J. Luo. A survey on 60 GHz broadband communication: capability, applications and system design. In *2008 European Microwave Integrated Circuit Conference (EuMIC 2008)*, October 2008.

[PKM+09] P. Paschalidis, A. Kortke, K. Mahler, M. Peter, M. Wisotzki, and W. Keusgen. Wideband car-to-car MIMO radio channel measurements at 5.7 GHz in typical communication scenarios. In *IEEE 70th Vehicular Technology Conference (VTC 2009-Fall)*, September 2009.

[PKS07] M. Peter, W. Keusgen, and M. Schirrmacher. Measurement and analysis of the 60 GHz in-vehicular broadband radio channel. In *IEEE 66th Vehicular Technology Conference (VTC 2007-Fall)*, September-October 2007.

[PKW15] M. Peter, W. Keusgen, and R. J. Weiler. On path loss measurement and modeling for millimeter-wave 5G. In *9th European Conference on Antennas and Propagation (EuCAP 2015)*, April 2015.

[PMK+10] P. Paschalidis, K. Mahler, A. Kortke, M. Peter, M. Wisotzki, and W. Keusgen. Statistical evaluation and modeling of the wideband car-to-car channel at 5.7 GHz. In *2010 URSI International Symposium on Electromagnetic Theory (EMTS)*, pages 876–879, 2010.

[PMK+11a] P. Paschalidis, K. Mahler, A. Kortke, M. Peter, and W. Keusgen. Pathloss and multipath power decay of the wideband car-to-car channel at 5.7 GHz. In *IEEE 73rd Vehicular Technology Conference (VTC 2011-Spring)*, 2011.

[PMK+11b] P. Paschalidis, K. Mahler, A. Kortke, M. Wisotzki, M. Peter, and W. Keusgen. 2 x 2 MIMO measurements of the wideband car-to-car channel at 5.7 GHz on urban street intersections. In *IEEE 74th Vehicular Technology Conference (VTC 2011-Fall)*, 2011.

[PMK+12] P. Paschalidis, K. Mahler, A. Kortke, M. Peter, and W. Keusgen. Statistical evaluation of multipath component lifetime in the car-to-car channel at urban street intersections based on geometrical tracking. In *IEEE 75th Vehicular Technology Conference (VTC 2012-Spring)*, 2012.

[PNM+16] P. Paschalidis, J. Nuckelt, K. Mahler, M. Peter, A. Kortke, M. Wisotzki, W. Keusgen, and T. Kürner. Investigation of MPC correlation and angular characteristics in the vehicular urban intersection channel using channel sounding and ray tracing. *IEEE Transactions on Vehicular Technology*, 65(8):5874–5886, August 2016.

[Pro01] J. G. Proakis. *Digital Communications*. McGraw-Hill, fourth edition, 2001.

[PW06] G. E. Pfander and D. F. Walnut. Measurement of time-variant linear channels. *IEEE Transactions on Information Theory*, 52(11):4808–4820, November 2006.

[PWG+16] M. Peter, R. J. Weiler, B. Göktepe, W. Keusgen, and K. Sakaguchi. Channel measurement and modeling for 5G urban microcellular scenarios. *Sensors*, 16(8):1330, 2016.

[PWK+08a] P. Paschalidis, M. Wisotzki, A. Kortke, W. Keusgen, and M. Peter. A wideband channel sounder for car-to-car radio channel measurements at 5.7 GHz and results for an urban scenario. In *IEEE 68th Vehicular Technology Conference (VTC 2008-Fall)*, 2008.

[PWK+08b] P. Paschalidis, M. Wisotzki, A. Kortke, M. Peter, and W. Keusgen. Wideband car-to-car MIMO radio channel measurements at 5.7 GHz and issues concerning application-oriented systems. In *1st IEEE VTS International Conference on Wireless Access in Vehicular Environments (WAVE 2008)*, 2008.

[PWK+15] M. Peter, R. J. Weiler, T. Kühne, B. Göktepe, J. Serafimoska, and W. Keusgen. Millimeter-wave small-cell backhaul measurements and considerations on street-level deployment. In *2015 IEEE Globecom Workshops (GC Wkshps)*, December 2015.

[PWK+16] M. Peter, R. J. Weiler, W. Keusgen, T. Eichler, M. Kottkamp, and A. Nähring. Characterization of mm-wave channel sounders up to W-band and validation of measurement results. In *10th European Conference on Antennas and Propagation (EuCAP 2016)*, April 2016.

[PWRM+12] M. Peter, M. Wisotzki, M. Raceala-Motoc, W. Keusgen, R. Felbecker, M. Jacob, S. Priebe, and T. Kürner. Analyzing human body shadowing at 60 GHz: Systematic wideband MIMO measurements and modeling approaches. In *6th European Conference on Antennas and Propagation (EuCAP 2012)*, March 2012.

[PWU+16] M. Peter, R. J. Weiler, F. Undi, F. El-Kanawati, S. Jaeckel, L. Raschkowski, L. Thiele, K. Sakaguchi, and W. Keusgen. Investigations on the frequency dependence of the delay spread in an UMi street canyon scenario. In *2016 International Symposium on Antennas and Propagation (ISAP)*, October 2016.

[Rap02] T. S. Rappaport. *Wireless Communications, Principles and Practice*. Prentice Hall PTR, 2nd edition, 2002.

[RASM12] S. Rajagopal, S. Abu-Surra, and M. Malmirchegini. Channel feasibility for outdoor non-line-of-sight mmWave mobile communication. In *IEEE Vehicular Technology Conference (VTC 2012-Fall)*, 2012.

[RBDMQ12] T. S. Rappaport, E. Ben-Dor, J. N. Murdock, and Y. Qiao. 38 GHz and 60 GHz angle-dependent propagation for cellular & peer-to-peer

wireless communications. In *2012 IEEE International Conference on Communications (ICC)*, pages 4568–4573, 2012.

[RFS10] M. E. Rasekh, F. Farzaneh, and A. A. Shishegar. A street canyon approximation model for the 60 GHz propagation channel in an urban environment with rough surfaces. In *2010 5th International Symposium on Telecommunications (IST)*, pages 132–137, 2010.

[RGBD+13] T. S. Rappaport, F. Gutierrez, E. Ben-Dor, J. N. Murdock, Y. Qiao, and J. I. Tamir. Broadband millimeter-wave propagation measurements and models using adaptive-beam antennas for outdoor urban cellular communications. *IEEE Transactions on Antennas and Propagation*, 61(4):1850–1859, 2013.

[RQT+12] T. S. Rappaport, Y. Qiao, J. I. Tamir, J. N. Murdock, and E. Ben-Dor. Cellular broadband millimeter wave propagation and angle of arrival for adaptive beam steering systems. In *2012 IEEE Radio and Wireless Symposium (RWS)*, pages 151–154, 2012.

[RRE14] S. Rangan, T. Rappaport, and E. Erkip. Millimeter-wave cellular wireless networks: Potentials and challenges. *Proceedings of the IEEE*, 102(3):366–385, 2014.

[RSR+02] N. C. Rogers, A. Seville, J. Richter, D. Ndzi, N. Savage, R. F. S. Caldeirinha, A. K. Shukla, M. Al-Nuaimi, K. Craig, E. Vilar, and J. Austin. A generic model of 1–60 GHz radio propagation through vegetation — final report. Technical report, QinetiQ, 2002.

[RSV+16] M. Rybakowski, K. Safjan, V. Venkatasubramanian, A. Vijay, L. Dussopt, A. Zaidi, M. Peter, J. Luo, M. Fresia, and M. Shariat. Challenges and solutions for above 6 GHz radio access network integration for future mobile communication systems. In *2016 IEEE International Conference on Communications Workshops (ICC)*, pages 614–619, May 2016.

[SA95] S. Seidel and H. Arnold. Propagation measurements at 28 GHz to investigate the performance of local multipoint distribution service (LMDS). In *IEEE Global Telecommunications Conference (GLOBECOM'95)*, volume 1, pages 754–757, 1995.

[Sal13] S. Salous. *Radio Propagation Measurement and Channel Modelling*. Wiley, 2013.

[SAN01] A. G. Siamarou and M. O. Al-Nuaimi. Effects of antenna directivity, height and room size on delay spread in LOS indoor radio channels at 62.4 GHz. In *Eleventh International Conference on Antennas and Propagation*, volume 1, pages 284–287, 2001.

[SAN10] A. G. Siamarou and M. Al-Nuaimi. A wideband frequency-domain channel-sounding system and delay-spread measurements at the license-free 57- to 64-GHz band. *IEEE Transactions on Instrumentation and Measurement*, 59(3):519–526, 2010.

[SC97] P. F. M. Smulders and L. M. Correia. Characterisation of propagation in 60 GHz radio channels. *Electronics & Communication Engineering Journal*, 9(2):73–80, 1997.

[Sch03] J. Schönthier. The 60 GHz channel and its modelling. WP3-Study, IST-2001-32686-BROADWAY, Version 1.0, May 2003.

[SEF+16] S. Salous, V. D. Esposti, F. Fuschini, R. S. Thomae, R. Mueller, D. Dupleich, K. Haneda, J. M. M. Garcia-Pardo, J. P. Garcia, D. P. Gaillot, S. Hur, and M. Nekovee. Millimeter-wave propagation: Characterization and modeling toward fifth-generation systems. [wireless corner]. *IEEE Antennas and Propagation Magazine*, 58(6):115–127, December 2016.

[Sev97] A. Seville. Vegetation attenuation: modelling and measurements at millimetric frequencies. In *Tenth International Conference on Antennas and Propagation*, volume 2, pages 5–8, 1997.

[SFRC16] S. Salous, S. M. Feeney, X. Raimundo, and A. A. Cheema. Wideband MIMO channel sounder for radio measurements in the 60 GHz Band. *IEEE Transactions on Wireless Communications*, 15(4):2825–2832, April 2016.

[Shu02] A. K. Shukla. Description of a generic vegetation attenuation model for 1-60 GHz. In *COST Action 280 First International Workshop on Propagation Impairment Millimetre Wave Radio Systems*, 2002.

[Sia09] A. Siamarou. Digital transmission over millimeter-wave radio channels: A review [wireless corner]. *IEEE Antennas and Propagation Magazine*, 51(6):196–203, 2009.

[SJK10] M. Schack, M. Jacob, and T. Kürner. Comparison of in-car UWB and 60 GHz channel measurements. In *Fourth European Conference on Antennas and Propagation (EuCAP 2010),*, April 2010.

[SMB01] M. Steinbauer, A. F. Molisch, and E. Bonek. The double-directional radio channel. *IEEE Antennas and Propagation Magazine*, 43(4):51–63, August 2001.

[SMI+97] K. Sato, T. Manabe, T. Ihara, H. Saito, S. Ito, T. Tanaka, K. Sugai, N. Ohmi, Y. Murakami, M. Shibayama, Y. Konishi, and T. Kimura. Measurements of reflection and transmission characteristics of interior structures of office building in the 60-GHz band. *IEEE Transactions on Antennas and Propagation*, 45(12):1783–1792, 1997.

[Smu95] P. F. M. Smulders. *Broadband Wireless LANs: A Feasibility Study*. PhD thesis, Eindhoven University of Technology, December 1995.

[SPF+11] B. Schulte, M. Peter, R. Felbecker, W. Keusgen, R. Steffen, S. Hermann, M. Hellfeld, A. Barghouthi, S. Krone, F. Guderian, G. Fettweis, and V. Ziegler. 60 GHz WLAN applications and implementation aspects. *International Journal of Microwave and Wireless Technologies*, 2:213–221, March 2011.

[SPH+10] J. Salmi, J. Poutanen, K. Haneda, A. Richter, V. M. Kolmonen, P. Vainikainen, and A. F. Molisch. Incorporating diffuse scattering in geometry-based stochastic MIMO channel models. In *Fourth European Conference on Antennas and Propagation (EuCAP 2010)*, April 2010.

[SR15] M. K. Samimi and T. S. Rappaport. Statistical channel model with multi-frequency and arbitrary antenna beamwidth for millimeter-wave outdoor communications. In *2015 IEEE Workshops (GC Wkshps)*, December 2015.

[SRS90] S. Y. Seidel, T. S. Rappaport, and R. Singh. Path loss and multipath delay statistics in four european cities for 900 MHz cellular and microcellular communications. *Electronics Letters*, 26(20):1713–1715, 1990.

[SS03] S. Stavrou and S. R. Saunders. Review of constitutive parameters of building materials. In *Twelfth International Conference on Antennas and Propagation (ICAP 2003)*, volume 1, pages 211–215, 2003.

[SSKW05] W. Sörgel, S. Schultheis, S. Knörzer, and W. Wiesbeck. Deconvolution of the antennas from directional UWB channel measurements. In *Joint 9th International Conference on Electromagnetics in Advanced Applications (ICEAA) and 11th European Electromagnetic Structures Conference (EESC)*, pages 589–593, September 2005.

[Ste92] R. Steele. *Mobile Radio Communications*. Pentech Press Limited, Graham Lodge, Graham Road, Lodon NW3DG, 1992.

[STO+09] H. Sawada, T. Tomatsu, G. Ozaki, H. Nakase, S. Kato, K. Sato, and H. Harada. A sixty GHz intra-car multi-media communications system. In *IEEE 69th Vehicular Technology Conference (VTC 2009-Spring)*, 2009.

[STS+15] K. Sakaguchi, G. K. Tran, H. Shimodaira, S. Nanba, T. Sakurai, K. Takinami, I. Siaud, E. C. Strinati, A. Capone, I. Karls, R. Arefi, and T. Haustein. Millimeter-wave evolution for 5G cellular networks. *IEICE Transactions on Communications*, E98-B:388–402, March 2015.

[SV87] A. Saleh and R. Valenzuela. A statistical model for indoor multipath propagation. *IEEE Journal on Selected Areas in Communications*, 5(2):128–137, 1987.

[SVE88] F. K. Schwering, E. J. Violette, and R. H. Espeland. Millimeter-wave propagation in vegetation: experiments and theory. *IEEE Transactions on Geoscience and Remote Sensing*, 26(3):355–367, 1988.

[SW92a] P. Smulders and A. Wagemans. Wideband indoor radio propagation measurements at 58 GHz. *Electronics Letters*, 28(13):1270–1272, 1992.

[SW92b] P. F. M. Smulders and A. G. Wagemans. Wide-band measurements of mm-wave indoor radio channels. In *Third IEEE International Symposium on Personal, Indoor and Mobile Radio Communications (PIMRC '92)*, pages 329–333, October 1992.

[TCS94] H. J. Thomas, R. S. Cole, and G. L. Siqueira. An experimental study of the propagation of 55 GHz millimeter waves in an urban mobile radio environment. *IEEE Transactions on Vehicular Technology*, 43(1):140–146, 1994.

[The14] The International Wireless Industry Consortium (IWPC), Mobile Multi Gigabit (MoGIG) Wireless Networks and Terminals – 5000x Working

Group. Evolutionary & disruptive visions towards ultra high capacity networks, IWPC White Paper, April 2014.

[TPJ06] L. Thiele, M. Peter, and V. Jungnickel. Statistics of the ricean K-factor at 5.2 GHz in an urban macro-cell scenario. In *IEEE 17th International Symposium on Personal, Indoor and Mobile Radio Communications (PIMRC 2006)*, September 2006.

[TvWA+16] M. Tercero, P. von Wrycza, A. Amah, J. Widmer, M. Fresia, V. Frascolla, J. Lorca, T. Svensson, M. H. Hamon, S. D. Roblot, A. Vijay, M. Peter, V. Sgardoni, M. Hunukumbure, J. Luo, and N. Vucic. 5G systems: The mmMAGIC project perspective on use cases and challenges between 6–100 GHz. In *2016 IEEE Wireless Communications and Networking Conference Workshops (WCNCW)*, pages 200–205, April 2016.

[ULP+10] A. C. Ulusoy, G. Liu, M. Peter, R. Felbecker, H. Y. Abdine, and H. Schumacher. A BPSK/QPSK receiver architecture suitable for low-cost ultra-high rate 60 GHz wireless communications. In *2010 European Microwave Conference (EuMC)*, pages 381–384, 2010.

[VEDS88] E. J. Violette, R. H. Espeland, R. O. DeBolt, and F. K. Schwering. Millimeter-wave propagation at street level in an urban environment. *IEEE Transactions on Geoscience and Remote Sensing*, 26(3):368–380, 1988.

[VZ12] R. Verdone and A. Zanella, editors. *Pervasive Mobile and Ambient Wireless Communications: COST Action 2100*. Springer, London, 2012.

[WIG] WIGWAM project: Wireless Gigabit With Advanced Multimedia Support. http://www.wigwam-project.com.

[WIN10] WINNER+ project. Deliverable 5.3: WINNER+ Final Channel Models, June 2010.

[Wis07] M. Wisotzki. Entwicklung und Test eines Synchronisationsgerätes für Funkkanalmessungen. Studienarbeit, TU Berlin, 2007.

[WKM+16] R. J. Weiler, W. Keusgen, A. Maltsev, T. Kühne, A. Pudeyev, L. Xian, J. Kim, and M. Peter. Millimeter-wave outdoor access shadowing mit-

igation using beamforming arrays. In *2016 10th European Conference on Antennas and Propagation (EuCAP)*, April 2016.

[WKNP14] R. J. Weiler, W. Keusgen, H.-A. Nguyen, and M. Peter. On the choice of carrier frequency and bandwidth for 5G small cell deployments. In *2014 IEEE 25th International Symposium on Personal, Indoor and Mobile Radio Communications (PIMRC)*, September 2014.

[WKP+15] R. J. Weiler, W. Keusgen, M. Peter, I. Filippini, V. Sciancalepore, and T. Haustein. Millimeter-wave small-cell deployment scenarios as an enabler for 5G applications and use cases. In *European Conference on Networks and Communications (EuCNC 2015)*, June 2015. Available online: http://eprints.networks.imdea.org/1052/1/1570138373.pdf.

[WPK+14a] R. J. Weiler, M. Peter, W. Keusgen, E. Calvanese-Strinati, A. De Domenico, I. Filippini, A. Capone, I. Siaud, A.-M. Ulmer-Moll, A. Maltsev, T. Haustein, and K. Sakaguchi. Enabling 5G backhaul and access with millimeter-waves. In *European Conference on Networks and Communications (EuCNC 2014)*, June 2014.

[WPK+14b] R. J. Weiler, M. Peter, W. Keusgen, H. Shimodaira, K. T. Gia, and K. Sakaguchi. Outdoor millimeter-wave access for heterogeneous networks – path loss and system performance. In *2014 IEEE 25th International Symposium on Personal, Indoor and Mobile Radio Communications (PIMRC Workshops)*, September 2014.

[WPK+15a] R. J. Weiler, M. Peter, W. Keusgen, A. Kortke, and M. Wisotzki. Millimeter-wave channel sounding of outdoor ground reflections. In *2015 IEEE Radio and Wireless Symposium (RWS)*, pages 95–97, Jan 2015.

[WPK+15b] R. J. Weiler, M. Peter, W. Keusgen, A. Maltsev, I. Karls, A. Pudeyev, I. Bolotin, I. Siaud, and A. M. Ulmer-Moll. Quasi-deterministic millimeter-wave channel models for access and backhaul in MiWEBA. In *COST IC1004, Workshop on Radio Channel Models for Higher Frequency Bands*, May 2015.

[WPK+15c] R. J. Weiler, M. Peter, T. Kühne, M. Wisotzki, and W. Keusgen. Simultaneous millimeter-wave multi-band channel sounding in an urban access scenario. In *9th European Conference on Antennas and Propagation (EuCAP 2015)*, April 2015.

[WPK+16a] R. J. Weiler, M. Peter, W. Keusgen, A. Maltsev, I. Karls, A. Pudeyev, I. Bolotin, I. Siaud, and A.-M. Ulmer-Moll. Quasi-deterministic millimeter-wave channel models in MiWEBA. *EURASIP Journal on Wireless Communications and Networking*, 2016(1):1–16, 2016.

[WPK+16b] R. J. Weiler, M. Peter, W. Keusgen, K. Sakaguchi, and F. Undi. Environment induced shadowing of urban millimeter-wave access links. *IEEE Wireless Communications Letters*, 5(4):440–443, August 2016.

[WPKW14] R. J. Weiler, M. Peter, W. Keusgen, and M. Wisotzki. Measuring the busy urban 60 GHz outdoor access radio channel. In *2014 IEEE International Conference on Ultra-Wideband (ICUWB)*, September 2014.

[XKR02] H. Xu, V. Kukshya, and T. S. Rappaport. Spatial and temporal characteristics of 60-GHz indoor channels. *IEEE Journal on Selected Areas in Communications*, 20(3):620–630, 2002.

[Xu00] H. Xu. *Terrestiral Radio Wave Propagation at Millimeter-Wave Frequencies*. PhD thesis, Virginia Polytechnic Institute and State University, May 2000.

[YWK98] C.-F. Yang, B.-C. Wu, and C.-J. Ko. A ray-tracing method for modeling indoor wave propagation and penetration. *IEEE Transactions on Antennas and Propagation*, 46(6):907–919, 1998.

[Zad50] L. A. Zadeh. Frequency analysis of variable networks. *Proceedings of the IRE*, 38(3):291–299, March 1950.

[ZBN05] T. Zwick, T. J. Beukema, and H. Nam. Wideband channel sounder with measurements and model for the 60 GHz indoor radio channel. *IEEE Transactions on Vehicular Technology*, 54(4):1266–1277, 2005.